

Sapienza University of Rome

Physics Department

PhD in Astronomy, Astrophysics and Space Sciences

Ionospheric Plasma Dynamics: Investigating Solar, Geomagnetic, and Seasonal Influences with Emphasis on GPS Signal Interruptions

Thesis Advisors
Dr. Paola De Michelis, INGV
Prof. Francesco Berrilli, Tor Vergata University

Candidate
Giulia Lovati
1941222

Academic Year 2022-2023 (XXXVI cycle)

"E tutto brilla
e tutto scintilla"

Abstract

The high-latitude ionosphere is a region of intricate plasma dynamics, deeply influenced by the local topology of the geomagnetic field forming a direct connection with the magnetosphere and the solar wind. This region manifests distinct characteristics under varying solar and geomagnetic conditions, directly influencing radio communication and satellite navigation systems. This study delves into the plasma dynamics across various scales, from a global perspective down to meso- and small-scale structures, emphasizing their potential impact on technologies like Global Navigation Satellite Systems (GNSS). The foundation of this comprehensive study was laid through continuous monitoring of plasma conditions over the past decade, made possible by the ESA Swarm mission.

Firstly, the research employs the Multivariate Empirical Mode Decomposition method to deconstruct the high-latitude electron density distributions. This analysis reveals fundamental modes associated with ionospheric large-scale dynamics, displaying distinct dependencies on seasons and geomagnetic activity. Then, the study explores the influence of plasma irregularities on ionospheric dynamics, specifically focusing on their role in originating pressure-gradient currents, which can have an effect on geomagnetic field measurements. Finally, the research addresses disruptions in GNSS signals, identifying the underlying irregularities and their characteristics. Notably, the study establishes a connection between GPS Loss-of-Lock events and a specific class of turbulent irregularities. Furthermore, it provides deeper insights into their climatological dependencies. These findings extend their relevance by shedding light on potential mitigation strategies for this damaging space weather effect.

This comprehensive investigation significantly advances our comprehension of ionospheric dynamics in this complex region profoundly influenced by space weather phenomena. It offers valuable insights for mitigating various adverse effects, pushing the boundaries of our understanding of the high-latitude ionosphere. Moreover, many aspects of this study can potentially be extended to explore the ionospheres of other planets.

Keywords: High-latitude ionosphere, Ionosphere dynamics, Space weather, GNSS signal degradation, GPS Loss of Lock;

Contents

List of Figures

List of Tables

Acronyms

ACC Accelerometer

ACE Advanced Composition Explorer

AE Auroral Electrojets

ASM Absolute Scalar Magnetometer

CHAMP CHAllenging Minisatellite Payload

CIR Corotating Interaction Regions

CME Coronal Mass Ejections

doy day of the year

DSFA Detrended Structure Function Analysis

EFI Electric Field Instrument

EIA Equatorial Ionization Anomaly

EMD Empirical Mode Decomposition

EPB Equatorial Plasma Bubble

EPIs Equatorial Plasma Irregularities

ESA European Space Agency

EUV Extreme Ultraviolet

FAC Field-Aligned Current

FN False Negative

FP False Positive

FTEs flux transfer events

GNSS Global Navigation Satellite System

GOME Global Ozone Monitoring Experiment

GPS Global Positioning System

GSE Geocentric Solar Ecliptic

GSM Geocentric Solar Magnetospheric

HF High Frequency

IAGA International Association of Geomagnetism and Aeronomy

IBI Ionospheric Bubble Index

IERS International Earth Rotation Service

IGRF International Geomagnetic Reference Field

IMF Interplanetary Magnetic Field

IMFs Intrinsic Mode Functions

IMP Interplanetary Monitoring Platform

IPIR Ionospheric Plasma IRregularities

ITRF International Terrestrial Reference Frame

LEO Low-Earth Orbit

LoL Loss of Lock

LP Langmuir Probe

LRR Laser Retro-Reflector

LSTM Long Short-Term Memory

MEMD Multivariate Empirical Mode Decomposition

MFA Mean-Field-Aligned

MIT Main Ionospheric Trough

ML Machine Learning

MS Main Sequence

NEC North-East-Centre

NOAA National Oceanic and Atmospheric Administration

NPV Negative Predictive Value

PB Plasma Bubble

PBIs Poleward Boundary Intensifications

PCP Polar Cap Patch

PCPs Polar Cap Patches

PDF Probability Density Function

PFSS Potential Field Source Surface

PMAFs poleward-moving auroral forms

POD Precise Orbit Determination

PRN Pseudo Random Number

PSD Power Spectral Density

QD Quasi-Dipole

ROD Rate Of change of electron Density

RODI Rate Of change of electron Density Index

ROTEI Rate Of change of electron TEmperature Index

ROTI Rate Of change of Total electron content Index

SED Storm-Enhanced Density

SEP Solar Energetic Particle

sfu solar flux units

SL Supervised Learning

SPDF Space Physics Data Facility

SSI Solar Spectral Irradiance

SSN Sunspot Number

sTEC slant Total Electron Content

STR Star Tracker

SuperDARN Super Dual Auroral Radar Network

SVM Support Vector Machines

TEC Total Electron Content

TIEGCM Thermosphere Ionosphere Electrodynamics General Circulation Model

TN True Negative

TOI Tongue-Of-Ionization

TP True Positive

VFM Vector Field Magnetometer

WDC World Data Center

Preface

The complex dynamics of the ionosphere in high-latitude regions have long been a subject of fascination and scientific inquiry. This doctoral work represents an exploration into the intricate interplay of the ionospheric plasma, ranging from large-scale structural phenomena to smaller-scale irregularities in electron density distributions. A central focus is dedicated to understanding how these ionospheric irregularities impact Global Navigation Satellite Systems (GNSS). In a modern world that increasingly relies on precise positioning, navigation, timing, and synchronization, this study assumes critical importance. This thesis endeavors to contribute to a comprehensive understanding of the ionospheric dynamics, particularly in regions profoundly influenced by Space Weather phenomena. The work is divided into several chapters, each addressing specific facets of this multifaceted research.

Chapter 1 briefly introduces the scientific context of the work.

Chapter 2 offers an in-depth overview of the datasets instrumental to this study, which include observations from Swarm ESA mission, solar, interplanetary, and geophysical parameters from sources such as the OMNI dataset, as well as SuperDARN potential maps. Additionally, it introduces the magnetic reference frame chosen for the analysis.

Chapter 3 elaborates on the analytical techniques employed throughout the thesis. These techniques encompass the Multivariate Empirical Mode Decomposition for large-scale analysis, the Structure Function Analysis for the characterization of ionospheric irregularities, and the utilization of two Machine Learning algorithms, namely Logistic Regression and Decision Trees. These models are used for classification tasks, particularly related to Loss of Lock (LoL) events in GNSS signals.

Chapter 4 delves into the complex dynamics of plasma in high-latitude regions. It starts by decomposing ionospheric density maps into their primary components, shedding light on their relationships with changing seasonal and geomagnetic conditions. The chapter proceeds to investigate the role of irregularities in the high-latitude ionosphere and their significance in the generation of pressure-gradient currents.

Chapter 5 investigates LoL events, identified as interruptions in the Global Positioning System (GPS) signal received by Swarm satellites. The objective is to uncover the specific ionospheric irregularities causing these disruptions. After identifying a category of electron density fluctuations that appear to be the source of GPS signal interruptions, their climatological dependencies are compared with those of LoLs. The aim is to determine if this particular type of irregularity can serve as a proxy for this adverse effect on GPS systems. In this context, climatological parameters used in the analysis are employed as input features for two Machine Learning models to assess their capacity to accurately predict the occurrences of Loss of Lock events in this region.

Finally, Chapter 6 summarizes the key findings and contributions of the thesis, offering insights into the implications of the research for Space Weather effect mitigation in the ionospheric high-latitude region.

Through this doctoral thesis, the hope is to achieve a greater understanding of the ionospheric dynamics and their interactions with GNSS systems, ultimately contributing to advancements in the field of Space Weather research.

Chapter 1

Introduction

The Earth and its environment are closely linked to the Sun through a chain of causes and effects summarized in the concept of solar-terrestrial physics. Space Weather is a subset of this field, which emphasizes the applications and societal relevance. It pertains to the conditions, in all regions of space, that can harm or disrupt human activity and technology both in space and on the ground, like radio communications, Global Navigation Satellite System (GNSS), spacecraft operations, electric power transmission and pipelines. Thus, to investigate Space Weather processes, it is necessary to form an integrated view of the entire chain of processes, from the solar activity to near-Earth space and to the surface of our planet. This means to analyze the effects of solar activity on solar wind, magnetosphere and Earth's upper atmosphere, both neutral and ionized (Echer et al., 2005).

In particular, the focus of this work regards some specific aspects of the ionospheric dynamics at high latitude, which can play a role in the understanding of Space Weather effects on this region. In the next Sections the chain of phenomena that connect the Sun activity to the ionospheric plasma conditions will be deepened.

1.1 The Sun and its activity

The Sun is a G-type star and its primary physical properties are given in Table 1.1. It is a Main Sequence (MS) star, because hydrogen is still burning inside its core. Furthermore, it is the only star that can be resolved at spatial scales that are typical of fundamental physics processes. It also allows to investigate particular physical topics, like magnetohydrodynamical processes, convection at high Reynolds numbers, nonlinear systems, particle physics, among others.

An important factor for Space Weather is that the Sun is a magnetically variable star, that fluctuates in a variety of ways, ranging from a very little annual variation in its total luminosity, to violent eruptions and explosions (Eddy, 2009). The main feature of solar activity is a quasi-periodic cycle of approximately 11-year, also known as the Schwabe cycle (Schwabe, 1844), which varies in both duration and amplitude. It can last from approximately 8 to 15 years and it can vary by several orders of magnitude (Usoskin, 2023). The solar magnetic polarity inverts during this cycle. In fact, the cyclic regeneration of the Sun's large-scale magnetic field is at heart of all solar activity-related events (Charbonneau, 2013).

The variation in the solar activity is evident from several phenomena happening in this star's atmosphere. The Sun's atmosphere is divided into three regions:

Parameter	Value
Mass $M_\odot$	$1.99 \cdot 10^{30}$ kg
Radius $R_\odot$	696.340 km
Average density	1408 kg/cm^3
Gravitational acceleration on surface	274 m/s^2
Luminosity $L_\odot$	$3.828 \cdot 10^{26}$ W
Effective Black Body Temperature	5772 K
Central Temperature	$1.57 \cdot 10^7$ K
Age	$4.6 \cdot 10^9$ years

Table 1.1: Sun's main physical characteristics

1. The *photosphere* is the layer in which the Sun becomes opaque and where most of the Sun's spectrum is emitted. It consists of a thin layer, approximately 1000 km thick, with a density of 10^{23} particles per cubic metre. It is the top of the convection zone, showing a granular structure, with each cell having a diameter of about 1000 km and a lifetime of typically 5 min (Kamide and Chian, 2007). It has a temperature that varies from approximately 6000-7000 K at its base to 4000-5000 K at the top (Engvold et al., 2018).

2. The *chromosphere* is rarer and more transparent, with a density of $10^{17}m^{-3}$. It goes from just above the photosphere to the solar transition region, with an average thickness of about 1500 km. Here, the temperature gradually rises to 10,000 K (Engvold et al., 2018). Its spectrum is dominated by emission lines, like, in particular, a strong Hα emission, which gives the typical reddish color to this strata. The division with the next atmospheric layer is given by the *transition zone*, where the temperature undergoes a steep increase, exceeding 10^6K.

3. The *corona* is the most external part of the solar atmosphere. It shows extremely high temperature, of the order of 10^6K and it is even less dense than chromosphere, with a density of $10^{15}m^{-3}$ (Kamide and Chian, 2007).

The structure of the solar magnetic field and its properties change dramatically with height (Solanki et al., 2006), and this is reflected in each layer of the solar atmosphere, which is defined by particular phenomena related to the level of solar activity.

The photosphere is characterized by an highly filamented field, with most of the magnetic energy residing in magnetic flux tubes. These concentrations of magnetic field influence the behavior of surrounding plasma, leading to the formation of the features that are the base of solar activity variation in this region. Indeed, the photosphere is characterized by a variation in *Faculae* concentrations and in the number of *Sunspot*. In particular, the *Sunspot Number (SSN)* is an important activity proxy, mainly for historical reasons, being the oldest evidence of the solar activity cycle. Sunspots are due to concentrations of magnetic field, of the order of kGauss. These concentrations hamper the energy transport by convection from the solar nucleus, resulting cooler than the surrounding quiet photosphere of approximately 1500-3000 K. In this way they appear darker (Foldes and Berrilli, 2020). On the other hand, Faculae are brighter, and hence hotter, regions on the photosphere, consequences of solar magnetic fields too. They present a more irregular and larger shape with respect to sunspots. The luminosity difference with respect to the surrounding photosphere is minimal when compared with the one between photosphere and sunspots, but faculae cover a wider

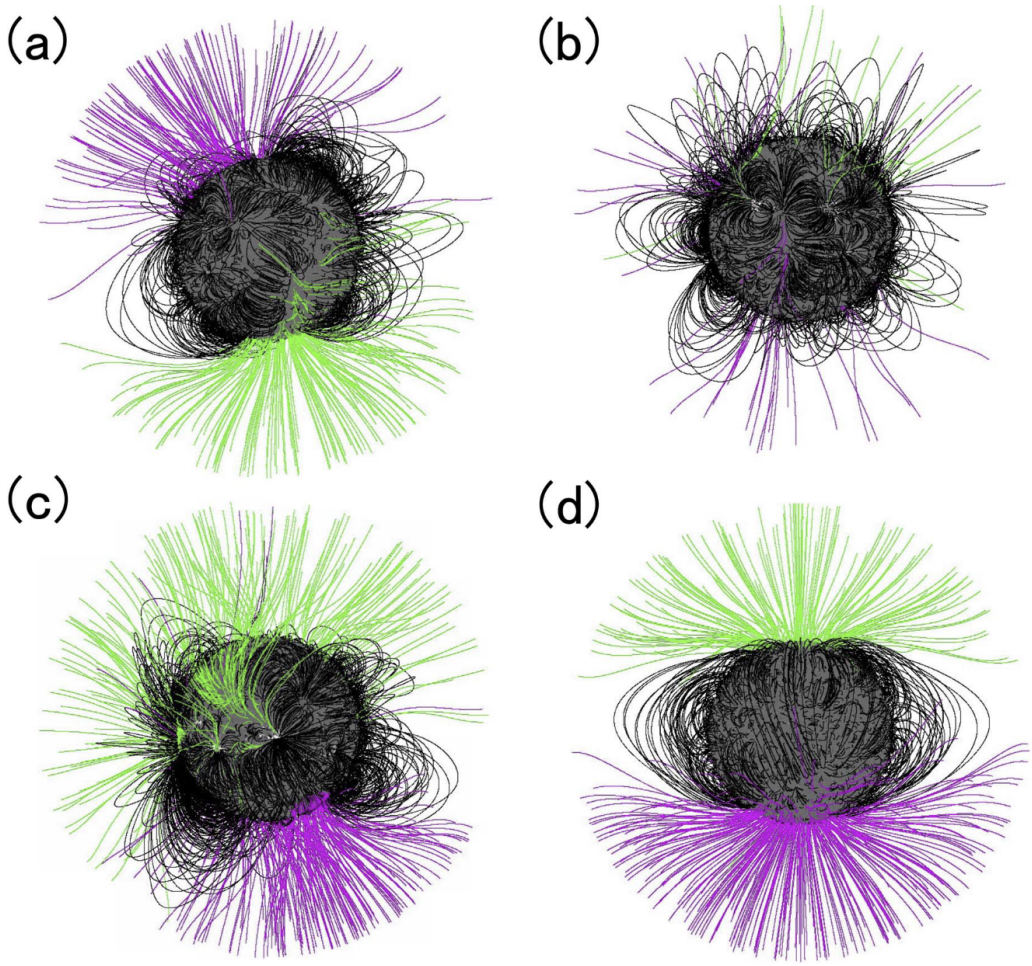

Figure 1.1: Structures of the coronal magnetic field using the Potential Field Source Surface (PFSS) model (Schatten et al., 1969) on four occasions. *(a):* CR2097 (2010 May to 2010 June), *(b):* CR2141 (2013 August to 2013 September), *(c):* CR2158 (2014 December to 2015 January), and *(d):* CR2228 (in 2020 March) Credits: Yoshida et al. (2023).

area of solar disk (Eddy, 2009). In terms of day-to-day variations, the decrease in luminosity due to sunspots prevails, turning down the Sun's output of energy of several tenths of a percent. However, the contribution from the faculae dominates when looking at greater temporal scales, averaging across months to years. This allows for an increase in solar radiation in accordance with the cycle's maximum, even if it also happens to coincide with the maximum SSN, and vice versa (Eddy, 2009).

Chromosphere, instead, is characterized by features like *prominences*, i.e. arches of cooler (with respect to the surrounding solar atmosphere) plasma, following the magnetic structure, like magnetic loops. They can extend even in the corona. They are associated with sunspot groups and, consequently, are correlated in numbers and activity with the solar cycle (Britannica et al., 2008).

Corona's dynamics and topology follow the magnetic structure too, being characterized by magnetically-formed arches, whose foot-points are rooted in the photosphere in regions of opposite magnetic polarity, most often in sunspots concentrations (Golub and Pasachoff, 2010). There are two different magnetic regions in the solar corona, exhibiting fundamentally different properties: open-field and closed-field regions. Open-field regions are typical of the polar area, although sometimes they can be found also toward the equator. They connect the solar surface with the Interplanetary Magnetic Field (IMF) and are at the origin of the fast solar wind (described in the

next Section). Thanks to these regions, an efficient plasma transport out into the heliosphere is possible, whenever chromospheric plasma is heated (Spohn et al., 2014). The consequent outflow of mass and energy results in a decreased density in open regions. In this way, they appear as *coronal holes* in X-ray images (Zirker, 1977), as there is just less of the ionized material that emits in this band. On the other hand, closed-field regions primarily contain closed-field lines, all connected to the photosphere at two ends. Here the field is strong and doesn't allow the plasma to expand (Antiochos et al., 2012). These closed magnetic field lines form loops and active regions in the solar corona (Fisk and Schwadron, 2001). An example of this configuration is recognizable in the fact that coronal magnetic loops at low and middle latitudes shape the outward-flowing coronal plasma into tapered forms, called *coronal streamers*, which extend far into interplanetary space and then curve back down. The number and distribution of these streamers varies systematically from year to year, becoming more numerous with the rising levels of solar activity (Eddy, 2009). Instead, at polar latitude, it is possible to find *polar plumes*, which are part of open-field regions. They follow the radial extension of the Sun's polar magnetic field (Golub and Pasachoff, 2010), appearing as narrow, jet-like structures. They dominate in period of low solar activity, playing a key role in the outflow of the solar wind.
Consequently, the behaviour of the coronal structures can be linked to the variations of the solar magnetic structure over the solar cycle. At solar minimum, the poloidal field dominates, i.e. the field component roughly aligned with the solar north-south poles, with open flux primarily extending from the polar areas into the interplanetary space. Instead, at solar maximum, the field is dominated by the irregular contributions from the toroidal (azimuthal) field, revealing a more complex configuration, marked by more coronal holes and active patches at lower latitudes (Yoshida et al., 2023). To better understand this point, a representation of the coronal magnetic field is reported in Figure 1.1, during different moments of the solar activity cycle, as defined by different Carrington Rotation numbers (CR)[1]. What this Figure highlights is the variation of the dipole structure and its magnitude depending on the cycle phase. Panel (a), for example, shows its configuration during the ascending phase after the solar minimum at the beginning of cycle 24th. The dipole axis results slightly tilted from the rotation axis, indicating the mixture of axial and equatorial dipoles (Yoshida et al., 2023). On the other hand, Panel (b) depicts the situation at the following solar maximum. In this period the axial dipole is unclear. Panel (c) shows the moment in which the equatorial dipole overcomes the axial dipole. Panel (d) shows again a solar minimum configuration, with the dipole field stable again and a dominant axial dipole.

During period of high solar activity also the number of eruptive events increases. As it is possible to see in the lower part of Figure 1.2, near each maximum *Flares* frequency is higher too. Flares are sudden localized release of magnetic energy, through thermal and non-thermal heating, acceleration of mass, and emission across the full electromagnetic spectrum (Buzulukova, 2017). In particular they cause an increase in the emission of ultraviolet and X-ray radiation, and produce large quantities of accelerated particles, in particular electrons in the deka-keV to deci-MeV range (Kontar et al., 2017). Together with flares (but can occur even independently) it is possible to have

[1]Integer number of Carrington rotations starting from November 9, 1853 and considering a fixed synodic rate of 27.2753 days (Ulrich and Boyden, 2006). Each Carrington Rotation starts when a specific solar feature, a sunspot for example, crosses the central meridian of the Sun. As the Sun rotates, this feature completes a full rotation and returns to the central meridian about 27 days later. This marks the end of one Carrington Rotation and the beginning of the next.

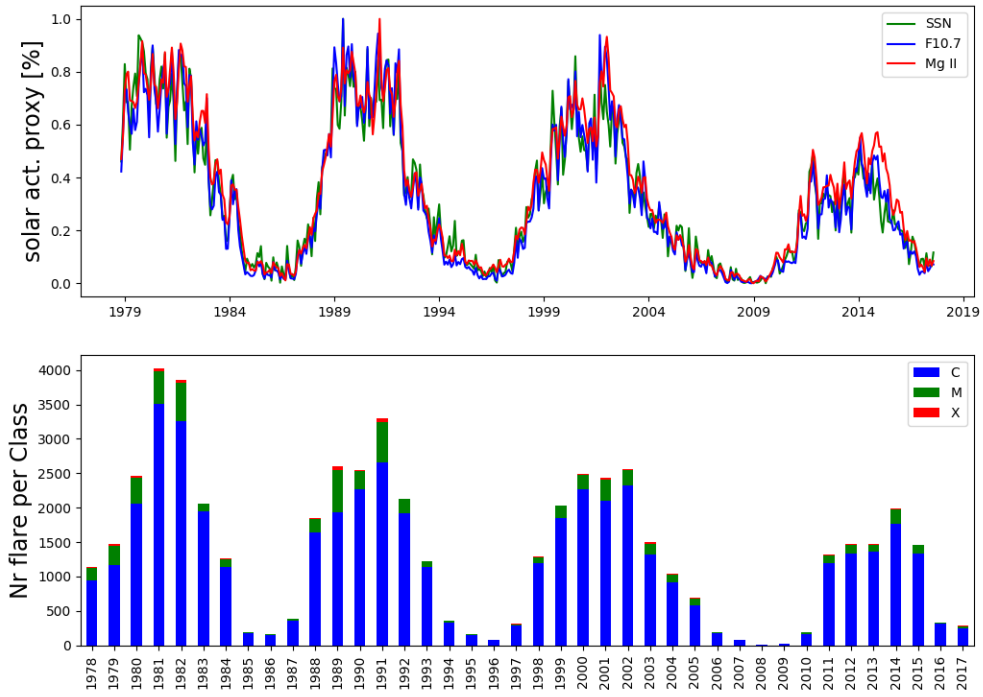

Figure 1.2: [Upper part:] Solar activity cycle highlighted by 3 proxies, i.e. Mg II, F10.7 and SSN, for the period September 1978 - September 2017. [Lower part:] Number of Solar Flares for each year. Credits: Foldes and Berrilli (2020).

Coronal Mass Ejections (CME), i.e. entire segments of the outer corona driven outward from the Sun and ejected into the solar wind streams, causing wind's largest transient disturbances and the most disruptive Space Weather events on the Earth system. It is believed that CME's formation is attributable to the destabilization of a flux rope, which is a twisted and helical magnetic structure in the Sun's lower corona. As the magnetic field lines become increasingly stretched, they can reach a state of critical instability. When this occurs, the magnetic energy stored in the twisted field lines is suddenly released thanks to magnetic reconnection. This rapid release of energy ejects the flux rope outward with respect to the solar surface, carrying with it a massive amount of charged particles. Large CMEs occur on average a few times a day at solar maximum, down to one every few days at solar minimum (Webb and Howard, 2012). The relationship between CME and flares is not straightforward. CMEs can be associated with solar flares but also not. Similarly, most flares are not associated with mass ejection. When these two types of events occur together, the CME onsets seem to precede the flares in most of the cases, containing far more total energy than the one radiated by the flare itself (Webb and Howard, 2012). Another important aspect of CMEs is that, if their velocity exceeds the the local Alfvén speed in the corona and interplanetary medium, they can originate forward shocks (Reames, 1999). These shocks can accelerate charged particles, particularly electrons and protons, to very high energies, producing the so-called Solar Energetic Particle (SEP) events (Eddy, 2009). Also solar flares can create conditions conducive to the acceleration of SEPs, through the intense ionization of the solar atmosphere, triggered by the intense bursts of X-rays and UV radiation. SEP events can play a significant role in the Space Weather context.

In order to monitor the cycle, it is possible to follow the behaviour of some solar activity proxies like the *Mg II core-to-wing ratio*, the *F10.7 index* or the already mentioned *SSN*, as it is possible

to see in the upper part of Figure 1.2. The Mg II index refers to a broad absorption feature with narrow emission peaks in the core. This emission doublet, near 280 nm, originates in the Sun's *chromosphere*, while the line wings part originates in the *photosphere*, showing much less variability. Therefore, the ratio of line core intensity to wing intensity provides a good estimate of solar variability, avoiding degradation effects (Peeters et al., 1997). F10.7 index, instead, is the radio emission at 10.7 cm, that originates high in the chromosphere and low in the corona, from regions of intense magnetic field, characterized by structures like plage, network and also sunspots (Foukal, 1998).

Lastly, another key quantity to understand the impact of solar activity on the Earth system, is the Solar Spectral Irradiance (SSI). It represents the distribution of the Sun's energy across different wavelength, providing a detailed breakdown of the amount of energy emitted by the Sun in specific regions of the electromagnetic spectrum. Indeed, besides the fact that the amount of solar energy in each part of the spectrum increases when the Sun is more active, i.e. in the peak of the ~ 11 years solar cycle, any different spectral component has its own timescales and magnitudes of variation (Eddy, 2009). This is evident when looking at Figure 1.3, which shows some characteristics of the total solar energy received at the Earth, isolating the contributes at different wavelength bands and showing their percentage variability. Even if the total irradiance, as well as its main contributors that are the near infrared and the visible bands, can vary of 0.1% at most (Fligge and Solanki, 2000), the amount of variability increases towards shorter wavelengths (Unruh and Solanki, 1998). In fact, if one focus on the central and lower parts of Figure 1.3, the greatest variation is found in the short-wave radiation, which emanates from the Sun's upper atmosphere. There the variation is of few percent in the near-UV and of $\sim 100\%$ in most of the Extreme Ultraviolet (EUV) and x-ray region. It can reach more than 1000% in narrow wavelength bands, corresponding to the wavelength of specific emission lines of highly-ionized atoms. One example is the strong emission line that can be found at 30.4 nanometers, produced by ionized helium (Eddy, 2009). Taking into account the conspicuous variability in EUV and X-ray in particular is of great relevance in the Space Weather context. In fact, even constituting only a little fraction of the total energy received at the Earth, they are sufficient to exert an almost complete control of the thermosphere and the ionosphere in particular (Eddy, 2009). Indeed, as will be deepened in the following, the solar emission in this spectral region plays a key role in affecting the propagation of radio waves and the operation of satellite-based communication systems.

1.2 Solar Wind

The high temperature and high thermal conductivity of the solar corona ensure that its plasma[2] keeps expanding outwards in the interplanetary space, reaching supersonic speeds and forming the *heliosphere* (Golub and Pasachoff, 2010). This flow of highly conductive plasma is called *solar wind*, and, inside the heliosphere, its pressure is greater than the interstellar medium one.

[2]When a gas is in a condition of sufficiently high temperature, its atoms and molecule may become ionized. Once exceeded a critical temperature, the dynamical behaviour of this collection of particles is dominated by electromagnetic forces and its properties become substantially different from the other states of matter, taking the name of *plasma* (Thompson, 2013). It consists of approximately equal numbers of free positive and negative charges. This makes plasma behave quasi-neutral on a global scale, since the randomly distributed particle electric charge fields mutually cancel. However, it remains sensible to electric and magnetic fields and it has the ability to carry electric currents and thus to generate magnetic fields (Baumjohann and Treumann, 1996).

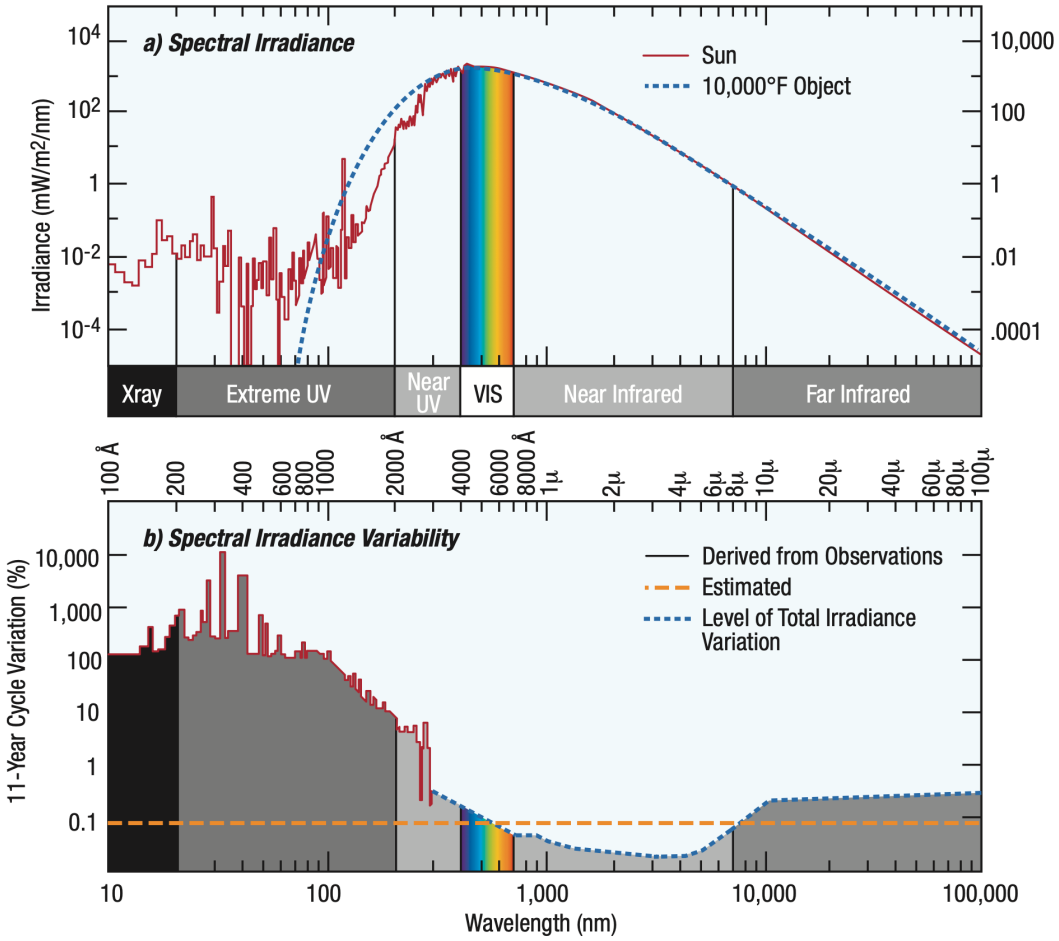

SOLAR ENERGY RECEIVED AT THE EARTH

FORM	TOTAL ENERGY IN WATTS PER ACRE AT THE TOP OF THE ATMOSPHERE	FRACTION THAT REACHES THE SURFACE	FRACTION OF TOTAL ENERGY RECEIVED	VARIABILITY
TOTAL IRRADIANCE	5500	60%	~100%	0.1%
Near infrared	2800	55%	51%	0.05%
Visible	2200	75%	40%	0.1%
Near-ultraviolet	490	40%	9%	1%
Far-infrared	10	20%	0.14%	0.1%
Far-ultraviolet	.5	0	0.01%	15%
EUV and x-ray	.2	0	0.005%	up to 200%
PARTICLES				
Solar protons	0.002		negligible	up to x100
Solar wind particles	0.0003		negligible	up to x30
Galactic cosmic rays	0.000006		negligible	20% due to solar modulation

Figure 1.3: *Upper part:* The red line indicates the amount of solar electromagnetic radiation at different wavelengths, as registered on the top of the Earth's atmosphere. The dashed blue line reports the relative amount of radiation expected from an ideal radiator at a photospheric temperature equal to the Sun's one. *Central part:* percentage variability of solar radiation at different wavelengths. *Lower part:* table reporting different characteristics of the solar energy received at the Earth, in terms of both the total irradiance, also divided into the different wavelength ranges contributions, and particles. Credits: Eddy (2009).

Solar wind is principally composed of electrons and protons (and a small percentage of ions). At 1 A.U. its temperature is about 10^5 K, while the number density is $\backsim 7\ cm^{-3}$, speed of $\backsim 450\ km/s$ and magnetic field strength $\backsim 5\ nT$ (Bhardwaj et al., 2014). On average, it results to lie near the ecliptic plane, in an Archimedean spiral pattern, but with highly variable direction (Russell, 2001). The electrical conductivity of the solar wind plasma is so high that the solar magnetic field results "frozen into" the wind flow, as stated by the *Alfvén theorem*. Since the surface magnetic field of the Sun is organized into discrete areas of either positive or negative polarity, solar wind preserves the signature of its place of origin (Eddy, 2009). The direction of the frozen-in magnetic field, also known as IMF, has a very important role in Space Weather phenomena, as it will be described in the following Sections.

In this regard, solar wind can be divided into two categories:

1. *High speed solar wind:* with bulk velocities between about 500 km/s and 800 km/s (Verscharen et al., 2019). It originates from the already mentioned *coronal holes*, where the magnetic field is nearly unipolar and the plasma density is low. As a result, the magnetic field carried by this sort of stream will have a specific polarity.

2. *Low speed solar wind:* with bulk velocities between about 300 km/s and 500 km/s (Verscharen et al., 2019). This wind typically originates in coronal streamers, which overlap regions of field polarity reversals. As a result, in this scenario, the reversal of IMF is achievable within the same stream.

The origin of the two types of solar wind on different coronal structures was confirmed by several studies based on Ulysses mission measurements (Ebert et al., 2009, McComas et al., 1998, 2000, 2003, Phillips et al., 1995). Since the provenience of a specific type of solar wind depends on solar atmosphere's structures, solar wind, and hence IMF, behaviour show a correlation with the 11-year cycle too. For example, as one can see in Figure 3 of Verscharen et al. (2019), during solar minimum there is a clear boundary between regions characterized by fast and slow wind at $\pm 20°$ heliographic latitudes. Instead, during solar maximum, fast and slow wind originate from neighboring patches everywhere in the solar corona. Thus, in period of high solar activity, the occurrence of the two types of wind streams does not strongly correlate with heliographic latitude. This highlights the crucial role of the coronal magnetic-field configuration in determining the properties of the wind streams (Verscharen et al., 2019).

Another important solar wind phenomenon is the one called *Corotating Interaction Regions (CIR)*. They are more frequent during the declining phase of the solar cycle, because coronal holes, and thus high speed solar wind, tend to dominate, expanding from the polar regions to equatorial regions (Kamide and Chian, 2007). During its expansion, high speed solar wind encounters low speed flows ahead. This interaction creates a long lasting large-scale plasma structure of enhanced pressure, the CIR (Richardson, 2004). Together with CME, CIR is one of the two primary mechanisms that are known to be the main sources of enhanced *dawn-to-dusk electric fields*, of substantial duration, in the interplanetary medium. As explained in the next session, these electric fields are caused by a combination of solar wind velocity and southward IMF and have a key role in Space Weather events like *Geomagnetic Storms* (Kamide and Chian, 2007).

1.3 Magnetosphere

The Earth has an internal dipole magnetic moment of $8 \cdot 10^{15}\, Tm^3$, generated by a magnetic dynamo deep inside the planet, in the fluid, electrically conducting core (Russell, 2000). The resulting magnetic field is called *main field* and it is one of the two contributions to the so-called *internal field*, together with the *lithospheric* or *crustal* one. This last field is generated by the remanent and induced magnetization of the crust and upper mantle (Lühr et al., 2009). Measurements at or close to the Earth's surface also record the fields generated by dynamic electrical currents flowing in the ionosphere and magnetosphere, the so-called *external field*. To this list, it is also possible to add the fields induced in the Earth by time variations in the ionospheric and magnetospheric currents, and the fields generated by ocean currents and tides. However, the most prominent contribution to the total geomagnetic filed is the one given by the main field (Lühr et al., 2009), which, in first approximation ($\sim 90\%$), can be described as a dipole magnetic field, with an axis which is tilted of about 10.3° with respect to the Earth rotation axis. A more detailed description can be obtained by adding higher degree multipoles. When using spherical harmonic analysis, it is necessary to consider about 12 degree terms to obtain a complete description of the field originated by the Earth's core (Lühr et al., 2009). Most global models of the Earth's magnetic field use spherical harmonics (Kono, 2010). For example, the last version of the International Geomagnetic Reference Field (IGRF), i.e. the most utilized model regularly published by International Association of Geomagnetism and Aeronomy (IAGA), arrives to a maximum degree of N=13 (Alken et al., 2021).

When solar wind reaches the region of space permeated by Earth's magnetic field, it is unable to pass through it and instead collides with the obstruction at supersonic speed, causing a *bow shock wave*. Successively, solar wind starts to slow down and part of its kinetic energy is converted into thermal energy, creating a region of thermalized subsonic plasma, called *Magnetosheat*, which has an average thickness of $2 - 3\, R_\oplus$ (Earth radius) (Kamide and Chian, 2007). Here, the plasma is denser and hotter than the solar wind one, and the magnetic field strength reaches higher values (Baumjohann and Nakamura, 2007). Then, it reaches the *Magnetopause*, the surface where, in first approximation, the solar wind's dynamic pressure and the Earth's magnetic pressure are equal. Actually, magnetopause is a boundary with a finite thickness, that depends on the gyro radius[3] of the incoming plasma particles (Russell, 2003). Here, the solar wind is deflected because the frozen-in IMF cannot penetrate in another magnetic field. Doing that it deforms the shape of the geomagnetic field, creating the already mentioned *Magnetosphere*, that is a highly dynamical system, compressed on the dayside and stretched out into a long magnetotail in the night side (Baumjohann and Nakamura, 2007). This structure keeps changing depending on the solar activity. Under nominal solar wind conditions, the nose of the magnetosphere is located $\sim 10\, R_\oplus$ on the side facing the Sun, while it has a more variable extension in the nightside, typically $\sim 20 - 30\, R_\oplus$. Also the magnetosphere's orientation depend on solar wind's direction (Kamide and Chian, 2007).

In some regions the conditions could be such as to allow the *magnetic reconnection* phenomenon. This can happen, for example, especially in the thin and intense current sheets of the magnetopause

[3]The *gyro radius*, or Larmor radius, is the radius of the circular orbit followed by a particle of mass m and charge q, that moves in the presence of a magnetic field B with a component of its velocity $v_\perp$ perpendicular to that field Prolss and Bird (2004):

$$r = \frac{m v_\perp}{|q|\, B}$$

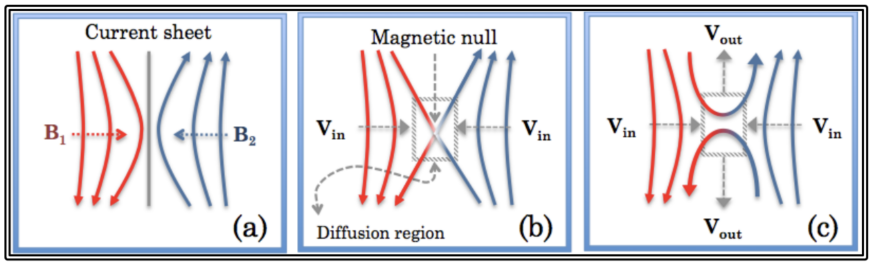

Figure 1.4: A 2-dimensional representation of the geometry of magnetic reconnection. (a): two magnetic fields delimited by a current sheet pinch together. (b): two opposite field lines reconnect because of the presence of a diffusion region of finite conductivity. (c): the newly reconnected field lines convect away, carrying plasma with them. Credits: Genestreti et al. (2012)

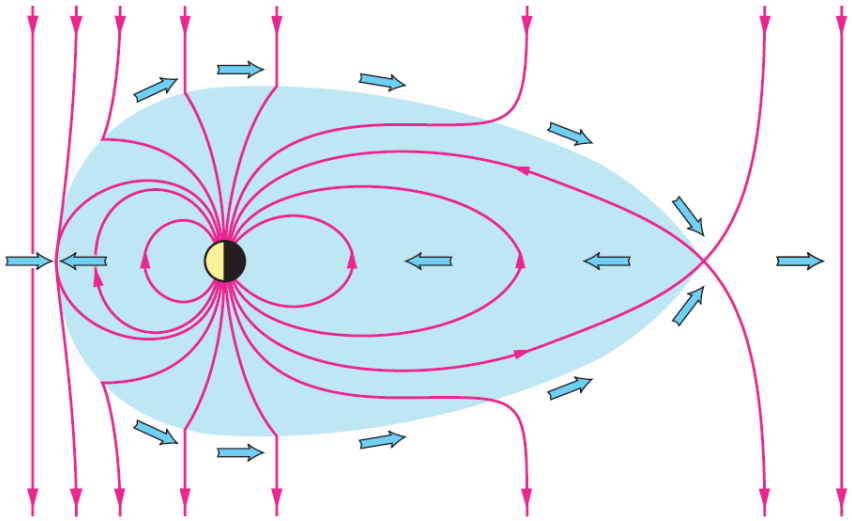

Figure 1.5: Magnetic reconnection and convection cycle in the magnetosphere. Credits: Baumjohann and Nakamura (2007)

and the magnetotail neutral sheet (as represented in Figure 1.5). Here, conductivity can pass from a near infinite value to a finite one. In this case, the magnetic field lines can diffuse through the plasma and originate the phenomenon that is summarized in Figure 1.4, changing the magnetic field topology and allowing the transfer of energy and particles inside the magnetosphere (Yamada et al., 2010). In fact, this phenomenon allows some of the solar wind lines to break and reattach to magnetosphere's lines, allowing the solar-wind plasma to penetrate the magnetosphere and generating global convection (Baumjohann and Nakamura, 2007), summarized in Figure 1.5. In this scenario, the angle between the IMF and the terrestrial magnetic field plays a key role, because field lines should be antiparallel in order to have reconnection. For example, in an idealized situation where IMF is directed completely southward, a reconnection line could form in the equatorial section of the dayside magnetopause. This helps understanding why phenomena like geomagnetic storms and substorms are related to prolonged flows of solar wind carrying mainly southward IMF. In actual cases, reconnection can occur in many different point of the magnetopause and IMF has the east or west component which more often exceeds the north-south component (Kamide and Chian, 2007).

Among the different phenomena caused by the interaction between solar wind and Earth, there is the development of a complex system of currents that affects both the magnetosphere and the ionosphere. These currents are important constituents of the dynamics of plasma around the Earth.

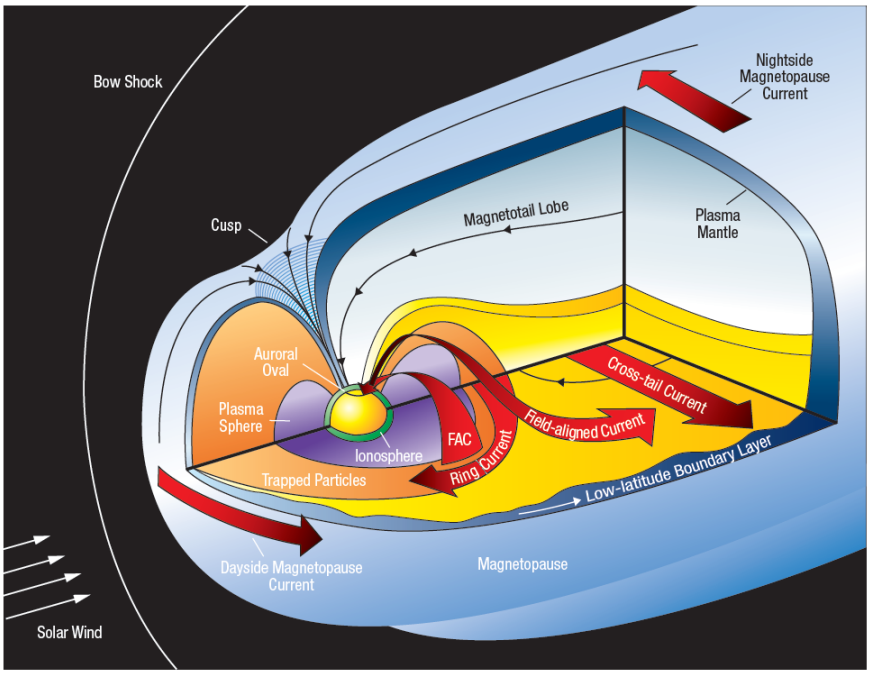

Figure 1.6: Representation of the main magnetospheric currents. Credits: Eddy (2009).

They transport charge, mass, momentum, and energy, and they generate their own magnetic fields, contributing to the already mentioned *external field*, which influences and perturbs significantly the preexisting field (Ganushkina et al., 2018). The magnetospheric current system is summarized in Figure 1.6. The principal types of current involved in this region are: the *Chapman-Ferraro magnetopause currents*, developing on the dayside and on the tailside magnetopause, flowing around the polar cusp in closed loops, the *cross-tail current*, which is a thin sheet of current flowing westward in the magnetotail, in correspondence of the near-equatorial plane (Tsyganenko, 1989), the *ring current*, which is a very important toroidal-shaped current, flowing westward around the Earth, in a region between $2\,R_\oplus$ to $9\,R_\oplus$ (Daglis, 2006), and the *Field-Aligned Current (FAC) or Birkeland currents*, flowing parallel to the magnetic field, connecting the magnetospheric current system to the ionospheric one (Iijima and Potemra, 1976).

During intense Space Weather events, like the arrival at the Earth of a CME characterized by a predominant southward IMF component, magnetic reconnection at the magnetopause can exhibit a significant increase. This phenomenon exerts notable effects on the magnetospheric shape, leading to its erosion on the dayside and an elongation on the nighside. Moreover, it influences the magnetospheric current system in terms of both its spatial distribution and intensity. In fact, through the magnetic reconnection process, there is a substantial transfer of energy from the solar wind to the inner regions of the magnetosphere. Additionally, a significant flux of particle can penetrate the magnetosphere, resulting in an augmentation of the existing currents. During geomagnetic storms, the horizontal component of the measured magnetic field at earth, H, drops significantly, especially at equatorial latitudes, where it can vary from -25 nT to -600 nT. The depression during a storm is caused by the enhanced ring current, with additional contributions from the magnetopause and tail currents (Kamide and Chian, 2007).

1.4 Ionosphere

The ionosphere is a layer within the Earth's atmosphere that extends from approximately 60 kilometers above the Earth's surface to an altitude of about 1,000 kilometers (Kamide and Chian, 2007). It is composed of charged particles, including electrons and ions, which arise from the ionization of neutral particles due to solar EUV and x-ray radiation and the collision of energetic particles coming from the solar wind or the magnetosphere. In fact, as the solar shortwave radiation reaches this region, it is gradually absorbed by the neutrals composing the upper part of the atmosphere. Being H, O, O_2 and N_2 the most abundant species, their ionization threshold require at least a radiation with wavelengths lower than 100 nm, corresponding to the EUV band (Kamide and Chian, 2007). Being sustained in great part from this part of the solar radiation spectra, ionosphere will be also deeply influenced by the conspicuous variability characterizing this wavelength range, as showed in Figure 1.3, being highly impacted by the solar cycle and, on shorted timescale, by momentary events like solar flares, among others. Moreover, the ionosphere undergoes the dramatic daily changes in received radiation due to fact that there is a portion which is directly exposed to the Sun and a portion on the nightside. This whole picture translates in an highly variable layers, both in terms of location and timescale, affecting its structure and density (Eddy, 2009). These characteristics are to a certain extent captured by the classification into different horizontal layers, which are:

- *D layer:* it extends approximately from 60 to 90 km, with a relatively low density, below $10^{10}\,\mathrm{m}^{-3}$ in normal condition. It is sustained principally by X rays and Lyman α emission line, but, during intense geomagnetic events, particle precipitation can contribute to ionization enhancement even at these altitudes (Kivelson and Russell, 1995);

- *E layer:* it goes from approximately 90 km to 130 km, with a density maximum around 120 km, due to the high production of O_2^+ ions (Kamide and Chian, 2007).

- *F layer:* the region above 130 km, where 2 other sublayers can be identified. The first, called F_1, goes from approximately 140 km to 180-200 km, with a density maximum at 150 km mainly due to the production of O^+ and N_2^+, which are at the origin of the NO^+ ion. Above 180 km there is the transition from molecular to atomic ions, with the dominance of O^+. Herein lies the F_2 layer, which has a maximum between 250 and 400 km (Kamide and Chian, 2007). The area above the F_2 density maximum is often referred to as *topside* ionosphere and it is characterized by a density decline up to a transitional altitude where O^+ ions become less abundant compared to H^+ and He^+. This transitional altitude can fluctuate, especially with the variation of geomagnetic activity, typically remaining above 500 kilometers at night and 800 kilometers in the dayside. In some cases, it may even extend as high as 1100 kilometers (NOAA).

These strata can significantly affect the propagation of radio frequency signals passing through the ionosphere. The possible effects are several and include reflection, absorption, refraction, retardation and scintillation. For example, the D layer, especially during daytime, can absorb frequencies above $\sim$ 1 MHz and reflect signals with a frequency below this value (Cannon et al., 2005). The extensive human use of the entire radio spectrum has revealed over the years that variations and irregularities in the ionosphere, occurring on a variety of spatial and temporal scales, can influence

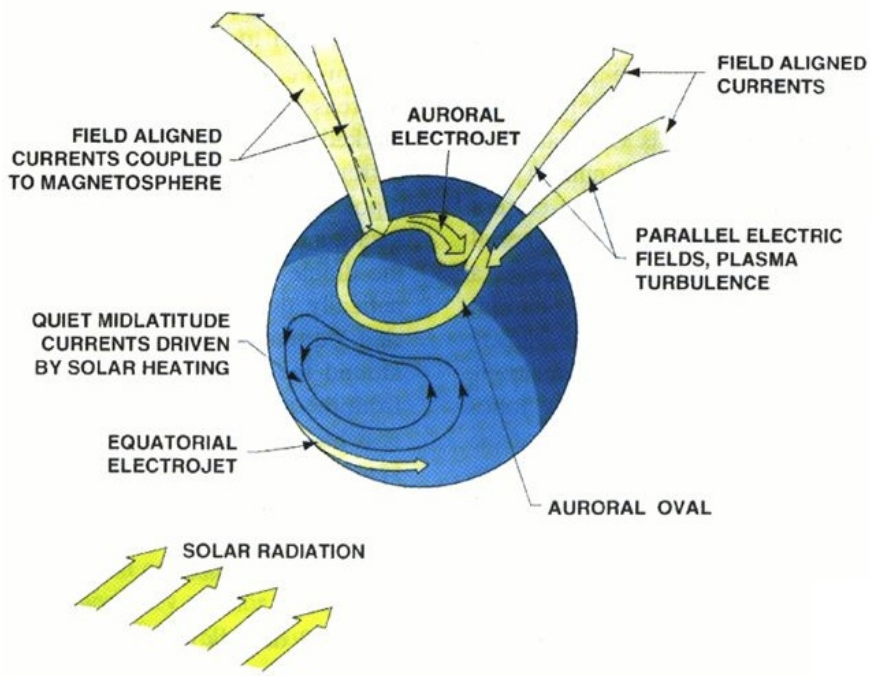

Figure 1.7: Summarized representation of the ionospheric current system. Credits: GFZ-Postdam.

a wide range of radio communications, including GNSS signals, as will be discussed further in this thesis.

Ionosphere is also characterized by a complex current system, as it is possible to see in Figure 1.7. In particular, ionospheric charged particle are in coupling with the upper atmosphere neutral component, because of the collisions. This means that specifically ions are influenced by atmospheric winds and tidal oscillations, being forced to move across the magnetic field lines, while the electrons move much slower and perpendicular to both the field and the neutral wind. This produces a current and an electric field due to charge separation, which in turn has an effect on the current (Baumjohann and Nakamura, 2007).

During the day, most ionospheric currents flow in the E-layer, while during the night, this layer, at least at low and middle latitudes, almost disappears, letting the currents flow for the most part in the F-layer, at around 300 km (Rishbeth and Müller-Wodarg, 2006). This wind-driven dynamo causes two current systems in the mid-latitude and equatorial ionosphere, mainly driven by the $\vec{E} \times \vec{B}$ field, induced by the motion of ions (Baumjohann and Nakamura, 2007). The first one is the *Sq (Solar Quiet)* current, result of the daily variation of the atmospheric motion caused by the tides of the atmosphere, excited by the heating of the atmosphere due to solar radiation. This current system is made of two vortex, one for each hemisphere, which come into contact at the geomagnetic equator (Baumjohann and Nakamura, 2007). The second current is the *Equatorial Electrojet* one, originating in the touching region of the two Sq vortexes. Here, the conditions are such as to have a huge enhancement in the effective conductivity, which leads to an amplification of the jet current. This happens not only for the encounter of the two Sq currents, but even because of the topology of the magnetic field at the equator, together with the nearly perpendicular incidence of solar radiation (Baumjohann and Nakamura, 2007).

Another ionospheric region characterized by important currents is the polar zone. Firstly, it is characterized by *ionospheric convection*, due to the movement of plasma flux tubes across the

polar caps. In fact, with the occurrence of magnetic reconnection at the magnetopause, solar wind IMF lines connect to the magnetospheric lines, dragging them tailward, as depicted in Figure 1.5. These field lines carry with them the magnetospheric and, at lower altitudes, also the ionospheric plasma. Once arrived at the nightside end of the magnetosphere, the field lines can reconnect, resulting in a closed and stretched terrestrial field line in the magnetotail and an open solar wind field line downtail. At this point, because of magnetic tension, the stretched tail field line relaxes and shortens in the earthward direction, transporting the plasma, to which it is frozen, back to the Earth again (Baumjohann and Nakamura, 2007). At ionospheric altitudes this translates into a two-cell convection pattern in the plane perpendicular to the magnetic field lines, with an anti-sunward flow over the polar cap and a sunward flow at lower latitudes, on both the dawn and dusk flanks of the auroral oval zone. (Lester, 2003, Tanaka and Mandic, 2007). This convection pattern is equivalent to an ionospheric electric field, directed dawn-to-dusk across the polar cap (Schunk and Nagy, 2009). This electric field in turn generates three types of currents: the already mentioned *FAC*, the *Pedersen currents*, which flow perpendicular to the magnetic field lines and parallel to the ionospheric convection field, and *Hall currents*, that flow perpendicular to both the magnetic and the electric field (Baumjohann and Nakamura, 2007). The resulting most prominent current in this region is the *Auroral Electrojet* one. The precipitation of particles in the auroral oval causes an increase of ionization and thus of the conductivity in this region. This translates into a jet-like current, of the order of some million amperes, formed predominantly by an eastward current in the dusk side of the oval and by a westward current in the dawn side (Vennerstrom and Moretto, 2013).

The ionosphere can be roughly dived into three region with distinct characteristics and dynamical properties, characterized by a different amount and orientation of the received solar radiation and the relative inclination of the Earth's magnetic field. These are the equatorial, mid-latitude and high-latitude regions. In this work the focus will be on the last mentioned, which is marked by an extremely complex plasma dynamics. Here the coupling with the magnetosphere is particularly intense, resulting in the already mentioned plasma convection motion. Since the dayside solar wind-magnetosphere coupling processes exhibit such strict control over the strength and morphology of the high-latitude ionospheric potential, it is necessary to further discuss the response of the convection patterns to the solar wind parameters such as the IMF. In fact, the shape and behavior of this pattern are highly dependent on the IMF's *orientation* and *magnitude*, as highlighted by Figure 1.8, because of the dominant role of this parameter in the magnetic reconnection process on the dayside magnetopause (Cowley, 1982), as anticipated in Section 1.3. The most favorable orientation for this phenomenon is the southward IMF ($B_z < 0$, see Figure 1.8 maps in the bottom row). When the IMF has a northward component ($B_z > 0$), a noticeable departure from the previously described convection patterns is observed. Although reconnection can still occur for positive B_z values, it will take place poleward with respect to the magnetic cusp, as can be seen in Figure 1.8 maps in the upper row. This can lead to a flow toward the Sun over the polar cap, resulting in smaller and reversed convection cells (Fear, 2021). Furthermore, the region of significant plasma motion is considerably restricted to higher latitudes compared to the southward IMF (Cowley et al., 1991). The high-latitude convection pattern can also be influenced by the IMF B_y and B_x component. When using the "dipole plus uniform field" model, IMF B_y component produces an asymmetry of the cells with respect to the noon-midnight meridian, while IMF B_x component creates an asymmetry

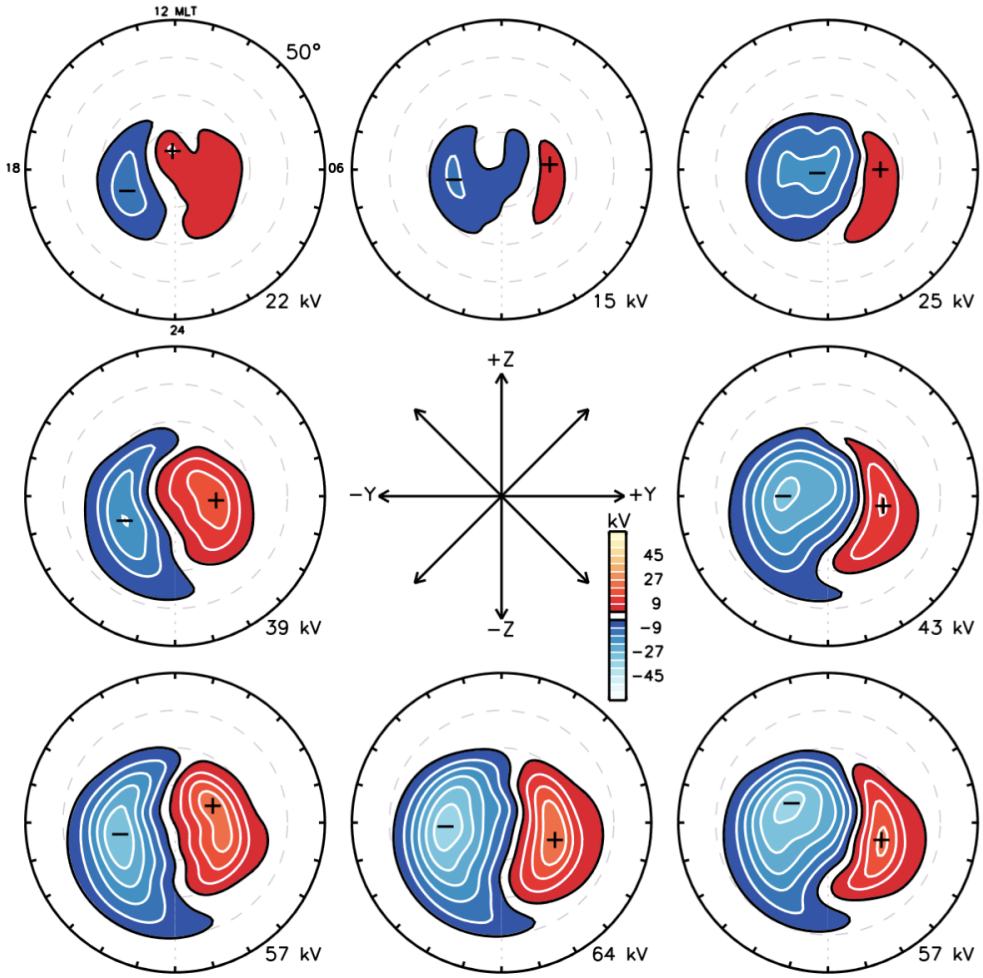

Figure 1.8: Convection patterns obtained using SuperDARN model, organized depending on the relative IMF clock angle. Color map refers to the electrostatic potential value. Maps are in Magnetic Local Time (MLT) and magnetic latitude coordinates, with a low-latitude boundary of 50° magnetic latitude. The positions of the potential maxima (plus signs) and minima (minus signs) are marked, and the cross-polar cap potential difference is given at the bottom right of each panel. Credits: (Thomas and Shepherd, 2018).

with respect to the dawn-dusk meridian (Cowley et al., 1991). However, in the literature, the effect of IMF B_x component is often overlooked, and most of the empirical functions proposed to describe the solar wind-magnetosphere-ionosphere coupling only consider the B_z and B_y components (Peng et al., 2010). The spiral structure of the IMF leads to a strong negative correlation between B_x and B_y components. As a result, a positive sign of one component is usually associated with a negative sign of the other one (Cowley et al., 1991, Karpachev et al., 1995). This means that the effect of IMF B_x component may already be accounted for when considering the B_y component alone. Therefore, some empirical functions used to describe the solar wind-magnetosphere-ionosphere coupling may implicitly include the influence of the B_x component, even if it is not explicitly included (Peng et al., 2010).

A key aspect of the work that will be presented in the following Chapters, is the presence of *irregularities* in the ionospheric plasma distribution.

1.4.1 Ionospheric irregularities

The ionosphere is subject to various forms of irregularities, manifesting as localized fluctuations in electron density, which give rise to inhomogeneities in the ionospheric refractive index (Jin et al., 2019). A profound knowledge of these irregularities is crucial because of their significant impact on radio wave propagation, satellite-based navigation systems, and space-based technologies.

The exploration of ionospheric irregularities has evolved substantially over the years. Early investigations were primarily conducted through ground-based observations of ionospheric scintillation and were characterized by limited spatial coverage (Aarons, 1982, Basu et al., 2002, Wernik et al., 2003). With the advent of satellite technology and advances in remote sensing techniques, researchers gained the ability to monitor irregularities on a global scale, with the possibility to have a better coverage also of the high-latitudes, which before were poorly monitored due to the limited number of ground receiving stations in these regions (Jin et al., 2019).

In any case, both ground-based scintillation measurements, as well as in-situ satellite measurements, showed from the beginning that ionospheric irregularities are concentrated mainly in three regions: near the magnetic equator, predominantly in the pre-midnight and midnight sectors, in the nightside auroral zone, and in the polar regions, observed at almost all local times (e.g. Basu et al. (1988), Kil and Heelis (1998), Tsunoda (1988), Watanabe and Oya (1986), Wernik et al. (2003), Woodman and La Hoz (1976), Yokoyama et al. (2007)). When considering different latitudes, one has to take into account different dynamical processes that are at the base of plasma irregularities and the consequent plasma structuring.

Irregularities in the equatorial ionosphere

The equatorial F-region ionosphere, which is the region approximately confined within $\pm 30^{\circ}$ in magnetic latitude, exhibits irregularities in the electron density distribution, primarily arising after sunset (Kil and Heelis, 1998), originated by the nonlinear evolution of the Rayleigh–Taylor instability (Kelley, 2009). The most relevant type is called Equatorial Plasma Bubble (EPB). After sunset, the ionospheric F region undergoes a transition due to the decreasing influence of solar EUV radiation. This results in a zone of reduced plasma density near the bottom of the equatorial ionosphere. These irregularities ascend, propelled by the ambient plasma drift, until they reach the topside of the ionosphere. This ascent can extend to altitudes as high as 1200 kilometers or more (Cherniak et al., 2019). These plasma depletions, with densities one to three orders of magnitude lower than the surrounding environment, occur in the nighttime equatorial ionosphere and are oriented to the geomagnetic field. Their typical size ranges from a few meters to hundreds of kilometers (Tsunoda et al., 1982).

Irregularities in the high-latitude ionosphere

The high-latitude ionosphere appears as highly structured, involving scales ranging from hundreds of km to few cm (Wernik et al., 2003). The regions which are more subject to the presence of irregularities are:

1. *the cusps:* i.e. the region of enhanced particle precipitation, around noon in the dayside auroral oval. It is characterized by localized and transient structures (Moen et al., 2013). One very diffuse type is poleward-moving auroral forms (PMAFs) (Nishimura et al., 2021). They

are an indication of bursty reconnection at the dayside magnetopause, with consequent flux transfer events (FTEs) (Lockwood et al., 2001) and they can be recognized as brightenings on the equatorial side of the auroral region, then moving poleward (Sandholt and Farrugia, 2007). Cusp is also characterized by smaller-scale variabilities, measuring less than 10 km, due to ion precipitation (Ebihara et al., 2008), FACs (Neubert and Christiansen, 2003) or rapid plasma jets (Rodger et al., 1994).

2. *the polar caps:* here the localized structure created in the cusp can arrive thanks to the antisunward movement of the ionospheric plasma (Nishimura et al., 2021). The most typical structures characterizing this region are Polar Cap Patches (PCPs), which are one of the most important phenomena related to high-latitude ionospheric irregularities (Spicher et al., 2017). They can be visualized as islands of plasma, whose density is at least double than the surrounding background and whose size's range is approximately $100 \div 1{,}000$ km. PCPs usually enter the polar cap from the dayside ionosphere then, driven by convection, they cross the polar cap, to finally exiting this region hours later, near midnight (Carlson, 2012). PCPs are likely to originate from the high-density plasma reservoir found in the dayside ionosphere, where the low solar zenith angles and resulting high solar EUV ionization supply a much higher plasma density than elsewhere. However, PCPs formation is still a debated topic and different mechanisms have been proposed (Clausen and Moen, 2015). According to Lockwood and Carlson Jr. (1992), for instance, these high density regions are produced by the bursty nature of dayside reconnection. Then, when the Dungey cycle is ongoing (Dungey, 1961), they are transported across the polar cap thanks to ionospheric convection, which acts exactly like a conveyor belt.
   Other than PCPs, another type of relevant structure is polar cap arcs, i.e. nearly Sun-aligned auroral arcs with an horizontal dimension of a few hundred kilometers, associated with electron precipitation of a few keV or less (Robinson and Mende, 1990). Polar cap regions can be also characterized by smaller-scale flow and density structures, with scales lower than 100 km (Golovchanskaya and Kozelov, 2010, Gondarenko and Guzdar, 2004), mainly attributed to gradient drift instabilities.

3. *the nighside auroral oval:* here the presence of localized and transient structures is mainly attributable to electromagnetic and precipitation energy from the magnetotail (Nishimura et al., 2021). A key role is played by *Substorms*, which are transient disturbances in the magnetosphere-ionosphere system, initiated by the rapid release of magnetic energy stored in the magnetotail region and released thanks to magnetic reconnection (Akasofu and Chapman, 1972). As substorms unfold, they set in motion a cascade of dynamic processes that reverberate through the nightside auroral oval ionosphere, generating a variety of irregularities (Blagoveshchenskii, 2013).
   One example of structures characterizing the nightside auroral oval region are auroral arcs, which are connected with enhanced precipitation, FAC and electric fields, and have typical widths from several hundred of meters to tens of km (Knudsen et al., 2001). Then there are Poleward Boundary Intensifications (PBIs), evidenced by auroral brightenings along the auroral oval's poleward boundary (Lyons et al., 1999). They can also emanate auroral arcs in the equator direction, forming the so called auroral streamers. Lastly, PCPs exiting from the

polar cap region and reaching the auroral oval are called auroral blobs. However, there can be also blobs produced locally through direct particle precipitation (Jin et al., 2016).

Moreover, an important aspect to take into account is the extremely dynamic nature of the high-latitude ionosphere, because of the large scale convective motion. As a consequence, here also the spatial distribution of plasma density fluctuations depend on the IMF orientation (Lockwood et al., 2000, Moen et al., 2008, Tsunoda, 1988). For instance, Jin et al. (2019) demonstrated how IMF's B_y component affects the distribution of the plasma density irregularities in the cusp and polar cap regions, resulting in an interhemispheric asymmetry in the spatial distribution of these irregularities. This finding are in line with the already mentioned response of the high-latitude ionospheric convection pattern to the B_y component. Furthermore, it has been shown that when IMF B_y component is negative, in the Northern hemisphere the irregularities near the cusp and in the polar cap region are more numerous in the postnoon sector, while in the Southern hemisphere they are more numerous in the prenoon sector. On the other hand, Jin et al. (2020) studied the effect of the IMF B_z component on the ionospheric plasma irregularities. They revealed that negative values of the B_z component cause a higher concentration of irregularities to occur at lower magnetic latitudes, compared to positive B_z values. Evidence of IMF dependence has also been discovered for *PCPs* (Spicher et al., 2017).

Ionospheric irregularities effect on GNSS

GNSS term refers to a network of satellites orbiting the Earth, designed to provide precise and continuous positioning, navigation, timing and synchronization information to users anywhere on or near the planet's surface (Hegarty and Chatre, 2008), playing a crucial role in modern society. The American GPS and its Russian counterpart GLONASS are currently in use in this context, along with the Chinese BeiDou, the European Galileo, and other regional systems such as the Indian IRNSS or the Japanese QZSS. GNSS signals fall into the L-band frequency domain, which corresponds to the part of the radio spectrum, covering frequencies between 1 and 2 GHz. Moreover, to take care of ionospheric delays in the measurements, these systems employ at least two different frequencies (Teunissen and Montenbruck, 2017). When traveling from a GNSS satellite to a receiver, either onboard a low Earth orbit satellite or on the ground, signals pass through the ionosphere and interact with its charged particles. The greater the number of electrons in the path between a GNSS satellite and a receiver, the greater is the signal delay.

The presence of fluctuations in ionospheric plasma density is one of the ionospheric phenomena that significantly lowers the performance of GNSS. Indeed, electron density irregularities can cause small-scale fluctuations in refractive index and subsequent differential diffraction of the plane wave, generating phase variations along the phase front of a signal propagating through the ionosphere, and thus affecting also GNSS signals. Then, the signal continues to propagate and the scintillation of its phase and amplitude grows through interference of multiple scattered signals. In the worst-case scenario, signals might be disrupted, causing the receiver to lose track of a transmitting satellite. This type of event is known as LoL, which can result in a decrease in GNSS positioning accuracy and the inability to obtain Total Electron Content (TEC) measurements. This last mentioned quantity represents an integral measurement of the total electron content along the signal path from the satellite to the receiver.

Therefore, the presence of ionospheric irregularities can affect several GNSS applications, as for instance the integrity and performance of positioning tasks, as well as the detection and tracking of several targets, like aircraft, missiles and satellites (Hegarty and Chatre, 2008), with an increase of these harmful effects during geomagnetic disturbed periods (Basu et al., 2001).

Chapter 2

Data

2.1 Swarm

Swarm is an ongoing European Space Agency (ESA)'s constellation mission (Friis-Christensen et al., 2006), selected in 2004 in ESA's Living Planet Programme. It is composed by three identical satellites, called Alpha, Bravo and Charlie (or A, B and C). They have been launched on 22 November 2013 into two different near-polar orbits: Alpha and Charlie, flying side-by-side (1.4° separation in longitude), at an initial altitude of about 470 km, while Bravo at an higher orbit of approximately 520 km. Because of the differences in altitude and inclination, Swarm B orbit drifts slowly away from the Swarm A and C orbits, at a rate of about 24°/year (difference in longitude of the ascending node). The orbital planes aligned again on October 2021, with Swarm B starting to counter-rotate with respect to Swarm A and C (ESA, 2023a).

The mission's aim is to study many different aspects of the Earth's magnetism, principally: core dynamics, geodynamo processes, core-mantle interaction, three-dimensional electrical conductivity of the mantle, lithospheric magnetisation and electric currents flowing in the magnetosphere and ionosphere. But there are also secondary objectives, like studying the ocean circulation thanks to its magnetic signature, or quantifying the magnetic forcing of the upper atmosphere.

In order to accomplish the mission's scientific tasks, every satellite has on board the same set of instruments (shown in Figure 2.1):

- *Accelerometer (ACC):* it measures the satellite's non-gravitational acceleration, making it possible to identify factors that cause this type of acceleration, such as air drag, winds, Earth albedo and direct solar radiation pressure on the spacecraft.
- *Absolute Scalar Magnetometer (ASM):* it's an optically pumped He magnetometer, that measures the absolute value of the magnetic field. These scalar measurements are necessary for the calibration of the vector field magnetometer.
- *Vector Field Magnetometer (VFM):* it has a fluxgate magnetometer design, which provides high-precision measurements of the magnetic field as a vector, measuring its module and direction.
- *Electric Field Instrument (EFI):* it's a thermal ion imager, used to characterise the electric field around Earth, thanks to its high resolution measurements of plasma density, drift and

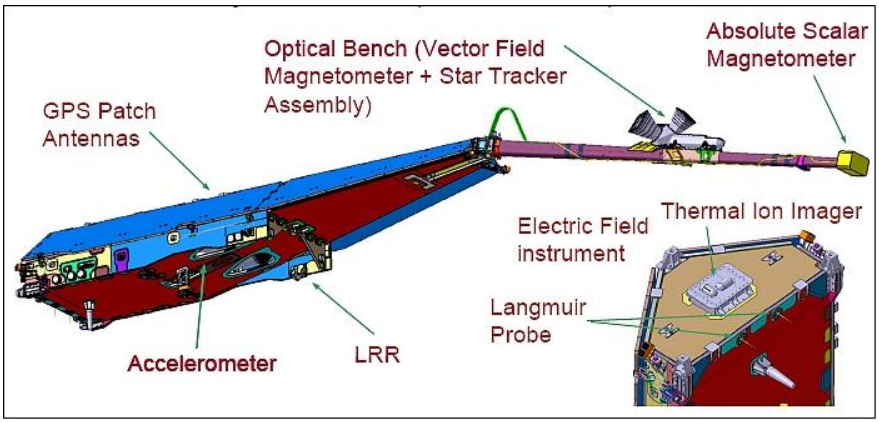

Figure 2.1: Artistic representation of one of the Swarm satellites and its instruments. Credits: ESA

velocity. This instrument is composed by three main parts: the Suprathermal Ion Imager sensors, the Langmuir Probe (LP) sensors, and the Electronics Assembly (electronics necessary to support power supply, sensor data acquisition, instrument control and communications with the spacecraft bus).

- *GPS Receiver:* necessary to obtain very accurate orbit determination. It is composed by a receiver electronics unit and a Precise Orbit Determination (POD) antenna, that receives the signals from eight of the visible GPS satellites, one for each of the eight channel available for dual-frequency tracking (Van Den Ijssel et al., 2016).

- *Laser Retro-Reflector (LRR):* it's a 45-degree pyramid-shaped retroreflector array, used for satellite laser ranging, i.e. a supporting and independent method for orbit determination.

- *Star Tracker (STR):* made of a Camera Head Unit, placed on an optical bench, which acts as a highly mechanical stable platform for this instrument and the magnetometer. STR is fundamental to determine the orientation of the magnetic field vector, measured by VFM.

The three Swarm satellites have a trapezoidal shape, measuring 9 m on the longer side, while the surface at the front measures only 1 m^2. The reduced front surface helps to lower the air drag effect and thus minimize the amount of propellant needed to stay at the correct altitude. On this surface is located the EFI instrument, allowing it to collect and measure the speed and direction of incident ions along the orbital path. On the other side, the elongated shape is necessary to overcome the challenges connected with the instrument package accommodation. In fact, to reduce any magnetic disturbance produced by the electrical units located in the front part, the satellites have a 4-m boom at their back. The ASM is mounted at the end of the boom, while the optical bench holding the VFM and the STR is located halfway (ESA, 2023b).

Swarm data are available for download at `https://swarm-diss.eo.esa.int/`, both via HTTP browser or ftp client. There are three different directories: Level 1, Level 2 and Advanced. *Level 1* data are available for each one of the three satellites individually, and consist of time series of the parameters measured along the orbit, corrected, calibrated and converted in physical units. Instead, *Level 2* is a unique set of data that gathers the measurements from the whole constellation, thanks to a complex assimilation. *Advanced* includes advanced data, namely ASM/VFM Residuals,

Provisional Plasma Data, Langmuir Data, Thermal Ion Images Data, 2 Hz TII Cross-track Data, 16Hz Plasma Density Data, 2Hz Langmuir Extended Data.

For the following analysis, both Level 1 and 2 data have been used. In particular, 1 Hz plasma and magnetic field data, recorded by EFI and VFM instruments respectively, have been obtained from Level 1 directory. *Electron density* N_e and *electron temperature* T_e were necessary to describe the properties of the ionospheric plasma in which Swarm is passing through. On the other hand, the VFM measures the *ambient magnetic field*, which is produced by all sources within and outside the Earth, up to the magnetopause. In fact, geomagnetic field is the sum of several contributions, which are internal ones, i.e. the core field, also known as the main field, and the crustal or lithospheric field, and external ones originating from ionospheric and magnetospheric currents (Lühr et al., 2009). When it was necessary, the internal and external contributions to the magnetic field measurements were distinguished using the CHAOS model[1] (Finlay et al., 2015). Moreover, in this work the magnetic field components have been downloaded in the North-East-Centre (NEC) frame, which is a local instrument frame, having the origin in the geometric center of the instrument. The Center direction (C) is the radial component, pointing from the frame's origin towards the Earth's center, as defined in the International Terrestrial Reference Frame (ITRF)[2]. The North (N) and East (E) components are directed along the local tangent of the meridian and the local tangent of the parallel respectively, with respect to the sphere (defined in ITRF) whose radius goes from the center of the Earth to the center of the instrument (Swa, 2007).

The most relevant parameter for the following analysis downloaded from Swarm Level 2 directory is the *slant Total Electron Content (sTEC)*, obtained through POD antennas measurements. More generally, the Total Electron Content (TEC) refers to the total number of electrons integrated between two points, along a tube of $1m^2$ cross section. Specifically in this case, the sTEC is the integrated electron density along the line of sight from Swarm to a GPS satellite. In fact, in general, signals transmitted by all kind of GNSS, undergo a deceleration due to the presence of electrons in their path. Therefore, it is possible to estimate the electron content between the transmitting GNSS satellite and the receiving one, by looking at the delay of arrival of the signal. In Swarm case, the sTEC values are obtained through equation 2.1 in $TECU = 10^{16} electrons/m^2$ units.

$$sTEC = \frac{f_1^2 f_2^2}{f_1^2 - f_2^2} \frac{L_1 - L_2}{K} \tag{2.1}$$

where f_1 and f_2 are the carrier frequencies of GPS signals, L_1 and L_2 the ambiguity-corrected carrier phase observations, while K is a constant equal to $40.3\, m^3 s^{-2}$. Before 15th July 2014 sTEC data were sampled at 0.1 Hz, while after that date the rate has been increased to 1 Hz (Van Den Ijssel et al., 2016). For this reason in the following work, when sTEC data are involved, the analysis starts from mid-July onwards, in order to use data that are near simultaneous with the other Swarm measurements. Sometimes sTEC measurements are not available. This can happen for two main

[1]CHAOS is an advanced geomagnetic field model by Olsen et al. (2006), derived from more than 6,5 years of high-precision geomagnetic data, obtained by Ørsted, CHAMP, and SAC-C satellites, in the period that goes from March 1999 to December 2005. It goes up to a maximum degree of Gauss coefficients of 50, however all degrees above the 18° are assumed to be constant. The time evolution of the low-degree coefficients, until the 14°, is described by cubic B-splines, while that of coefficients from 15° to 18° is described by a linear Taylor expansion (Kono, 2010).

[2]ITRF is an Earth-fixed Cartesian system. Its origin is in the Earth's center of mass. The x-axis points towards the International Earth Rotation Service (IERS) Reference Meridian, the z-axis towards the Reference North Pole, while the y-axis completes a right-handed system.

Index	Meaning
0	Outside Plasma Bubble (PB)
1	Inside PB
-1	Unanalyzable data point

Flag	Meaning
0	Quiet
1	PB confirmed by high-correlation between plasma density and magnetic field
2	PB unconfirmed by high-correlation between plasma density and magnetic field
4	Large jump in magnetic field
8	Data gap
16	Pulsations in magnetic field
32	Outside the night-time low-latitude region where PB can be found

Table 2.1: Possible values of Swarm Ionospheric Bubble Index (IBI) index (on the left) and IBI flag (on the right) (Swa, b).

reasons: the GPS satellite exits from Swarm's field of view, or a *LoL event* is ongoing. In this second case, the GPS signal, traveling towards one of the Swarm satellites, is degraded to the point of being interrupted. This results in the impossibility to obtain sTEC measurements and in a lowering of the positioning accuracy. With the aim of studying the properties of the ionospheric irregularities at the base of LoL events, as well as LoLs' spatial distribution and dependence on external parameters, in this work these events are identified following the procedure firstly proposed by Pezzopane et al. (2021). For each one of the 32 GPS satellites, the procedure is the following:

- from the sTEC time series, relative to the specific GPS satellite under analysis, only the portions during which the satellite is in Swarm's field of view are selected.
- from each obtained portion, the sTEC interruptions ranging from 2 to 1200 s are selected as LoL events.

The second point excludes the events lasting 1 s, which have been found to be most likely due to hardware outages (Pezzopane et al., 2021), and the ones over 1200 s, which are not LoL events, but represent the case in which the GPS satellite is no more in Swarm's field of view. This methodology can be applied to each one of the three Swarm satellites.

In order to study an important phenomenon that affects the equatorial latitudes, also the *IBI index* has been downloaded from Level 2 directory. This index highlights the presence of an Equatorial Plasma Bubble (EPB) (described in more detail in Section 1.4.1), an electron density irregularity, originating after sunset by the nonlinear evolution of the Rayleigh–Taylor instability (Kelley, 2009). The identification of this phenomenon is based on the diamagnetic effect. Specifically, the reduction in density observed in correspondence of EPBs generates gradients in plasma pressure. As a result, the magnetic pressure must vary in the opposite direction to maintain a constant total pressure. This leads to regions of enhanced magnetic field strength within EPBs (Park et al., 2013). Based on this premise, the development of the IBI product has been carried out through the following steps, as described in Park et al. (2013):

- The model values representing the magnetic fields generated by Earth's core, lithosphere, and magnetosphere are combined to calculate the composite magnetic field known as the "Mean Field";

- The Mean Field is subtracted from 1 Hz VFM original data;
- The obtained Residual Field, which represents the magnetic field variations originating from the ionosphere, is projected onto the Mean Field, transforming it into the Mean-Field-Aligned (MFA) coordinate system.
- The MFA-Z component undergoes a high-pass-filter (-3 dB cutoff at the period of approximately 24 s), which limits the signal to a passband of approximately 0.04–0.5 Hz, where 0.5 Hz corresponds to the Nyquist frequency. This step is necessary to remove large-scale magnetic field variations not related to EPBs (like the Equatorial Ionization Anomaly (EIA))
- The filtered residual MFA-Z component is then rectified and compared to an event detection threshold equal to 0.15 nT (Swa, b). Fluctuations exceeding this value are considered as possible EPBs events and their IBI index will have a non-zero value.
- To finally prove the presence of EPBs, the filtered residual MFA-Z component is compared to the plasma density filtered in the same way, checking if these two quantities are correlated around the detected events. If the square of their correlation coefficient is higher than a certain threshold, there is actually a diamagnetic effect and the event is confirmed. In this case the IBI index will be set equal to 1 (as one can see in the left Table 2.1) and will also be accompanied by an IBI Flag equal to 1. On the other hand, when the correlation coefficient is lower than the threshold, the IBI Flag will be set equal to 2, as it is possible to see in the right Table 2.1.

The IBI Flag describes also other possible cases, giving an explanation of which could be the source of the identified magnetic field fluctuation (see Table 2.1 on the right).

Another Level 2 parameter which has been used is the *Polar Cap Patch (PCP) flag*, part of the Ionospheric Plasma IRregularities (IPIR) (IPDxIRR_2F) product (Swa, a). This directory contains also other parameters derived from several Swarm L1b and L2 data products, with the aim of providing a comprehensive dataset, at the temporal resolution of 1 Hz, for the study of plasma structuring along all Swarm orbits (Jin et al., 2022). The PCP flag in particular states if a Swarm satellite is passing through a PCP as it travels its orbit. This term refers to plasma density enhancements in the polar ionosphere, which originate from the segmentation of the ionization tongue, whose triggering mechanism is still debated (Clausen and Moen, 2015). The method followed to obtain the flag is the same described in Spicher et al. (2017). First it is necessary to estimate the background density, obtained computing the 35th percentile filter of 551 data points along the N_e 2 Hz time series. Then, following the same procedure but selecting the 50th percentile with respect to 7 data points, one obtains also the foreground density. When it exceeds by a factor of two the background density, for at least 100 km, the satellite is considered to be within a PCP and the flag is set to non-zero values. The possible values of the PCP flag are listed in table 2.2. The flag gives also information about the PCP edges, identified when the background density drops to 30% of its average value within the identified patch. When the plasma velocity is also available it is possible to distinguish between the leading and trailing edges of the patch (Jin et al., 2022).

Flag	Meaning
0	Outside PCP
1	PCP edge (not possible to distinguish if the leading or trailing one)
2	PCP leading edge
3	PCP trailing edge
4	Inside PCP

Table 2.2: Possible values of Swarm IPIR PCP flag (Jin et al., 2022).

2.1.1 Magnetic reference frame

Since geospace phenomena such as plasma motions, ionospheric currents and associated magnetic field disturbances are highly organized by Earth's main magnetic field, is useful to present them using a *magnetic frame of reference* (Laundal and Richmond, 2017). Therefore, in the context of the following analysis, all the just listed Swarm data have been converted into *Quasi Dipole (QD)* system, defined by Richmond (1995), which was specifically chosen for its suitability in studying phenomena associated with horizontally stratified ionospheric currents. The non-orthogonal QD system of coordinates is based on the definition of *apex*, i.e. the point on a International Geomagnetic Reference Field (IGRF)'s[3] field line corresponding to the maximum height above the reference ellipsoid used for modelling the Earth (Giannattasio et al., 2019). In this frame the *Magnetic Latitude* is given by Equation 2.2.

$$\lambda_{QD} = \pm \cos^{-1} \sqrt{\frac{R_E + h}{R_E + h_A}} \tag{2.2}$$

where h is the distance from the geoid surface, h_A is the apex altitude respect to the reference ellipsoid and R_E is the semimajor equatorial axis. In order to always consider the position respect to the Sun, it is useful to use the *Magnetic Local Time (MLT)* coordinate (Baker and Wing, 1989), instead of magnetic longitude. It is given by the Equation 2.3, where ϕ is the magnetic longitude of the specific point, Φ_N the geographic longitude of the North pole of the Centered Dipole system, and UT is the Universal Time (Laundal and Richmond, 2017).

$$MLT = UT + \frac{\phi + \Phi_N}{15} \tag{2.3}$$

2.2 OMNI dataset

OMNI is a comprehensive dataset of interplanetary and geophysical parameters, produced and distributed by NASA Space Physics Data Facility (SPDF). SPDF is a a project of the Heliophysics Science Division at NASA's Goddard Space Flight Center, which provides an active and permanent archive for non-solar heliophysics data.

OMNI database is composed by two main data sections, one at *Low Resolution* and the other at *High Resolution*. The first contains mainly hourly-averaged data of magnetic field and plasma parameter relative to the near-Earth solar wind, obtained from several spacecraft in geocentric or in

[3]IGRF is an Earth's magnetic field dipole model, which provides a representation of the slowly changing large-scale part of the internal field. It is regularly published by the International Association of Geomagnetism and Aeronomy (IAGA) and its last version has a degree of truncation of Gauss coefficients at N = 13. It has a reference ellipsoid with a semi-major equatorial axis $R_E = 6378.137\,km$, and an ellipticity of 1/298.51 (Thébault et al., 2015).

first Lagrangian point (L1) orbits. It contains also protons fluxes and a wide range of geomagnetic and solar activity indices. This dataset covers the period that goes from approximately 1963 to the present time; the availability period for each parameter is visible in detail at `https://omniweb.gsfc.nasa.gov/html/ow_data.html`.

On the other hand, High Resolution OMNI dataset provides 1-min and 5-min solar wind magnetic field and plasma data from Interplanetary Monitoring Platform (IMP) 8, Geotail, Wind and Advanced Composition Explorer (ACE) missions. In particular, ACE was launched on August 25, 1997 in a L1 orbit, and keeps providing magnetic field, plasma and energetic particle data. *Wind* was launched on November 1, 1994, as part of NASA's contribution to the International Solar Terrestrial Program. It continues to obtain magnetic field, plasma, energetic particle and plasma wave data. *IMP 8* was launched on October 26, 1973, into a low eccentricity Earth orbit. Its magnetometer stopped working on June 10, 2000, while data from its plasma instrument and from three energetic particle detectors are available until October, 2006. Finally, *Geotail* was launched on July 24, 1992, into an eccentric orbit with apogee deep in the geotail. Thanks to a complex assimilation of data from these missions, high resolution data are available since 1995 to the present day.
High Resolution OMNI data are time-shifted to the Earth's bow shock nose, based on the assumption that the observed solar wind magnetic field values, measured by a spacecraft at a specific time and location, lie on a planar surface known as the "phase front". This phase front follows the solar wind convection. As a result, the same values will be observed at a different location when the phase front sweeps over that particular area.

Here, parameters from both low and high resolution datasets have been utilized. The following paragraphs describe the indices and parameters that have been utilized, beginning with solar and geomagnetic indices and followed by interplanetary parameters.

F10.7: It's a solar activity proxy, given by the radio emission at 10.7 cm, which originates from regions of intense magnetic field, characterized by structures like plages, networks, and sunspots (Foukal, 1998). It is recorded by the Dominion Radio Astrophysical Observatory (Canada) with three flux determinations for each day. Each measurement represents the total emission at 10.7 cm, from all sources present on the solar disk, made over a 1-h period centfered on a stated epoch. During summer, these epochs are 17:00, 20:00, and 23:00 UT, while during winter 18:00, 20:00, and 22:00 UT, because of the latitude, the hilly shape of the local horizon and the lower elevation of the Sun (Tapping, 2013). Measurements are expressed in solar flux units (sfu), where $1\,\text{sfu} = 10^{-22}\,\text{Wm}^{-2}\text{Hz}^{-1}$. In particular, this index includes the free-free emission from both chromosphere and corona, as well as from concentrations of plasma supported by active region magnetic fields. These three types of emission vary on different timescales and have each one its own distribution over the solar disk surface (Tapping, 2013).

In the OMNI dataset, F10.7 daily values are available in the Low Resolution section.

AE: It is one of the Auroral Electrojets (AE) indices, together with AU, AL and AO, originally defined and developed by Davis and Sugiura (1966), with the goal of characterizing global auroral electrojet currents, which are high-latitude current flows, concentrated inside the *auroral oval*. Specifically, the current's upper envelope defines the AU index, while the lower envelope defines AL; then AE = (AU - AL) and AO = (AU + AL)/2. This current carries some million amperes,

and, flowing only 100 km above the Earth's surface, it produces a magnetic disturbance of 100–1000 nT, but it can reach 3000 nT during the largest magnetic substorms (Baumjohann and Nakamura, 2007). That makes it the most evident current at auroral latitude.

For this reason the AE index in particular should reflect the entity of this current. Actually, it's important to keep in mind that the measured magnetic disturbance reflects the integrated effect of different current systems present at these latitudes. Therefore, it is more correct to say that AE index provides a global, quantitative measure of *auroral zone magnetic activity*, produced by the whole set of enhanced ionospheric currents, flowing below and within the auroral oval, that are associated with solar wind magnetosphere interactions and energy release processes in the magnetotail.

AE indices are produced by the World Data Center (WDC) for Geomagnetism of Kyoto (`http://wdc.kugi.kyoto-u.ac.jp/aeasy/index.html`) from the horizontal magnetic field component (H) recorded with 1-min time resolution at 10-13 magnetic observatories, located under the average auroral oval in the Northern Hemisphere (geomagnetic latitudes $60° - 70°$).

IMF components: B_x, B_y and B_z are available at 1-min cadence and have been downloaded in the Geocentric Solar Magnetospheric (GSM) coordinate system. This system has the X-axis that goes from the Earth to the Sun, the Y-axis perpendicular to the Earth's magnetic dipole, so that the X-Z plane contains the dipole axis; the positive direction of the Z-axis is the one with the same sense as the northern magnetic pole.

Solar wind velocity: the x-component of the solar wind velocity was downloaded in Geocentric Solar Ecliptic (GSE) coordinate system. The X-axis of this system coincide with the GSM X-axis. This component, together with the y- and z-components of the IMF, is necessary as an input parameter to obtain SuperDARN electric potential maps, which will be described in Section 2.3

2.3 SuperDARN

The Super Dual Auroral Radar Network (SuperDARN) consists in more than 30 ground-based coherent-scatter radars, operating in the High Frequency (HF) band (8-20 MHz). Combining the radars' fields-of-views, this network cover extensive regions of both the Northern and Southern hemisphere polar ionospheres, starting from mid-latitudes (Chisham et al., 2007).

The radars transmit pulses of radio waves, which travel from the antenna arrays toward the Earth's ionosphere. Here, the radio signal is partially reflected by plasma irregularities and the back-scattered part can travel back to the radars. Thanks to Doppler shift measurements, it is possible to obtain an estimation of the ionospheric plasma's speed. In this way, SuperDARN provides a comprehensive view of the high latitude plasma motion, giving the possibility to deepen the electromagnetic coupling of the solar wind-magnetosphere-ionosphere system. In particular, some of the main research objectives of SuperDARN are to study the global configuration and dynamics of plasma convection, as well as its mesoscale properties. It also aims to measure FAC, define ionospheric signature of magnetic reconnection at the Earth's magnetopause and magnetotail, as well as investigating substorm conditions and ionospheric irregularities (Chisham et al., 2007).

Thanks to SuperDARN data, Ruohoniemi and Baker (1998) developed a "map potential" model. It provides a map of the high-latitude convection pattern, depending on a set of external parameters.

They used a statistical model (Ruohoniemi and Greenwald, 1996) that reproduces the mesoscale features of ionospheric convection patterns, in both polar regions, for a wide range of solar wind, IMF, and dipole tilt angle parameter values. This model has been combined with SuperDARN data, in order to produce a electrostatic potential map that is in the best agreement with the line-of-sight velocity measurements provided by the radars network.

The potential maps used in this work have been generated and downloaded from the SuperDARN Dynamic Model Web Interface (`http://sdnet.thayer.dartmouth.edu/models/dynamicmodel.php#SDDM`), which is based on the CS10 model (Cousins and Shepherd, 2010) coefficients. Each map is obtained considering as input data the values of IMF B_z, B_y, and solar wind velocity obtained from the already described OMNI dataset (see Section 2.2), while the dipole tilt angle was chosen depending on the orbital configuration at the time of the phenomena under analysis.

2.4 Additional indices

Two additional indices were utilized in the study, which were not included in the OMNI dataset (described in Section 2.2).

Mg II

The Mg II index refers to a broad absorption feature with narrow emission peaks in the core. This emission doublet, near 280 nm, originates in the Sun's *chromosphere*, while the line wings part originates in the *photosphere*, showing much less variability over time. Therefore, the ratio of line core intensity to wing intensity provides a robust estimate of solar variability, less susceptible to instrumental and degradation effects (Peeters et al., 1997). In addition, this index has already shown its effectiveness in the study of ionosphere-thermosphere region response to solar activity (Bigazzi et al., 2020, Perna and Pezzopane, 2016, Vaishnav et al., 2019).

Mg II index is provided by Global Ozone Monitoring Experiment (GOME)-2 mission instruments (Snow et al., 2019) and its time series can be downloaded from from UVSAT Bremen University (GOME-2A, `http://www.iup.uni.bremen.de/UVSAT/Datasets/mgii`).

SuperMAG SME Index

SuperMAG is a worldwide collaboration between organizations and national agencies, which gathers data from nearly 600 geomagnetic ground station across the globe, providing several products and services (Gjerloev, 2012). Its purpose is to monitor magnetic variations caused by electric currents flowing in the ionosphere and magnetosphere.

SuperMAG provides data with two different temporal resolution, 1-min and 1-sec, with the latter being a subset of the former as not all stations provide data at a frequency of 1-sec. As part of the 1-min products, there are also Magnetic Indices. Even though these are not official indices, since they are not authorized by IAGA, they can be useful for periods which are not covered by the official indices. For example, the already mentioned AE index (see Section 2.2), has not validated values after March 2019. When this index was needed after this date, in the present work it was substituted by SuperMAG SME index. This was done after confirming its correlation with the AE index, during a period in which they are both available (see Section 4.1.1).

The *SME index* is derived considering data from ground magnetometer stations located at geomagnetic latitudes between +40° and +80°, which are approximately 110 stations. After removing the baseline from the magnetic field H component, its maximum and minimum values are computed. The former is indicated as SMU, while the latter as SML. SME is obtained as the difference SMU-SML (Newell and Gjerloev, 2011).

Chapter 3

Method

This chapter presents the main methodologies utilized in this work.

3.1 Multivariate Empirical Mode Decomposition

The Multivariate Empirical Mode Decomposition (MEMD) is the extension of Empirical Mode Decomposition (EMD) to multivariate signals (Rehman and Mandic, 2010).

Empirical Mode Decomposition: the *EMD* is a technique firstly introduced by Huang et al. (1998), with the aim of adaptively represent nonlinear and non-stationary signals. The key concept at its base is that each one of these signals can be decomposed in a finite, and often small, number of intrinsic oscillatory modes, called Intrinsic Mode Functions (IMFs). Each one of these IMFs reproduces the repeating behaviour of the signal at a particular time scale (Maheshwari and Kumar, 2014). EMD method is particularly important because it allows to analyze signals that are not compatible with the Fourier Transform restrictions. In fact, Fourier analysis is a powerful method to extract the energy-frequency distribution of a signal, widely used for its simplicity and its general applicability. However, it can not produce physically meaningful results when dealing with non-linear systems or when data are not periodic or stationary (Huang et al., 1998). In these cases EMD can absolve the role of reducing the signal into a set of basis signals, which are derived directly from the data itself (Maheshwari and Kumar, 2014).
The IMFs must fulfill two criteria: the first is that considering the entire dataset, each of these function has the same number of extrema and zero crossing, or they can differ at most by one; secondly, considering any point, the mean value between the envelope defined by the local maximum and the one define by the local minimum is zero (Huang et al., 1998). The resulting functions are simple oscillatory modes, which differ from simple harmonic components because their frequency and amplitude can change along the time axis. The procedure to extract IMFs is the following and it is called *sifting*:

1. the dataset's local extrema are identified;
2. a cubic spline is used to connect all the local maxima, in order to obtain the upper envelope;
3. another cubic spline is used to connect all the local minimum and thus obtain the lower envelope;

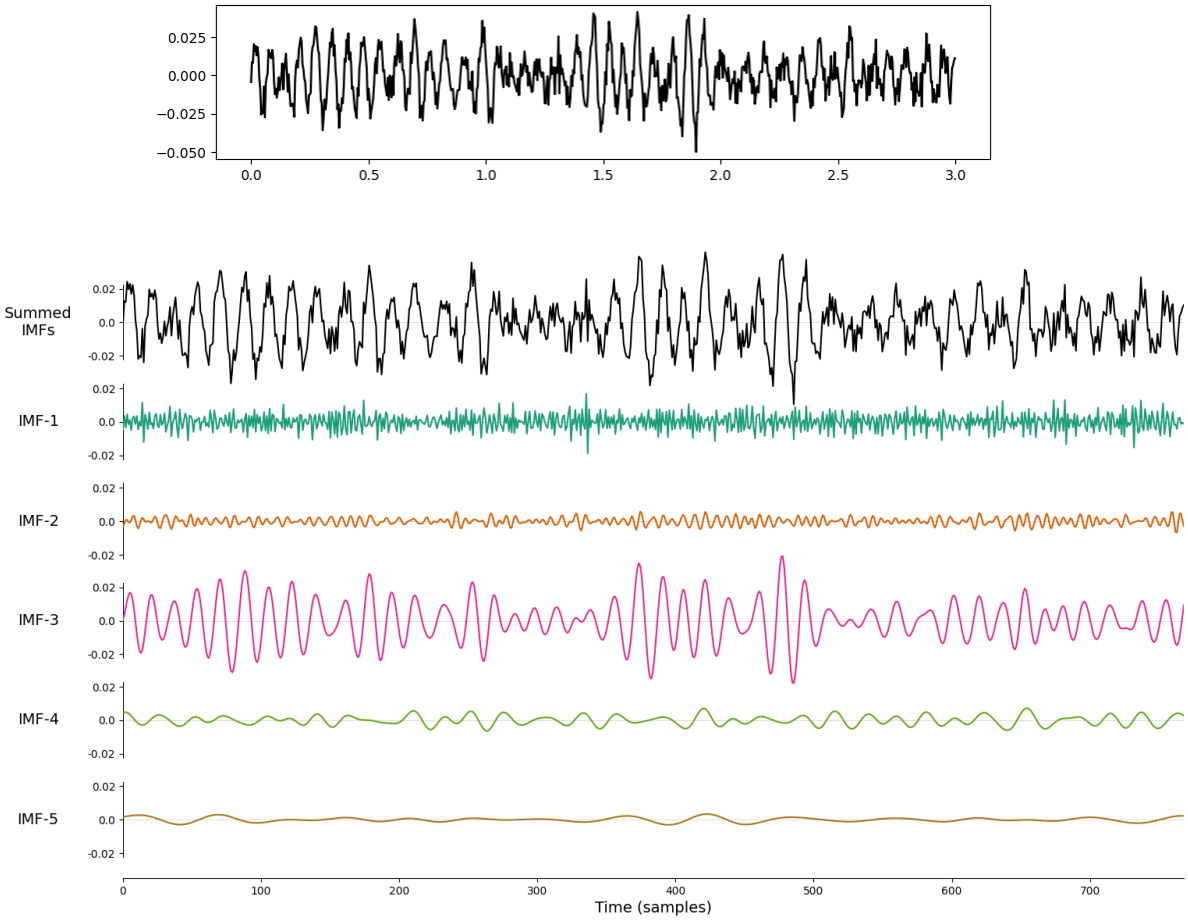

Figure 3.1: *Upper part:* a simulated noisy signal with a 15Hz oscillation. *Lower part:* the resulting IMFs obtained applying the EMD method to the signal represented in the upper panel. *Credits:* Empirical Mode Decomposition in Python (Quinn et al., 2021).

4. the mean between the two envelopes (m_1) is computed;
5. the first component h_1 is obtained subtracting m_1 from the data: $h_1 = x(t) - m_1$.
6. if h_1 is a zero-mean function it is accepted as the first one of the IMFs, $IMF_1 = h_1$. Otherwise, h_1 undergoes itself the steps 1-5. The procedure is repeated until h_1 fulfill the zero-mean criterion.

It is necessary to apply a *stopping criteria* to the number of sifting iterations, in this way the obtained IMFs preserve an amplitude and frequency modulation, together with their physical sense (Huang et al., 1998). One example of stopping criteria is deciding a threshold limit for the size of the standard deviation between two consecutive sifting results. Successively, to obtain the following IMFs, the process is applied to the residual $r_1 = x(h) - IMF_1$. The procedure is repeated until the residual becomes or a constant, or a monotonic function or a function with only one maxima and minima from which it is not possible to extract other IMFs (Maheshwari and Kumar, 2014). If it is needed, it is then possible to compute instantaneous frequencies and amplitudes of each obtained

mode by applying the *Hilbert transform*[1] to each one of the IMFs. By adding this final step, the entire process is called *Hilbert Huang Transform* (Maheshwari and Kumar, 2014). An example of an IMFs set obtained decomposing with EMD a particular signal is reported in Figure 3.1.

Multivariate Empirical Mode Decomposition: When dealing with multivariate signals, it is not possible to apply directly EMD, but it is necessary to use its multivariate extension. In fact, multivariate data does not have a straightforward concept of local extrema, making not obvious the step of local mean computation (Rehman and Mandic, 2010). After the first proposals of EMD extension to complex/bivatiate (Altaf et al., 2007, Tanaka and Mandic, 2007) and trivariate data (Rehman and Mandic, 2009), Rehman and Mandic (2010) proposed a way to build more suitable multivariate decomposition by extending the concept of local extrema on a k-dimensional space. It consists in subdividing a k-variate signal into k-dimensional datasets. Each one of these is projected along different directions in the k-dimensional space. Then, each projected signal will have its own envelopes for each one of the directions and the local mean can be computed by averaging over the k-dimensional space. The local mean computation can be done through two different methods, concerning the selection of a suitable set of direction vectors in the k-dimensional space. The first is the uniform angular sampling of a unit sphere in an k-dimensional hyperspherical coordinate system, obtaining a set of direction vectors that covers the whole (k-1) sphere. The second is based on low-discrepancy pointsets, in which discrepancy refers to a quantitative measure for the irregularity, or non-uniformity, of a distribution. It belongs to the class of quasi-Monte Carlo methods (Niederreiter, 1992). Through both methods an uniform distribution of direction vectors is obtained, providing more accurate local mean estimates in k-dimensional spaces. Successively, multivariate IMFs are obtained following the already mentioned procedure of standard EMD, using multivariate spline interpolation and checking the obtained modes properties Alberti et al. (2020). An important difference with EMD is that in MEMD case the condition for equality of the number of extrema and zero crossings is not imposed, because of the not straightforward definition of extrema for multivariate signals (Mandic and Goh, 2009).

In this work, in order to apply the MEMD method, a Python algorithm was used, which is available at `https://github.com/mariogrune/MEMD-Python-`. It is an adaptation of the procedure described in Rehman and Mandic (2010) and produced in Matlab (freely available at: `http://www.commsp.ee.ic.ac.uk/~mandic/research/emd.htm`). The Python version was chosen because of its applicability to input data characterized by any number of channels.

[1]The Hilbert transform of a signal consists in its convolution with the function $f(t) = \frac{1}{\pi t}$. It represents the response of a linear time-invariant filter (called a Hilbert transformer), having impulse response $\frac{1}{\pi t}$, to the signal (Kschischang, 2006).

3.2 Structure Function Analysis

With the goal of investigating the possible turbulent nature of the ionospheric plasma, one noteworthy aspect to inspect is the *scale-invariance*, being a fundamental characteristic of the plasma fluctuations in turbulent state. It means that the fluctuations structures do not have a preferential scale. To determine whether scaling features appear in a time series, a simple technique is to evaluate the so-called *Generalized* q^{th}*-order Structure Function* S_q (Frisch, 1995), which is defined by Equation 3.1.

$$S_q(t) = \langle \mid f(t+\delta t) - f(t) \mid^q \rangle, \tag{3.1}$$

where $f(t)$ is the time series under analysis, δt is the temporal increment, and $\langle ... \rangle$ stands for a statistical mean. In this way it is possible to evaluate the scaling features of the moments of the signal increments at different spatial scales. In fact, using an Eulerian observational approach for turbulent flow analysis, it is possible to assume the Taylor's hypothesis (Taylor, 1938) to be valid and δt can be read as a spatial scale of interest, if one assumes that the transit time of the structure under observation is faster than its evolution time.
When a signal is scale-invariant, the q^{th}-order structure function is predicted to scale as a power-law:

$$S_q(t) = \delta t^{\gamma(q)}, \tag{3.2}$$

where $\gamma(q)$ is the q^{th}-order scaling exponent. For simple fractal signals, these exponents are expected to be a linear function of the moment order q, while in the case of more complex fractal signals, they deviate from such a linear dependence. Among all the possible exponents, the first- and second-order ones are very useful in the investigation of plasma fluctuations properties.
In particular, $\gamma(1)$, also called the *Hurst exponent* (Hurst, 1956), gives information about the long-term memory of the time series, measuring the signal's self-affinity. When $\gamma(1) < 0.5$ the signal is characterized by an *antipersistent* character, meaning that its fluctuations tend to induce stability within the system. In this case successive fluctuations will have alternate signs. On the other hand, when $\gamma(1) > 0.5$ the signal has a *persistent* character, marked by fluctuations most probably followed by another ones of the same sign, making the time series to cluster, or persist, in a particular direction (Consolini et al., 2021). At its extreme values, $\gamma(1)$ represents a white noise, when it is equal to zero, or a completely predictable linear trend for $\gamma(1) = 1$. The value that divides the antipersistent from the persistent behaviour, $\gamma(1) = 0.5$, indicates a totally uncorrelated time series, like the case of Brownian random motion.
Then, there is the second-order scaling exponent, $\gamma(2)$, which is connected to the spectral characteristics of the fluctuations. Indeed, as stated by the Wiener-Khinchin theorem (Wiener, 1964), there exists a relationship between $\gamma(2)$ and the signal's Power Spectral Density (PSD) exponent β (PSD $\simeq -f^{\beta}$), through the following equation: $\gamma(2) = \beta - 1$. Thanks to this relationship, $\gamma(2)$ allows to indirectly infer the spectral features of the analyzed time series and thus distinguish the different types of instabilities or turbulent processes that lead to the observed fluctuations.

3.2.1 Detrended Structure Function Analysis

When dealing with real signals, it is necessary to pay attention to some aspects. In this work, the scaling exponents are evaluated from Swarm measurements time series (the mission and its data are described in detail in Section 2.1). The three satellites pass trough different regions, characterized by different physical mechanisms with their typical spatial and temporal scales. Therefore, the resulting measurements can have *local* space and time dependencies. In order to take this aspect into account, in this work the structure function method is adapted to extract local scaling features, using the so called *Detrended Structure Function Analysis (DSFA)* (De Michelis et al., 2015). It consists in applying the structure function analysis to locally detrended time series, obtaining local scaling exponents within a moving window.
Going into detail, given a particular point of a Swarm time series $y(t_0)$, identified by the time instant t_0, a time interval centered on this instant is considered: $[t_0 - \frac{T}{2}, t_0 + \frac{T}{2}]$. T should be of the order of 10 times the maximum timescale δt one wants to investigate. In the selected interval, the average long-term trend is computed thanks to a 7^{th}-order polynomial fit $p(t)$, which is then subtracted from the original time series:

$$x(t) = y(t) - p(t) \quad \forall t \in \left[t_0 - \frac{T}{2}, t_0 + \frac{T}{2}\right] \tag{3.3}$$

with $x(t)$ representing the detrended time series for the selected time interval. At this point it is possible to evaluate the $S_q(t)$ relative to $x(t)$, as indicated by Equation 3.1, letting δt varying between a minimum and maximum value. From the obtained $S_q(t)$, the first- and second- order scaling exponent are evaluated and associated with the central point of the window. Successively the window is shifted by one point and the procedure repeated. This is done until the complete time series under investigation is covered.
Dealing with Swarm data, a window of 301 points is taken into account. This choice allows to analyze the scaling properties of the selected parameter over a spatial range of approximately 2400 km, since Swarm constellation's orbital speed is ~ 8 km/s. Moreover, the window size appears to be a good compromise in the perspective of avoiding the mixing of the various physical processes crossed by the satellites along their orbits. The analyzed time increments δt span between 1 and 40 seconds in each window, corresponding to spatial increments from 8 to 320 km. This procedure is done assuming that the evolution time of the spatial structures is longer than Swarm's transit time through them. Additionally, this scale band choice is consistent with several interesting processes which are typical of the high- and low-latitude ionosphere. In fact, in the meso-scale domain, which goes from approximately tens to hundreds of km, one can find the signatures of polar cap patches, blobs, auroral arcs, field-aligned currents, as well as plasma bubbles.

The DSFA method has proven to be a powerful tool for analysing the scaling features of Swarm time series in several studies, both in case of the electron density (Consolini et al., 2021, Giannattasio et al., 2019) and of the magnetic field measurements (De Michelis et al., 2015, De Michelis et al., 2016, 2017).

3.3 Machine Learning algorithms for classification

The term *Machine Learning (ML)* refers to a set of methods utilized to make and improve predictions or behaviors based on data. These methods are not based on a set of instruction, explicitly written inside an algorithm, which is typical of traditional programming. Instead, the main point is providing the data that the model will use to learn to make predictions, without being explicitly programmed (Molnar, 2020). One important branch of ML is *Supervised Learning (SL)*, which comprises the prediction problems characterized by the prior knowledge of the outcome of interest. In fact, the training is done on past data which have been already labeled, with the goal of producing a model that will be able to assign correct label to future input data (Sen et al., 2020). SL covers two principal tasks: *regression* and *classification*. The first one is characterized by continuous outputs, while the second provides categorical outputs. In this paragraph the focus is on classification. In fact, in many cases it can be necessary to label the available data, choosing among a given, finite group of classes, which rely on data features. In this context, classifier algorithm are built by learning from a training set, constructing some valid mapping function which will be able to assign to a particular class new, unseen data (Sen et al., 2020). To achieve this, it is necessary to utilize a training dataset sufficiently representative of the considered situation, having available enough examples of each class label (Brownlee, 2020a).

Classification problem has some subcategories:

- *Binary Classification:* when there are only two possible classes, often denoted by 0 and 1 labels;
- *Multi-Class Classification:* when there are more than two possible classes to be predicted;
- *Multi-Label Classification:* when the output of the classification task, for each input data, consists of two or more class labels, differently from binary and multi-class classification, which have only one single class label for identifying each example.

Besides being part of one of these categories, a classification problem can be also *imbalanced*. It happens when the problem is characterized by classes that are unequally populated. Typically this category comprises mostly binary classification tasks. There are different methodologies to deal with imbalanced dataset, like oversampling the minority class or undersampling the majority class, or using specific algorithms which give more relevance to the less populated class during the training phase of the model. This last mentioned category is called *cost-sensitive ML* (Brownlee, 2020a).

In this work the issue of predicting if a LoL event would happen or not will be treated also as a binary classification problem (see Section 5.3). Being LoLs extremely rare, with respect to the total amount of instants in which TEC measurements are actually available, makes necessary to adapt the methodology to an unbalanced dataset.

Another relevant aspect when dealing with SL tasks is the *interpretability*, or the degree to which a human can understand the cause of a model's decision (Miller, 2019). In fact, in addition to providing accurate predictions, these ML methods could be used in the context of providing knowledge about the relationships contained in data. This can help in the model's final evaluation, eventually in model's correction (Murdoch et al., 2019), and also in giving suggestions on possible still unknown connections hidden in the data. A simple way to attain interpretability is using

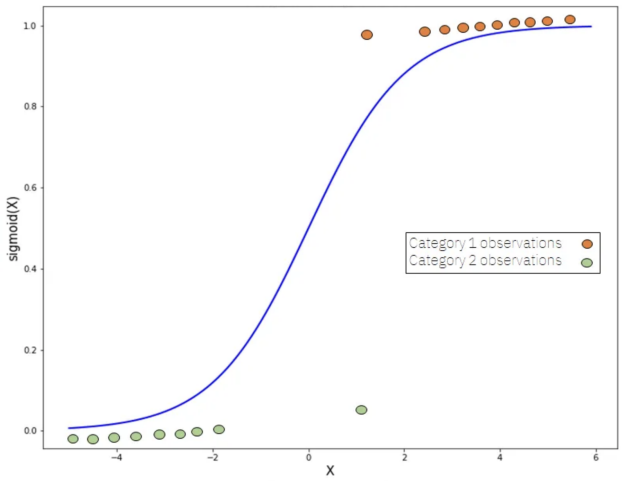

Figure 3.2: Example of a logistic function, where x represents the measurements' values, which could belong to two categories, indicated with two different colors. The sigmoid function is indicated in blue. Credits: Towards Data Science (2020)

interpretable models, like linear regression, logistic regression and decision trees (Molnar, 2020). In this work only the latter two have been applied, and will be explained in the next two Sections.

3.3.1 Logistic Regression

Logistic Regression is a method which principally aims to state if a particular event occurred (or will occur) or not. Therefore it deals with dichotomous outcomes, predicted from one or more independent variables (Hosmer Jr et al., 2013). Typical examples of its application are identification of spam between regular emails, or, in the medical framework, determination of a person's disease or healthy state.
Therefore, the Logistic Regression model will be characterized by a depended variable, called Y, which can take two values, i.e. 1 or 0, stating respectively if there is a particular event or not. The model the will then assign to each predictor a coefficient, which gives an indication on its independent contribution to variation in the dependent variable Y (Boateng and Abaye, 2019). The predictors are explanatory variables, which could be both qualitative or quantitative. The model provides the natural logarithm of the odds ratio, as showed in Equation 3.4.

$$\ln \frac{P(Y)}{1-P(Y)} = \beta_0 + \beta_1 X_1 + \beta_2 X_2 + ... + \beta_k X_k \tag{3.4}$$

where $\frac{P(Y)}{1-P(Y)}$ is the odds ratio, X_1, ... X_k are the explanatory variables, β_1, ... β_k their coefficients and β_0 the intercept. Making the proper calculations, Equation 3.4 can be written in the form of Equation 3.5.

$$P(Y) = \frac{e^{\beta_0+\beta_1 X_1+\beta_2 X_2+...+\beta_k X_k}}{1+e^{\beta_0+\beta_1 X_1+\beta_2 X_2+...+\beta_k X_k}} \tag{3.5}$$

With the aim of finding the $k+1$ coefficients β, the *maximum likelihood estimation* is utilized (King and Zeng, 2001). In this way the β_i coefficients would be the ones that maximize the probability of the observed data.
The obtained probability has the form of a *logistic function* $f(x) = \frac{1}{1+e^{-x}}$, which is part of the

sigmoid curves, having an S-shaped behaviour, as represented in Figure 3.2. This curve makes sure that the predicted values fall within the same range as the binary dependent variable, namely 0 and 1. In fact, going towards low values of the independent variable, it returns probability near to 0. On the other hand, reaching high values of the independent variable, the function approaches to 1 (Boateng and Abaye, 2019).

A crucial step in building a Logistic Regression model is the choice of the independent variables. Even if the model is flexible regarding the input quantities, which could belong to different types like continuous, ordinal or categorical, it is a good practice to make the variable selection relying on previous research about the problem and making preliminary statistical analysis (Stoltzfus, 2011). For example it is important to take into account if some variables are *confounding*, i.e. the ones that influence both dependent and independent variables. These can play a role in obscuring the real connection between the independent variable and the model outcome (Hosmer Jr et al., 2013). Another important aspect is to avoid *redundancy*. If some of the chosen variables are highly correlated, the resulting model will have large standard errors for the estimated β coefficients (Tabachnick et al., 2013).

In this work, after a detailed analysis of the scientific problem, the construction of a Logistic Regression model is done thanks to the *Scikit-learn* class *sklearn.linear_model.LogisticRegression*, described in detail at the following link `https://scikit-learn.org/stable/modules/generated/sklearn.linear_model.LogisticRegression.html`. Scikit-learn is a project, started in 2007, providing Python modules that comprehend a wide range of state-of-the-art machine learning algorithms for both supervised and unsupervised problems (Pedregosa et al., 2011).

3.3.2 Decision Tree

Decision Trees are predictive models, part of the non-parametric supervised learning methods, employed both for regression and classification problems. They are examples of *logic-based* algorithms, that learn simple logic decision rules deduced from the data features. A distinctive component of this type of algorithms is the so-called *node*. When utilized for classification, decision trees classify given data by posing a list of questions regarding the features associated with the items (Kingsford and Salzberg, 2008). Each node entails a question that has the effect of splitting the data into the branches that depart from the node. This process is repeated following the subsequent nodes, resulting in a recursive subsetting of the data. The subsets of data created in this way will be gradually more similar, looking at target values within a node, while will be more dissimilar for inter-node values (De Ville, 2013). The starting node is called *root node*, while at the end of the tree there are the *leaf nodes*, generally associated with the outcomes or class labels (Murty et al., 2011). This structure is schematically reproduced in Figure 3.3.

There are different possible ways to decide how to split the data at each node and progressively build a tree. It is important to identify each step the most significant attribute to obtain a split into groups that are as distinct as possible. Hence, the evaluation of the degree of inhomogeneity, or impurity, in a set of items plays a key role. Possible techniques to achieve this task are information gain, chi-square, Gini index and entropy. The last two are the most widely used. The basic idea is that, when a leaf node is reached, the items contained in it will be classified with the same value as the most commonly occurring class in that leaf. Thus, the fraction of the training observation in that region that do not belong to the most common class can give an estimate of the classification

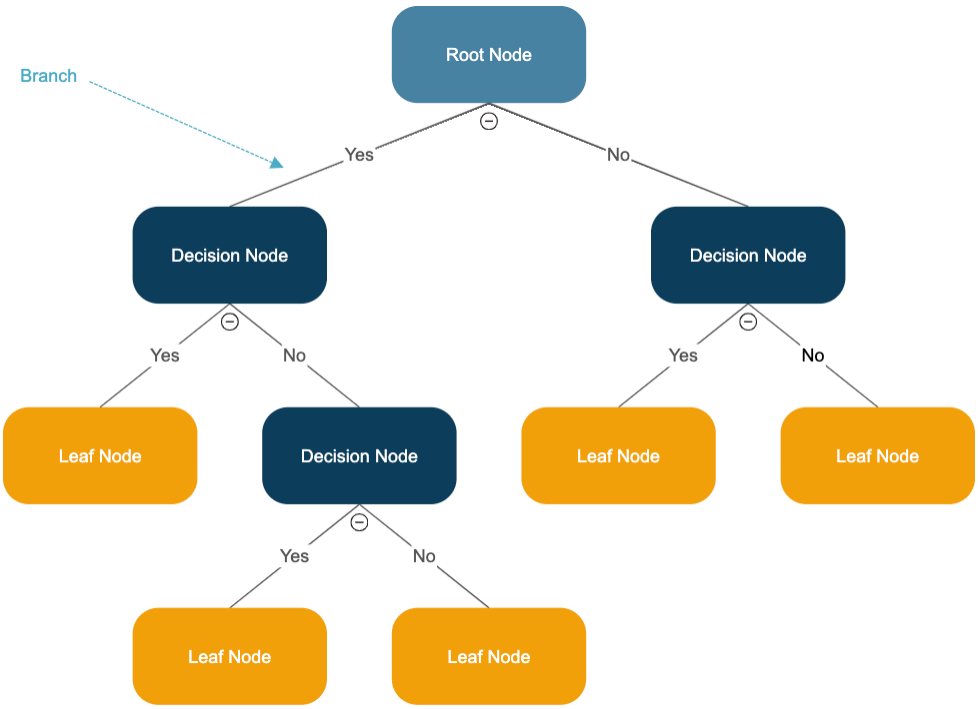

Figure 3.3: Schematic view of a Decision Tree. Credits: SmartDraw Software

error. However, minimizing this value is not enough sensitive for tree-growing. Therefore, more accurate techniques have been introduced. In this context, the *Gini index* is defined as:

$$G = \sum_{k=1}^{K} \hat{p}_{mk}(1 - \hat{p}_{mk}) \tag{3.6}$$

where $\hat{p}_{mk}$ indicates the percentage of training observations in the m_{th} region that belong to the k_{th} class. Consequently, G gives an estimation of the total variance across the K classes. When the majority of $\hat{p}_{mk}$ are close to zero or one, Gini index decreases, meaning that the each node contains predominantly observations from a single class (James et al., 2013).
Another possibility is to evaluate the *entropy*, which defines the amount of randomness in features and measures the discriminatory capability of a particular attribute to make classification (Sen et al., 2020). It is described by Equation 3.7.

$$D = -\sum_{k=1}^{K} \hat{p}_{mk} \log \hat{p}_{mk} \tag{3.7}$$

Even in this case, D will be minimized when the nodes are pure, where pure means that there is a clean separation of examples into groups. Therefore, at each step of a decision tree building, the chosen question to split the training observation into sub-branches will be the one that minimizes the weighted average of the impurity of the resulting nodes (Kingsford and Salzberg, 2008).
For the building of the decision tree described in Section 5.3 the chosen criterion to evaluate impurity is entropy, because of its discriminatory power for classification problems (Sen et al., 2020).

The decision tree method's success is partly due to the fact that it clearly shows how the relationships underneath some problems need multiple contributors to be explained. Figure 3.3

brings out also one of the positive aspects on decision trees, which is that they can be visualized, helping their comprehension and interpretation. Other advantages of this method are, for example, that they require minimal data preparation in confront with other algorithms, they can be feed with both numerical and categorical data and they are based on a white box model, meaning that each condition can be explained by boolean logic (Pedregosa et al., 2011).
On the other hand, there are also some disadvantages. Changing only a little the input data can sometimes produce large changes in the constructed tree, making this methodology *unstable* and *non-robust*. This can be mitigated by using decision trees within an ensemble (Pedregosa et al., 2011). Another big issue is that the resulting tree can be very complicated, with a huge number of levels, which entails the inability of the produced model to generalize on new data, while it describes very well the dataset given for the training. This phenomenon is called *overfitting*. However there are some tools to take care of this problematic aspect. To avoid overfitting, one can limit the complexity of the tree. This can be done by requiring that each leaf node must have at least a minimum number of samples, so as to prevent the presence of excessively subdivided portions of the tree, with very few samples in it. Another way is to set the tree's maximum depth. Moreover, an additional methodology is called *pruning*. It consists in simplifying the tree into a "subtree" by removing internal nodes and make them collapse earlier into leaves when this operation reduces the classification error on a portion of data unseen during the training (Quinlan, 2014). This passage allows to get rid of non-significant and redundant branches, without reducing predictive accuracy. An example of this operation is through *cost complexity pruning*. It considers a set of possible subtrees, each one characterized by a parameter called α, which has the role to control a trade-off between the subtree's complexity and its fit to the training data (James et al., 2013). When $\alpha = 0$ the subtree corresponds to the original tree, when it increases it corresponds to more and more pruned subtrees. The more suitable α value will be found using a validation set or cross-validation.

Another issue that needs to be cared of when building a decision tree is the balance between different classes in the available dataset. In fact, it is possible to introduce some biases in the model if one class dominates (Pedregosa et al., 2011). It is evident if one thinks at the splitting procedure necessary to construct a tree: both sets of observations obtained after the division at a particular node will be dominated by one class, while the other, representing the minority of the cases, will be ignored. Nevertheless, the criterion used to evaluate the purity of the obtained sub-sets will see a good performance (Brownlee, 2020c). As mentioned in the first paragraph of Section 3.3, it is important to adapt the model to be able to deal with an imbalanced dataset. In this case, it is possible to overcome the issue during the splitting process, by taking care not only of the purity of the obtained classes, but also of the importance weight of each class. By giving an higher weight to the minority class, it will gain more importance and higher impact on node purity. A widely used practice for class weighting is to chose the inverse of the class distribution present in the training dataset. In this cases the obtained decision trees are called weighted decision trees, class-weighted decision trees, or cost-sensitive decision trees (Brownlee, 2020c).

It is possible to implement a cost-sensitive tree by using a Scikit−learn package *sklearn.tree.DecisionTreeClassifier* (see `https://scikit-learn.org/stable/modules/generated/sklearn.tree.DecisionTreeClassifier.html#sklearn.tree.DecisionTreeClassifier` for more details) and modifying the *class_ weight* hyperparameter.

Chapter 4

Ionospheric dynamics

4.1 High-latitude plasma dynamics

Earth's ionosphere can be roughly dived into three region with different characteristics, mainly attributable to the amount and orientation of the received solar radiation and the relative inclination of the Earth's magnetic field. These are the equatorial, mid-latitude and high-latitude regions. The most well-understood is the one ad mid-latitudes, where the ionization is almost entirely due to the diurnal and seasonal amount of received energetic X-ray and UV solar radiation, whit winds and neutral air also playing important roles (Hunsucker and Hargreaves, 2007). In addition to these effects, the equatorial ionosphere is deeply influenced by the electromagnetic forces produced by the nearly horizontal magnetic field lines, which cause a significant enhancement in the effective conductivity near the magnetic equator, leading for example to the amplification of the equatorial electrojet current (Baumjohann and Nakamura, 2007). Instead, the high-latitude ionosphere is traversed by nearly vertical geomagnetic field lines, producing an extremely complex ionospheric plasma dynamics. As deepened in Section 1.4, thanks to the Earth's magnetic field, this region results coupled with the magnetosphere, which is in turn highly influenced by the solar wind action. This chain of interactions induces the high-latitude ionospheric plasma to drift together with magnetic field lines, generating a two-cells convection pattern. This macroscopic motion is highly variable, with size and shape being dependent on the IMF orientation and module. The high-latitude ionosphere is also affected by particle precipitation, which contributes to the ionization, particularly in the magnetic cusp and auroral oval regions. Other processes, such as frictional heating, particle and heat exchange with the plasmasphere, and interaction with thermospheric winds (Tashchilin and Romanova, 2002), have an effect on the polar ionosphere, contributing to the significant complexity of this region. Furthermore, while photoionization has a key role in all the ionospheric region, in the mid- and high-latitude one it is particularly important to take into account the local season conditions, which determine the portion of this region that is interested by direct sunlight.

In recent times, an increased interest has been developed to ionospheric modeling, with the goal of reproducing and predicting the behavior of ionospheric dynamics over varying temporal and spatial scales. These models are extremely useful for advanced technological systems that heavily rely, for example, on radio signal propagation applications. Their principal target is the ionospheric electron density's dynamics description. One of the fundamental aspects for ionospheric models' progression is the knowledge of the dynamic processes that characterize the ionosphere at various

altitudes, latitudes, and under different environmental conditions. Therefore, in the perspective of building more and more accurate models of the mid- and high-latitude region, or improve the existing ones, it is important to distinguish the many different physical mechanisms that influence the local electron density behavior, as well as to understand the scales at which they act, their relative weight, and their dependence on external parameters. In order to recognize and isolate the different contributors and spatial scales affecting these regions, in this work the MEMD method, described in Section 3.1, is applied to the electron density distribution at mid and high latitude (above 50° magnetic latitude), obtained through data collected by Swarm mission (see Section 2.1).

4.1.1 MEMD applied to ionospheric density maps

The MEMD technique applied to the ionospheric density distribution identifies its main intrinsic modes, which are associated with specific spatial scales. Once these modes are extracted, their relative contributions to the original distribution can be assessed, allowing us to identify the most significant modes and the spatial scales at which they operate.

Data selection

For this specific type of analysis, the period January 01, 2016, to December 31, 2021, was chosen because it is characterized by low solar activity level. In fact, this six-year time interval enables a robust analysis of electron density distribution at medium and high latitudes in the Northern hemisphere, during a period characterized by a mean value of the solar radio flux at 10.7 cm (2800 MHz) of 80±20 sfu (see Section 2.2 for more details on this index). This choice enables a better study of other parameters that influence the shaping of the electron density distribution under similar solar activity conditions. Specifically, the aim was to analyze how the resulting modes vary depending on the season and geomagnetic activity conditions. Consequently, the dataset was divided into sections based on local seasons, centered around equinoxes and solstices. Indeed, each year was divided into four three-month periods, in order to capture the seasonal changes accurately. This division guarantees that the observed spatial distributions of electron density corresponds to specific solar illumination conditions at the satellite's position. For this reason, the spring and autumn equinoctial periods have been considered together, because referring to the same illumination configuration.

On the other hand, to consider the impact of geomagnetic activity on the distribution of electron density, the dataset was divided into two distinct periods: one corresponding to low geomagnetic activity conditions and the other to high geomagnetic disturbance. The identification of these periods was accomplished using the SME index, which complements the AE index obtained from the global magnetometer network, SuperMAG (Gjerloev, 2012). Both indices are better described in Sections 2.2 and 2.4. The choice to use the SME index (Newell and Gjerloev, 2011) instead of the more-widely-used AE index (Davis and Sugiura, 1966) was done since the latter is not available for the entire period under analysis. However, recent studies (Bergin et al., 2020) have demonstrated the trustworthiness of the SME index as a robust indicator of geomagnetic activity at high latitudes, similar to the AE index. SME index is obtained through the same calculation method as the AE index, but using a significantly larger number of magnetometer stations, typically ten times more than those used for the AE index. The wider station coverage improves the accuracy of timing, intensity and event location determination, resulting in an enhanced precision in capturing

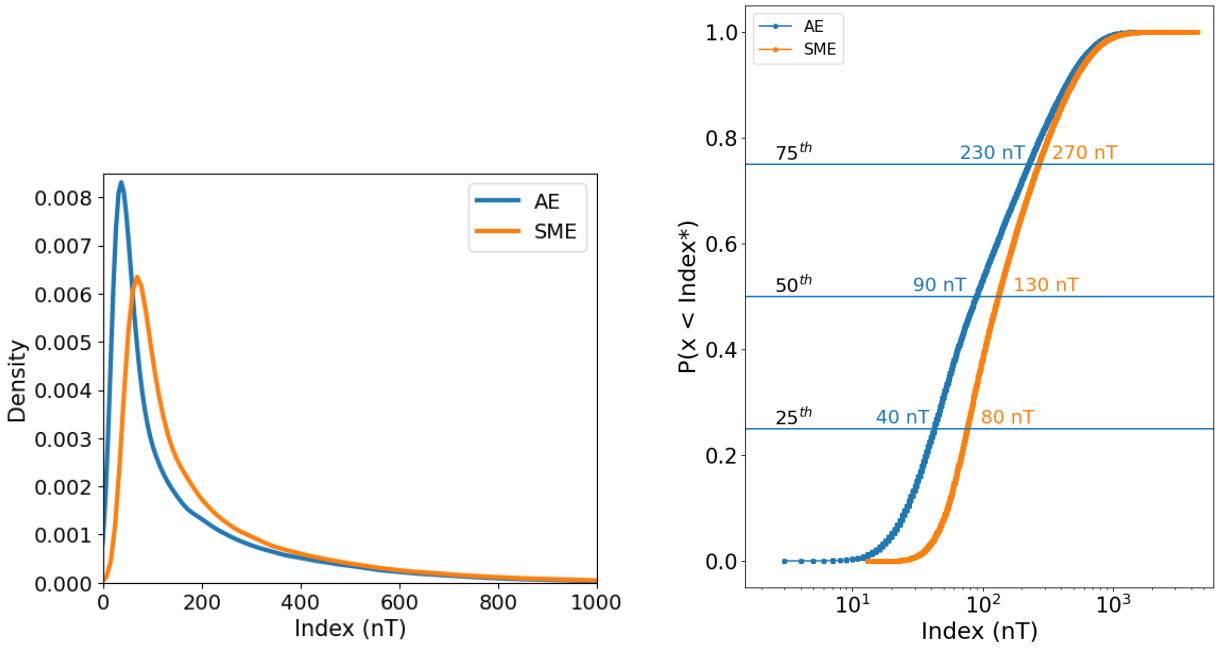

(a) (b)

Figure 4.1: a): Probability density distributions of AE (in blue) and SME (in orange) values. **b):** Cumulative distributions of AE (in blue) and SME (in orange), with three horizontal lines indicating the 25^{th}, 50^{th} and 75^{th} percentiles. At the interception of the horizontal lines and the cumulative distributions, the associated value in nT is indicated with the same color as the index it refers to. Both **a)** and **b)** panels distributions refer to the period that goes from January, 1 2016 to March 31, 2019.

the dynamics of geomagnetic disturbances. In order to have a additional confirmation of the interchangeability of the two indices, a test was made for the period in which they are both available, i.e. from January 2016 to March 2019. The two time series have a correlation coefficient of 0.94, with SME reaching slightly higher values, as one can notice from the distributions in Figure 4.1 a. As it is possible to notice in the next Sections, when the AE index can be used as an indicator of the high-latitudes geomagnetic activity because the selected period is covered by this index, threshold values are chosen by looking at the percentiles of the cumulative distribution. To find the correct analogues for SME, taking into account the fact that SME reaches higher values for the same level of geomagnetic activity, the cumulative distributions of the two indices are compared in Figure 4.1 b. Here it is possible to see that to the same percentile is always associated with higher values of SME, confirming that it is not possible to use the same values in nT that work for AE. Therefore, considering the SME cumulative distribution that refers to the entire period under analysis, thus including the months between April, 2019 and December, 2021, which were not included in the distributions of Figure 4.1, the resulting SME's thresholds, chosen to distinguish between quiet and disturbed geomagnetic conditions, are 70 nT and 230 nT, which represent respectively the 25^{th} and 75^{th} percentiles of the cumulative distribution during the entire period under analysis. More specifically, at high and mid-latitudes and during the selected period, SME values below 70 nT indicate low geomagnetic activity conditions, while values above 230 nT denote periods characterized by the presence of generalized geomagnetic disturbance.

Often in literature, Kp index is used to describe the level of geomagnetic activity in the geospace. It provides a global measure of subauroral disturbance and is widely used in various geospace models

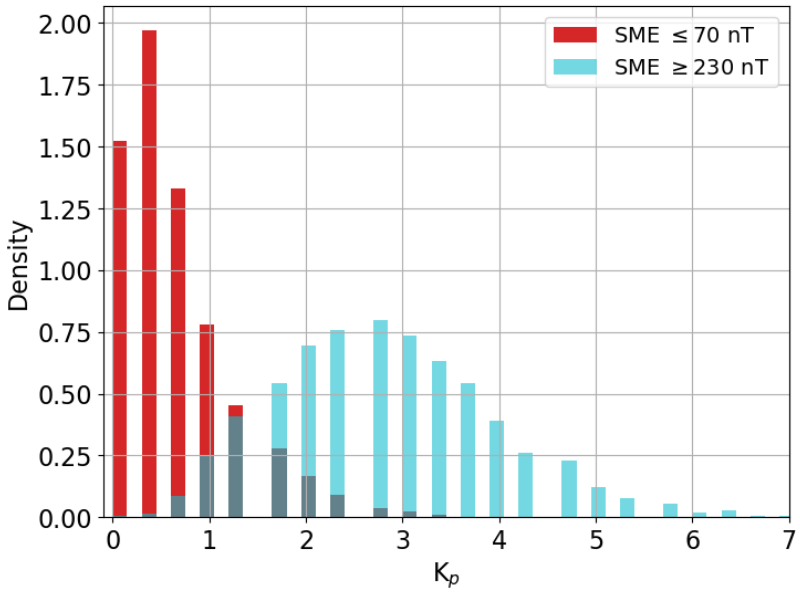

Figure 4.2: Kp index distributions associated with value of SME $\leq$ 70 nT (red) and SME $\geq$ 230 nT (cyan).

and studies. In fact, Kp is utilized to parameterize empirical geospace models and is correlated with various parameters in near-Earth space, including magnetic field geometry, electron and ion fluxes, electric fields, wave activity, auroral phenomena, and more. It is also employed in physics-based geospace models for simulating the magnetosphere and ionosphere. However, for this study, SME index was used instead of Kp because it focuses on the auroral zone and offers a high-resolution measure of auroral electrojet activity. In contrast, the Kp index provides a global perspective on overall geomagnetic activity at mid-latitudes but with a lower temporal resolution of 3 hours. During the selected quiet periods, where SME values are below 70 nT, the corresponding average Kp value is 1-. On the other hand, periods of disturbance align with a Kp value of 3-. This last value, generally, is not considered as indicative of high geomagnetic disturbance. For example, the National Oceanic and Atmospheric Administration (NOAA) service for Kp index issues an alert only when Kp is greater then 4. However, one has to keep in mind the different temporal resolution and the more global character of Kp index. Figure 4.2 shows that Kp values associated with the two SME conditions have a completely different distribution, confirming the different geomagnetic conditions chosen in this manner.

Electron density maps for different seasons and geomagnetic activity conditions

Following the data selection, it is possible to produce six maps of the Northern mid and high-latitude region to be used as input for the MEMD algorithm (described in Section 3.1), with each map referencing a seasonal period and one of the two levels of geomagnetic activity. Six two-dimensional matrices are obtained binning the electron density data of each one of the subsets into a grid of 1° x 1° in magnetic latitude and MLT (1° corresponds to 4 minutes in MLT). They are reported in Figure 4.3. Each bin in the maps reports the mean electron density value (N_e) considering all the Swarm measurements that fall within it. Specifically, Figure 4.3 displays six distinct maps arranged in two columns. The column on the left corresponds to the period of low geomagnetic activity (SME $\leq$ 70 nT), while the column on the right represents the period of high geomagnetic activity (SME $\geq$ 230

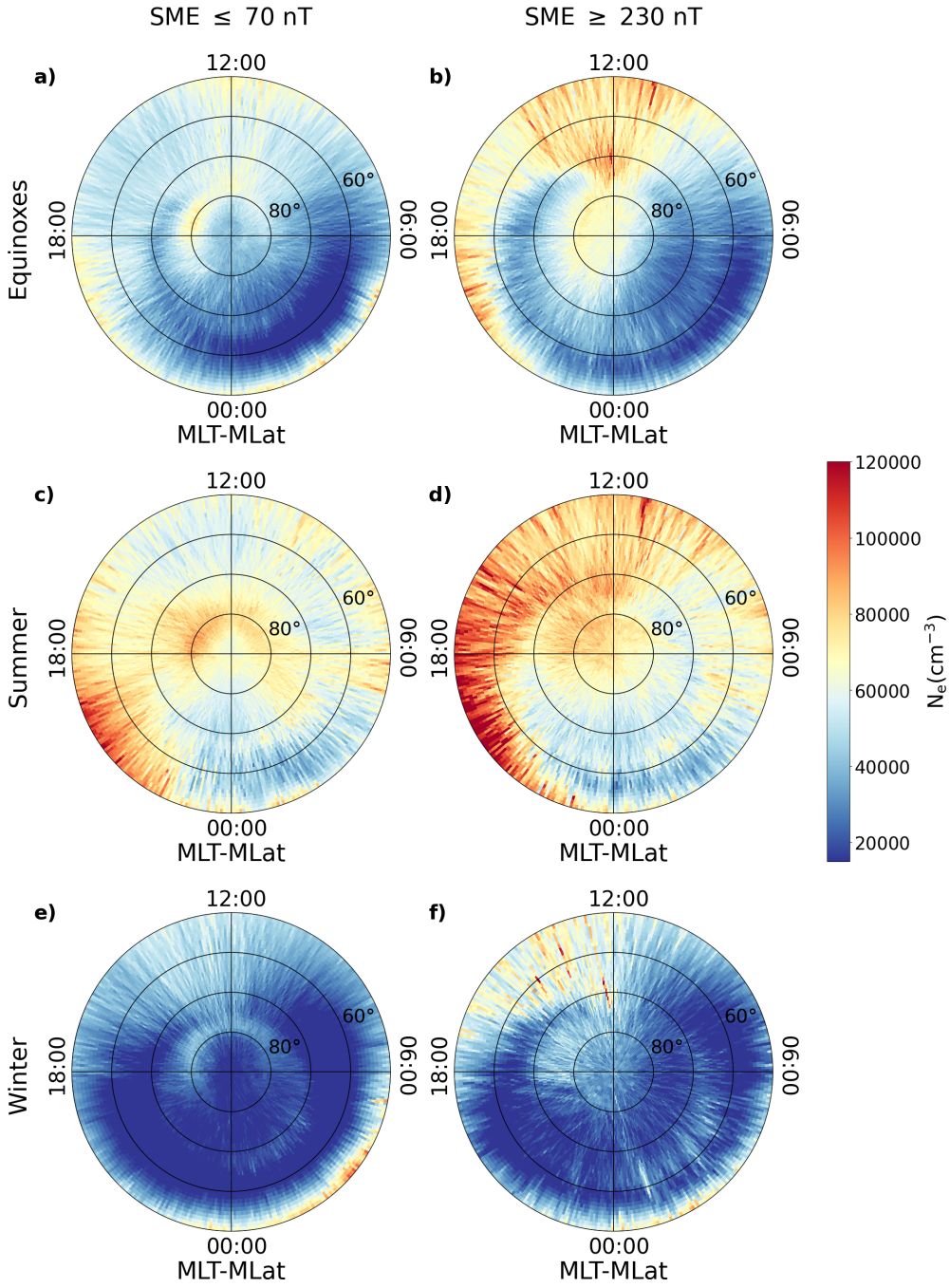

Figure 4.3: Polar view of the average spatial distribution of electron density (N_e) for low (left column) and high (right column) geomagnetic activity conditions in the Northern hemisphere, represented in the QD-magnetic latitude (MLat) and MLT reference system. Each column shows the average spatial distribution of electron density during three different periods of the year: equinoxes, summer, and winter. The maps are based on data collected by Swarm A satellite from January 1, 2016, to December 31, 2021, and reflect an average altitude of approximately 460 km. The concentric circles are plotted in 10° intervals, the outermost circle corresponds to 50°. Credits: Lovati et al. (2023a)

nT). The polar views depict the average spatial distribution of electron density during the equinox period (with spring and autumn equinoxes grouped together as electron density is subject to the same solar illumination conditions during these periods), as well as the summer and winter solstice periods for the Northern hemisphere. Data are plotted in a coordinate system that combines quasi-dipole (QD) latitude and magnetic local time (MLT) (see Section 2.1.1 for further details). The spatial distributions of electron density clearly show a dependence on both magnetic coordinates, as well as variations associated with seasonality and the level of geomagnetic activity.
These maps offer valuable insights into several well-known features of electron density in the high-latitude ionosphere. One is that the electron density values during most of the daylight hours can reach values that are nearly twice the ones characterizing the nighttime. This stark contrast can be attributed to the solar ionization process, which serves as the primary mechanism for generating free electrons in the ionosphere. Remarkably, this characteristic remains consistent regardless of the geomagnetic activity levels, while it clearly shows a dependence on season.
Another notable aspect is the electron density depletion observed in the sub-auroral ionospheric region, on the nightside, known as the Main Ionospheric Trough (MIT), which acts as a boundary separating the auroral and mid-latitude regions Rodger et al. (1992). The MIT is a highly dynamic structure that serves as a signature of the magnetospheric plasmapause in the nighttime ionosphere. This characteristic remains consistent across various levels of geomagnetic activity and throughout different seasons.
Lastly, another notable characteristic, particular evident during equinoxes, is the presence of a region of enhanced electron density values in the mid-latitude and subauroral ionospheric band, which can be observed especially in periods of disturbed geomagnetic activity. This phenomenon is known as the Storm-Enhanced Density (SED), and its generation and decay mechanisms have been studied through ground-based and space observations Zou et al. (2014). Figure 4.3 panel b and d show that the SED region can form a plume, which extends from the dayside into the polar cap, along the convection streamlines, originating the well-known Tongue-Of-Ionization (TOI). Foster et al. (2002) proposed that the TOI represents the ionospheric projection of the equatorial plume in the magnetosphere. Its spatial distribution within the polar cap region is deeply influenced by the orientation of the IMF, specifically the B_y and B_z components. In particular, in the Northern hemisphere the TOI moves towards the dawn sector with positive IMF B_y and towards the dusk sector with negative IMF B_y. Moreover, for negative IMF B_z, the TOI appears narrower but more intense over the polar cap, compared to positive B_z values. This behavior is consistent with the influence of IMF B_z and B_y components on the polar ion convection pattern: B_z governs the cross polar cap potential and ion convection pattern, while B_y determines the dawn-dusk asymmetry in this convection. While in this section the average distribution of electron density is not compared directly with the orientation of the IMF, it is evident that this description aligns well with the average distribution obtained during periods of high geomagnetic activity, during which, as will be discuss later, the IMF B_z component is negative.

MEMD application

The polar maps showed in Figure 4.3 are used as an input for the MEMD algorithm, described in Section 3.1. In particular, with the goal of studying the region above 50° in magnetic latitude, but in order to avoid a poor description of the lower latitude border, the considered maps start at

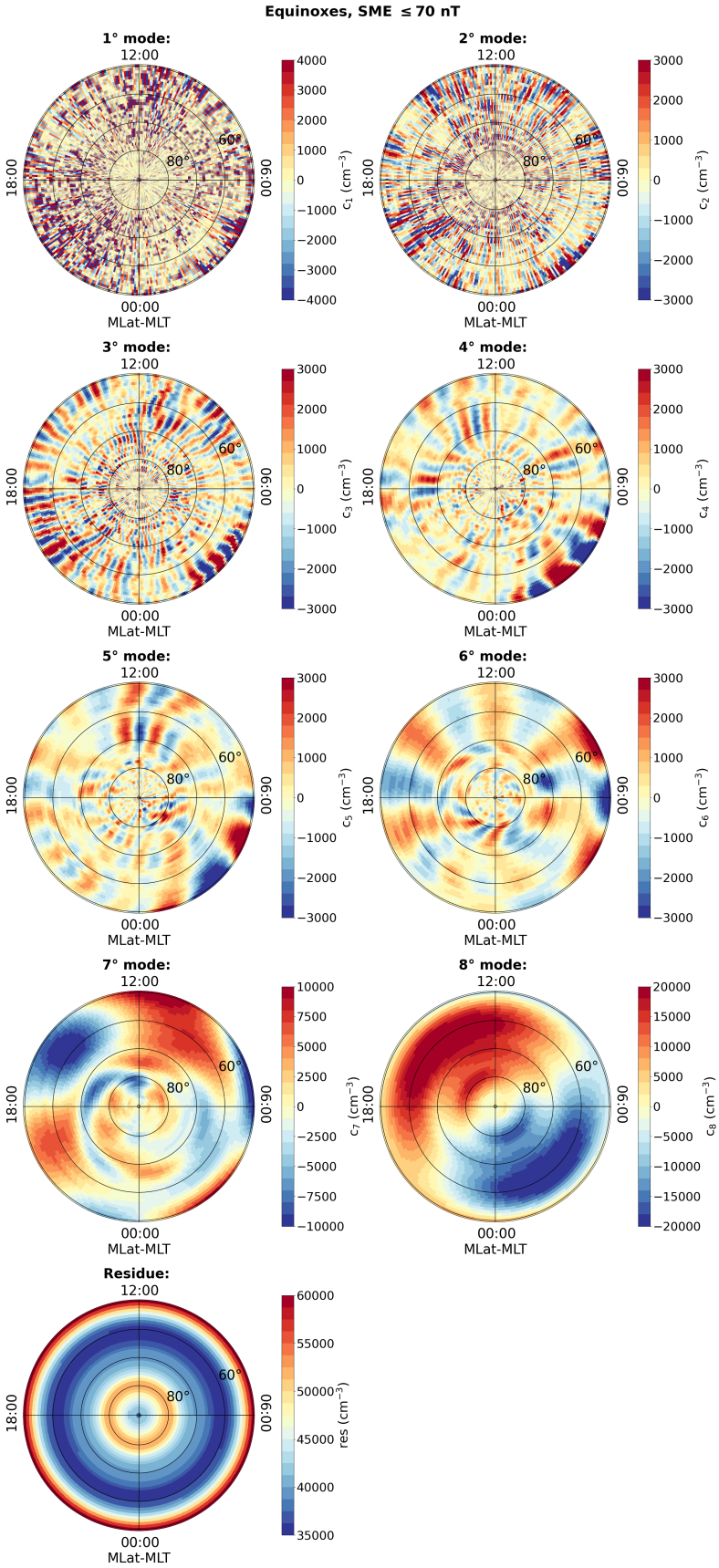

Figure 4.4: Polar view of the 8 modes and the residue obtained from the MEMD of electron density distribution during equinoxes period, specifically under low geomagnetic activity, in the Northern hemisphere. Maps are represented in the QD-magnetic latitude (MLat) and MLT reference system. The concentric circles are plotted in 10° intervals, the outermost circle corresponds to 50°. Credits: Lovati et al. (2023a)

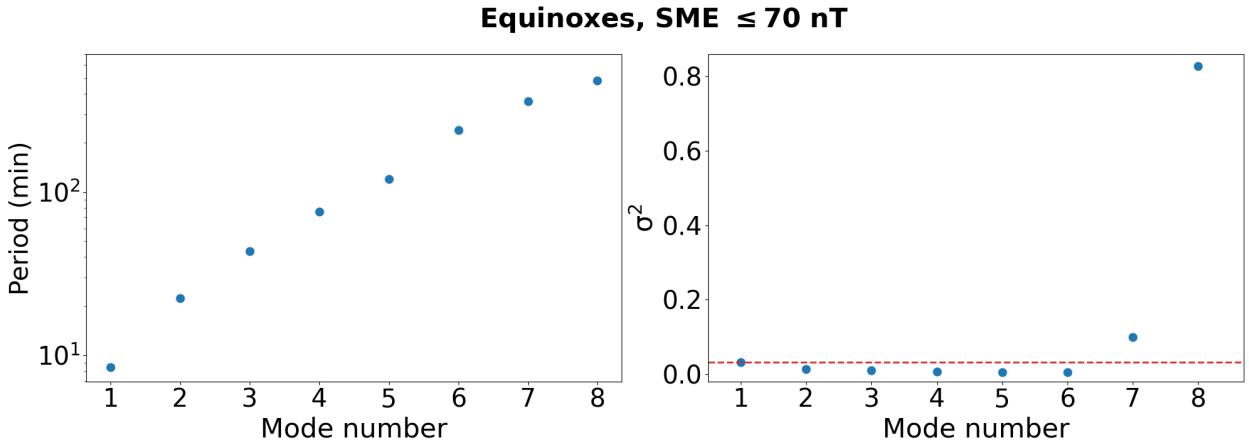

Figure 4.5: *On the left side:* time periods obtained from the frequency analysis of each one of the modes of Figure 4.4. *On the right side:* energy content of each one of the modes of Figure 4.4 evaluated as the normalized variance. The horizontal dashed line indicate the energy value of the first mode which is associated with noise. Credits: Lovati et al. (2023a)

45° (even if in Figure 4.3 only the part above 50° is showed). On the other hand, to take care of the fact that the initial column of the matrix refers to a MLT coordinate range which is connected with the one of the last column, the considered matrix have been triplicated, in order to avoid problems also at the MLT edges of the matrix. In this way the input matrix has a dimension of 45° x 1080°. MEMD algorithm thus returns (N+1) matrices 45° x 1080°, representing the N modes plus the residue in which the signal is decomposed. Of each of these (N+1) matrices, the 360 central columns and the rows representing the latitudes above 50° are selected. (N+1) rectangular maps of 40° x 360° are thereby obtained and then represented in polar coordinates, in order to better visualize the spatial distribution of the different features characterizing each mode.

The analysis is presented by describing all the decomposition's steps in the case of the electron density distribution during the equinox period and under low geomagnetic activity. For the other configurations the passages are the same and only the final decomposition will be showed later. Figure 4.4 presents the results of the initial decomposition. By using as input the map obtained during the equinoctial quiet period, a total of 8 modes plus the residue are obtained. These are visualized by plotting their average electron density value on polar maps, in QD magnetic latitude and MLT coordinates. The top of the maps corresponds to noon, the bottom to midnight, and a binning grid of 1° × 1° is utilized.

For each obtained multivariate empirical mode it is possible to evaluate its characteristic scale/MLT period. This is done by evaluating the periodogram of each series obtained at a fixed magnetic latitude (i.e. with the selected binning this translated in 40 series of 360 points). Then all the periodograms are averaged, to obtain one mean periodogram describing the spectral density distribution of the mode. Finally, to obtain an indication of the longitudinal variability associated with each mode, the main peak of the periodogram is individuated and, from the inverse of its frequency position, a scale is obtained. Since the series depend on the MLT coordinate, the average periods are represented in units of time (min). In this context, Figure 4.5 reports the average periods, obtained through the just described latitudinal-averaged frequency analysis, associated with each mode on the left side, while on the right side the energy distribution is reported, in terms of the normalized variance of each mode with respect to the total variance of the signal. By observing

the energy trend of each mode, it becomes evident that the first six exhibit extremely low energy levels, being characterized by a normalized value of the variance lower then the one of the first mode. Thus, since the EMD acts as a dyadic filter (Flandrin et al., 2004) and since the first mode is usually associated with the noise content of the signals (Wu and Huang, 2004), if the normalized variance is below that of the first mode, then it cannot be physically meaningful in a statistical way. Therefore, upon analyzing the energy contribution of each mode to the original signal, it becomes evident that the last two modes, together with the residue, are the ones that significantly contribute to the description of the initial distribution. On the other hand, by examining the time periods associated with each mode, three distinct trends seem to emerge. For this reason the obtained modes are grouped into three classes: the first one consists of the first two modes, the second class encompasses the four subsequent modes, ranging from the third to the sixth mode, and the third class is comprised of the seventh and eighth modes.
A detailed frequency analysis of the modes belonging to the second class was conducted, in order to see if there was a variation of the average period value with latitude for each of these four modes. The periodograms computed by considering the series of density values corresponding to different MLTs, at fixed magnetic latitudes, were considered separately. With a resolution of 1° for both magnetic latitude and MLT, this entails analyzing 40 distinct periodograms for each mode, obtained from series consisting of 360 data points. From each periodogram, the representative frequency value was determined based on the peak position. Based on the frequency values, the average period was then calculated. It is observed that for all the four analyzed modes of the second class, the period remains practically constant with latitude. The average periods obtained for each one of the four modes are 41 ± 4, 81 ± 9, 130 ± 10 and 235 ± 25 min, which appear to align with the satellite's rotation period of approximately 94 minutes. These modes exhibit harmonic and sub-harmonic characteristics in relation to this fundamental period. The spatial structure of the electron density distribution associated with these modes, as one can see in Figure 4.4, closely resembles the traces observed from the satellite, indicating a potential connection to the data acquisition process. However, it is important to note that these modes do not significantly contribute to the overall decomposition, as their energy remains below that of the first one. Therefore, this second class of modes is combined together and a reduced number of modes is considered for further analysis.

Figure 4.6 illustrates the grouped modes that effectively describe the fundamental modes present in the spatial distribution of electron density in the Northern hemisphere during the equinoctial period and under quiet geomagnetic activity conditions. It includes four modes (now labeled in roman number notation) and the residue. The first mode (I mode), essentially a noise term, is the sum of the initial two modes. The second mode (II mode), a combination of the third to sixth initial modes, seems to be associated with the satellite's orbit. The third (III) and fourth (IV) modes directly result from the initial decomposition and represent the primary modes through which the original signal is decomposed, given their higher energy contribution.

The same identical procedure was applied to the electron density distributions obtained during the summer and winter seasons under low geomagnetic activity conditions, and then repeated for the geomagnetically disturbed period. In all the analyzed cases, the original electron density distribution is consistently decomposed into eight modes, along with the residue. Figure 4.7 displays, in the left column, the time periods, obtained with the latitudinal-averaged frequency analysis, associated with each mode for the equinoxes, summer, and winter periods, while the right column presents

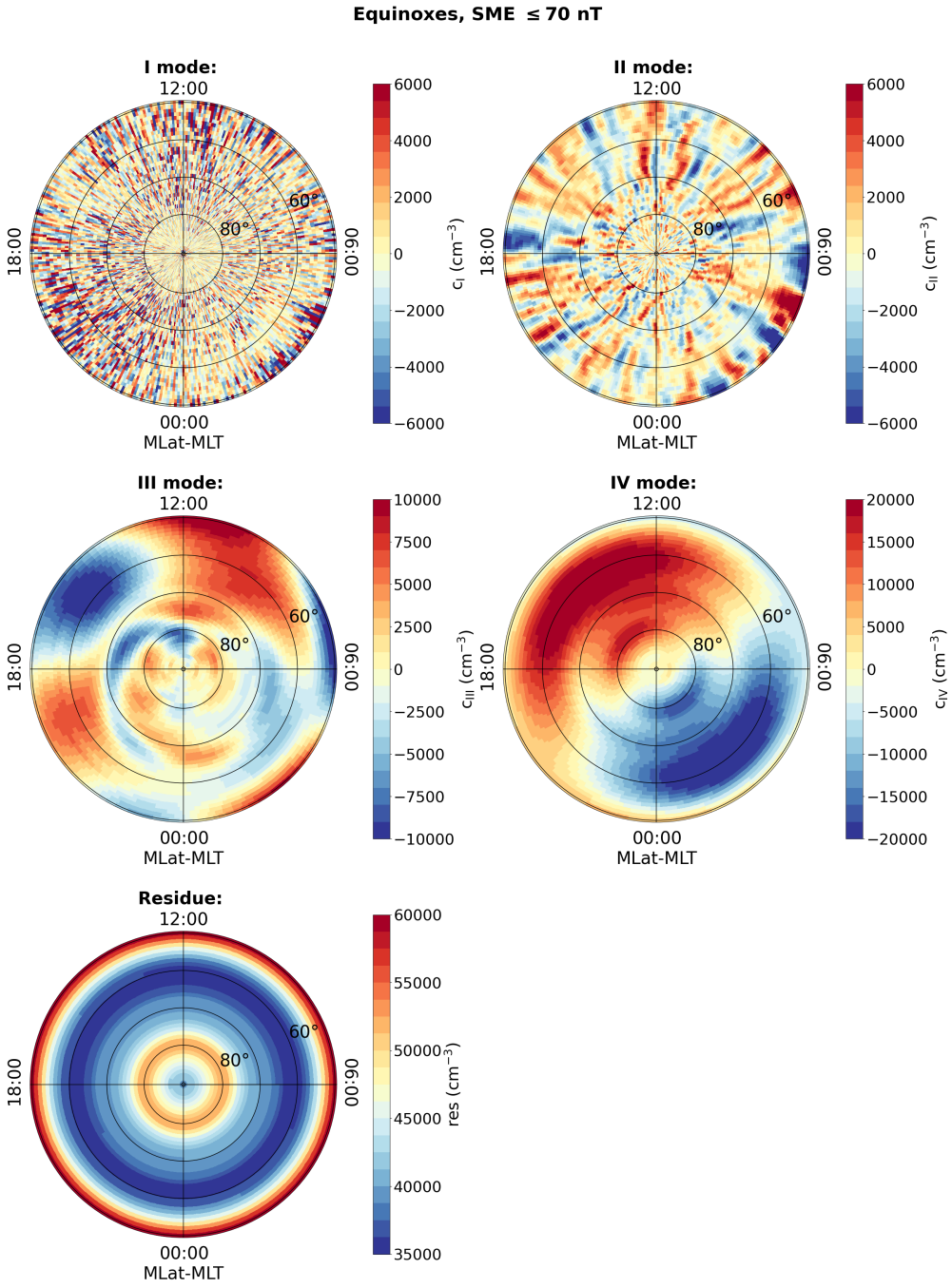

Figure 4.6: Polar view of the fundamental modes and the residue obtained from the MEMD of electron density distribution during equinoxes period, under low geomagnetic activity, in the Northern hemisphere. *I* mode corresponds to the sum of 1° and 2° modes reported in Figure 4.4. *II* mode corresponds to the sum of 3°, 4°, 5° and 6° modes of Figure 4.4. *III* and *IV* modes are equal to the 7° and 8° modes of Figure 4.4 respectively. Maps are represented in the QD-magnetic latitude (MLat) and MLT reference system. The concentric circles are plotted in 10° intervals, the outermost circle corresponds to 50°. Credits: Lovati et al. (2023a)

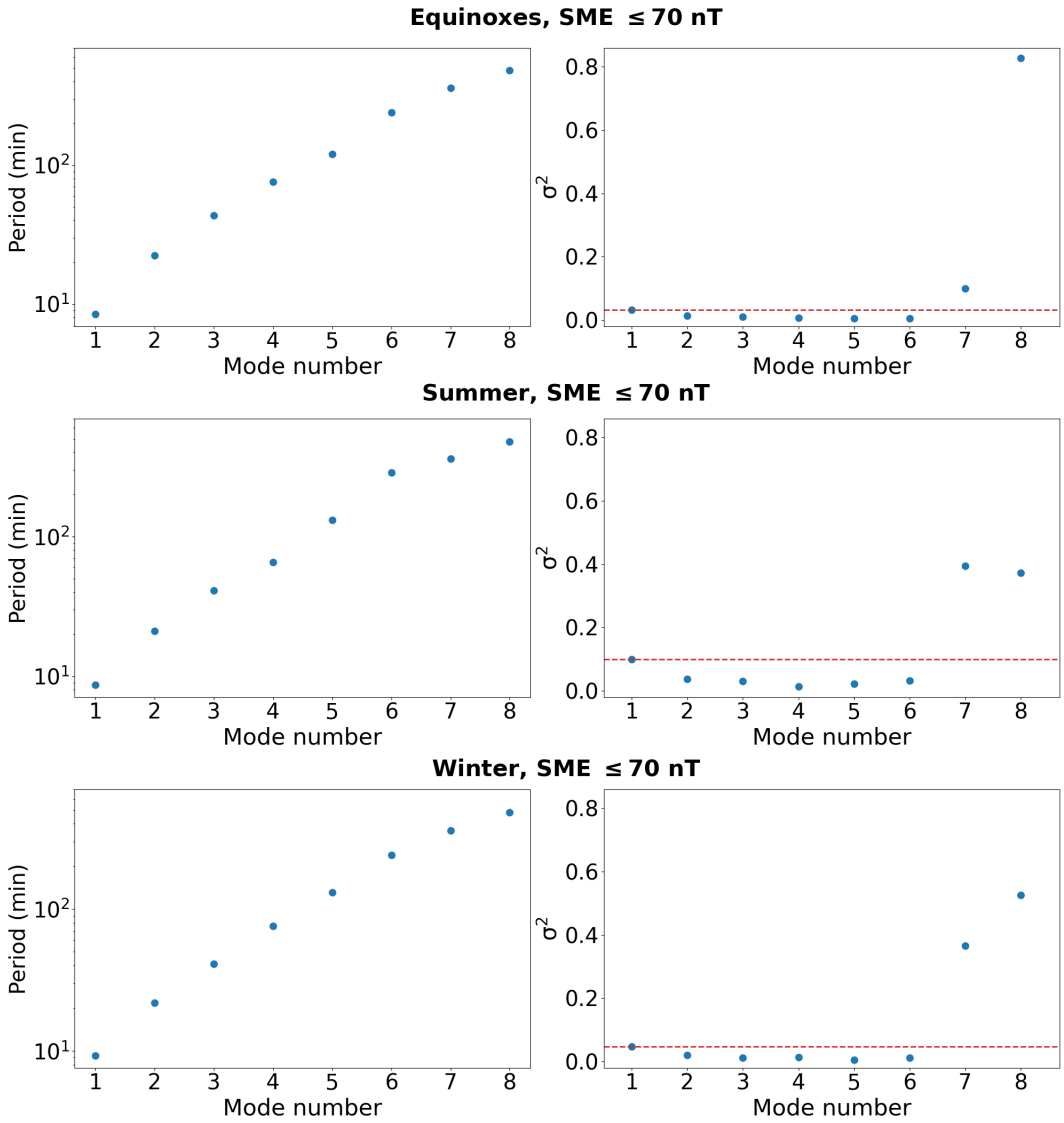

Figure 4.7: *On the left column:* time periods obtained from the frequency analysis of each one of the modes obtained from MEMD of the electron density distribution during equinoctial (*first row*), summer (*second row*) and winter (*third row*) periods, for the Northern hemisphere and during low geomagnetic activity. *On the right side:* energy content of each one of the modes obtained from MEMD of the electron density distribution during equinoctial (*first row*), summer (*second row*) and winter (*third row*) periods, for the Northern hemisphere and during low geomagnetic activity, evaluated as the normalized variance. The horizontal dashed line indicates in each case the energy value of the first mode, which is associated with noise.

the corresponding energy distribution in terms of normalized variance for each mode. Figure 4.7 specifically refers to low geomagnetic activity. In contrast, Figure 4.8 showcases the results obtained for the analysis conducted during high geomagnetic activity.

Regardless of the geomagnetic activity and season, three distinct classes of modes are individuated, carrying different contributions in terms of energy to the original signal. Therefore the same mode grouping approach used during the equinox period under low geomagnetic activity is applied, as previously described in detail. The results are presented in five separate figures, each following a consistent structure, with the four fundamental modes resulting from the decomposition procedure, accompanied by their residue. Figure 4.9 depicts the summer period under low geomagnetic activity, while Figure 4.10 represents the winter period, also under low geomagnetic activity. On the other hand, Figures 4.11, 4.12, and 4.13 correspond to the equinox period, summer period, and winter period, respectively, during high geomagnetic activity.

Discussion of the results and concluding considerations

The application of the MEMD method to the spatio-temporal distribution of electron density at mid and high latitudes in the Northern hemisphere, under different seasonal and geomagnetic activity conditions, has revealed the presence of fundamental modes that underlie the initial distributions. Remarkably, these modes are consistently observed in all six datasets, regardless of the specific season or level of geomagnetic activity being analyzed. By combining the residue with these four distinct fundamental modes, each dataset of electron density can be accurately reconstructed.

To understand the physical processes associated with each mode, their spatio-temporal distributions and how their variation across different seasons and levels of geomagnetic activity are analyzed. Let's begin by examining the residue term, which forms the basis of the electron density distribution and to which the modes are subsequently added to reconstruct the initial distribution.

Residues: When focusing on the residues obtained under low geomagnetic activity, there is a striking similarity in the spatio-temporal structure across the three selected periods: equinoxes, summer, and winter. The electron density, highest at lower latitudes, gradually decreases moving towards higher latitudes until reaching a minimum around 60°-65°. From there, it starts to increase again, reaching a maximum near 80°, before decreasing near the magnetic pole. This pattern reveals two prominent bands of maximum intensity: one at latitudes below 55° and another between 75° and 85° magnetic latitudes. Regions with lower electron density primarily exist between 55° and 75° latitudes and close to the magnetic pole, corresponding to the polar cap. While the spatio-temporal position of these bands remains consistent across seasons, the absolute values of electron density vary, as well as the intensity ratios between the different bands.

To visualize the spatio-temporal distributions of residues, which cannot be effectively represented using a single value scale in all cases, Figure 4.14 is proposed. It displays various electron density profiles as a function of magnetic latitude, for the analyzed seasons and two different levels of geomagnetic activity. It provides a comprehensive view of the spatial variations in electron density across different latitudes, enabling a detailed examination of the patterns and changes associated with each specific season and level of geomagnetic activity. These profiles, which correspond to MLT=12:00, unequivocally show that, at all latitudes, electron density is higher during summer than it is during winter. It also exceeds the density seen during the equinoxes, which is in turn

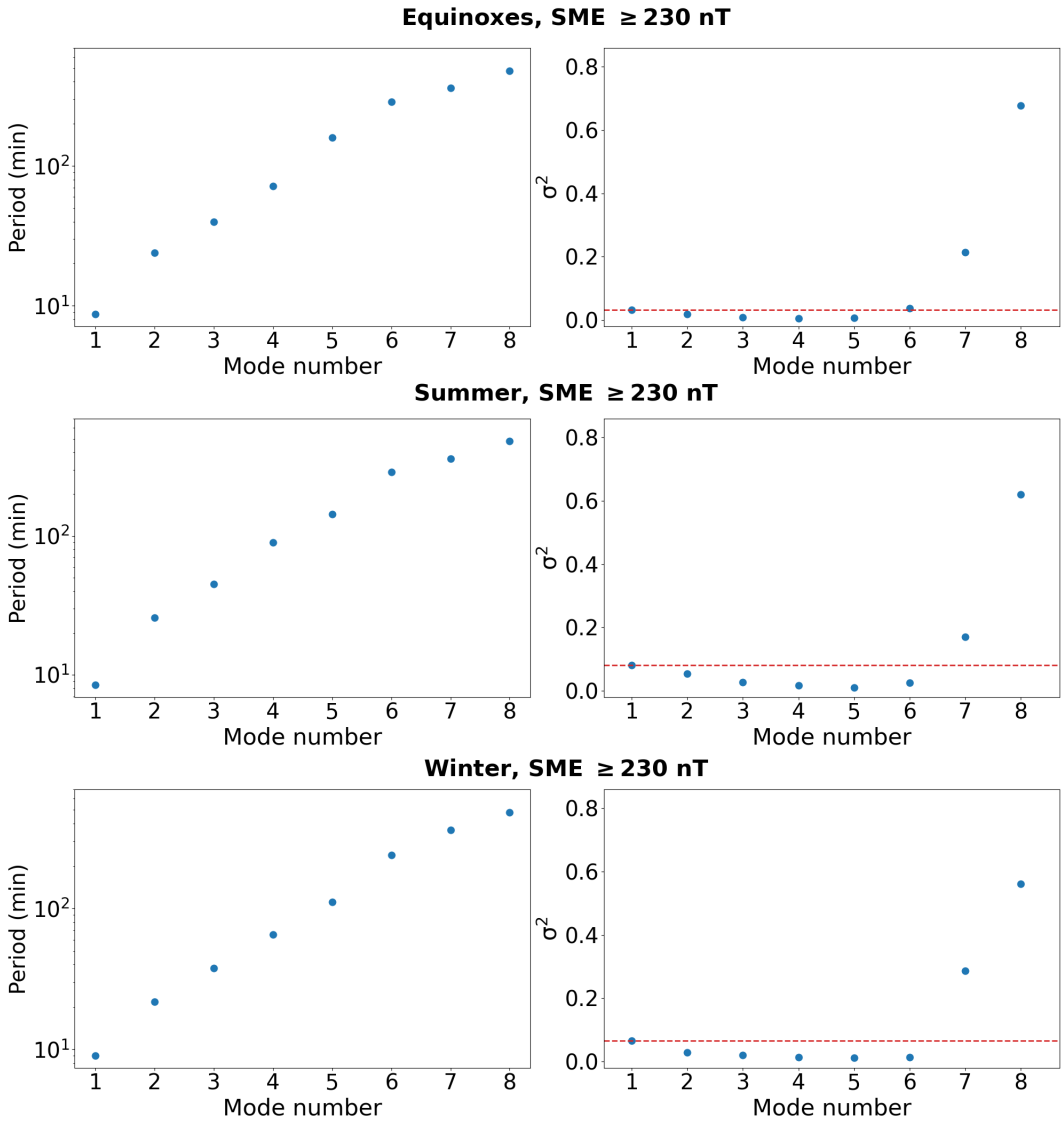

Figure 4.8: *On the left column:* time periods obtained from the frequency analysis of each one of the modes obtained from MEMD of the electron density distribution during equinoctial (*first row*), summer (*second row*) and winter (*third row*) periods, for the Northern hemisphere and during high geomagnetic activity. *On the right side:* energy content of each one of the modes obtained from MEMD of the electron density distribution during equinoctial (*first row*), summer (*second row*) and winter (*third row*) periods, for the Northern hemisphere and during high geomagnetic activity, evaluated as the normalized variance. The horizontal dashed line indicates in each case the energy value of the first mode, which is associated with noise.

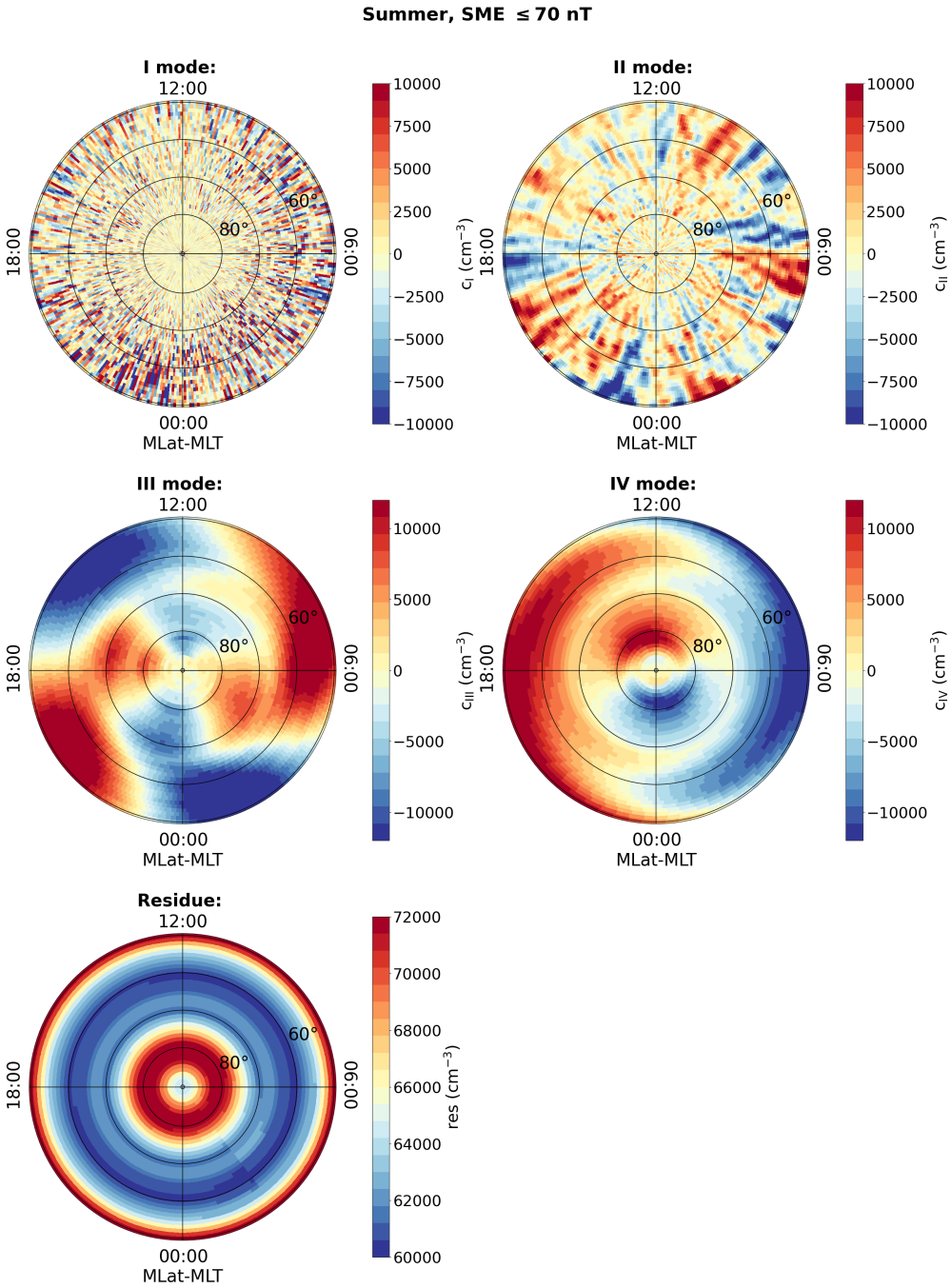

Figure 4.9: Polar view of the fundamental modes and the residue obtained from the MEMD of electron density distribution during summer period, under low geomagnetic activity, in the Northern hemisphere. Maps are represented in the QD-magnetic latitude (MLat) and MLT reference system. The concentric circles are plotted in 10° intervals, the outermost circle corresponds to 50°.

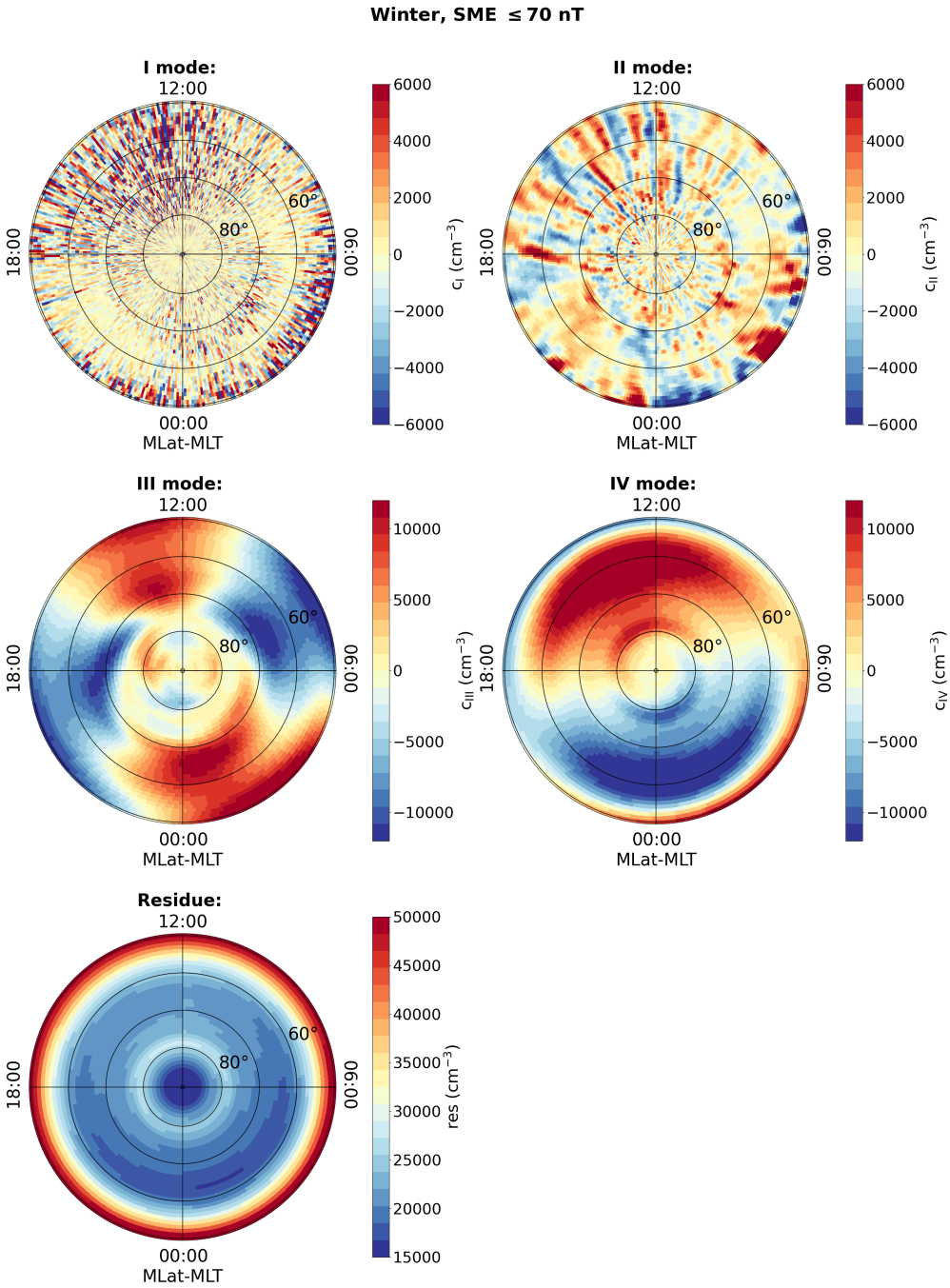

Figure 4.10: Polar view of the fundamental modes and the residue obtained from the MEMD of electron density distribution during winter period, under low geomagnetic activity, in the Northern hemisphere. Maps are represented in the QD-magnetic latitude (MLat) and MLT reference system. The concentric circles are plotted in 10° intervals, the outermost circle corresponds to 50°.

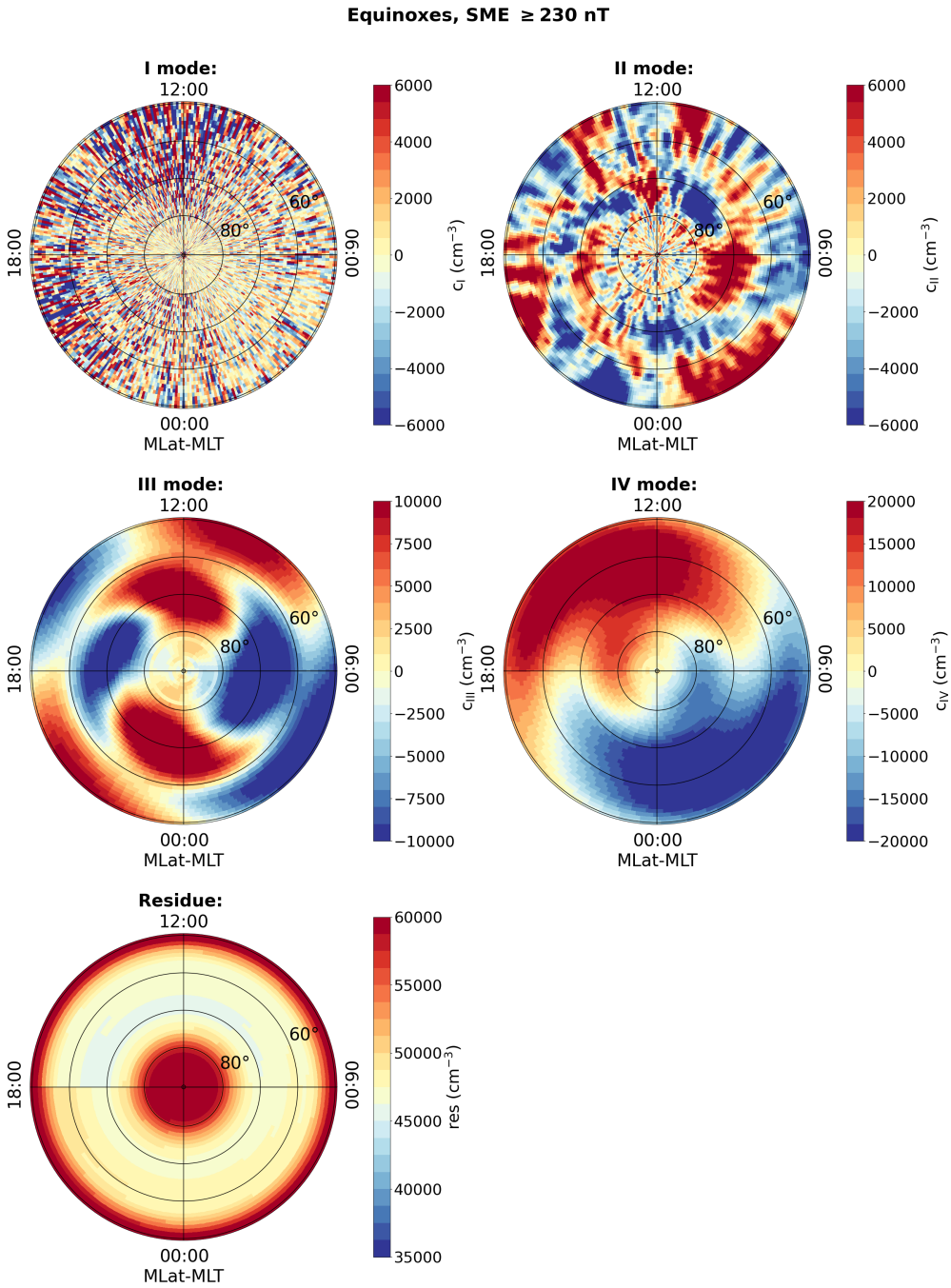

Figure 4.11: Polar view of the fundamental modes and the residue obtained from the MEMD of electron density distribution during equinox period, under high geomagnetic activity, in the Northern hemisphere. Maps are represented in the QD-magnetic latitude (MLat) and MLT reference system. The concentric circles are plotted in 10° intervals, the outermost circle corresponds to 50°.

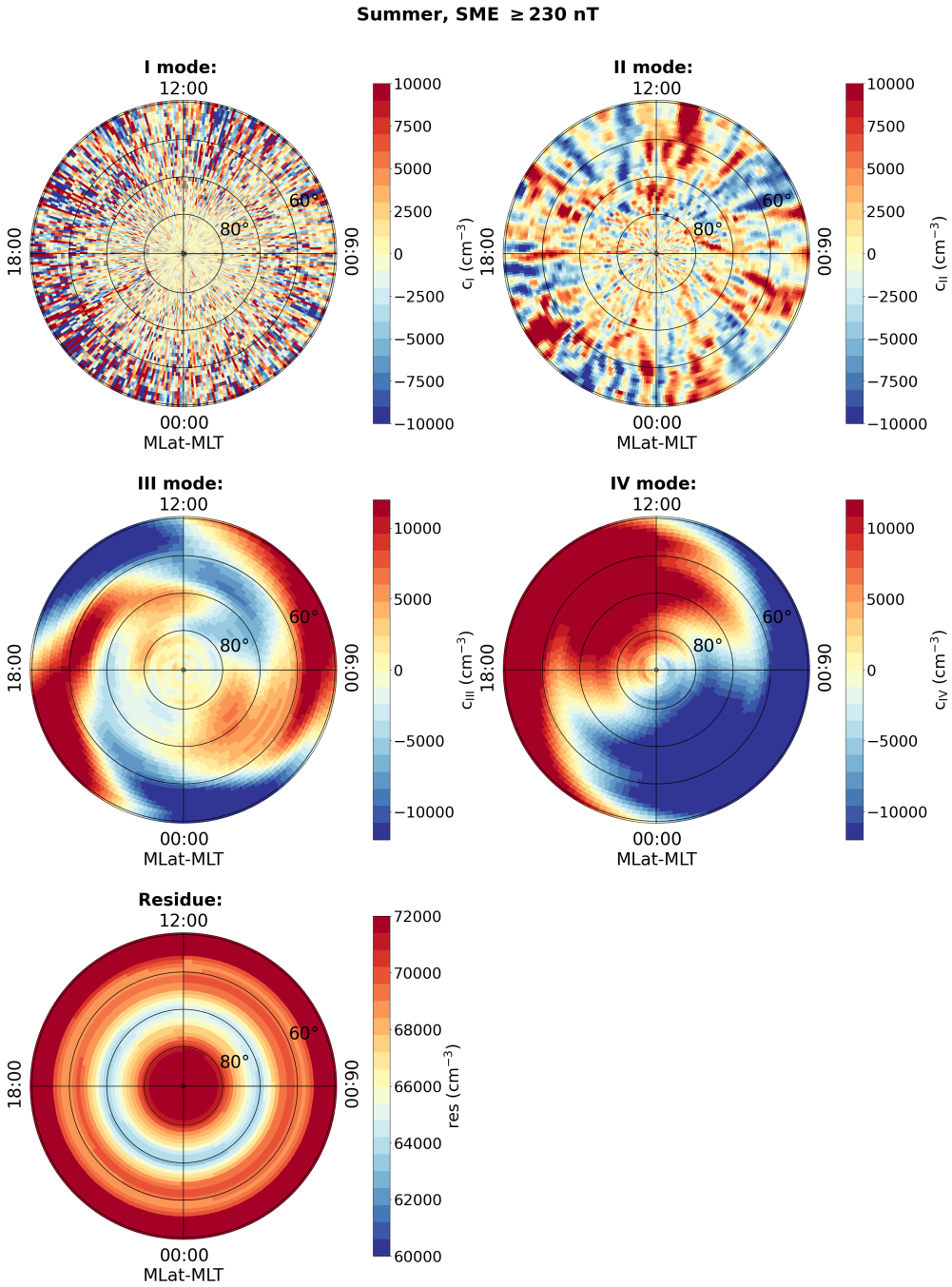

Figure 4.12: Polar view of the fundamental modes and the residue obtained from the MEMD of electron density distribution during summer period, under high geomagnetic activity, in the Northern hemisphere. Maps are represented in the QD-magnetic latitude (MLat) and MLT reference system. The concentric circles are plotted in 10° intervals, the outermost circle corresponds to 50°.

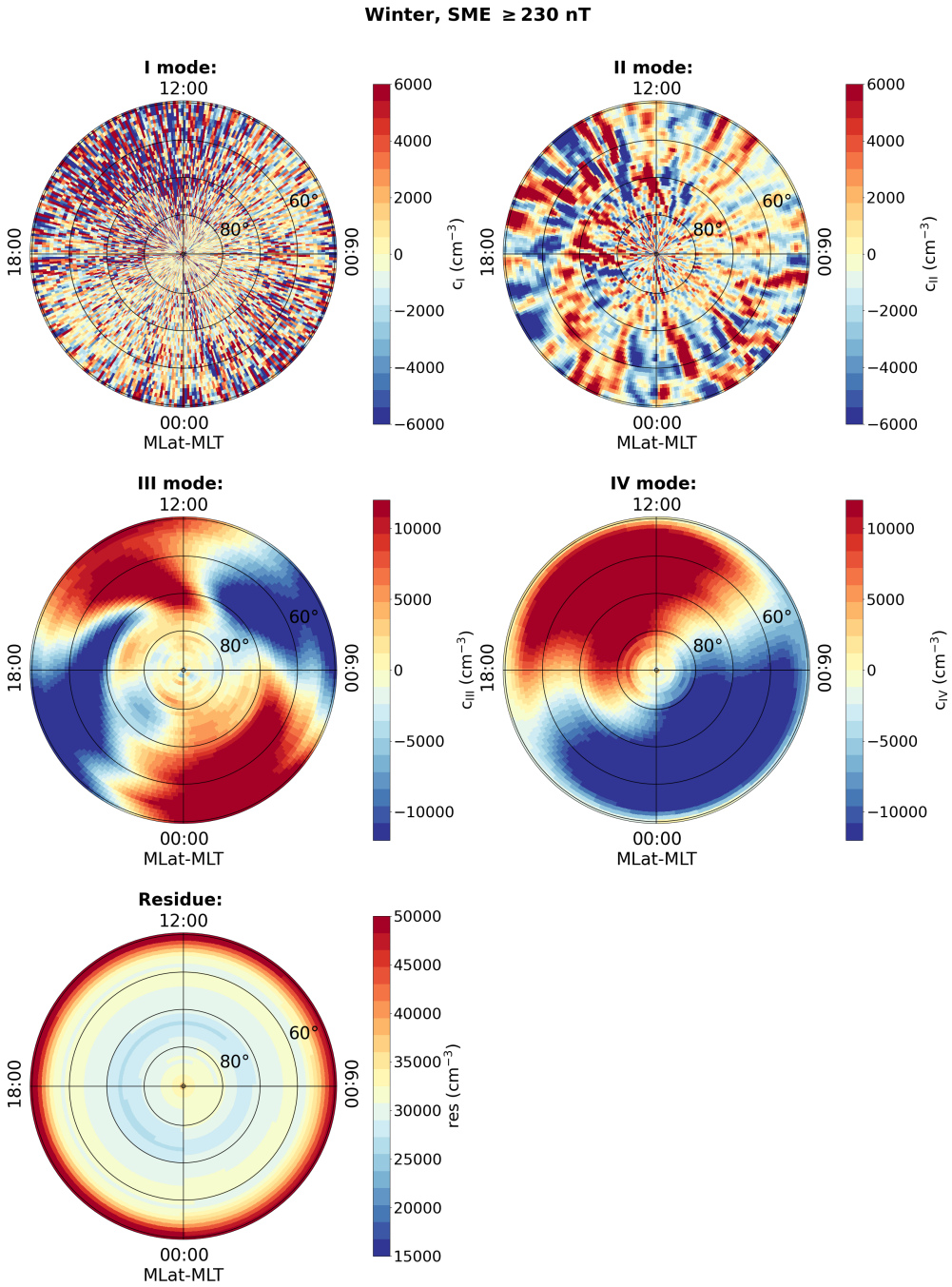

Figure 4.13: Polar view of the fundamental modes and the residue obtained from the MEMD of electron density distribution during winter period, under high geomagnetic activity, in the Northern hemisphere. Maps are represented in the QD-magnetic latitude (MLat) and MLT reference system. The concentric circles are plotted in 10° intervals, the outermost circle corresponds to 50°.

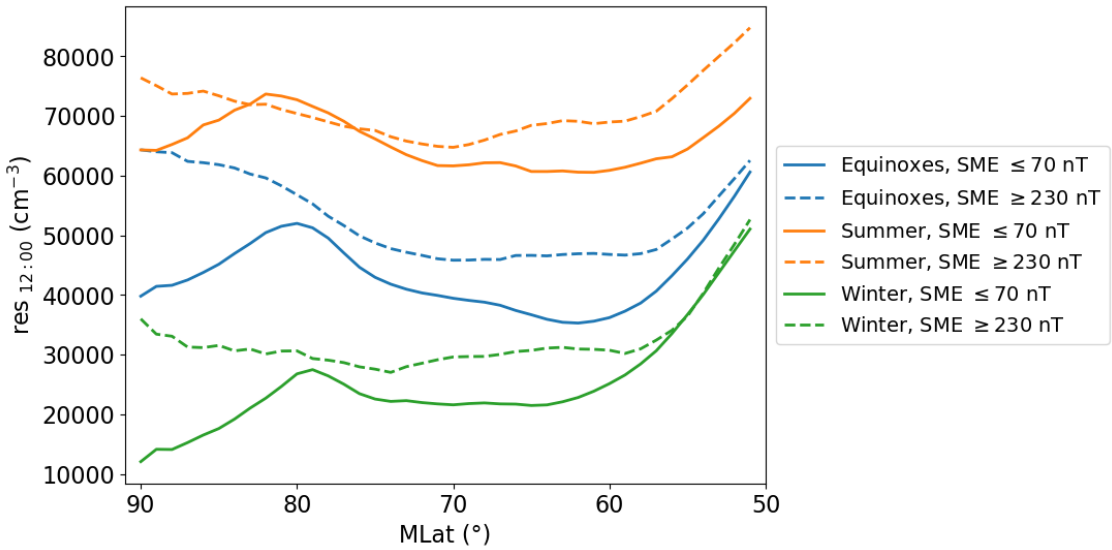

Figure 4.14: Residue trend as a function of magnetic latitude at a fixed MLT value of 12:00 for the three seasons and the two levels of geomagnetic activity. Credits: Lovati et al. (2023a)

higher than winter. This consistent trend holds true regardless of the level of geomagnetic activity. The variation in the baseline electron density aligns with the significant seasonal differences observed in its distribution in the ionospheric F-layer. During summer, there is generally a higher electron density compared to other seasons. This can be attributed to increased solar radiation, which heats up both the atmosphere and the ionosphere. The elevated temperatures facilitate the ionization of atoms and molecules, resulting in a greater electron density in the F-layer. This effect is particularly pronounced in equatorial and low-latitude regions, where solar radiation is more intense. However, similar phenomena can also be observed at higher latitudes, as indicated in this study. Conversely, winter sees a decrease in electron density in the F-layer of the ionosphere. During this season, solar radiation is less intense, and the atmospheric and ionospheric temperatures are generally lower. Consequently, there is reduced ionization of atoms and molecules in the atmosphere, leading to a generally lower electron density. This decrease is particularly noticeable in polar regions, where solar radiation is limited or absent during the winter months. During equinoxes, which mark the transition between summer and winter, there is an intermediate distribution of electron density in the F-layer of the ionosphere. Moderate solar radiation and temperatures during these periods result in a relatively balanced electron density compared to other seasons. Therefore, the spatio-temporal pattern of the residues reflects the fluctuations in electron density within the F-layer of the ionosphere throughout the seasons, which arise from the complex interplay between solar radiation, atmospheric temperatures, and ionization processes.

Moreover, Figure 4.14 provides further insights, revealing that the average level of electron density is influenced not only by the season but also by the level of geomagnetic activity. In the case of high geomagnetic activity, some notable changes occur. The single peak in the density distribution at approximately 80° disappears, replaced by a more constant trend that spans the entire polar region, starting above 60°, with a slight increase over 80°, more marked in the equinoctial case. The increase in electron density with disturbed geomagnetic activity conditions is consistent with existing literature. It can be attributed to several factors that have been extensively studied and documented. One of them is the enhanced energy input from the magnetosphere during periods of

Condition	$\mathbf{v}_{sw,x}$ (km/s)	IMF $\mathbf{B}_y$ (nT)	IMF $\mathbf{B}_z$ (nT)	Dipole tilt
Equinoxes, SME $\leq$ 70 nT	-367	-0.13	1.36	0°
Equinoxes, SME $\geq$ 230 nT	-482	0.10	-2.08	0°
Summer, SME $\leq$ 70 nT	-355	0.19	1.17	10°
Summer, SME $\geq$ 230 nT	-451	-0.36	-2.06	10°
Winter, SME $\leq$ 70 nT	-366	-0.67	0.88	$-10°$
Winter, SME $\geq$ 230 nT	-491	0.24	-1.66	$-10°$

Table 4.1: Interplanetary parameters and dipole tilts necessary as input values for SuperDARN model, relative to each one of the seasonal and geomagnetic activity conditions considered in the present study.

geomagnetic activity. Geomagnetic disturbances, such as substorms and magnetic storms, can lead to the injection of energetic particles into the ionosphere. These particles ionize the neutral particles in the F region, causing an increase in electron density. Another factor is the enhancement of electric fields and plasma convection associated with geomagnetic activity. Electric fields generated by the interaction between the solar wind and the Earth's magnetosphere can accelerate charged particles in the ionosphere, leading to increased electron density. Plasma convection, driven by the motion of plasma within the magnetosphere, can transport higher-density plasma from lower latitudes to higher latitudes in the ionosphere. Furthermore, increased geomagnetic activity can also lead to changes in the thermospheric composition and temperature. These changes can affect the ionization and recombination rates in the F region, influencing the electron density. It is important to note that the relationship between geomagnetic activity and electron density in the F region is complex and can vary depending on specific conditions and locations. However, it is interesting to observe that the residues obtained from the analysis appear to capture these changes, providing insights into the variations of electron density associated with geomagnetic activity.

This is followed by the analysis of the four fundamental modes that emerged from each decomposition.

I and II fundamental modes: as mentioned earlier, the first of these modes essentially represents a noise component present in the data. Its associated energy is extremely low, and the distribution on the MLat-MLT plane does not exhibit any significant structures. On the other hand, the second mode is quite different. As extensively discussed in the previous section, it exhibits a spatial structure that closely resembles the orbit of the satellite from which these data are acquired. Indeed, the average frequency of this mode shows consistency across different latitudes and is comparable to the satellite's rotation period around the Earth. This means that the second mode could capture the effect due to the data collection configuration.

III and IV fundamental modes: these are the most interesting ones, as they are intrinsically linked to dynamic processes occurring within the ionospheric layer under investigation. These modes exhibit a strong dependence on both the season and the level of geomagnetic activity, making them particularly intriguing and worthy of further exploration.

To gain insight into the dynamic processes that contribute to the distribution of electron density for these two modes, regardless of season and activity level, a comparison with the convective pattern was done, overlaying the convection cell structures onto the maps depicting these modes. Indeed, at

high latitudes, the ionized region of the upper atmosphere undergoes a dynamic circulation known as convection, driven by the interaction between the magnetized solar wind and the Earth's magnetosphere. This convection plays a significant role in shaping the distribution of electron density in the ionosphere. The convection patterns exhibit a twin-cell configuration, characterized by the flow moving away from the Sun at the poles and toward the Sun at lower latitudes. The strength of this circulation is influenced by the north-south component of the IMF (represented as B_z), while any asymmetries between the dawn and dusk regions are associated with the east-west component of the IMF (B_y). Convection, in general, exhibits a highly dynamic nature, displaying sensitivity to intermittent phenomena such as variations in the IMF and magnetospheric processes like substorms. One effective method for capturing and analyzing these convection patterns is by utilizing data from SuperDARN, described in details in Section 2.3. To obtain representative average convection motions that reflect the interplanetary conditions underlying the originated data, the mean values of the x-component of the solar wind velocity ($v_{sw,x}$), the y- and z-components of the IMF, and dipole tilt were calculated for each of the six different datasets analyzed and presented in Figure 4.3. The obtained values, which refer to the time intervals used to build the different datasets, were incorporated into the CS10 model Cousins and Shepherd (2010), in order to obtain average trends of electrostatic potential distributions. Table 4.1 reports the used values of solar wind velocity, the two components of the IMF, and dipole tilt in the different cases. Figure 4.15 illustrates the spatial distributions of electron density for the third and fourth fundamental modes obtained from decomposition, during periods of low geomagnetic activity. The Figure consists of six maps, with each pair representing the III and IV modes for the analyzed equinoxes, summer, and winter periods. Each map includes the average electrostatic potential level curves overlaid on top of the electron density distribution. Similarly, Figure 4.16 follows the same structure as Figure 4.15 but focuses on the period of high geomagnetic activity.

Let's begin by analyzing the fourth mode (right panels in Figures 4.15-4.16) and its dependence on the season and geomagnetic activity, also in relation to the structure of the convection cells superimposed on each map. The electron density distribution exhibits a clear day-night difference. During equinoxes there are higher density values within the MLT interval between 7:00 and 20:00, with a peak occurring between 11:00 and 18:00. This pattern holds true across all latitudes analyzed, with a "rotation" of this region toward later or earlier morning hours for summer and winter periods respectively. This day-night asymmetry is primarily attributed to the increased ionization due to the direct interaction between solar radiation and the Earth's atmosphere. Conversely, during the night, radiation is absent or significantly reduced, leading to a decrease in ionization and electron production. Moreover, one has to take into consideration the recombination effect that takes place during the night. Without direct solar radiation, electrons in the ionospheric plasma tend to recombine with ions, leading to a decrease in electron density within the F-layer throughout nighttime. Furthermore, ionospheric wind movements and diffusion processes can influence electron distribution, giving their contribution to the day-night asymmetry. It is important to note that the day-night asymmetry also depends on other factors such as latitude, solar activity, and the presence of geomagnetic events. The proposed study fixes the level of solar activity while analyzing two different levels of geomagnetic activity. When examining the characteristics of the fourth mode during high geomagnetic activity across different seasons, as depicted in the maps presented in the right column of Figure 4.16, one can notice that the day-night asymmetry maintains the same

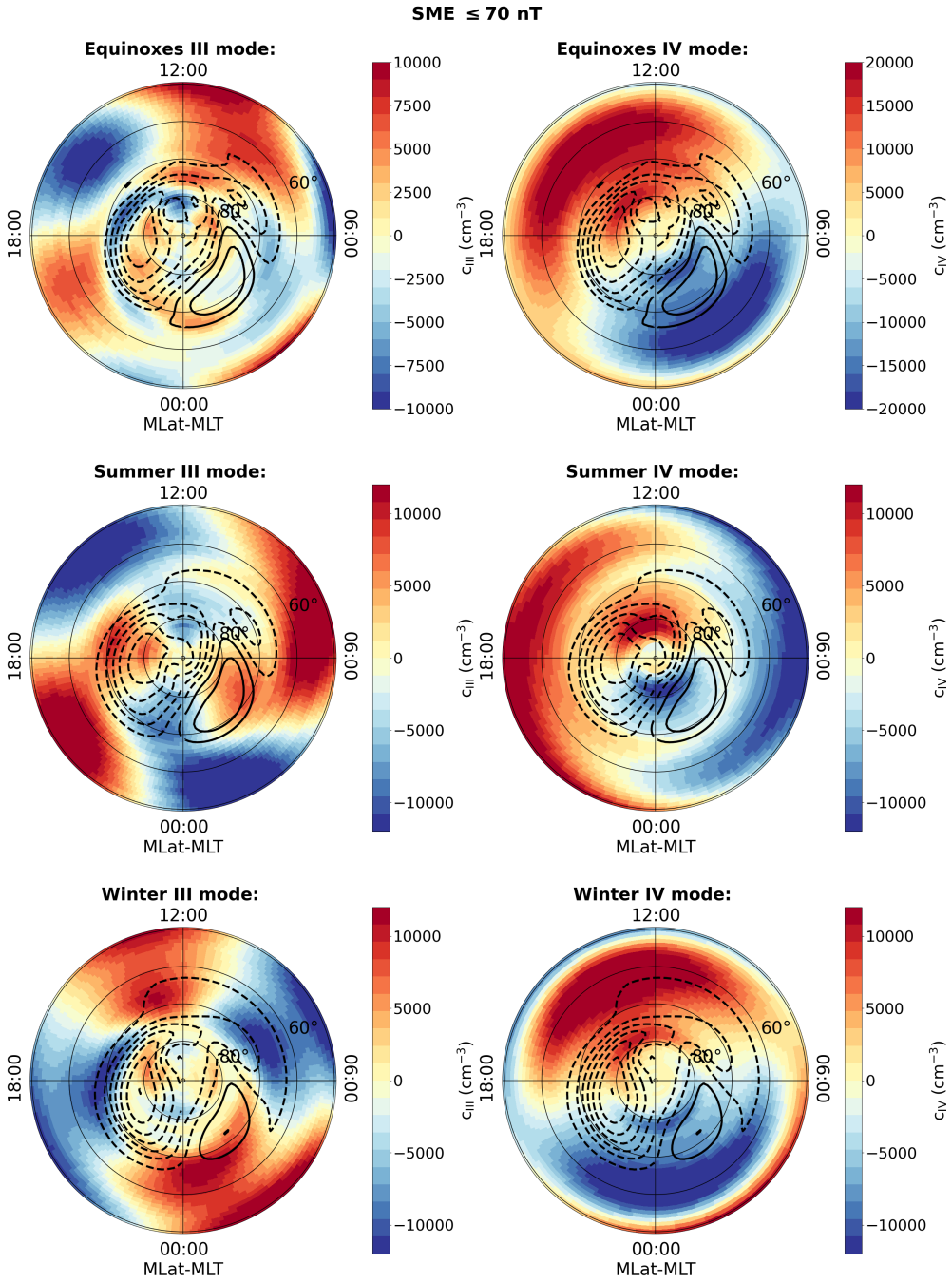

Figure 4.15: Polar view of the III and IV fundamental modes obtained from the MEMD of electron density distribution during equinoxes (*first row*), summer (*second row*) and winter (*third row*) periods, under low geomagnetic activity, in the Northern hemisphere. SuperDARN polar potential maps, obtained using the statistical convection model CS10, are superimposed to each mode as level curves. Maps are represented in the QD-magnetic latitude (MLat) and MLT reference system. The concentric circles are plotted in 10° intervals, the outermost circle corresponds to 50°. Credits: Lovati et al. (2023a)

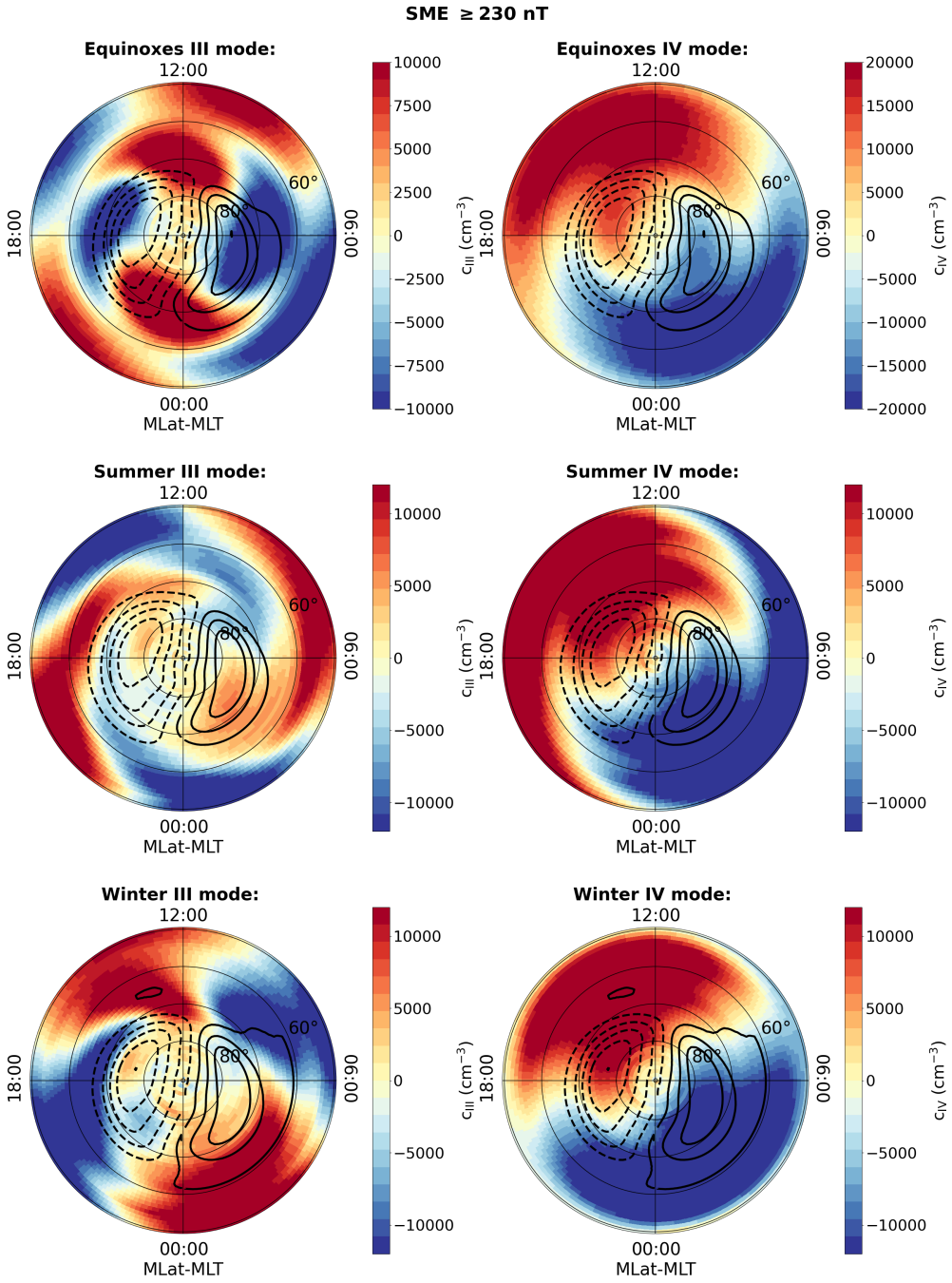

Figure 4.16: Polar view of the III and IV fundamental modes obtained from the MEMD of electron density distribution during equinoxes (*first row*), summer (*second row*) and winter (*third row*) periods, under high geomagnetic activity, in the Northern hemisphere. SuperDARN polar potential maps, obtained using the statistical convection model CS10, are superimposed to each mode as level curves. Maps are represented in the QD-magnetic latitude (MLat) and MLT reference system. The concentric circles are plotted in 10° intervals, the outermost circle corresponds to 50°. Credits: Lovati et al. (2023a)

seasonal patterns, with only the intensity level varying. Overall, it is possible to conclude that the fourth mode is the result of a combination of factors, including interaction with solar radiation, the electron recombination process during the night, and ionospheric wind movements. These processes play a dominant role compared to the other modes, given that the fourth mode is the most energetic one in all the cases, with the exception of the summer period during quiet geomagnetic activity conditions. In this last case the energy is just below the one of the third fundamental mode.
The analysis of the convection cells structure did not significantly contribute to a better understanding of the electron density distribution in the fourth mode. However, it plays a crucial role in understanding the third one. The third mode is presented in relation to the season and the level of geomagnetic activity in Figures 4.15 and 4.16 left columns. During periods of high geomagnetic activity, the third mode exhibits a region of high electron density at high latitudes on the dayside. This characteristic is consistently observed across all seasons, even if less intense during summer. This region corresponds to the cusp, which is a distinct area within the day-side auroral oval, near noon. The cusp is known for enhanced ion and electron precipitation and is considered the primary location for the transport of magnetosheath plasma into the ionosphere. It appears typically as a single spot that spans a few hours of MLT and its position is influenced by the IMF's B_y and B_z components. However, it's important to note that the cusp doesn't always manifest as a single structure. In certain cases, especially when the IMF B_y component is large or when there are changes in IMF orientation, the cusp can bifurcate into two or more distinct regions. This bifurcation phenomenon adds complexity to the cusp structure and highlights the dynamic nature of the interaction between the solar wind and Earth's magnetosphere. During periods of high geomagnetic activity, various additional phenomena contribute to the dynamic nature of the high-latitude ionosphere at mesoscales. Precipitating electrons propagate towards the pole, and localized structures of electron density known as polar cap patches can be observed moving into and across the polar cap region. Additionally, FTEs occur, where photoionized plasma from closed field lines on the dayside is transported into the polar cap across the boundary between open and closed field lines. These processes lead to plasma redistribution and changes in plasma density structures in surrounding regions. The third mode effectively captures the overall result of electron motion, showing an evident increase in electron density along the two convection cells in the polar cap region and subsequent accumulation on the nightside at high latitudes. The outcome of this dynamics is significantly less pronounced during periods of low geomagnetic activity, likely due to the influence of a predominantly positive IMF z-component (see Table 4.1), which affects the configuration of the convection cells, as well as a lower overall dynamics in the region compared to the geomagnetic disturbance period.

In summary, this analysis has revealed important insights into the spatio-temporal distribution of electron density. Four fundamental modes were identified and their relative significance was examined, as well as their dependence on seasonal variations and geomagnetic activity levels. These findings can give a contribute in the understanding of the dynamic processes that govern the distribution of electron density at mid and high latitudes, considering both the specific time of the year and the level of geomagnetic activity, providing key information about its structure, dynamics, and energy contribution. They can be helpful for ionospheric models, as an aid in the identification of the spatio-temporal distributions of electron density associated with various dynamic processes specific to the analyzed ionospheric region, but also in the estimation of the contribution in terms

of energy provided by each of them. In fact, by incorporating the spatio-temporal distributions of electron density and the energy contribution of the different dynamic processes into the models, a more accurate and detailed representation of the ionosphere can be obtained. This, in turn, enables more precise predictions of future ionospheric conditions.

4.2 Irregularities in the high-latitude ionosphere

The ionosphere is characterized by a broad spectrum of irregularities, which are apparently random structures in the plasma density distribution, ranging on different temporal and spatial scales and having different origins, depending also on the latitudinal band. In fact, these fluctuations in the electron density characterize two ionospheric regions in particular: the equatorial band and the high-latitudes. Speaking about the latter, it is a highly structured region, with scale sizes ranging from few centimeters up to hundreds of kilometers and characterized by an extremely dynamic nature (Wernik et al., 2003), attributable largely to the already cited convective motion.
These irregularities depend on both geophysical parameters such as spatial coordinates, local time, and season, as well being favored by high levels of solar activity. Geomagnetic activity also has a significant impact on irregularities in the high-latitude region because substorm conditions support them (Jin et al., 2014). The majority of high-latitude ionospheric irregularities cluster in some specific locations, like the dayside cusp, the nighside auroral oval and within the polar cap (Basu et al., 1988) and are related to large-scale plasma structures like PCP, cusp auroras and auroral blobs, whose evolution and position depend on both the solar wind and the polarity and strength of the IMF (Basu et al., 2002, Jin et al., 2020).

The most well-known and significant effect of ionospheric irregularities on human technologies is the resulting inhomogeneity of the plasma refractive index. Electromagnetic waves passing through region affected by this inhomogeneity undergo a distortion of their original wavefront (Wernik et al., 2003) and, at certain spatial scales, this can cause radio wave scintillation and radar backscatter. This has a degradation effect on both communication and navigation satellite systems. The effect on GNSS in particular will be deepened in Chapter 5. However, there are also a few other minor effects. As an illustration, the Section below discusses a less prominent consequence of the presence of irregularities in the high-latitude ionosphere.

4.2.1 Pressure-Gradient current

The presence of irregularities in the magnetosphere-ionosphere coupled system gives rise to inhomogeneities and pressure gradients in the local plasma distribution. This can in turn give rise to a specific type of current called *pressure-gradient current*, which includes for example the neutral sheet, the magnetopause and the ring currents, all flowing in the Earth's magnetosphere (Ganushkina et al., 2018). In the ionosphere the pressure-gradient current is among the weakest ionospheric current systems arising from plasma pressure variations. Here, because of the coupling between geomagnetic field and plasma pressure gradient, electrons and ions drift in opposite directions, generating an electric current whose intensity is of the order of a few nA/m^2. This current is also called *diamagnetic* because it produces a magnetic field, whose orientation is opposite with respect to the ambient magnetic field, causing its reduction. This magnetic reduction can be captured by Low-Earth Orbit (LEO) satellites flying in proximity to ionospheric plasma regions where rapid

changes in density occur. Anyway, identifying diamagnetic current by using its magnetic signature is not easy due to the weak intensity of generated magnetic perturbation, that is about 10,000 time smaller than the ambient geomagnetic field. This explains why studies investigating this type of current are quite recent, since it was necessary to wait until high-accuracy satellite magnetic field measurements became available. Due to its originating mechanism, the diamagnetic current can be revealed at both low and high latitudes, and more generally in all those regions where the plasma pressure gradients are greatest.

Several studies on this phenomenon focus on low latitude, in the equatorial belt, where irregular plasma density structures of various scale sizes, from centimeters up to hundreds of kilometers, can be observed after sunset and where exists a region with increased plasma density, known as Appleton or EIA. The first work that revealed presence of these currents in the ionosphere was the one of Lühr et al. (2003), thanks to the high-resolution magnetic field data and the plasma density observations recorded by CHAllenging Minisatellite Payload (CHAMP) satellite (Reigber et al., 2003). They revealed the magnetic signatures of plasma density variations at low latitudes and reconstructed the strength and geographic location of diamagnetic field caused by the Appleton anomaly. The estimated field strength reached up to 5 nT at various local times, demonstrating how the diamagnetic effect could severely affect the correct estimation of the ionospheric current distributions from space, and how it could be capable of producing artifacts in the new generation main field models (Lühr and Maus, 2010).

Successively other papers dealt with this subject. One example is the study carried out by Alken et al. (2011). They modeled the global gravity and diamagnetic current systems in the ionospheric topside F2 region by using the Thermosphere Ionosphere Electrodynamics General Circulation Model (TIEGCM) (Richmond et al., 1992) with empirical density, wind and temperature as input parameters. The diamagnetic current structure at low latitude reconstructed in this way was found to be prominent near the EIA. Even though the obtained results showed some discrepancies with what found using the diamagnetic effect equation proposed by Lühr et al. (2003), even this study confirmed the need to pay attention to all those ionospheric current systems that, although less intense than others well-known systems, could play a role in the ionospheric dynamics and help in the development of more accurate magnetic models.

Successively also Alken (2016) reconstructed the gravity and diamagnetic currents flowing at low latitude in the topside F2 region, by considering 10 years of CHAMP measurements (2000-2010) and two years of Swarm data (late 2013-2015). The strength of these currents was found to depended on season, local time and solar activity. They were found to be strongest during spring and fall and their magnetic signatures ranged from 1 to 7 nT, depending on solar activity level. Moreover, their presence was confirmed until midnight, revealing the incorrectness of the assumption, made by many magnetic models, according to which the ionospheric currents were negligible during the nighttime and geomagnetically quiet periods.

Given the growing awareness of the existence of a large amount of plasma density irregularities at high latitude, especially at polar latitudes, recently the hypothesis that diamagnetic currents had to exist also in these regions took hold, as well as the interest in their role in the ionospheric dynamics. In this region the pressure-gradients are mainly related to the convection pattern and to electron precipitation, that characterizes both the polar cap and the auroral oval (Park et al., 2012). In particular, soft electron precipitation caused by the direct entry of magnetosheath electrons in the

cusp region and from electrons of ionospheric origin that are energized at intermediate altitudes by wave-particle interactions with dispersive Alfvén waves, are supposed to generate density anomalies with elevated electron temperature in the F region ionosphere (Lotko and Zhang, 2018). At the time of writing this work, only few studies have been published on the diamagnetic currents at high latitudes. Two known papers investigating these currents thanks to their magnetic signatures are Park et al. (2012) and Laundal et al. (2019). By using the magnetic data from CHAMP satellite and a combination of plasma density measurements from both the Digital Ion Drift Meter and the Planar Langmuir Probe on board CHAMP, Park et al. (2012) conducted a climatological study of the diamagnetic signatures at high latitude due to ionospheric plasma irregularities. They found that ionospheric irregularities have not uniform zonal spatial distribution, but exhibit a maximum at pre-midnight ionosphere and dayside cusp. The geographic location of the irregularities also depends on geomagnetic activity and season. Hence in this paper, the authors used the diamagnetic current's magnetic signatures in order to investigate the occurrence rate of ionospheric irregularities, without reconstructing the current itself. On the other hand, analyzing two years of magnetic and plasma density measurements from Swarm constellation, Laundal et al. (2019) showed that the magnetic field variations recorded at satellite altitude were often associated with plasma pressure variations in the polar cap. They found that superposed on the magnetic perturbations due to the auroral electrojet currents was an irregular pattern, anticorrelated with plasma density measurements: a signature of the diamagnetic current. They suggested that this current could dominate the disturbances in the magnetic field strength at small-scale size of a few tens of kilometers.

In this section the flow patterns of the diamagnetic current at high-latitude are reconstructed in both hemispheres, by using measurements made by Swarm constellation (see Section 2.1). Their dependencies on geomagnetic activity, season and solar forcing drivers are also investigated. In order to accomplish this task, the employed dataset included magnetic field components, electron density N_e and electron temperature T_e measurements acquired by Swarm A (Lomidze et al., 2018), at a rate of 1 Hz, during a period of four years, from 1 April 2014 to 28 February 2018. The choice to star from April 2014 was made to exclude the period where Swarm constellation was stabilizing its orbit, making possible to assume that Swarm A is approximately at the same altitude for all the period under analysis. The choice of stopping the selected period at February 2018 was connected to the part of the study that investigates the diamagnetic current's relationship with geomagnetic activity. The AE index (see Section 2.2), chosen as an indicator of the geomagnetic conditions in the analyzed region, at the time of the analysis was not available beyond this period.

Since the ionospheric currents are mainly organized by Earth's magnetic field, the study is done using the Quasi-Dipole (QD) magnetic coordinate system described in Section 2.1.1. In order to focus on mid- and high-latitude ionospheric region, selected data are characterized by a quasi-dipole magnetic latitude $\lambda_{QD} \geq |50°|$. To report selected data on the λ_{QD} - MLT plane, the maps representing the distribution of required parameters are obtained with a $1° \times 1°$ binning ($1°$ in longitude corresponds to 4 minutes in MLT). Time series belonging to each bin are initially filtered, removing values beyond 3σ from the mean value in order to take off possible spikes. The value representative of each bin corresponds to the average of the filtered time series. As anticipated, the AE index was used to study the dependence of the pressure-gradient currents on the geomagnetic activity. While, to analyse the dependence on the solar activity two different proxies have been

used: the Mg II core-to-wing ratio and the F10.7 index (explained in Section 2.2 and 2.4).

Pressure-gradient current reconstruction

To reconstruct the flow patterns of the pressure-gradient current at high latitude, it is possible to assume that, for time scales longer than about 1 minute, the ionospheric electrodynamics is approximately in a steady-state with divergence-free current density ($\vec{J}$), and time-invariant electric field ($\vec{E}$). From the *generalized Ohm's law*, the current density $\vec{J}$ can be expressed as the sum of different contributes due to the neutral wind ($\vec{J}_w$,), the global electrostatic electric field ($\sigma\vec{E}$, with σ equal to the conductivity tensor), gravitational force ($\vec{J}_g$), and pressure-gradient force ($\vec{J}_P$). At large spatial scale the electric force and the neutral wind dominate the pressure-gradient and the gravitational forces. Thus, the first two forces are responsible for the main ionospheric currents, while the other two generate currents that can usually be neglected. However, on smaller spatial scale, these currents can become relevant and can have non-negligible effects on LEO satellite, because of their magnetic perturbations.
Assuming that it is possible to ignore the effects of neutral collisions, the current density connected to pressure-gradient force can be expressed as in Equation 4.1 (Richmond, 1995, Richmond and Maute, 2014).

$$\vec{J_P} = -\frac{\nabla P \times \vec{B}}{B^2} \tag{4.1}$$

where $P = N_e k_B (T_i + T_e)$ is the plasma pressure, k_B is the Boltzmann constant, T_e is the electron temperature, T_i is the ion temperature, and $\vec{B}$ is the ambient magnetic field, produced by all sources within and outside the solid Earth, up to the so-called magnetopause. The resulting pressure-gradient current has its major component in the zonal direction, because of the strong vertical gradient of the plasma density. In first approximation, the magnetic field variations associated with this current can be evaluated by considering the balance between the plasma and magnetic pressures. According to Lühr et al. (2003), in a quasi-stationary plasma where the structures are much smaller than the geomagnetic field curvature radius, the signature in the magnetic variation strength due to plasma pressure gradient is equal to:

$$\Delta B = -\frac{\mu_0 k_B}{B} \Delta(N_e(T_e + T_i)) \tag{4.2}$$

where μ_0 is the susceptibility of free space and k_B the Boltzmann constant. Here, the main assumption is that the measured magnetic fluctuations are spatial on the time scale for the satellite to traverse them. This interpretation holds when the wave frequency in the plasma rest frame is much less than the Doppler frequency due to spacecraft motion across the horizontal spatial structure. Assuming a local thermodynamic equilibrium, magnetic field perturbations are anticorrelated with variations in plasma density. Therefore a plasma density depletion is associated with a magnetic field enhancement while a reduction in the magnetic field is related to an increase in plasma density. This results in a current density, driven by the presence of pressure gradient, which flows around a density enhancement in a direction that produces a magnetic field capable of reducing the ambient magnetic field. On the other hand, when flowing around a depletion in the plasma density, the produced magnetic field has an enhancing effect, like the configuration presented in Figure 4.17, assuming that the decreasing in the plasma pressure is completely attributable to the density

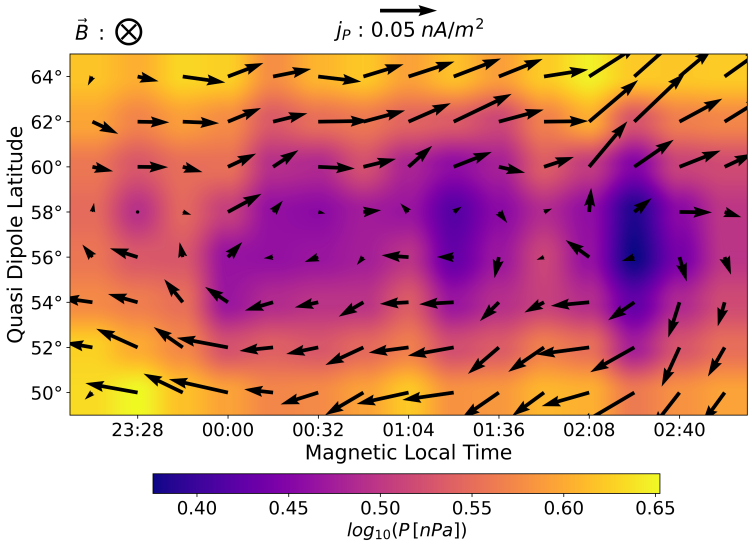

Figure 4.17: Example of a region in the magnetic latitude-MLT space, characterized by a depletion in the plasma pressure and an entering ambient magnetic field. The vector field represent the diamagnetic current that originates with this configuration.

distribution, while temperature remain constant (an assumption that is not valid anywhere).

To be able to reconstruct the flow patterns of the plasma pressure-gradient current at Swarm altitude, it is necessary to estimate the plasma pressure. This requires to know the temperature and electron density distributions within the region of interest, being $P = N_e k_B (T_e + T_i)$, according to the equation of state. Swarm satellites measure only density and temperature due to the electron population. However, at their altitude, the temperature of oxygen ions (O^+), which can be assumed as the main ionic species present, is of the same order of magnitude as the electron temperature. Therefore it is possible to assume that $T_e \simeq T_i$ (Kamide and Chian, 2007, Laundal et al., 2019), obtaining a plasma pressure approximately equal to $P = 2N_e k_B T_e$. At this stage, it is possible to compute the pressure gradient (∇P) on the horizontal plane. In order to approximate the geometry of the system, the gradient in spherical coordinates is considered:

$$\nabla P = \frac{\partial P}{\partial r}\hat{r} + \frac{1}{r}\frac{\partial P}{\partial \theta}\hat{\theta} + \frac{1}{r\sin\theta}\frac{\partial P}{\partial \phi}\hat{\phi} \tag{4.3}$$

where θ is the magnetic co-latitude, and ϕ is the longitude, which, in this case, corresponds to MLT. Since Swarm A flies approximately at the same altitude during the selected period, r is assumed to be constant. In addition, with the given configuration, it is not possible to evaluate the gradient along this direction. Therefore, the pressure gradient is calculated in the plane perpendicular to the radial direction:

$$\nabla P_\perp = \frac{1}{r}\frac{\partial P}{\partial \theta}\hat{\theta} + \frac{1}{r\sin\theta}\frac{\partial P}{\partial \phi}\hat{\phi} \tag{4.4}$$

However, relying on Equation 4.1, the neglected $\frac{\partial P}{\partial r}$ term provides only a small contribution to the plasma pressure-gradient current, being the magnetic field nearly parallel to it. Indeed, at high latitudes the magnetic field is approximately aligned with the radial direction and, compared to this term, the other two components result negligible. Therefore, in this approximation, the lack of information on $\frac{\partial P}{\partial r}$ does not affect significantly the analysis.

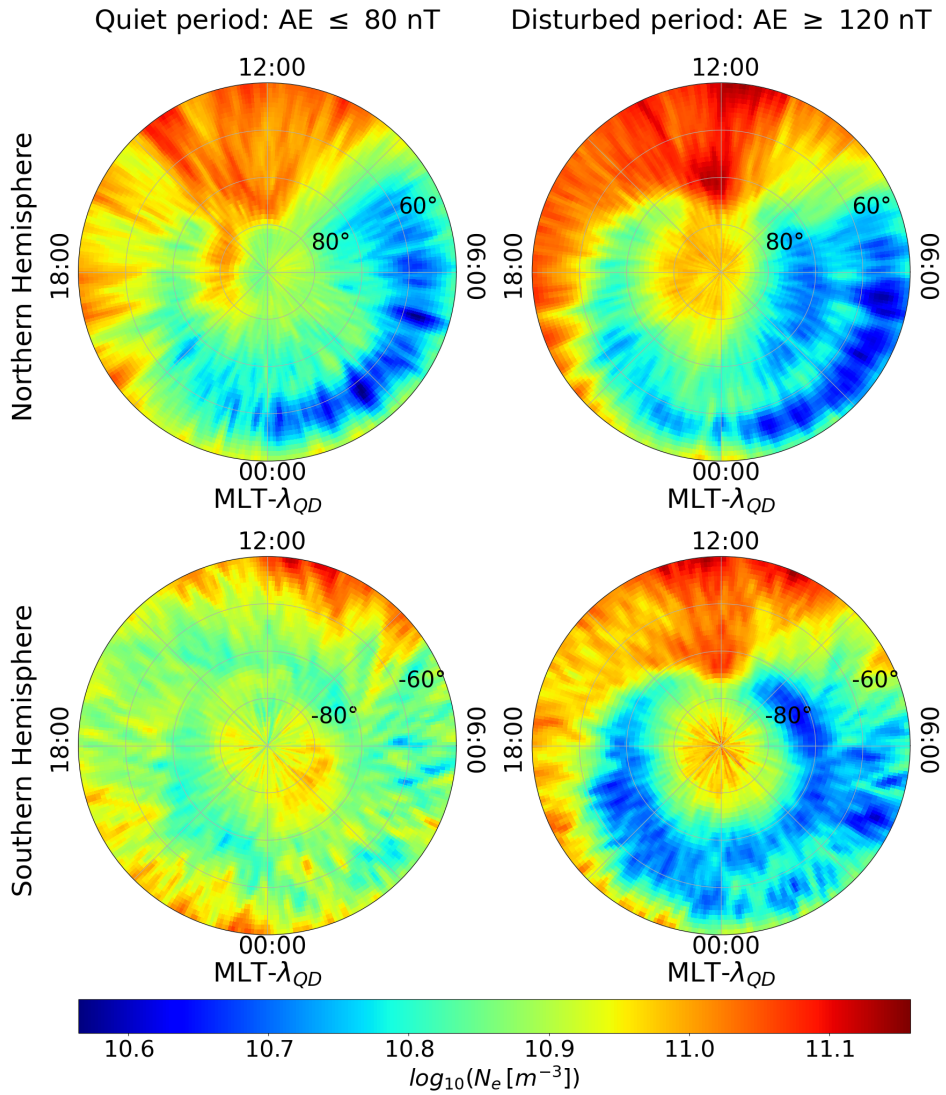

Figure 4.18: Polar view of the average spatial distribution of electron density (N_e) for quiet (left column) and disturbed (right column) geomagnetic activity conditions, for the Northern and Southern hemispheres, in QD-latitude ($\lambda_{QD} > |50°|$) and MLT reference system. Maps are obtained using data recorded by Swarm A from 1 April 2014 to 28 February 2018. The concentric circles are plotted in 10° intervals, the outermost circle corresponds to |50°|. Credits: Lovati et al. (2022)

In order to estimate $\frac{\partial P}{\partial \theta}$ and $\frac{\partial P}{\partial \phi}$, the matrix of pressure binned values is considered. It has a number of rows equal to QD-latitude bins and a number of column equal to MLT bins, which translates in a 40×360 matrix, having selected latitudes from |50°| upwards and a binning of $1° \times 1°$. The gradient is evaluated through *second order accurate central differences* (Quarteroni et al., 2010). Once obtained $\frac{\partial P}{\partial \theta}$ and $\frac{\partial P}{\partial \phi}$, the gradient estimation in spherical coordinate, dictated by Equation 4.4, is completed considering r as fixed at the altitude of Swarm A, and θ equal to the mean QD-latitude of each bin under consideration. Finally, the current density due to pressure-gradient force is estimated according to Equation 4.1.

Dependence of pressure-gradient current on geomagnetic activity

The analysis of the current density spatial distribution due to pressure-gradient force at high latitude in the Northern and Southern hemispheres starts investigating the dependence on the geomagnetic

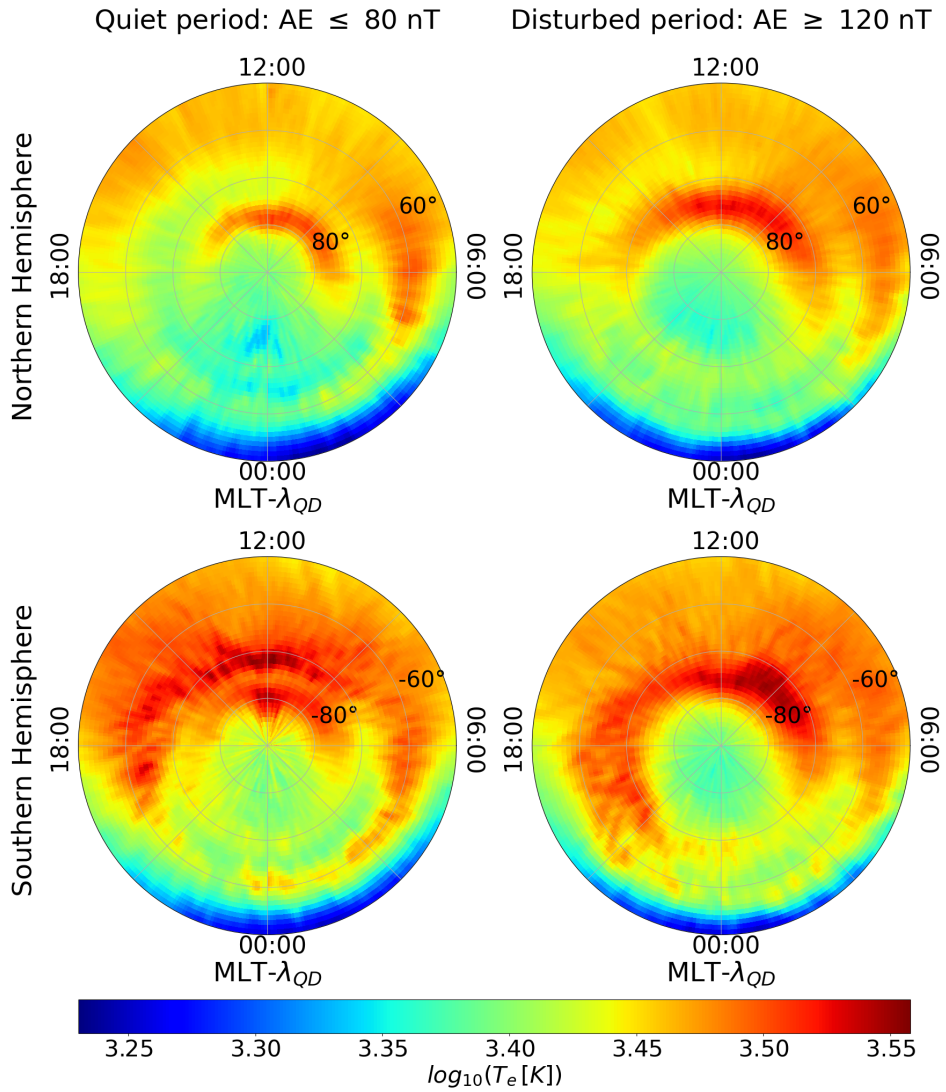

Figure 4.19: Polar view of the average spatial distribution of electron temperature (T_e) for quiet (left column) and disturbed (right column) geomagnetic activity conditions, for the Northern and Southern hemispheres, in QD-latitude ($\lambda_{QD} > |50°|$) and MLT reference system. Maps are obtained using data recorded by Swarm A from 1 April 2014 to 28 February 2018. The concentric circles are plotted in 10° intervals, the outermost circle corresponds to |50°|. Credits: Lovati et al. (2022)

activity level. Using the AE index, two different levels of geomagnetic activity are individuated: quiet periods correspond to values of $AE \leq 80$ nT while disturbed ones to $AE \geq 120$ nT (Alberti et al., 2020, Consolini, 2002). The two levels are chosen in order to clearly separate active and quiet periods according to the distribution function of AE index values, which is bimodal with a crossover around 100 nT. For this type of analysis, electron density, electron temperature, and magnetic field distributions, relative to the period that goes from 1 April 2014 to 28 February 2018, are considered.

Figure 4.18 and 4.19 report a polar view of the large-scale spatial distribution of electron density (N_e) and electron temperature (T_e) in the Northern and Southern hemispheres during quiet and disturbed periods, respectively. Data are mapped into grid binned at $1° \times 1°$ in magnetic latitude and MLT coordinates. The same type of representation is used in Figure 4.20 for the plasma pressure (P), obtained through the already mentioned equation of state and thus intrinsically tied to the distributions of Figure 4.18 and 4.19. The two selected geomagnetic activity levels correspond

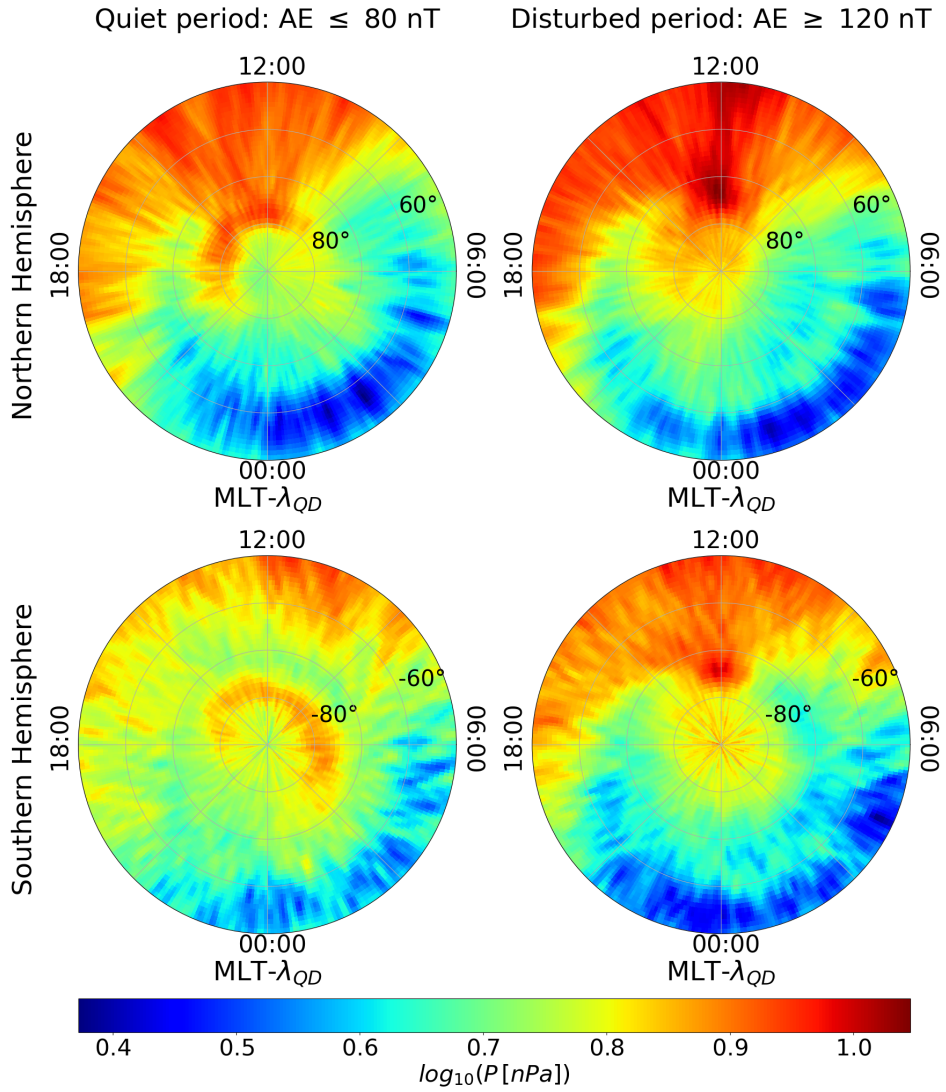

Figure 4.20: Polar view of the average spatial distribution of plasma pressure for quiet (left column) and disturbed (right column) geomagnetic activity conditions, for the Northern and Southern hemispheres, in QD-latitude ($\lambda_{QD} > |50°|$) and MLT reference system. Maps are obtained using data recorded by Swarm A from 1 April 2014 to 28 February 2018. The concentric circles are plotted in 10° intervals, the outermost circle corresponds to |50°|. Credits: Lovati et al. (2022)

to different spatial distributions of the plasma parameters in the two hemispheres.

Focusing on plasma pressure, it shows a spatial distribution characterized by a marked dayside/nigthside asymmetry, which mainly reflects the dayside/nigthside asymmetry of the electron density and temperature spatial distributions. In fact, as reported in Figure 4.18, the electron density is generally almost twice in the dayside compared to the nightside, because of its dependence on the upper atmosphere ultraviolet ionization. The marked dayside/nigthside asymmetry that also characterizes the spatial distribution of the electron temperature (see Figure 4.19) is, even in this case, attributable to the increase of ultraviolet photoionization. However, the electron temperature is also influenced by particle precipitation caused by magnetosphere-ionosphere coupling. Indeed, soft particle precipitation heats the F region ionosphere and is a likely source of the observed correlation of the anomalous density with elevated particle temperature. Thus, the magnetosphere-ionosphere coupling is responsible of the temperature enhancement both in the cusp region around noon (Mi-

lan et al., 2007), where particles of solar origin are directly injected into the ionosphere, and at auroral and sub-auroral latitudes where particles arrive directly from the geomagnetic tail regions and plasmasphere during disturbed periods (see Figure 4.19).

Not all the features of the electron density and electron temperature are recognizable in the plasma pressure spatial distribution. For example, the so-called MIT, which corresponds to a prominent plasma depletion in the night hours, in a latitudinally limited band in the subauroral region, between 60° and 70° (see Figure 4.18), is not clearly recognizable in the pressure data. This is linked to the fact that, in the same region, the electron temperature presents an enhancement owing to the joint action of particle precipitation and decreased collisional cooling (Prölss, 2006, Wang et al., 2006). In the nightside, at auroral and sub-auroral latitudes, this process is dominant and becomes more and more important with the increase of the geomagnetic activity level (see Figure 4.19 right column). Because of the anticorrelation between the electron density and electron temperature, the plasma pressure does not show a distinctive behaviour in this region. Conversely, Figure 4.20 reveals a plasma pressure depletion at low latitudes, between 50° and 65°, in the nightside, between 21:00 and 06:00 MLT, whose position moves progressively to a lower latitude as the level of geomagnetic activity increases.

Another interesting feature of the plasma pressure is its marked increase in the cusp region around noon, which becomes more marked in the disturbed periods in both hemispheres. This increase is associated with the observed enhancements in both electron temperature and density distributions.

Lastly, Figure 4.20 shows two other interesting characteristics, mainly reflecting N_e spatial distribution features. Firstly, the enhancement of plasma pressure from noon across the polar cap to the nightside during disturbed conditions in both hemispheres (right column), which corresponds to the characteristic TOI of N_e (Foster et al., 2005, Knudsen, 1974), a large-scale feature of the F-region polar ionosphere. Secondly, there is a plasma pressure increase around dusk in disturbed conditions, reflecting the well-known SED plumes, which are prominent ionospheric electron density increases at the dayside mid and high latitudes (Foster, 1993).

Figure 4.21 reports the flow patterns of the pressure-gradient current (black arrows) at high latitudes in the Northern and Southern hemispheres obtained during the two periods characterized by different geomagnetic activity levels. Only for graphical reasons, the black arrows are mapped into grids binned at $2° \times 4°$ in QD latitude and MLT coordinates, where 4° magnetic longitude corresponds to 16 minutes. Below the flow patterns of the reconstructed current there is the corresponding plasma pressure map, which allows to better visualize the regions where the current develops. As expected, the current tends to flow around the plasma pressure enhancements and is stronger in region where the plasma pressure changes rapidly. Some well defined patterns can be recognized for this current, regardless of geomagnetic activity disturbance.

A vortex exists around the cusp (or cleft) region, whose position shifts toward the equator as magnetic activity increases, following the natural shift of center of the precipitation region. Here the current flows counter-clockwise in the Northern hemisphere and clockwise in the Southern one, following the direction which reduces the ambient geomagnetic field. In fact, at high latitude the magnetic field is nearly vertical and the horizontal pressure-gradient current produces a magnetic field which is, in first approximation, parallel to the main field but with opposite direction. In this way the current produces a reduction of the magnetic field inside the plasma region around

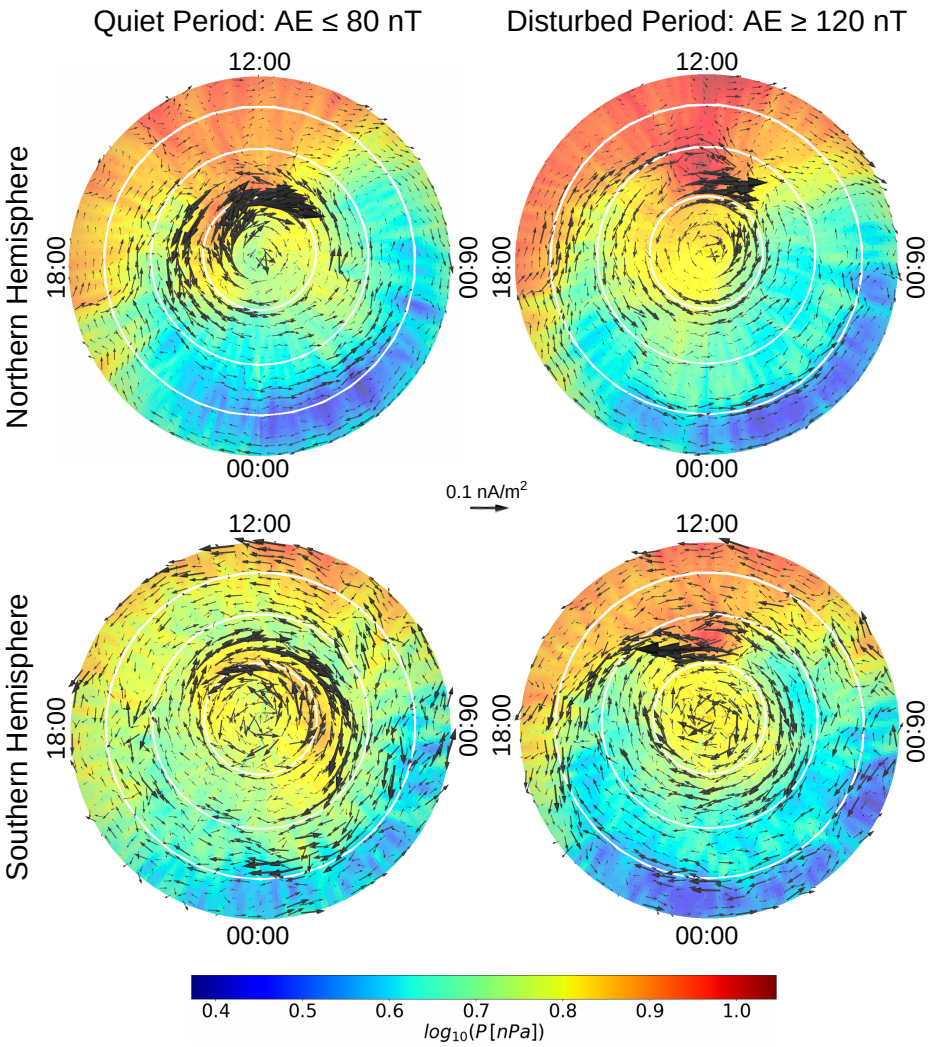

Figure 4.21: Flow patterns of pressure-gradient current (black arrows) superimposed on the plasma pressure spatial distribution for quiet (left column) and disturbed (right column) geomagnetic activity conditions, for the Northern and Southern hemispheres, in QD-latitude ($\lambda_{QD} > |50°|$) and MLT reference system. Maps are obtained using data recorded by Swarm A from 1 April 2014 to 28 February 2018. For graphical reasons, the current's vector field is mapped into grids binned at $2° \times 4°$, where 4° magnetic longitude corresponds to 16 minutes. The concentric white circles are plotted in 10° intervals, corresponding to QD-latitudes of |80°|, |70°| and |60°| starting from the centre, respectively. Credits: Lovati et al. (2022)

which the current flows. The existence of this current structure is indirectly confirmed by Park et al. (2012), who analysed the diamagnetic signatures of high-latitude ionospheric irregularities. They found depletions in magnetic field strength of about 1 nT concentrated in the cusp region of both the hemispheres, explained with the presence of local plasma irregularities with scale sizes below some hundred kilometers. Anyway, this region can be also characterized by large anomalies in the electron density, correlated with intense small-scale magnetic fluctuations, which are associated with incident Alfvén waves, producing local heating. This means that, in this region, an opposite scenario to the one that is implicitly assumed may be possible: the observed pressure gradients may be also produced by magnetic disturbances (Lotko and Zhang, 2018).

At high latitudes ($\lambda_{QD} > 75°$) the current flows around the polar region counter-clockwise in the Northern hemisphere and in opposite direction in the Southern one. The spatial distribution of the current seems to identify, especially during disturbed periods (right column), another region

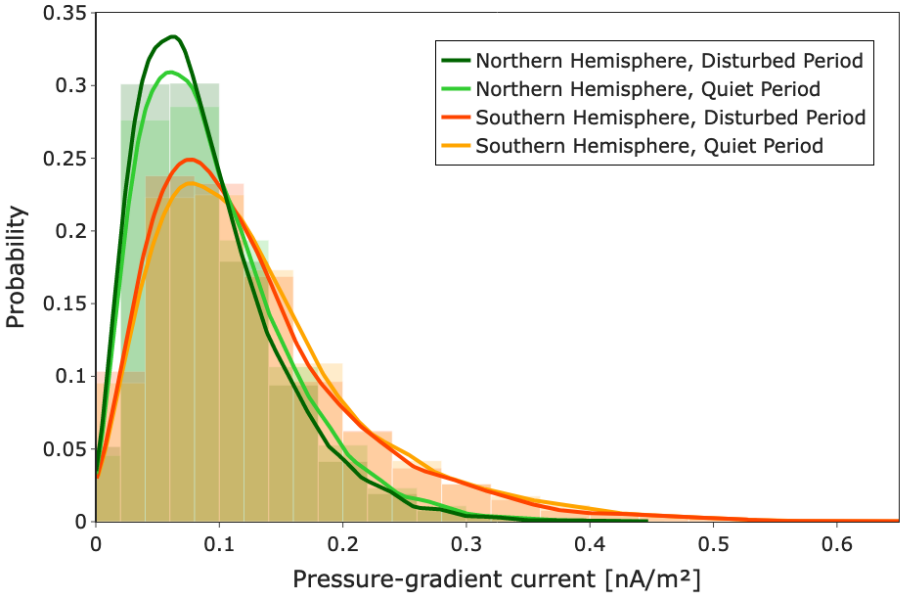

Figure 4.22: Distributions of the pressure-gradient current values for disturbed and quiet geomagnetic activity conditions, for the Northern and Southern hemispheres. Solid line represents the continuous probability density curve and it is plotted above the more transparent relative histogram. Credits: Lovati et al. (2022)

characterized by an enhancement of plasma density, which is probably linked to the propagation of plasma from the cusp to the polar cap. This region, visible in both hemispheres, is known to be characterized by the presence of plasma instability and the formation of ionospheric irregularities known as polar cap patches, where the density is at least twice that of the background (Spicher et al., 2017). However, the reconstructed flow patterns of the pressure-gradient currents can capture plasma pressure variations which are not necessary due to the presence of plasma density irregularities, as for example polar cap patches and auroral blobs. At lower latitudes in the Northern and Southern hemispheres the flow pattern of the pressure-gradient current identifies another region where the ambient magnetic field can be reduced by this current. In first approximation, this region corresponds to the auroral zone from 15:00 MLT to 09:00 MLT, passing by 24:00 MLT. Thus, the pressure-gradient currents characterize also the auroral zone and equatorward of the auroral zone on the nigthside.

In general, the flow patterns of the pressure-gradient current are similar in both hemispheres and they shift towards lower latitudes with the increase of the geomagnetic activity, as it is possible to see comparing the maps on the same row of Figure 4.21.

Figure 4.22 reports the distributions of the pressure-gradient current values for disturbed and quiet geomagnetic activity conditions, for the Northern and Southern hemispheres. The comparison among the four distributions shows that the pressure-gradient current intensity is slightly higher in the Southern hemisphere, than in the Northern one, while there is no great difference between quiet to disturbed periods. At high latitudes the mean values of these currents are quite low, around 1 order of magnitude less than the same diamagnetic currents observed at low latitudes (Alken et al., 2017).

However, the presented findings aligned with previous studies. Analyzing two years of Swarm measurements, Laundal et al. (2019) estimated the small variations in the magnetic field strength

due to pressure-gradient currents at polar latitudes, by evaluating the magnetic field intensity variations which were anticorrelated with plasma density variations. Their results showed that the polar caps, the auroral zone, and equatorward of the auroral zone on the nightside were the regions where the magnetic field variations were well explained by plasma pressure gradients. Their findings are slightly different from the ones by Park et al. (2012), where the highest occurrence rates between the magnetic field and the electron density variations are found in the auroral oval. In both papers the flow pattern of the pressure-gradient current is not calculated, nor its intensity. The existence of this current is invoked to justify the variations of magnetic field correlated with those of plasma density and climatological analyses of their correspondence are proposed. This implies that, to make a comparison with the results presented in this work, it is necessary to keep in mind that the pressure-gradient currents flow around the plasma pressure enhancement regions, which are often characterized by the occurrence of ionospheric irregularities, i.e. the regions identified in the previous papers. It is also important to notice that both Laundal et al. (2019) and Park et al. (2012) assume that the variations in plasma pressure are dominated by electron density, under the hypothesis of a local thermodynamic equilibrium. However, looking at Figure 4.19, it is possible to notice that also the temperature plays a role in the plasma pressure, mainly in the auroral and sub-auroral latitudes.

To evaluate the pressure-gradient current, the magnetic field measurements recorded by Swarm A have been used. These contain all the different contributes coming from sources that are both internal (core and crust) and external (magnetospheric and ionospheric currents) to the Earth. As a result, the retrieved pressure-gradient current flow pattern may be influenced by remote currents. The current systems flowing about 300 km below Swarm A, in particular, is expected to produce a smooth magnetic signature on the measured magnetic field (Olsen, 1996). Therefore, the pressure-gradient current was also estimated in another way, by considering only the magnetic field strength associated with internal sources. The internal part of the magnetic field is estimated using the CHAOS model (Finlay et al., 2015). Thus, a new version of the pressure-gradient current is evaluated and then compared with the one estimated using the ambient magnetic field.
Figure 4.23 reports the percentage difference between the current evaluated in the two ways. This procedure should leave only the contribute of external sources to the pressure-gradient current. The obtained effect on the pressure-gradient currents at Swarm altitude of the remote current systems is very low: it does not exceed 0.3%. However, it is not uniform, depending on the geographic location, magnetic local time, and geomagnetic activity level. In particular, the major percentage difference can be found during disturbed period, in two regions of opposite sign above 60° in magnetic latitude, roughly symmetric with respect to the 03:00-15:00 meridian. Hence, the features of the reconstructed pressure-gradient currents at Swarm altitude depend only partially on geomagnetic field variations due to external disturbances. They mainly depend on the main field structures and on the features of pressure distribution.

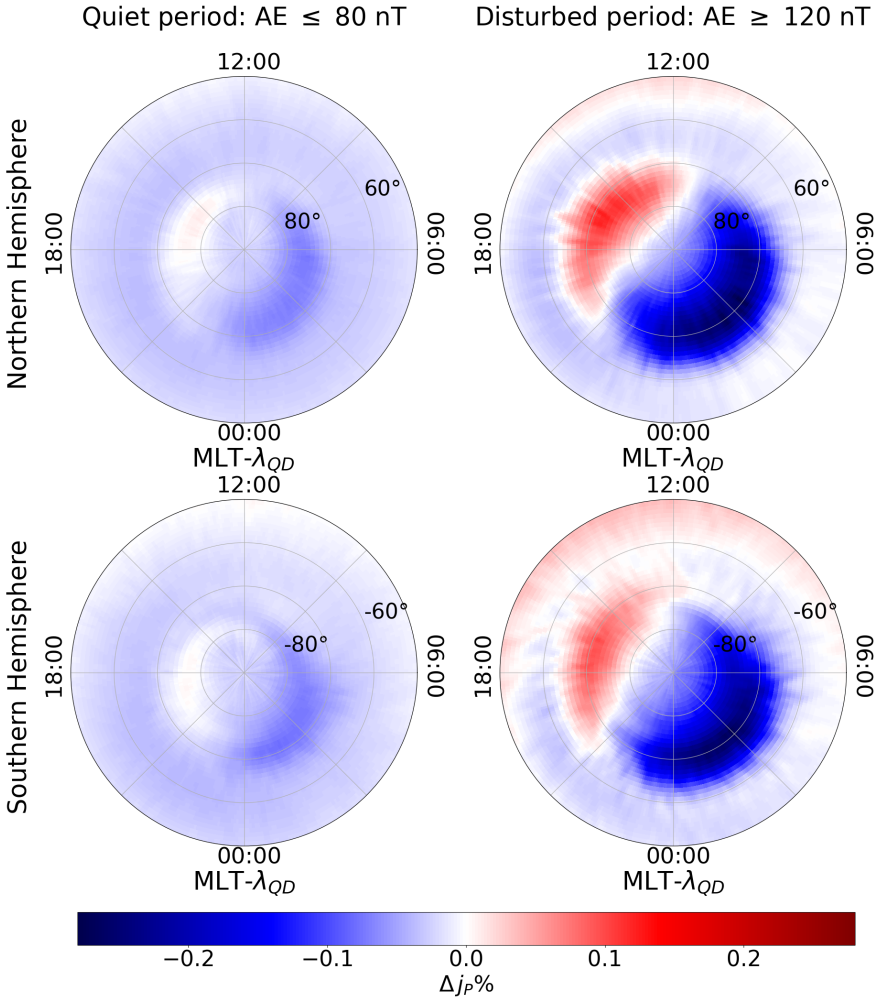

Figure 4.23: Difference in percentage between the pressure-gradient current evaluated using the magnetic field measured by Swarm A and that evaluated using the magnetic field of internal origin, in the case of quiet (left column) and disturbed (right column) geomagnetic activity conditions, for the Northern and Southern hemispheres, in QD-latitude ($\lambda_{QD} > |50°|$) and MLT reference system. Credits: Lovati et al. (2022)

Dependence of pressure-gradient current on local season

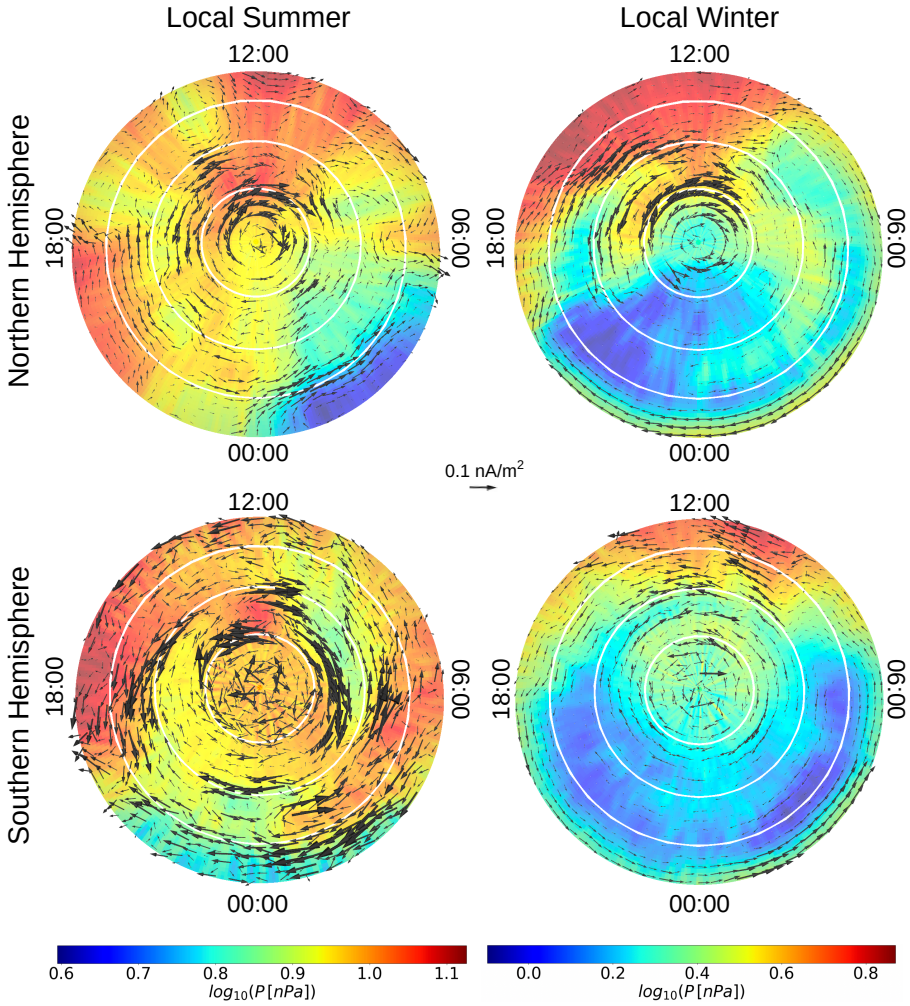

Figure 4.24: Flow patterns of pressure-gradient current (black arrows) superimposed on the plasma pressure distribution during summer (left column) and winter (right column) periods, in the Northern and Southern hemispheres. Maps are in QD-latitude ($\lambda_{QD} > |50°|$) and MLT reference system. The binning window is $1°\lambda_{QD} \times 4'$ MLT for the pressure map, while for the current's vector field the window is $2°\lambda_{QD} \times 16'$ MLT for graphical reasons. The concentric white circles are plotted in 10° interval, corresponding to QD-latitudes of |80°|, |70°| and |60°| starting from the centre. Credits: Lovati et al. (2022)

In order to investigate the seasonal dependence of the pressure-gradient current, the period between 5^{th} May and 5^{th} August of each year was considered to identify the Northern local summer and the Southern local winter. While, the period between 5^{th} November and 5^{th} February of each year identified the Northern local winter and Southern local summer. Thus, by portioning the entire dataset according to summer and winter solstices, it is possible to study the dependence of the pressure-gradient current on solar illumination.

Figure 4.24 reports the obtained plasma pressure distribution according to the selected seasons for both hemispheres, together with the resulting flow patterns of the pressure-gradient current. The current is represented by using black arrows whose lengths are proportional to the intensity. Differently from previous figures in this Section, different scales have been used for the plasma pressure in the two seasons. Indeed, the plasma pressure is almost three times higher in summer than in winter. Looking at Figure 4.24 from winter (right column) to summer (left column), it is

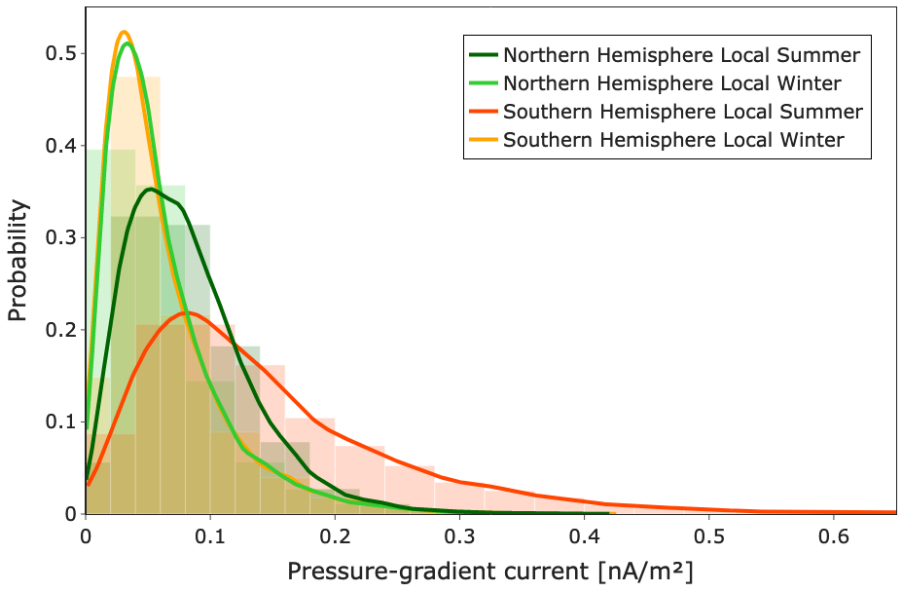

Figure 4.25: Distributions of the pressure-gradient current values for local summer and local winter conditions in the Northern and Southern hemispheres. Solid line represents the continuous probability density curve and is plotted above the more transparent relative histogram. Credits: Lovati et al. (2022)

possible to notice an increase of plasma pressure in the dayside ionosphere at all MLTs, especially between noon and dusk at middle latitudes. Plasma pressure increases even in the post-nightside sector at low latitudes in the Southern hemisphere, and at high latitudes in the polar cap. Lastly, an increase is observable in the polar cusp during summer in both hemispheres.
The plasma pressure distributions reported in Figure 4.24 show that summer-winter asymmetry is more pronounced in the Southern hemisphere with respect to the Northern one. This is attributable to the different summer-winter asymmetry of N_e spatial distribution between the two hemispheres, which is a combination of two different effects, the first produced by the solar radiation and the second by the F region annual anomaly (Rishbeth and Müller-Wodarg, 2006, Torr et al., 1980). Indeed, N_e values are higher during summer than during winter, as a result of a larger solar radiation but, at the same time, they are higher during December solstice than during June one. Since in the Southern hemisphere the increase in N_e values happens during summer season, it amplifies the difference with respect to local winter. Conversely, the F region annual anomaly has the effect of reducing the asymmetry between local seasons in the Northern hemisphere.

The dependence of the plasma pressure on the seasons also involves a dependence of the pressure-gradient current on the solar illumination. The flow patterns of the currents and their strengths change from winter to summer. These currents are visible especially during summer where the structures, which were previously identified by studying the dependence on geomagnetic activity, can be easily recognized even in this case. Once again, three regions are distinguished by the presence of these currents, one near the cleft region, another at high latitudes near the magnetic poles, and the third at auroral latitudes. These regions should identify the zones characterized by the occurrence of ionospheric irregularities.

As regards the current intensity in the two hemispheres during the two selected seasons, the distributions of their values is reported in Figure 4.25. In the same hemisphere, the current intensity results higher during summer than winter, when more plasma is produced by sunlight and plasma

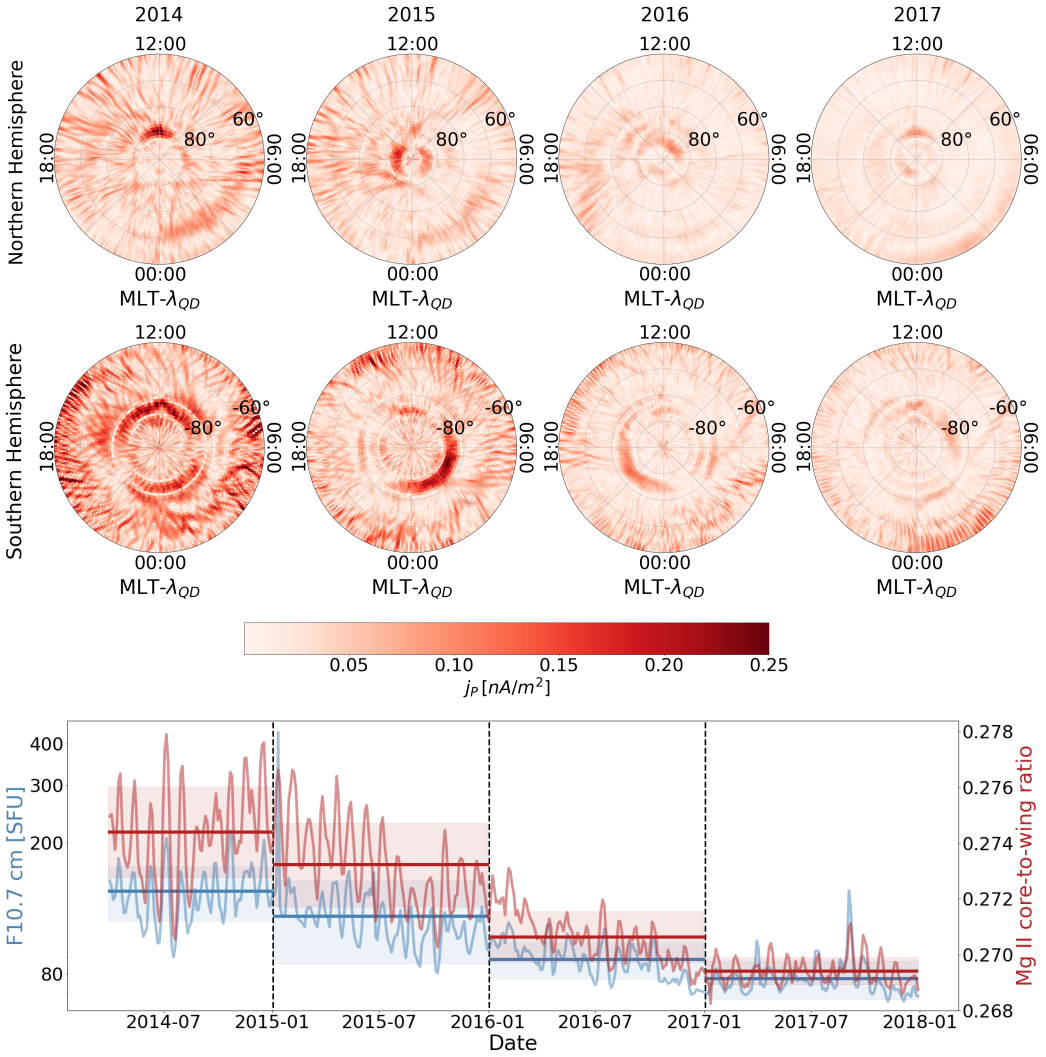

Figure 4.26: From top to bottom: Polar view of the average spatial distribution of the pressure-gradient current intensities, year by year, for the Northern and Southern hemisphere, respectively; F10.7 (blue) and the Mg II (red) indices during the 4 years of Swarm observations. The vertical dotted lines indicate the transition from one year to the next, the horizontal lines identify the yearly mean values, while the shaded parts cover the values between the yearly mean values ± one standard deviation year by year for each index. Credits: Lovati et al. (2022)

pressure gradients are greater. The current intensity is also greater in the Southern hemisphere than in Northern one during local summer, while it has comparable distributions during local winter.

Dependence of pressure-gradient current on solar activity

The daily solar flux at 10.7 cm (F10.7) and the Mg II core-to-wing ratio proxies are employed here for the evaluation of the solar activity level during the selected period of Swarm observations. Their values, covering the period from 1^{st} April 2014 to 31^{st} December 2017, are reported in the lower panel of Figure 4.26. Here, the vertical dotted lines indicate the transition from one year to the next, the horizontal lines identify the yearly mean values, and the shaded parts cover the values between the yearly mean values ± one standard deviation year by year, for each index. The analysed period corresponds to the decreasing phase of the 24^{th} solar cycle, and is characterized by a decrease in the F10.7 and Mg II yearly mean values.

For what concerns the pressure-gradient current intensity, the most remarkable features emerging from Figure 4.26 are a decrease in maximum and minimum values of the current intensity with the decrease of solar activity, as well as a decrease of the intensity around the cusp. Moreover, regardless of the solar activity level, the pressure-gradient current is significantly stronger in the Southern hemisphere than in the Northern one at almost all magnetic latitudes and MLTs, as emerged in the case of the dependence on both geomagnetic activity and local season. In the Southern hemisphere, besides the three main regions already identified, another region of enhanced current is visible. It is located in a latitude between 70° and 80° in the nightside. This structure is well visible in 2014 and 2015, when the solar activity is higher.

Concluding remarks

The aim of the analysis presented in this Section was to examine the flow patterns of the pressure-gradient currents and their strengths at high-latitude ionospheric topside F2 region in both hemispheres, and investigate their dependence on magnetic latitude and magnetic local time, geomagnetic activity, season and solar forcing drivers. All this has been achieved thanks to the magnetic field, electron density and electron temperature data, recorded by Swarm A satellite from 2014 to 2018. The flow patterns of the pressure-gradient currents have been estimated under the hypothesis that it is possible to ignore the effects of neutral collisions and consider the electron and ion temperature as equal. This study showed the polar flow patterns of the pressure-gradient currents and their strengths at Swarm altitude. From this analysis, the following conclusions can be drawn:

- During geomagnetically disturbed periods ($AE \geq 120$ nT) the plasma pressure gradients are particularly large around cleft region, where the electron density is changing rapidly. The pressure-gradient current flows around this plasma pressure enhancement region in both hemispheres. The existence of this flow pattern agrees with an increased probability of finding magnetic field variations correlated with plasma density ones around cleft region (Park et al., 2012). Anyway, it's important to remark that additional contributions to the observed magnetic field variations and plasma pressure gradients can be due to incident Alfvén wave (Lotko and Zhang, 2018);

- Regardless of the level of geomagnetic activity, at high latitudes ($\lambda_{QD} > 75°$) the flow patterns of the pressure-gradient current identify another region characterized by large plasma pressure gradients, which is around the polar cap. It is observable in both hemispheres and it's known to be characterized by the presence of plasma instabilities and the formation of ionospheric irregularities (Spicher et al., 2017). Also in this case, previous studies (Laundal et al., 2019) found a high occurrence rate of magnetic field variations well explained by plasma density variations;

- At lower latitudes in both hemispheres the flow patterns of the pressure-gradient current identify another region where the plasma pressure is changing. In first approximation, it corresponds to the auroral oval and equatorward of the auroral oval on the nigthside. These flow patterns move to lower geomagnetic latitude with increasing geomagnetic activity;

- The pressure-gradient current mean intensity is quite low, around 1 order of magnitude less than the same current observed at low latitudes. In addition, the mean value found in this

analysis is lower than that obtained by Laundal et al. (2019) at high latitudes. The reasons are probably due to the different method used to estimate the currents and to the different size of the window used to evaluate the pressure gradients. In this case, a larger window is used with respect to the one employed by Laundal et al. (2019). For this reason the pressure gradients resulting in this analysis are sharper and the pressure-gradient current intensities smaller.

- Pressure-gradient current shows a clear dependence on solar illumination, and its intensity appears to be influenced by the F region annual anomaly. This is probably the reason why the asymmetry summer/winter is more marked in the Southern hemisphere than in the Northern one. Using the diamagnetic effect, Park et al. (2012) and Laundal et al. (2019) investigated the dependence on season of the ionospheric irregularity occurrences at high latitude. At the degree of which it is possible to make a comparison, the just presented findings are in agreement with those reported by Laundal et al. (2019), who found higher occurrence rates of magnetic field variations well explained by plasma pressure in summer than winter. However, in Laundal et al. (2019), the region characterized by a higher probability to find a correspondence between magnetic field and electron density variations is mainly confined in the polar cap, whereas here the geographic location of the currents' pattern is wider here. Nevertheless, a more precise comparison is not possible since there is not a distinction between the two hemispheres in Laundal et al. (2019). Conversely, the findings of the just presented study do not seem to be in fully agreement with Park et al. (2012), who reported higher occurrence rates of plasma density irregularities in winter than summer. This is probably due to a different data selection, Park et al. (2012) studied the seasonal dependence considering measurements relative to geomagnetically active periods ($AE \geq 200nT$). Here, the seasonal dependence is studied regardless of geomagnetic activity level and the percentage of data that satisfies the AE threshold fixed by Park et al. (2012), is approximately of 28%;

- Regardless of geomagnetic and solar activity, the pressure-gradient current intensity is always slightly greater in the Southern hemisphere than in the Northern one;

- The pressure-gradient current intensity decreases with the solar activity level.

4.3 Turbulent character of ionospheric irregularities

Ionospheric irregularities can have also a turbulent character (Basu et al., 1988, Earle et al., 1989). The term *turbulence*, in this context, refers to space and time chaotic behaviour of a fluid (Benzi and Toschi, 2023). It's a non-linear phenomenon, characterized by power-law statistics. In fact, the onset of a turbulent regime coincide with the nonlinear terms starting to be non-negligible and a wide range of scales inside the flow are characterized by random activity (Carbone and Pouquet, 2009). The increasing importance of nonlinear terms is marked by the increase of the so-called *Reynolds number* R_e, which is equal to $\frac{uL}{\nu}$, where u is the typical velocity, L is the characteristic length of the considered phenomena, which in case of a plasma corresponds to the scale of the macroscopic gradients of the fields, while ν is the kinematic viscosity. This dimensionless number is obtained from the ratio of the convective and the diffusive terms. When it has a small value, the velocity gradients are rapidly dissipated and the fluid follows a laminar motion. On the other hand, when $R_e \gg 1$, a cascade mechanism is triggered and the disturbance at the higher macroscopic scales is segmented towards the microscopic scales, where it can be dissipated. This process, which is at the base of the turbulent regime, is a multiscale phenomena, because it is accompanied by the presence, over a wide range of spatio-temporal scales, of a particular type of structures, the vortexes. Moreover, according to the phenomenological description made by Richardson (1922), the scales in turbulent regime can be divided into three ranges with different behaviours. The *integral or injection scales* L_0 are the ones characterized by the energy injection, carried out by some external forces. For example, the injected energy can be due to the presence of a Kelvin-Helmholtz instability, when kinetic energy is generated because of the velocity difference between two strata of fluid, or in presence of convection, when there is a difference of thermal energy between two layers (Chiuderi and Velli, 2015). On the opposite site there are the *dissipation scales* l_D, where the viscosity term acts and the dissipation of energy takes place. In the middle of these two regimes, i.e. when $l_D \ll l \ll L_0$, there is the *inertial range*, characterized by the energy redistribution over different scales. Here the nonlinear terms dominates (Carbone and Pouquet, 2009). It is important to note that, in the inertial range, this energy redistribution follows a hierarchical structure, characterized by a power law energy distribution.

In the ionosphere, turbulence typically arises because of the interplay among the solar wind, magnetosphere, and ionosphere, which is at the base of large-scale plasma motion and particle precipitation. This chain of phenomena can considerably impact both the dynamic behavior of ionospheric plasma and the charging of ionospheric particles.
In order to investigate the possible presence of turbulence triggering conditions, different regions of the ionosphere have been studied both with in situ observations and also with numerical simulations (Hysell and Shume, 2002, Kintner and Seyler, 1985). These studies evidenced that, in the F layer, both equatorial and high latitudes can be characterized by irregularities and instabilities that favor the development of a turbulent regime. In the presence of cascade processes, the irregularities in the plasma follow a power spectra distribution in a wide range of scales, which follows a power law behavior characterized by a certain slope (Tsunoda, 1988). Different studies have focused on the value of this slope for the ionospheric electron density distribution, finding predominately values in the range that goes from 1.5 to 2.5 (Di Mare et al., 2021, Hobara et al., 2005, Jahn and Labelle, 1998, Kelley et al., 2002, Labelle et al., 1986, Spicher et al., 2014), with the most common value

equal to approximately 1.9 (Basu et al., 1988, Kintner and Seyler, 1985, Tsunoda, 1988).

As a result of turbulence, various physical parameters such as electron and ion densities, velocities, temperatures, as well as magnetic and electric fields, can exhibit fluctuations across diverse spatial and temporal scales, among which nonlinear energy transfer can verify. As a consequence, it is possible to study the presence of turbulence in the ionospheric plasma by investigating the properties of electric and magnetic fluctuation (De Michelis et al., 2015, De Michelis et al., 2016, 2017, Golovchanskaya et al., 2006, Kozelov and Golovchanskaya, 2006, Tam et al., 2005), as well as of electron density (Consolini et al., 2021, De Michelis et al., 2020, De Michelis et al., 2021a,b, Giannattasio et al., 2019).

In particular, a way to investigate the possible turbulent nature of ionosphere is studying the scaling features of the parameters that describe the plasma state. In fact, when the fluctuations follow scaling laws, in general it is a signature of self-similarity (Carbone and Pouquet, 2009). When the plasma fluctuations are in turbulent state they are characterized by scale-invariance and, in particular by self-affinity (a kind of self-similarity) of the velocity field. This latter aspect can be confirmed by studying the scaling features of the qth-order moments of the velocity field increments, as firstly proposed by Kolmogorov (1941), by computing the qth-order structure functions $S_q(t)$ as described in Section 3.2 and generalizing $f(t)$ to the available time series describing the plasma fluctuations.

A few of the already cited works used this method to investigate the presence of turbulence in the ionospheric F-layer. In particular, De Michelis et al. (2021a) and De Michelis et al. (2021b), applying the just described methodology to Swarm's (see Section 2.1) electron density time series, deepen the ionospheric dynamic both at high and low latitudes. The two works identified a specific class of plasma density irregularities, whose turbulent character was confirmed by the energy spectrum, as reported in Figure 4.27 for De Michelis et al. (2021a) and in Figure 4.28 for De Michelis et al. (2021b). Moreover, this class of irregularities is also characterized by considerably high values of the RODI, which is an indicator of the fluctuations entity. In fact, the irregularity class to which reference is made can be recognized as the one over the dashed line indicating Log(RODI) = 3.25 in Figure 4.27, and the one individuated by plasma bubbles properties reported in Figure 4.28, which is almost completely located over Log(RODI)=4.

As indicated by Equation 4.5 and described extensively in Pignalberi (2021), RODI index is computed as the standard deviation of the electron density N_e time derivative, calculated over a window of fixed width (Δt) centered at time t, which slides along Swarm's time series.

$$\mathrm{RODI}(t) = \sqrt{\frac{1}{N-1}\sum_{t_i=t-\frac{\Delta t}{2}}^{t_i=t+\frac{\Delta t}{2}} (\mathrm{ROD}(t_i) - \overline{\mathrm{ROD}(t)})^2} \tag{4.5}$$

In this Equation, Rate Of change of electron Density (ROD) indicates the N_e time derivative at each one of the N instants t_i inside the window, while $\overline{\mathrm{ROD}(t)}$ is its arithmetic mean calculated over the sliding window. The RODI index will be employed frequently in the next Sections. The chosen window width, which coincide with the one utilized in De Michelis et al. (2021a) and De Michelis et al. (2021b), is $\Delta t = 10$ s. Depending on the chosen N_e sampling rate, which in case of Swarm can be of 1 or 2 Hz, the number of values included in the window will change, being $N = 11$ or $N = 21$ respectively.

Returning to the class of irregularity identified by De Michelis et al. (2021a) and De Michelis et al.

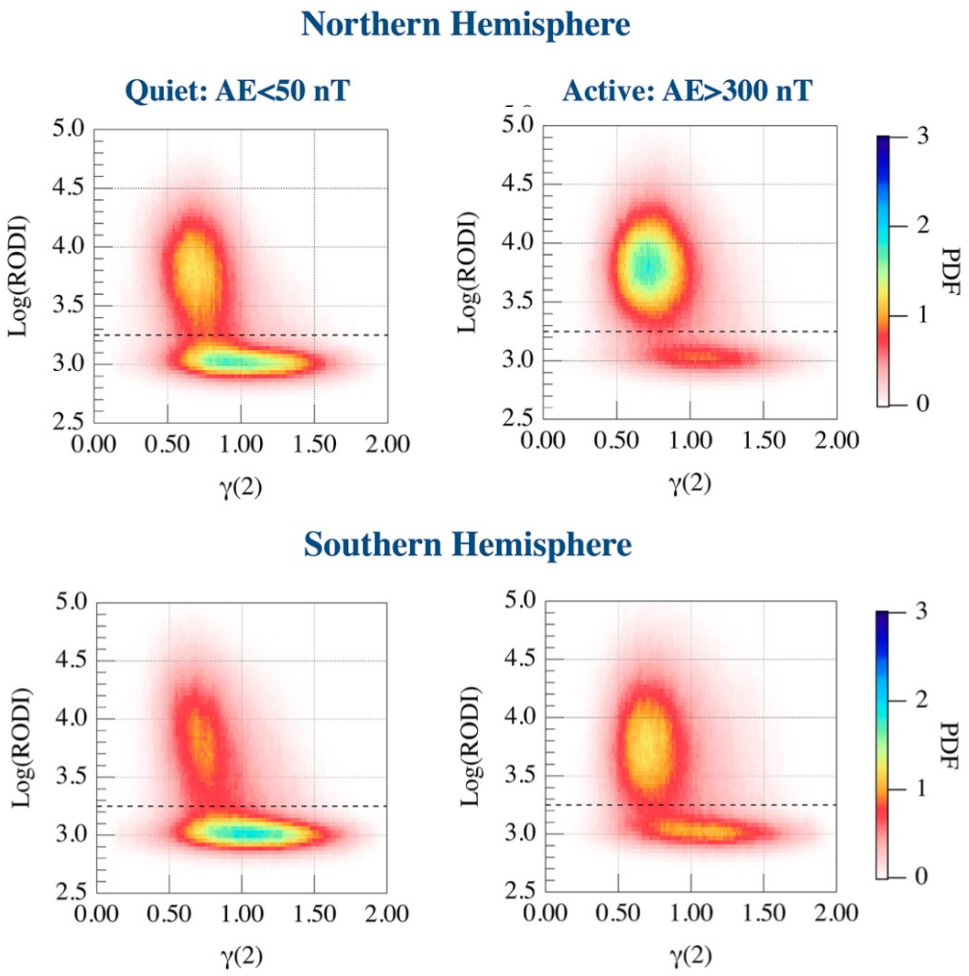

Figure 4.27: Joint probability distributions in the Northern (first row) and Southern (second row) hemispheres between Rate Of change of electron Density Index (RODI) and the second-order scaling exponent ($\gamma(2)$), obtained using data from Swarm A, during a period of about 4 years (from April 2014 to February 2018), and considering quiet (left column) and active (right column) geomagnetic periods. The black horizontal dashed lines shown in each panel correspond to Log(RODI) = 3.25. Credits: De Michelis et al. (2021a)

(2021b), the indication of its possible turbulent character is given by the restricted range of values assumed by the second-order scaling exponent. As explained in Section 3.2, $\gamma(2)$ is connected to the PSD exponent β, giving an indication on the potential type of turbulence that is going on. The fact that this class of irregularities of turbulent origin, is also characterized by very high values of RODI, implies that these are associated with plasma density variations that are stronger with respect to those generated by other mechanisms.

With a focus on the high-latitude region, which is particularly affected by processes that can favor the injection of turbulent regimes, such as the large scale convection pattern, the mean ionospheric conditions recorded from Swarm A and B from July 15th, 2014 to December 31st, 2014 are presented, using the same key parameters of De Michelis et al. (2021a) and De Michelis et al. (2021b). In detail, to have an indication on the fluctuations' entity, the mean values of RODI are reported in the first row of Figure 4.29. On the other hand, to have a metric capable of identifying potential turbulent processes in the plasma density, as previously mentioned, through the Structure Function Analysis described in Section 3.2, it was possible to obtain the second-order scaling

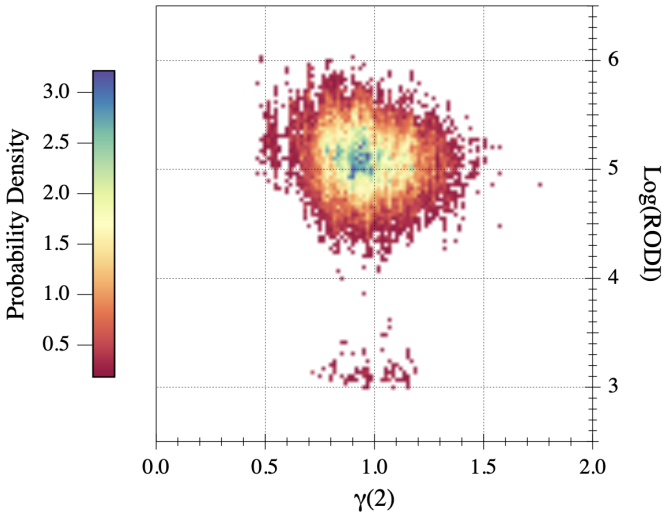

Figure 4.28: Joint probability densities between RODI and $\gamma(2)$, inside equatorial plasma bubbles. It is obtained using Swarm A data from 1 April 2014 to 31 January 2016. Plasma bubbles are identified using IBI = 1, and BF = 1 (see Table 2.1). Credits: De Michelis et al. (2021b)

exponent $\gamma(2)$ relative to plasma density time series. Its mean distribution for the selected period is reported in the second row of Figure 4.29. In fact, this parameter is connected to the spectral features of the analyzes time series, being related with the signal's PSD exponent (see Section 3.2 for more details). Therefore $\gamma(2)$ allows to differentiate the various types of instabilities and turbulent processes that caused the observed fluctuations.

The maps presented in Figure 4.29 demonstrate that, depending on MLat, MLT, and hemisphere, N_e fluctuations are characterized by different values of the second-order scaling exponent and RODI. In particular, the dayside subauroral region presents extremely low values of RODI, while in the polar cap and particularly at the cusp the index reaches its highest levels. When the same latitudes are compared, RODI is higher on the nightside of the auroral oval than the dayside, especially between 20:00 and 03:00 MLT. Considering $\gamma(2)$ distribution, it shows a value around 0.66 in the polar cap region, indicating that the electron density fluctuations here are characterized by power spectrum densities with spectral exponents of $\beta \sim 5/3$. It is interesting to note that the outer rim of this region (evidenced by the blue color in the Figure) has a shell-like shape in both hemispheres. This is the typical mark of the plasmapause, which results typically eroded in the dusk-to-noon sector, particularly during disturbed periods (see, for example, Goldstein and Sandel (2005)). Regarding the auroral oval region, here the density fluctuations are characterized by a $\gamma(2)$ value between 0.7 and 1, which translates in a spectral exponent between 1.7 and 2.0. Moving to lower latitudes $\gamma(2) \sim 1.3$ and consequently $\beta \sim 2.3$. This steeper spectral slope may be connected with a weaker turbulence regime, such as an electrostatic drift wave turbulence in low-β plasmas, which is accompanied by spectral exponents in the range of -2 to -3 at low frequency (Pécseli, 2015, Pécseli et al., 1983).

Although the main interest of this kind of investigation is in the type of ongoing turbulence regime, which can be more directly deduced from the value of β, the subsequent discussion is done maintaining the focus on $\gamma(2)$. This in order to have the possibility to make a comparison with the behaviour of another scaling exponent, $\gamma(1)$, and, consequently, to infer information on the occurrence of anomalous scaling features, i.e., on the departure from a linear trend of the scaling

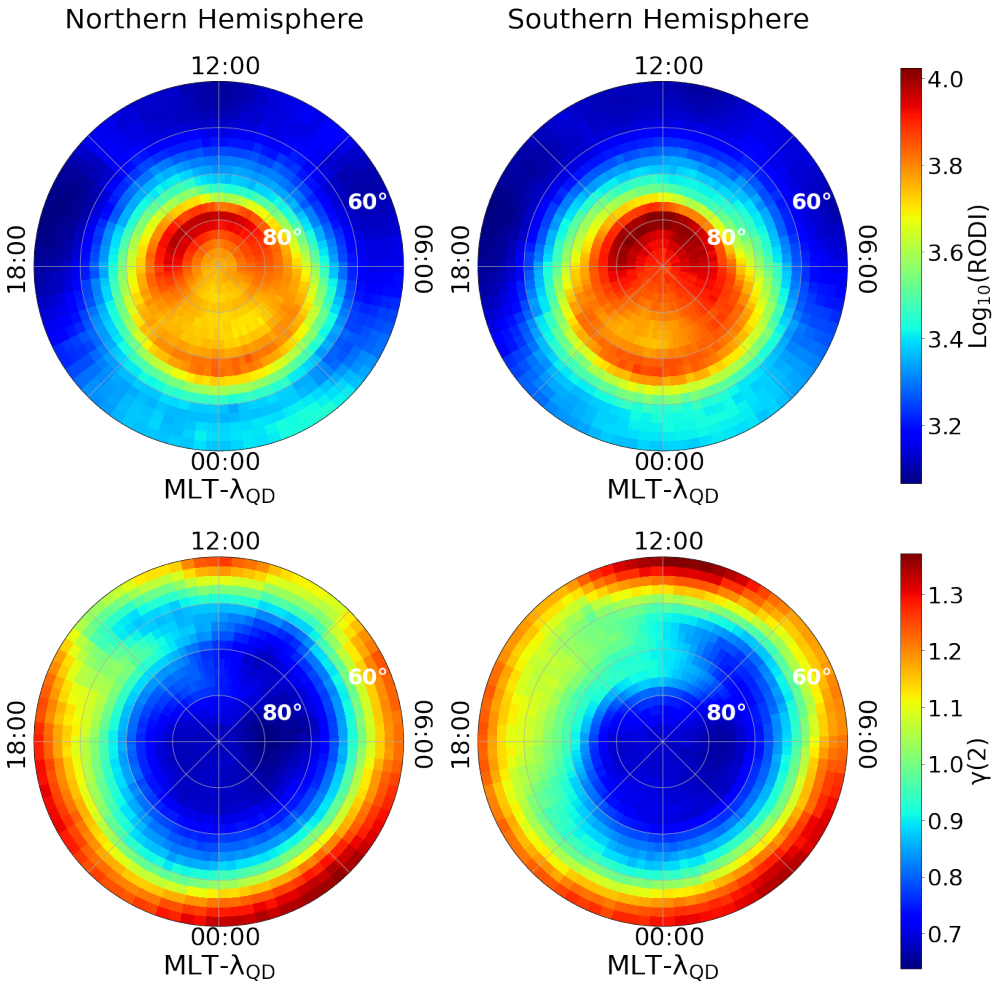

Figure 4.29: Polar view maps of the mean RODI (*first row*) and the mean second-order scaling exponent ($\gamma(2)$) values (*second row*), obtained using data recorded from July 15$^{\text{th}}$, 2014 to December 31$^{\text{st}}$, 2021 onboard Swarm A and Swarm B, in the mid- and high-latitude region ($|\text{MLat}| > 50°$) of the Northern (left column) and Southern hemisphere (right column), respectively. Maps are in MLat and MLT reference frame. The data are binned in cells of 2° in latitude and 4° in MLT. Credits: Lovati et al. (2023b)

exponents $\gamma(q)$ on moment order q, as will be explained in Section 5.2.1. However, the value of β remains easily accessible from the simple relation $\gamma(2) = \beta - 1$ (see Section 3.2 for more details).

Chapter 5

GPS Loss of Lock events

GNSS have a fundamental role in our society, being essential for many vital infrastructures, including power systems, railway control, sea transport, civil and military aircraft, communication technologies, government services, banking and finance systems, and others (Moldwin, 2008). In fact, they are required for precise positioning on our planet, as well as the timing and synchronization functions that remain at the heart of a wide range of activities.

As already mentioned in Sections 1.4.1 and 4.2, the presence of irregularities in the plasma density contributes to degrade GNSS signals during their propagation through ionosphere, lowering positioning accuracy (Kintner et al., 2001). Indeed, plasma density irregularities can affect how electromagnetic signals travel through the ionosphere, causing random fluctuations and, in some cases, a total reflection. In our modern society, it is critical to understand the causes of ionospheric irregularities and monitor their dynamics, particularly during Space Weather events, when the number of ionospheric irregularities tends to increase significantly.

The presence of irregularities in plasma density lowers the performance of GNSS by affecting both the phase and amplitude of electromagnetic waves propagating through it, and thus GNSS signals. In the worst-case scenario, signals might be disrupted, causing the receiver to lose track of a transmitting satellite. This type of event is known as Loss of Lock (LoL), which can result in a decrease in GNSS positioning accuracy and the impossibility to obtain TEC measurements. This last mentioned quantity represents an integral measurement of the total electron content along the signal path from the satellite to the receiver.

The deleterious effects of GPS LoL events have been extensively deepened in recent years, in order to determine the most affected locations and the circumstances that favor their onset. They have been discovered to happen more frequently under specific conditions, such as increased solar activity (Liu et al., 2017, Pezzopane et al., 2021) and geomagnetic storms (Jin and Oksavik, 2018, Zhang et al., 2020). Speaking about the most affected locations, GPS LoLs appear to occur in three distinct magnetic latitude bands: one near the magnetic equator and the other two at high latitudes, above 50° for the Northern hemisphere and below -50° for the Southern one. While the majority of GPS LoL events appear to occur in correspondence of equatorial plasma bubbles at low latitudes (Buchert et al., 2015, De Michelis et al., 2022), the ones at high latitudes take place in a more complex environment and there is still no clear explanation for their origin.

5.1 Swarm GPS LoL events

Shortly after the launch of Swarm mission (explained in details in Section 2.1), it was noted that, during the first two months of 2014, GPS receiver started to record LoL events on some of the available eight channels (Buchert et al., 2015). Afterwards the events rate decreased for some months, until October of the same year, when they started to occur more often again. As reported by Buchert et al. (2015), during some of these events, the GPS signal connection was lost on so many channels that it was not possible to estimate the satellite position and velocity for brief periods, until the signal tracking was recovered. This made clear that it was necessary to deepen the triggering mechanisms and the conditions that favor this type of events.

Other works followed in an attempt to better characterize Swarm LoL events. For example, Xiong et al. (2016) studied total interruptions of GPS signal, i.e. when loss of lock occurs in all the 8 channels of Swarm, during the period from December 2013 to November 2015. They discovered that the majority of the total interruptions happens in two bands along the magnetic equator, between $\pm 5^\circ$ and $\pm 20^\circ$ magnetic latitude in correspondence of the ionization anomaly crests. Also these low-latitude events mainly occur in postsunset hours, from 19:00 to 22:00 local time. They found that all of these events coincided with Equatorial Plasma Irregularities (EPIs), which are ionospheric plasma fluctuations created by the nonlinear evolution of the Rayleigh–Taylor instability (Kelley, 2009, Woodman and La Hoz, 1976). Furthermore, they identified 5 events of total loss of GPS signal also at high latitudes, most of which occurred around noon in the Southern hemisphere. They discovered that these events were connected to significant spatial density gradients by examining the corresponding electron density time series, which was consistent with polar patch characteristics and climatology. In addition, all the 5 events happened during moderate or disturbed geomagnetic conditions.

Another significant work in this context is the one of Xiong et al. (2018). With the availability of a longer period of data, they were able to conduct a climatological study of Swarm LoLs, covering one year more than Xiong et al. (2016). They confirmed the two low-latitude bands along the magnetic equator as one of the most affected regions, together with the areas at high latitudes, above 50° magnetic latitudes in both hemispheres. In the last-mentioned regions, the events are more common in the Southern Hemisphere and tend to cluster in the dayside cusp and in the nightside auroral oval. Another interesting characteristics of Swarm's LoLs is that they show similar seasonal dependence regardless of the latitude. Their occurrence is higher during equinox and December solstice, while they tend to disappear during the June solstice.

Pezzopane et al. (2021) studied Swarm LoL events as well, this time by looking at TEC interruptions occurred on all the three satellites from December 2013 to December 2020. Even here, the dependencies on latitude, local time and season are deepened, but the significance of solar activity is also taken into account. The regions most impacted by this phenomenon match those identified by Xiong et al. (2018) and exhibit similar seasonal patterns. Regarding solar activity, LoL events maximize during years of maximum solar activity, while their number reduces significantly during years of solar minimum. Another interesting part of this study is the characterization of the ionosphere background conditions during LoLs. This was done by analyzing the relation with two ionospheric indices: the RODI (explained in Section 4.3) and the Rate Of change of Total electron content Index (ROTI), which is calculated as RODI but considering TEC time series instead of N_e ones.

It emerges that LoLs are more likely to be accompanied by extremely high values of both indices, being connected with regions of large electron density gradients, as it is possible to visualize directly from the example on their Figure 1. Another two examples regarding the behaviour of RODI in particular, in correspondence of three different LoL events, as identified from the interruptions in sTEC time series, are reported in Figure 5.1. These events were recorded on board Swarm A during the particularly disturbed conditions of the St. Patrick storm in March 2015. During an ascending orbit on March 17$^{\text{th}}$, 2015, between 13:46:35 and 14:06:50 UT and 13:51:16 and 14:21:27 UT, two of the eight GPS receiving channels of Swarm A were in contact with GPS satellites identified by Pseudo Random Number (PRN) = 9 and PRN = 17. Figure 5.1 points out that for PRN = 9, sTEC cannot be calculated in one segment of the orbit, whereas for PRN = 17 it can not be calculated in two segments of the orbit due to LoL events occurring between the GPS receiver on board Swarm A and satellites. As anticipated, RODI, which is shown for the same orbit, significantly increases during the events. This is an important aspect of the research presented in the following sections, because it confirm that the irregularities responsible for the occurrence of LoL events appear to be close to Swarm satellites.

For the further analysis Swarm LoL events have been identified following the procedure proposed by Pezzopane et al. (2021) and described in Section 2.1. The events were selected in the period starting from July 15$^{\text{th}}$ 2014, when sTEC sampling rate was increased to 1 Hz (Van Den Ijssel et al., 2016), to December 31$^{\text{st}}$ 2021 and considering two satellites, Swarm A and B. The retrieved events have different duration: from a few tens of seconds down to a single second. However, a check of LoL events whose duration is 1 s, evidenced that most of them are most likely not real (Pezzopane et al., 2021). This is the reason why they are removed from the dataset. Another curious aspect about LoLs duration is that an extremely high number of events (nearly 70%) lasts 18 or 19 seconds, as also found by Xiong et al. (2018)

Figure 5.2 shows the geographical distribution of LoL events occurrence, recorded by Swarm A and B during the selected period. Most events cluster, in both hemispheres, at equatorial and high latitudes, where their occurrence maximizes along the crests of the equatorial anomaly at low latitudes, and inside the auroral oval at high latitudes. It is worth highlighting that, even though the utilized LoL identification procedure is based on sTEC time series (see Section 2.1 for more details) and not on carrier phase and pseudo-range time series as done by Xiong et al. (2016, 2018), the distributions shown in Figure 5.2 are highly comparable with those found by Xiong et al. (2018). Moreover, as highlighted by Xiong et al. (2016), also in this analysis emerged a lower number of LoL events for Swarm B than for Swarm A, suggesting that the presence of irregularities decreases as the altitude increases. This is consistent with the fact that the investigated plasma environment is the topside ionosphere, where the electron density undergoes a nearly-exponential decrease with altitude. Indeed, at Swarm altitudes, the ionospheric plasma scale height is of the order or 50-100 km depending on latitude, local time, season, and solar activity (e.g., Pezzopane and Pignalberi (2019), Pignalberi et al. (2022)). Therefore at the altitude of Swarm B, flying about 50 km above Swarm A, the electron density is significantly reduced. More in general, after three scale heights (150-300 km) the electron density is reduced by a factor $1/e^3 \sim 0.05$, which reasonably suggests that 95% of the topside electron density is concentrated in a narrow range of altitudes above Swarm satellites and not much further away.

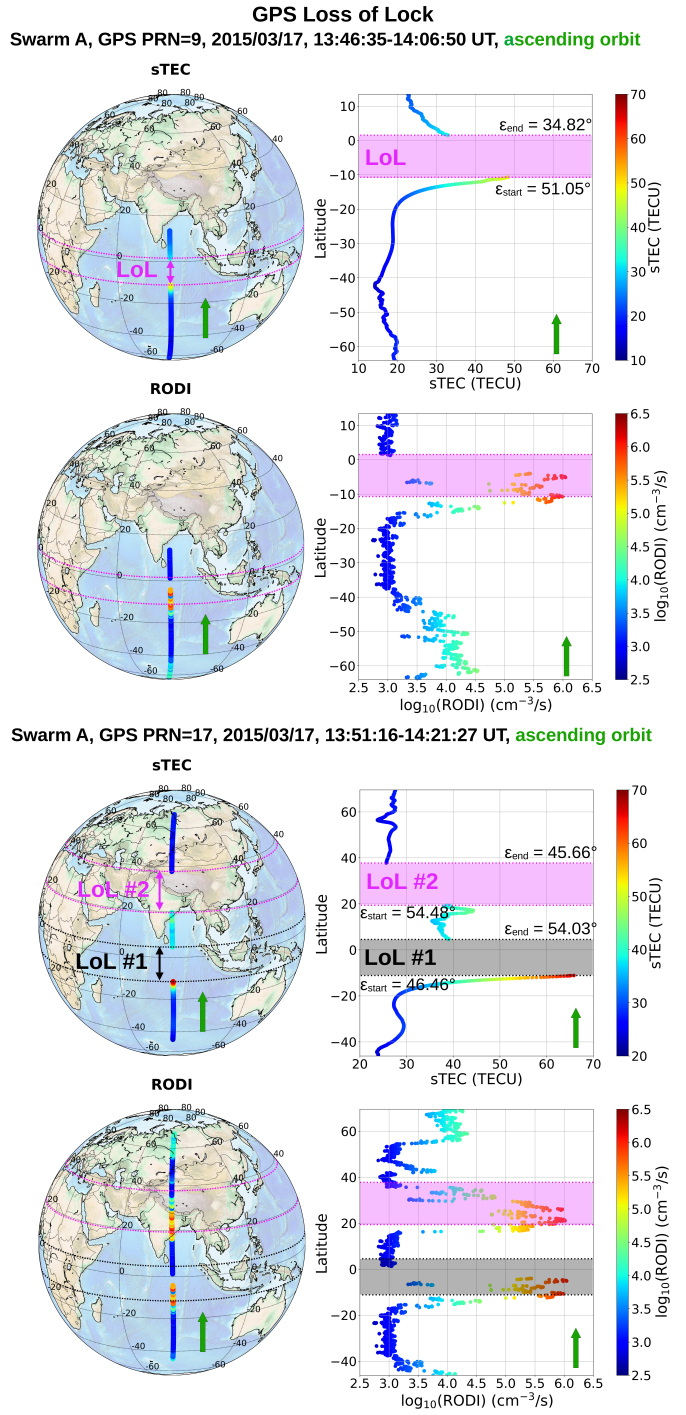

Figure 5.1: Examples of GPS LoL events as identified on March 17$^{\text{th}}$, 2015 in the sTEC time series, measured by Swarm A during the same orbit (the green arrow indicates whether the orbit is ascending or descending), but related to different satellites, PRN = 9 (top) and PRN = 17 (bottom), and corresponding RODI values calculated from electron density measurements. The magenta and grey belts identify the GPS LoL duration. Left panels represent the satellite track in a geographic coordinates map, while right panels show the corresponding plot latitude vs value (sTEC or RODI). The sTEC plot shows also the elevation angle of the satellite at the start (ϵ_{start}) and at the end (ϵ_{end}) of the LoL event. Credits: De Michelis et al. (2022)

One remarkable advantage of Swarm mission is the availability of simultaneous measurements from its instruments. This, for example, gives the possibility to know the local electron density conditions in the exact instant a LoL event is recorded by the POD antennas, allowing to track

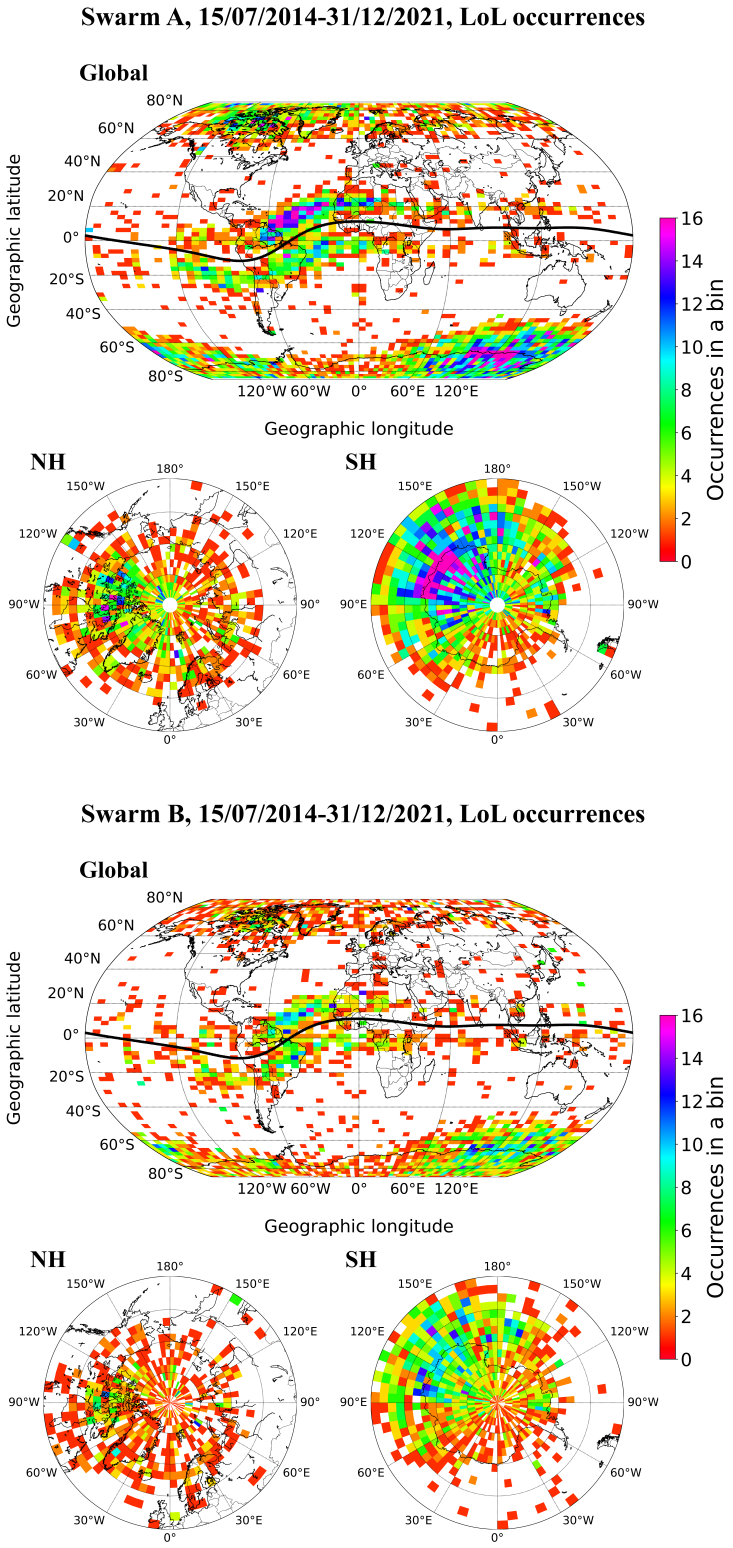

Figure 5.2: Geographic distribution of GPS LoL occurrence for Swarm A and Swarm B, from July 15$^{\text{th}}$ 2014 to December 31$^{\text{st}}$ 2021, as global projection and as Northern hemisphere (from 50° N to the North pole) and Southern hemisphere (from 50°S to the South pole) polar projections, respectively. Bins are 2.5° wide in latitude, and 5° wide in longitude. The black curve in the global projection represents the magnetic equator. Credits: De Michelis et al. (2022)

the amplitudes, variability, and scaling invariance properties of the plasma irregularities along the satellite orbit. Moreover, this is possible for a period that goes from the beginning of the mission to the present days, which, at the time of writing this work, covers more than half of the 24^{th} solar cycle and up to nearly 4 years of the 25^{th}.
Taking advantage of this aspect, in the following Sections the correlation between LoL events and ionospheric plasma irregularities is deepened, focusing on their possible turbulent character and their dependence on external parameters like solar and geomagnetic activity, interplanetary and seasonal conditions.

5.2 Relationship between GPS LoLs and ionospheric irregularities at their origin

As anticipated in Section 4.3, De Michelis et al. (2021a) and De Michelis et al. (2021b) identified a class of plasma density irregularities in a turbulent state and characterized by very high values of RODI. These two studies suggested that these irregularities can play an important role in the Space Weather framework, contributing to the degradation of electromagnetic signals passing through the ionospheric medium, thereby affecting the performance of systems that rely on their propagation, such as GNSS. As a result, precise identification of this specific type of irregularity could be very helpful for avoiding harmful effects on GNSS in their comunication with LEO satellites, as in the case of LoLs.

In the following analysis, LoL events recorded on two of the three Swarm satellites (Swarm A and Swarm B) are studied in relation to the local ionospheric plasma conditions, with a focus on the types of irregularities identified by De Michelis et al. (2021a) and De Michelis et al. (2021b). This is carried out with the aim of determining whether ionospheric irregularities, exhibiting turbulence and characterized by exceptionally high RODI values, could potentially underlie LoL events. However, once this correspondence is potentially established, it becomes crucial to verify whether the family of irregularities identified as a potential proxy for a LoL event displays the same typical spatio-temporal dependencies observed in LoL events, as extensively described in the previous section. As a result, the following sections present a comparison of the characteristics of LoL events and those of the identified plasma density fluctuations as a function of magnetic latitude, magnetic local time, geomagnetic activity, local season, solar activity and interplanetary conditions. Understanding whether this class of plasma density fluctuations can be used as a proxy for LoL events could be critical for the development of an empirical model that can highlight the areas where specific physical conditions could trigger disturbances potentially harmful to radio signal propagation.

5.2.1 Identification of irregularities at the base of GPS LoL events

To accomplish the proposed task, all the starting times of LoL events longer than 1 s are considered and analyzed in terms of the corresponding local fluctuation scaling properties of the electron density measurements. Specifically, the local scaling properties concern the behavior of a structure, which in this case corresponds to an irregularity, as a function of the scale at which it is viewed. These features are essential to understand and characterize the complexity of the structure (Schmitt and Huang, 2016). In this specific case, they allow to capture some peculiar features of the local electron

density fluctuations and shed light on the so-called multiscale dynamics, which characterizes all those complex systems in which a large range of time and/or spatial scales may interact with each other. As explained in details in Section 3.2, the local scaling properties, which can be inferred, for example, with the structure function analysis, provide information on the persistent or anti-persistent nature of the fluctuations and, indirectly, on their spectral features. This last aspect in particular allows discriminating among the different kinds of instabilities or turbulent processes that originated the observed fluctuations. For example, slopes of the power spectrum ranging between -5/3 and -3 are associated with different turbulent regimes like, e.g., the shear-flow turbulence with a direct or an inverse energy cascade, the turbulence driven by the $\vec{E}$ x $\vec{B}$ convective instability, or the turbulence driven by strong electron density gradient drifts (Kintner and Seyler, 1985).

Since LoL events are mainly located in two specific regions, i.e. the equatorial and polar ones (as seen in Figure 5.2), the analysis regards two well-defined regions:

1. the mid- and high- magnetic latitudes ($|\text{MLat}| > 50°$)
2. the equatorial belt ($|\text{MLat}| < 30°$)

In order to study high-latitude behavior in its entirety, the Northern and Southern hemispheres will not be distinguished at first. Then, the two hemispheres will be studied separately one at a time, with a particular emphasis on the mid- and high-latitude regions, being the equatorial band more deeply understood.

Figure 5.3 displays the joint PDF of RODI and the first- and second-order scaling exponents, conditioned to the occurrence of LoL events at mid- and high- latitudes, analyzing Swarm A and Swarm B separately, and considering only the points at which LoL events start. The conditioned PDFs obtained using data from Swarm A and Swarm B separately appear very similar to each other, as also confirmed by Figure 5.4, where the conditioned PDFs shown in Figure 5.3 are overlapped. Therefore, at mid- and high- latitudes the features of electron density fluctuations associated with LoL events do not seem to be affected by the altitude difference ($\sim$ 50 km) between the orbits of the two satellites. Once this was ensured, the two datasets of Swarm A and B were merged together, and Figure 5.5 reports the analysis already shown in Figure 5.3 but carried out on the joint dataset. The conditioned PDFs of RODI and the first- and second-order scaling exponents values indicate that GPS LoL events are primarily associated with electron density fluctuations characterized by $\gamma(1) = (0.47 \pm 0.12)$, $\gamma(2) = (0.8 \pm 0.2)$, and RODI $> 10^4 (\text{cm}^{-3}\text{s}^{-1})$.

The same procedure is applied to the equatorial region ($|\text{MLat}| < 30°$). Figure 5.6 reports the conditioned PDFs of RODI and the first- and second-order scaling exponents obtained considering the two satellites separately, and then overlapped in Figure 5.7. Even in this case, the altitude difference ($\sim$ 50 km) between the orbits of the two satellites does not affect the resulting distributions. Thus, Figure 5.8 reports the joint PDFs, already shown in Figure 5.6, but performed on the joint dataset. Differently from the case of mid- and high- latitudes, here electron density fluctuations are mainly characterized by a mean value of the first-order scaling exponent $\gamma(1) = (0.64 \pm 0.13)$, suggesting a more persistent character of the fluctuations, and by a mean value of the second-order scaling exponent $\gamma(2) = (1.0 \pm 0.2)$. In this case, RODI values are extremely high, even higher than those obtained for mid- and high-latitude regions. However, there is also an additional class of events for which the electron density fluctuations show completely different properties: RODI$< 10^{3.5}$ $\text{cm}^{-3}\text{s}^{-1}$, $\gamma(1) > 0.6$, and $\gamma(2) > 1$. This class consists of nearly 25%

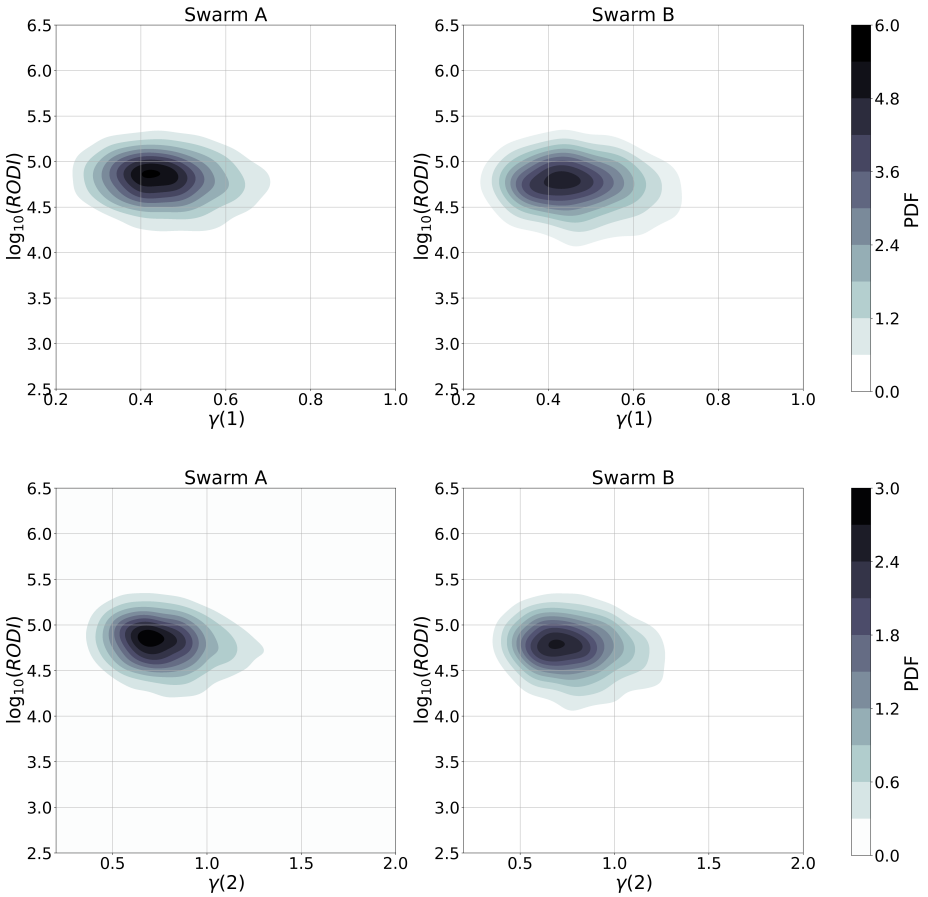

Figure 5.3: Conditioned joint Probability Density Function (PDF) of RODI and $\gamma(1)$ (top panels) and $\gamma(2)$ (bottom panels) analyzing Swarm A (left column) and Swarm B (right column) separately. Data refer to mid- and high- latitudes ($|\text{MLat}| > 50°$) and are those calculated simultaneously to the occurrence of GPS LoL events. Credits: De Michelis et al. (2022)

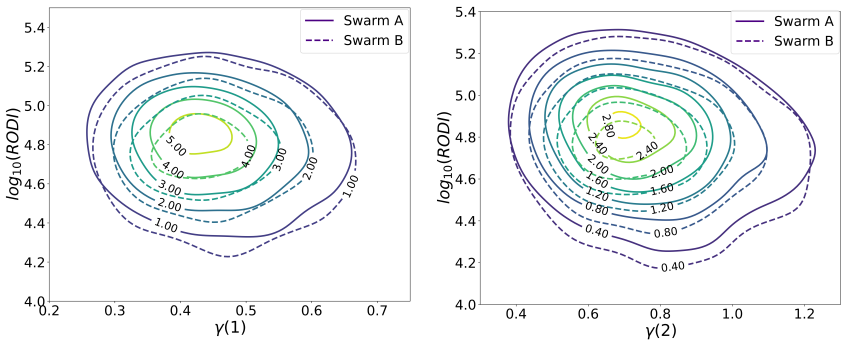

Figure 5.4: Overlap of the conditioned joint PDF of RODI and $\gamma(1)$ (left panel) and $\gamma(2)$ (right panel), evaluated using Swarm A and Swarm B data, shown separately in Figure 5.3. Credits: De Michelis et al. (2022)

of all recorded events and the values of the scaling exponents associated with the electron density fluctuations suggest a different origin this group of LoLs.

In order to investigate this additional class of events, a pseudo-intermittency parameter μ is introduced (briefly called *intermittency* in the following). It provides information on the occurrence of anomalous scaling features, i.e., on the departure from a linear trend of the scaling exponents

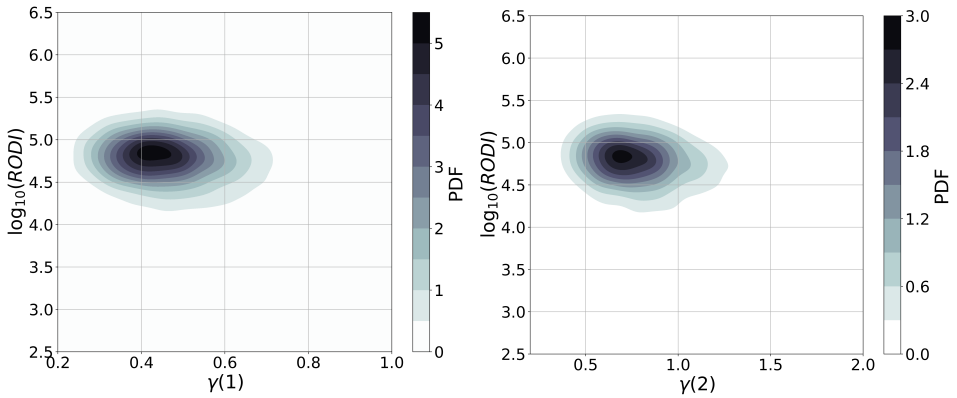

Figure 5.5: Conditioned joint PDF of RODI and $\gamma(1)$ (left panel) and $\gamma(2)$ (right panel) for the joint dataset (Swarm A + Swarm B). Data refer to mid- and high- latitudes ($|\text{MLat}| > 50°$) and are those calculated simultaneously to the occurrence of GPS LoL events. Credits: De Michelis et al. (2022)

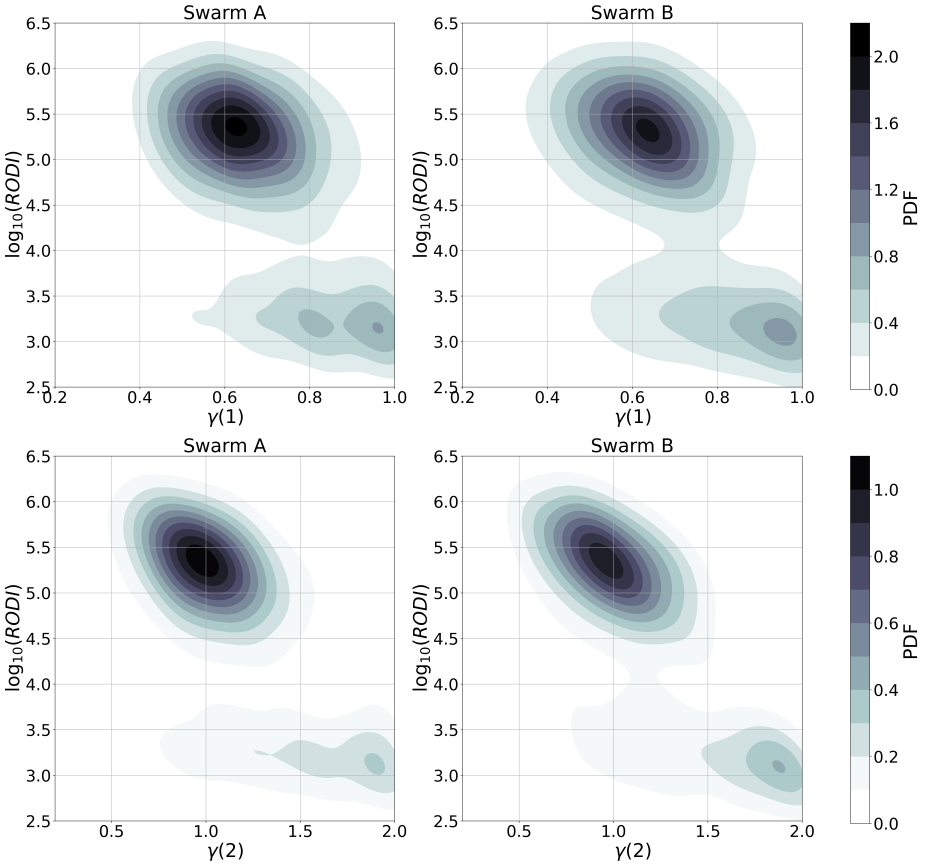

Figure 5.6: Conditioned joint PDF of RODI and $\gamma(1)$ (top panels) and $\gamma(2)$ (bottom panels) analyzing Swarm A and Swarm B separately. Data refer to the equatorial belt ($|\text{MLat}| < 30°$) and are those calculated simultaneously to the occurrence of GPS LoL events. Credits: De Michelis et al. (2022)

$\gamma(q)$ on moment order q. It is defined according to the equation 5.1.

$$\mu = \gamma(1) - 2\gamma(2), \tag{5.1}$$

being a measure of how the scaling exponents ($\gamma(1)$ and $\gamma(2)$) depart from a linear dependence on q. When $\mu > 0$, then the trend of $\gamma(q)$ is convex. This is exactly what is observed for the occurrence

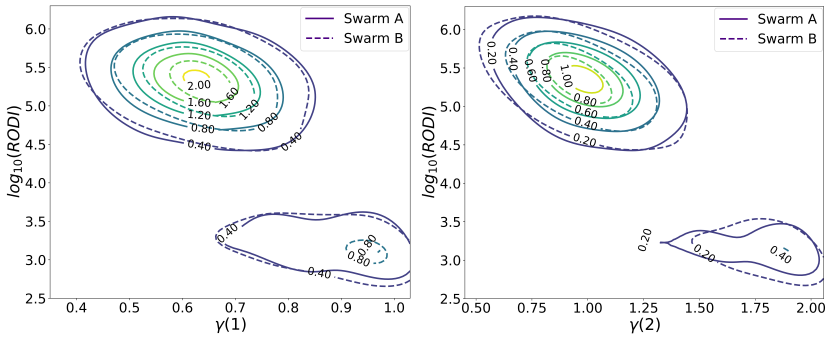

Figure 5.7: Overlapping of the conditioned joint PDF of RODI and $\gamma(1)$ (left panel) and $\gamma(2)$ (right panel), evaluated using Swarm A and Swarm B data, shown separately in Figure 5.6. Credits: De Michelis et al. (2022)

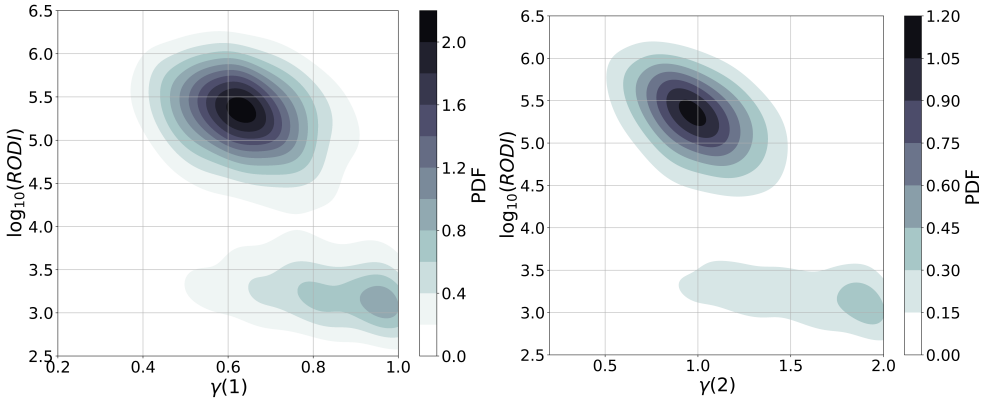

Figure 5.8: Conditioned joint PDF of RODI and $\gamma(1)$ (left panel) and $\gamma(2)$ (right panel) considering the joint dataset (Swarm A + Swarm B). Data refer to the equatorial belt ($|\text{MLat}| < 30°$) and are those calculated simultaneously to the occurrence of GPS LoL events. Credits: De Michelis et al. (2022)

of intermittency in turbulence (Frisch, 1995) and is an evidence of a multifractal character of the cascading process (i.e., the energy transfer among the scales). Moreover, as the intermittency value increases, the greater will be the non-homogeneity with which the energy is redistributed at all the time and/or spatial scales. Figure 5.9 shows the conditioned joint PDF of RODI and pseudo-intermittency (μ) during GPS LoL events considering the joint dataset (Swarm A + Swarm B) for both mid- and high- latitudes (left panel) and the equatorial belt (right panel). Regarding the mid- and high-latitudes, the plasma density irregularities associated with GPS LoL events are in a turbulent state, always characterized by a certain degree of intermittency. Conversely, at low latitudes there are again two different families of irregularities associated with GPS LoL events, characterized by significantly different values of intermittency. The plasma density irregularities with higher intermittency values are also characterized by extremely high values of RODI and $\gamma(2)$ around 1, as can be seen from the three-dimensional plot of Figure 5.10. Therefore, as in the case of the high latitudes, also in the equatorial belt, plasma density irregularities with extremely high values of RODI are in a intermittent turbulent state.

Figure 5.11 presents a comparison of joint PDFs for RODI-$\gamma(1)$ (on the left) and RODI-$\gamma(2)$ (on the right). In one case, the data includes all available electron density recordings in the mid- and high-latitude region over a specific period, as for De Michelis et al. (2021a), displayed using red-scale surfaces. In the other case, represented by blue-scale level-curves, the distribution is

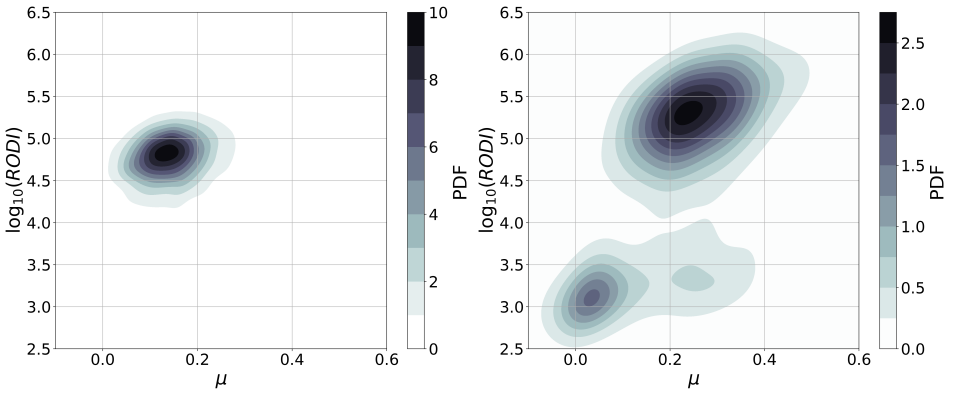

Figure 5.9: Conditioned joint PDF of RODI and intermittency (μ) at mid- and high-latitude regions (left panel) and equatorial belt (right panel) during GPS LoL events considering the joint dataset (Swarm A + Swarm B). Credits: De Michelis et al. (2022)

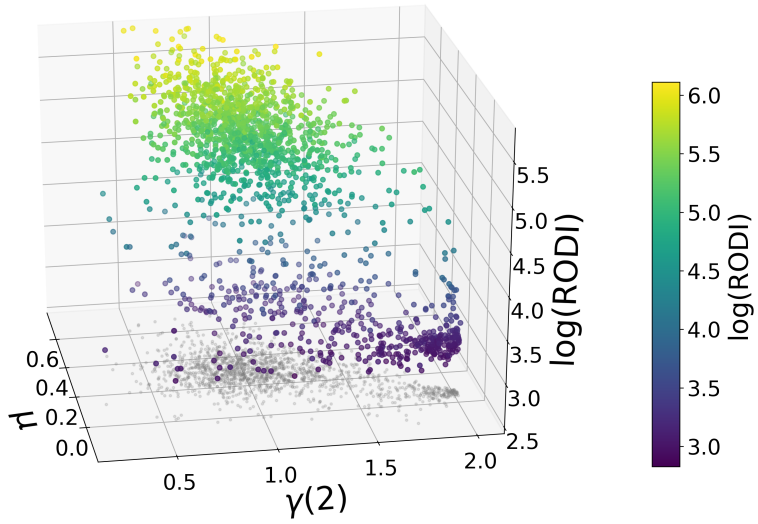

Figure 5.10: RODI, intermittency parameter (μ) and second-order scaling exponent ($\gamma(2)$) values of plasma density irregularities during GPS LoL events in the equatorial belt ($|\text{MLat}| < 30°$). The joint dataset (Swarm A + Swarm B) is considered. Credits: De Michelis et al. (2022)

specifically conditioned on the occurrence of GPS LoL events, as those depicted in Figure 5.5. It is evident that the occurrence of GPS LoL events is associated with a specific class of electron density fluctuations, showing a second-order scaling exponent $\gamma(2) \leq 1$ and extremely high values of RODI. Moreover, RODI seems to be a proxy of this class, as values of Log(RODI)>4 are associated with the occurrence of LoL events.

Similar findings are also observed in the equatorial region, as depicted in Figure 5.12. This figure illustrates a comparison between the scaling characteristics of electron density fluctuations associated with GPS LoL events, as shown in Figure 5.8, and those observed in conjunction with plasma bubbles identified by the IBI index, as described in Section 2.1, following the methodology presented in De Michelis et al. (2021b). In De Michelis et al. (2021b), it was shown that plasma bubbles present both spectral features and RODI values that are significantly different from those of their background environment. Specifically, they found that electron density fluctuations associated

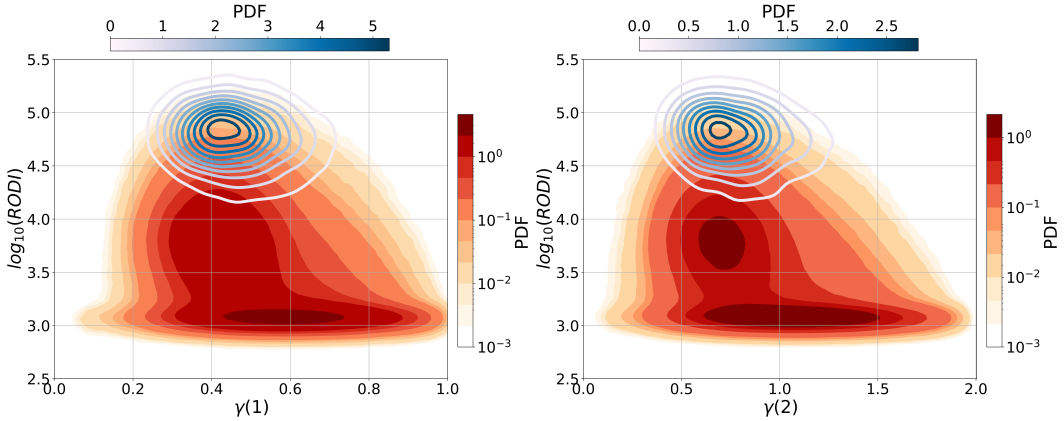

Figure 5.11: Conditioned joint PDF of RODI and $\gamma(1)$ (left panel) and $\gamma(2)$ (right panel) at mid- and high-latitude regions ($|\text{MLat}| > 50°$) during GPS LoL events (the same reported in Figure 5.5, here shown as blue-scale line contours) and the same quantity obtained considering all data and not only those corresponding to a LoL event (here shown as red-scale filled contours). Credits: De Michelis et al. (2022)

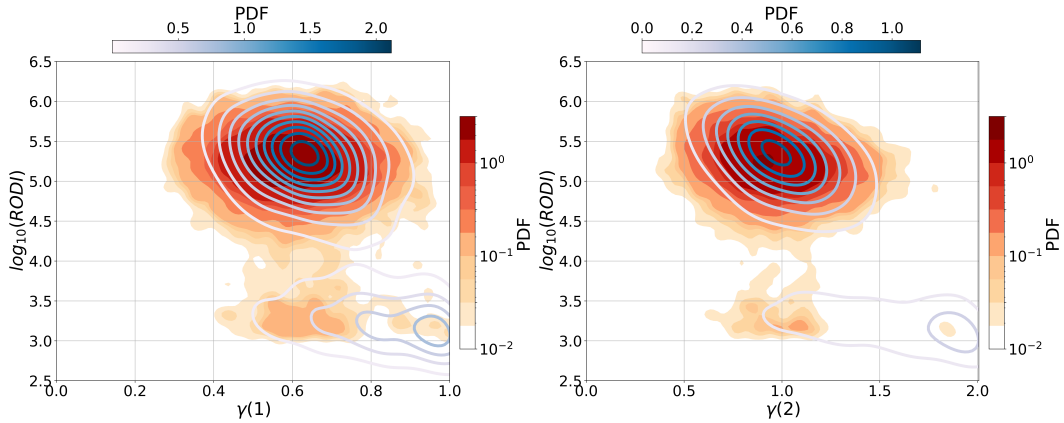

Figure 5.12: Conditioned joint PDF of RODI and $\gamma(1)$ (left panel) and $\gamma(2)$ (right panel) at low latitude ($|\text{MLat}| < 30°$) during GPS LoL events (the same reported in Figure 5.8, here shown as blue-scale contours) and the same quantity obtained considering plasma bubbles occurrence (here shown as red-scale filled contours). Credits: De Michelis et al. (2022)

with plasma bubbles fall right into the class showing a second-order scaling exponent $\gamma(2) \leq 1$ and extremely high values of RODI. Figure 5.12 clearly evidences how, in the equatorial belt, the features shown by the electron density fluctuations associated with GPS LoL events are really similar to those of plasma bubbles. This suggests that, in the equatorial ionosphere, most of GPS LoL events could be triggered by the plasma bubbles development. However, by checking the IBI index in correspondence of LoL events, it results that about 25 % of the ones recorded in the equatorial belt do not seem to be related to the presence of plasma bubbles. As already noticed discussing Figure 5.8, this portion of events is characterized by electron density fluctuations with low RODI values ($\log(\text{RODI}) < 4$) and different scaling properties. To deepen the behavior of this group of LoL events, Figure 5.13 shows its distribution in the MLat-MLT plane with blue dots. The fact that they are more equally distributed at all hours, with respect to the events with $\log(\text{RODI}) > 4$ indicated with yellow dots, highlights that they are most likely related also to physical phenomena different

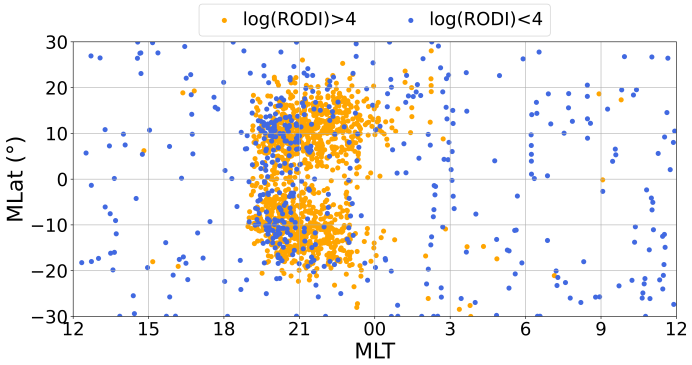

Figure 5.13: Low latitude (|MLat| < 30°) distribution in the MLat-MLT plane of GPS LoL events for Swarm A and Swarm B, from July 15^{th} 2014 to December 31^{st} 2021 according to different log(RODI) values. Credits: De Michelis et al. (2022)

from those at the base of the plasma bubbles development. In detail, only a small number of these events occur under conditions (MLT and MLat values) compatible with the development of plasma bubbles, i.e. in the post sunset sector and with a characteristic appearance along the geomagnetic equator. In fact, during the day, the high conductance of the E region with respect to the F region prevents the appearance of plasma bubbles, which are generated by the transport of plasma from the bottomside to the topside ionosphere by the generalized Rayleigh-Taylor instability. A possible explanation is that the group of LoL events at lower Log(RODI), also associated with electron density fluctuations characterized by completely different scaling properties, can be triggered by plasma blobs, that are mesoscale plasma density enhancements relative to the ambient plasma with longitudinal widths comparable to those of equatorial bubbles. These plasma density irregularities, unlike equatorial bubbles, are more frequently detected around ±20° – 30° MLat (Choi et al., 2012, Haaser et al., 2012, Watanabe and Oya, 1986), although they can also be observed at night at low- and mid- latitudes in association with equatorial plasma bubbles (Martinis et al., 2009, Park et al., 2003, Yokoyama et al., 2007).

These results indicate that both the scaling exponent values and the RODI values associated with LoL events in the two examined regions (mid- and high-latitudes and the equatorial belt) exhibit latitude-dependent variations. This implies that the underlying physical mechanisms governing these phenomena can vary across different latitudinal bands. Indeed, the values of the second-order scaling exponents are slightly different moving from high to low latitudes. Also the persistence character of the high/low-latitude fluctuations is different, being $\gamma(1)$ below 0.5 at high latitudes (anti-persistent fluctuations) and above 0.5 at low latitudes (persistent fluctuations). Furthermore, generally $\gamma(2) < 2\gamma(1)$, which translates in $\mu > 0$, so that the dependence of the scaling exponents of the structure functions on the moment order q is expected to be concave, which could be an indication of a multifractal (intermittent) character of the density fluctuations.
The different values of the first and second order scaling exponents at high/low latitudes suggest that different instability/turbulence processes can be at the origin of the ionospheric irregularities' generation. Indeed, for example, the Rayleigh-Taylor instability plays a fundamental role at low latitudes (e.g., Kelley (2009)), while the high latitude region is more characterized by the occurrence of the gradient drift instability, the Kelvin-Helmholtz instability, the $\vec{E} \times \vec{B}$ instability and/or the drift wave turbulence (e.g., Tsunoda et al. (1985)). This could explain the observed differences in

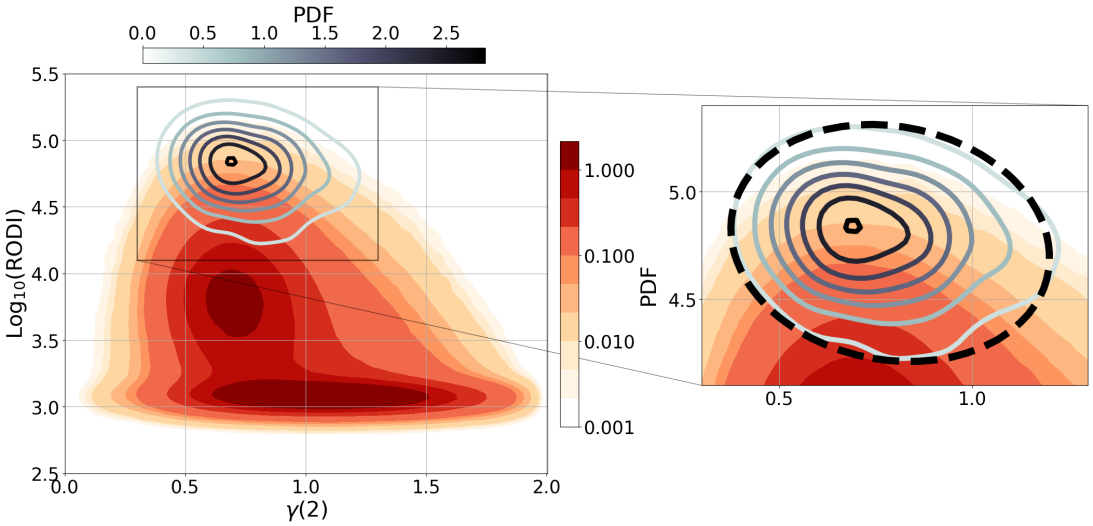

Figure 5.14: Conditioned joint PDF of RODI and $\gamma(2)$ in the mid- and high-latitude regions ($|\text{MLat}| > 50°$), considering all data recorded from July 15$^{\text{th}}$, 2014 to December 31$^{\text{st}}$, 2021 onboard Swarm A and Swarm B (red scale). Superposed the same quantity obtained considering data corresponding to the loss of lock events (grey-scale line contours). On the right a magnification of the figure on the left, where the red dashed curve identifies the ellipse obtained minimizing the sum of the squares of the residuals from the points of probability density equal to a tenth of the maximum. Credits: Lovati et al. (2023b)

the high/low-latitude scaling exponents that characterize the electron density turbulent fluctuations during the GPS LoL events.

The significance of this analysis lies in the identification of the features of the electron density fluctuations at the base of GPS LoL, which exhibit specific scaling features, intermittent behavior, and are typically accompanied by extremely high values of RODI ($> 10^4$ cm^{-3}s^{-1}). In the case of the equatorial region the majority of the events can be attributed to the presence of plasma bubbles, while the high-latitudes are characterized by a wide range of phenomena and, consequently, a broad range of instability types. The goal of the following Sections will be to delve deeper into the characteristics and dependencies of irregularities at mid- and high-latitudes, in order to see if they can act as proxy of GPS LoL events in this region, and thus help in the attempt of prevent their harmful effect on radio signal propagation. This step is required because the previous results have highlighted the statistical relationship between LoL events and specific ionospheric plasma conditions, but without establishing whether these specific plasma density fluctuations actually exhibit spatio-temporal behaviors similar to LoL events. As a result, a comparison of the properties of LoL events and those of the identified plasma density fluctuations as a function of magnetic latitude, magnetic local time, solar and geomagnetic activity, local season, and interplanetary conditions is required.

High-latitude irregularity selection

The initial step involves selecting the electron density fluctuations of interest. As outlined in the preceding section, this category of electron density fluctuations, believed to underlie LoL events, defines a distinct region within the Log(RODI)-$\gamma(2)$ space, as illustrated on the right side of Figure 5.11. The level curves relative to the joint PDF, conditioned to the presence of GPS LoLs, closely resemble irregular ellipse contours. As a result, the level curve corresponding to $\frac{1}{10}$ of the probability

Coefficient	Value
a	-0.07
b	-0.01
c	-0.04
d	0.18
e	0.40

Table 5.1: Coefficients of the ellipse in the $\gamma(2)$-Log(RODI) space, found minimizing the sum of the squares of the residuals with respect to the points of probability density equal to a tenth of the maximum.

density maximum was fitted with an ellipse using the least squares method. The resulting ellipse is represented by the black dashed curve in the right panel of Figure 5.14 and is described by the following equation:

$$ax^2 + bxy + cy^2 + dx + ey = 1$$

where x corresponds to $\gamma(2)$, y to Log(RODI) and the coefficient retrieved with the least squares method are listed in Table 5.1.

In this way, a new subset of Swarm data was obtained, which corresponds to all those instants of time when $\gamma(2)$ and RODI together were both inside this curve and met the so-called *ellipse's criterion* for brevity. Thus, this subset includes all the events that, regardless of whether a LoL event is actually occurring, have $\gamma(2)$ and RODI values that could theoretically trigger one. In the following analysis, the GPS LoL event distribution is also conditioned to meet the ellipse's criterion. This primarily removes some of the already few events occurring in years of low solar activity, as well as the final portion of some longer-duration events, from the distribution.

Figure 5.15 compares the spatial distribution of GPS LoL events at mid and high latitudes ($|\text{MLat}| > 50°$) in the Northern and Southern hemispheres, as well as the spatial distribution of N_e fluctuations as defined by $\gamma(2)$ and RODI values satisfying the ellipse's criterion. In both hemispheres, there is a high degree of agreement between the two distributions. Below $|60°|$ of MLat, the occurrence of GPS LoL events is generally low. It increases in the dayside band between $|70° - 80°|$ of MLat, centered in the position of the cusp, and in the nigthside auroral oval between 18:00 and 06:00 MLT. The spatial distribution of N_e fluctuations with $\gamma(2)$ and RODI values within the ellipse exhibits similar patterns.

Figure 5.16 shows the superposition of the two spatial distributions reported in Figure 5.15. In this case the spatial distribution of GPS LoL events is reported using grey-scale contour lines.The spatial distributions of the ionospheric N_e fluctuations satisfying the ellipse's criterion and the GPS LoL events agree well with one another in the Mlat- MLT plane. It's also interesting to note that for both data sets, the Southern hemisphere has a significantly higher proportion of GPS LoL events as well as ionospheric N_e fluctuations meeting the ellipse's criterion. It was suggested that the larger number of ionospheric irregularities characterizing the Southern hemisphere could be related to the different offset of the geographic and geomagnetic poles in the two hemispheres, which would cause ionospheric convection in the polar cap of the Southern hemisphere to pull in more high-density plasma (Jin et al., 2019).

The major difference between the two distributions is the number of GPS LoL events which is lower

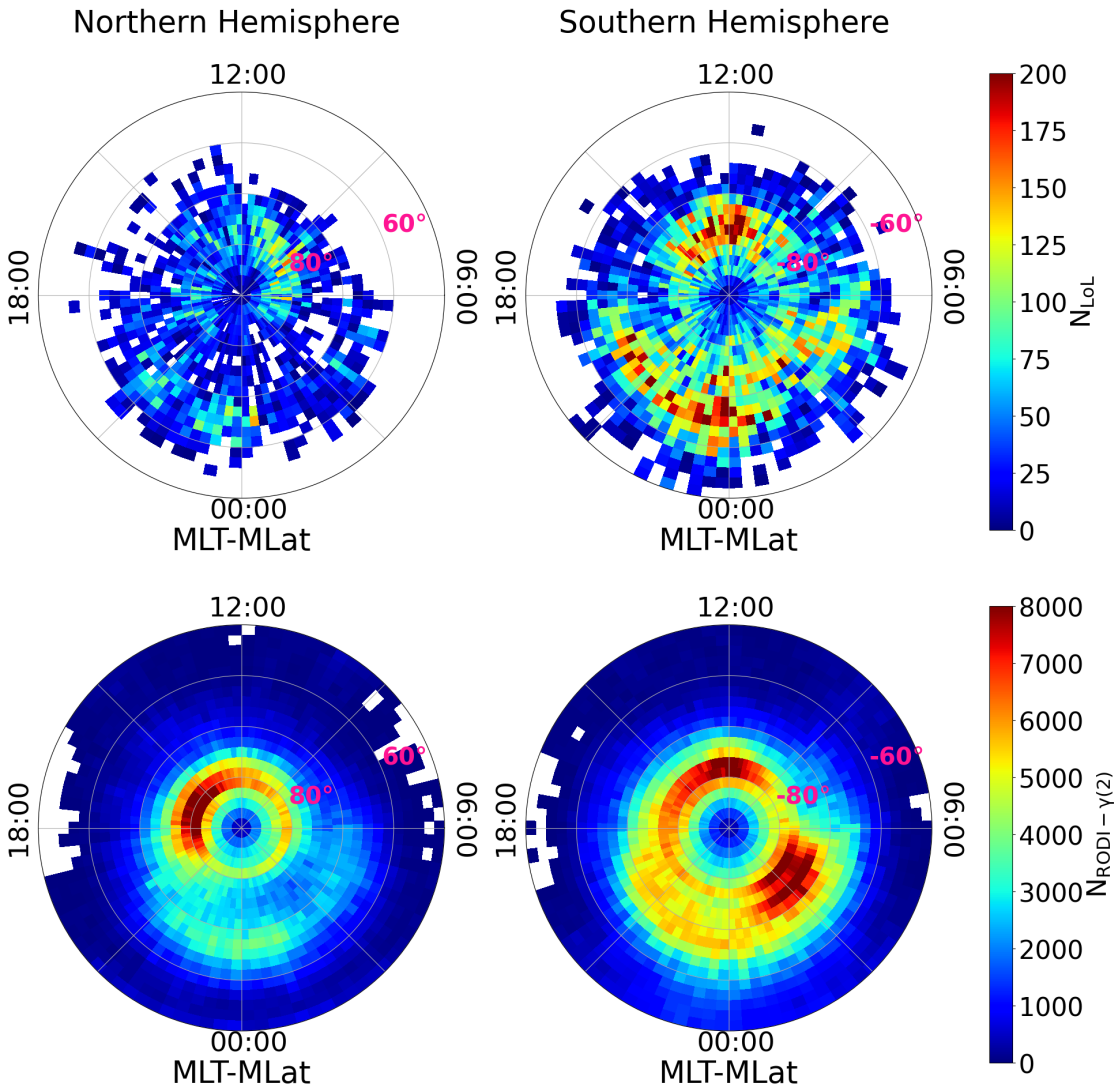

Figure 5.15: Comparison of the spatial distribution of GPS LoL events at mid and high latitudes (|MLat| > 50°) in the Northern and Southern hemispheres and the spatial distribution of N_e fluctuations as defined by $\gamma(2)$ and RODI values within the ellipse identified in Figure 5.14. Credits: Lovati et al. (2023b)

by one or two orders of magnitude than the number of N_e fluctuations with values of $\gamma(2)$ and RODI potentially capable of producing GPS LoL events. Moreover, there are some areas where the location of the maximum values of the two distributions differ (see in particular Figure 5.15). At the cusps, which are areas in the dayside auroral oval close to noon in the Northern and Southern high-latitude ionosphere, a maximum occurrence rate is clearly visible in both data sets. This region is within a few hours of MLT, and its location depends on how the IMF is oriented. In the displayed case, the maxima of the two distributions relative to the cusp are nearly symmetrical with respect to noon in the Southern hemisphere and do not move before or after this, as it should when the IMF's orientation changes. Indeed, the distributions are derived by averaging about 7 years of data, without making any assumptions about the orientation of the IMF for the moment, and thus have a climatological validity. However, in the Northern hemisphere the maxima in proximity on the cusp result shifted toward the morning hours for the GPS LoL distribution, while it moves toward the evening hours in the case of the N_e fluctuations defined by the ellipse's criterion. This could be due to the different prevailing conditions of the IMF relative to the two groups of events. Section 5.2.5

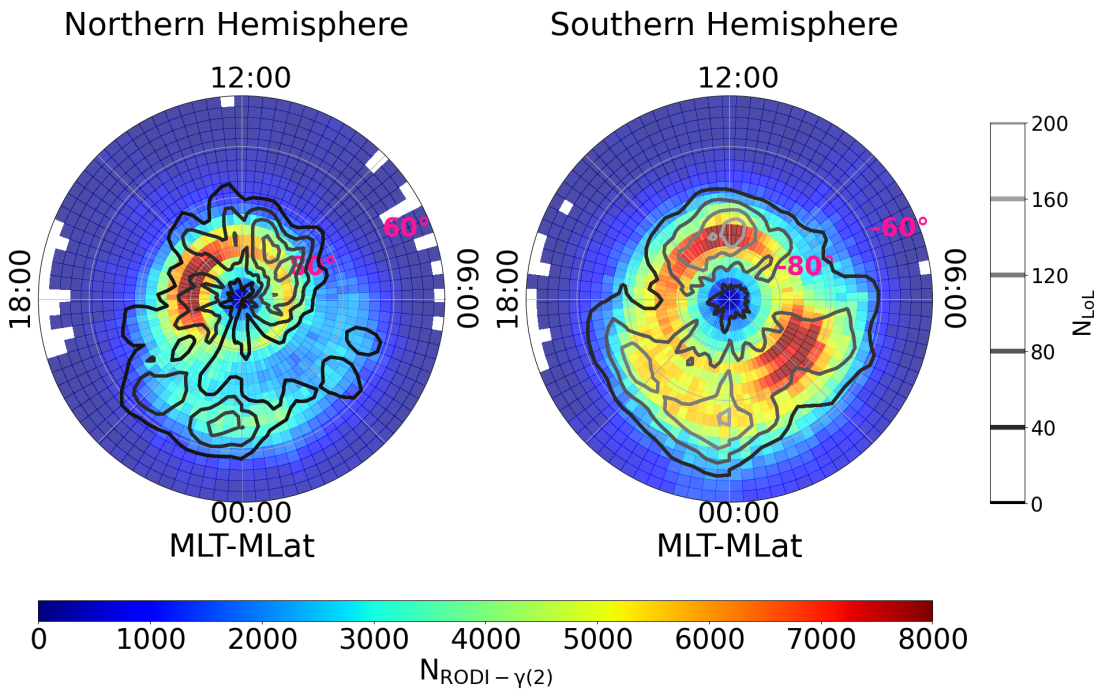

Figure 5.16: Superposition of the spatial distribution of the locations where N_e fluctuations exhibit $\gamma(2)$ and RODI values consistent with the occurrence of GPS LoL events (colored scale) and the spatial distribution of GPS LoL events (grey-scale line contours) at mid and high latitudes ($|\text{MLat}| > 50°$) in the Northern and Southern hemispheres. Credits: Lovati et al. (2023b)

will delve deeper into this topic. Anyhow, the solar-wind condition changes have a direct impact on the cusp region, which is characterized by enhanced ion and electron precipitation. As confirmed by these findings, cusp processes can generate localized plasma density irregularities in a turbulent state, which can be also responsible for LoL occurrences.

It is possible to notice another difference between the two datasets in the night side, between $-80°$ <MLat< $-70°$ in the Southern hemisphere, where N_e fluctuations with $\gamma(2)$ and RODI values that meet the ellipse's criterion are maxima between 01:00 MLT and 05:00 MLT while LoL events tend to cluster between 18:00 MLT and 01:00 MLT. While there are typical turbulent N_e fluctuations in these regions, LoL events tend to occur less frequently there, suggesting that the factors identified (RODI and $\gamma(2)$) are necessary but not sufficient. This aspect is also confirmed by the already mentioned difference in the number of LoL events with respect to the number of N_e fluctuations presenting RODI and $\gamma(2)$ values compatible with the occurrence of LoL, which is independent of the hemisphere under consideration.

These differences demonstrated that tracking the ionospheric conditions that favor GPS LoL events could be accomplished more effectively by introducing additional parameters that, in addition to those already identified, can better capture the N_e fluctuations at the base of LoL events. In any case, the good agreement between the two distributions is encouraging and demonstrates the significance of this class of RODI-$\gamma(2)$ values in predicting the occurrence of GPS LoL events.

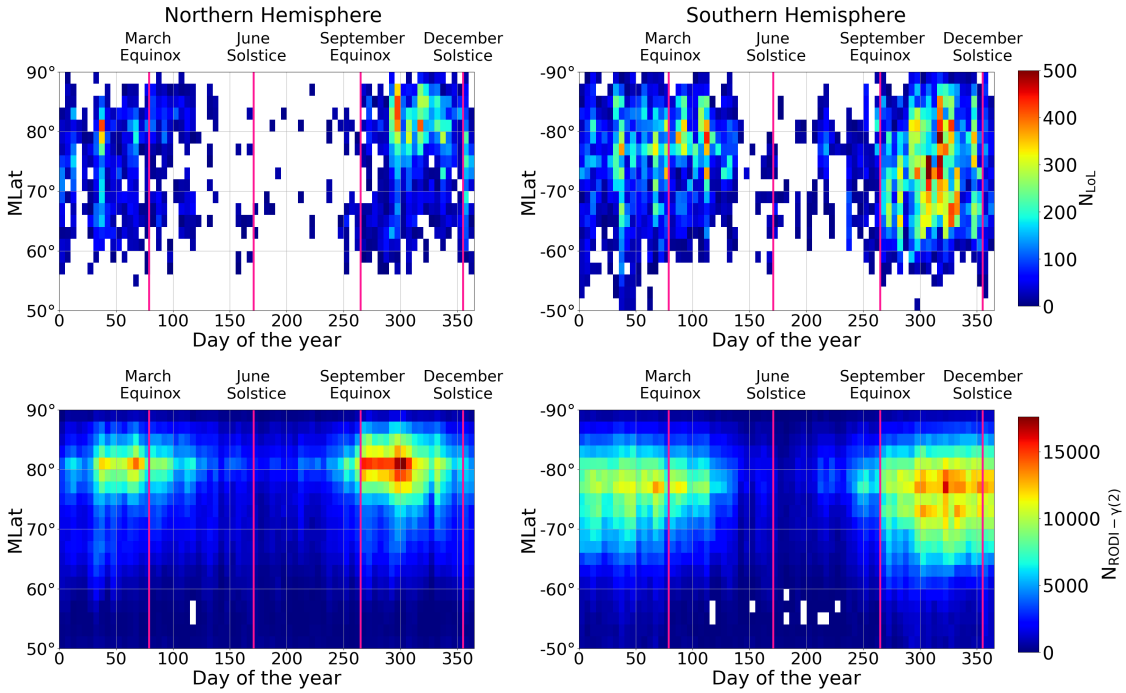

Figure 5.17: Distribution of GPS LoL events and N_e fluctuations with values of $\gamma(2)$ and RODI inside the ellipse of Figure 5.14 as a function of MLat and day of the year for the Northern and Southern hemispheres. The distributions are obtained considering data recorded from July 15th, 2014 to December 31st, 2021. Credits: Lovati et al. (2023b)

5.2.2 Dependence on local season

In order to determine whether N_e fluctuations, which seem to be at the origin of GPS LoL events, could be utilized as a proxy for their occurrence, firstly their possible seasonal dependence is checked. The purpose is to see if the two quantities exhibit the same annual trend. For this reason, Figure 5.17 shows the distribution of both GPS LoL events and N_e fluctuations with values of $\gamma(2)$ and RODI inside the ellipse of Figure 5.14 as a function of MLat and day of the year, in bins 2°-wide in MLat and 5-days wide. These trends were obtained by separating the two hemispheres and analyzing the data over the entire time period.

GPS LoL events are limited to the months from September to May. Regardless of latitude, the months of June, July, and August have the lowest incidence of LoL events. N_e fluctuations with values of $\gamma(2)$ and RODI satisfying the ellipse's criterion show the same annual trend as the GPS LoL events. Indeed, the incidences are concentrated between September and May, while their number is incredibly low between June and August. This reveals that there is no true seasonal dependence, but rather a lower occurrence rate in the months surrounding the June solstice in both hemispheres, regardless of the corresponding local season. At very high latitude ($|\text{MLat}| > 75°$), this behavior seems to be consistent with the annual occurrence rate of the polar cap patches, which are plasma density irregularities with densities that are at least twice as high as the surrounding plasma (Crowley, 1996). Indeed, it has been observed that polar cap patches occur more in winter than in summer in the Northern hemisphere, while in the Southern hemisphere Noja et al. (2013), using the upward-looking GPS TEC data from CHAMP, identified more patches during the local summer. It should be noted that Chartier et al. (2018) found a different result using electron density data collected by Swarm, concluding that polar cap patches are more prevalent during local

winter in both hemispheres, whereas the same investigation using upward-looking TEC revealed a completely different result: polar cap patches appear to occur more frequently in both hemispheres in December. The method of identifying the polar cap patches, which is based on in-situ density measurement or integrated TEC, may be the cause of the discrepancy. In order to further investigate the possible link between GPS LoLs and polar cap patches, an additional analysis has been carried out and will be presented in Section 5.2.6.

The impact of solar Extreme Ultraviolet (EUV) radiation, which ionizes the E region during the summer and may short-circuit the F-region irregularities, can explain this cyclical trend in the Northern hemisphere. Because this argument is no longer valid in the Southern Hemisphere, alternative processes should be investigated to explain the apparent reduction of irregularities between June and August. Another possible explanation could be the ionospheric annual anomaly, which corresponds to the fact that the global maximum of electron density appears higher in December than in June.

Finally, for both types of events, the maximum occurrence regions appear wider and shifted at slightly lower latitudes in the Southern hemisphere than in the Northern, most likely due to the different offset of the geographic and geomagnetic poles in the two hemispheres.

5.2.3 Dependence on solar activity

The dependence of LoL events and N_e fluctuations with values of $\gamma(2)$ and RODI inside the ellipse of Figure 5.14 on solar activity is also studied. Figure 5.18 shows the evolution of the two distributions (second and third rows), as a function of MLat and day of the year, in bins 2°-wide in MLat and 9-days wide, over the solar cycle, as highlighted in the first row by two solar activity proxies: F10.7 (red curves) and Mg II core-to-wing ratio (blue curves). The two indices are described in details in Sections 2.2 and 2.4.
As seen in the second row, GPS LoL events are mainly concentrated during solar maximum years, namely in 2014 and 2015, and then they almost disappear in both hemispheres. Looking at the third row, one can see that the N_e fluctuations that meet the ellipse's criterion tend to peak during periods of higher solar activity. In the following years of low solar activity, only a background remains, interspersed with evenly distributed minima corresponding to the period from June to August of each year, as shown in Figure 5.17.

The reduction in the occurrences of GPS LoL events and N_e fluctuations with RODI and $\gamma(2)$ inside the ellipse with the lowering of solar activity, follows the previously observed behavior of ionospheric irregularities, regardless of latitude (Aarons et al., 1981, Rodger and Graham, 1996). During periods of increased solar activity, irregularities in the ionospheric F-region occur against a background of increased ionization density (Basu et al., 2002). This is also evident in the work of Jin et al. (2019), which shows the annual trend of three parameters related to the presence of ionospheric irregularities from 2014 to 2018, namely the electron density gradient ∇N_e, the RODI, and the ROTI. The values of these irregularity parameters decrease significantly at all locations (cusp, polar cap, and nightside auroral oval) as the solar cycle declines, following the electron density background decline.

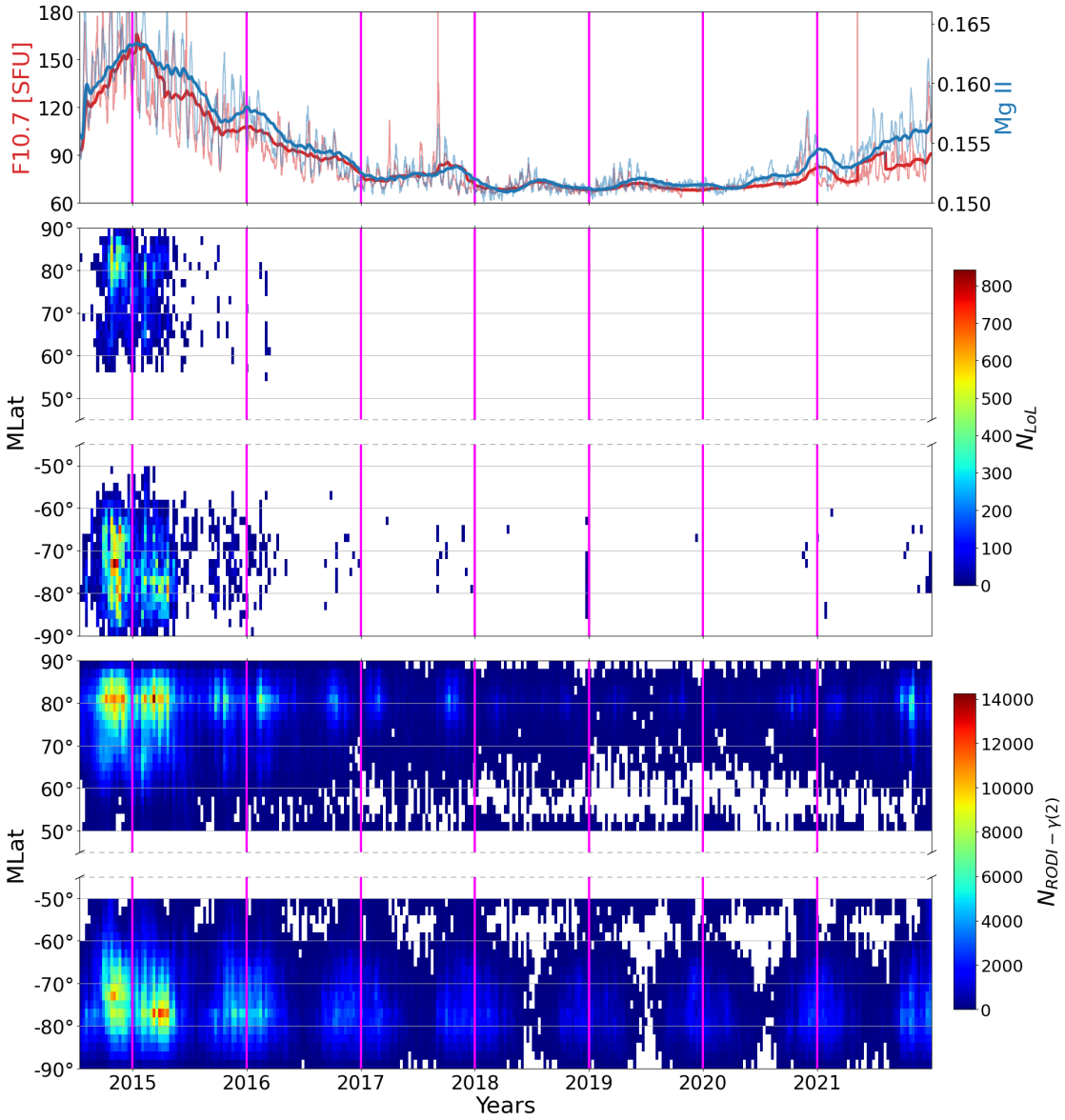

Figure 5.18: *First panel:* hourly values of the F10.7 solar index (thin red curve) and corresponding 81-day running mean (thick red curve), together with daily values of Mg II index (thin blue curve) and corresponding 81-days running mean (thick blue curve). *Second and Third panels:* distribution of GPS LoL events as a function of MLat and time, for the Northern and Southern hemisphere, respectively. *Fourth and Fifth panels:* distribution of N_e fluctuations with values of $\gamma(2)$ and RODI inside the ellipse of Figure 5.14 as a function of MLat and time, for the Northern and Southern hemisphere, respectively. The time frame covered by all of the panels is from July 15th, 2014, to December 31st, 2021. The transition from one year to the next is represented by vertical magenta lines. Credits: Lovati et al. (2023b)

5.2.4 Dependence on geomagnetic activity

Lastly the dependence of GPS LoL events and N_e fluctuations with values of $\gamma(2)$ and RODI inside the ellipse of Figure 5.14 on geomagnetic activity is investigated using the AE index (Davis and Sugiura, 1966). For more details about this index, the reader may refer to Section 2.2. It was used to distinguish between two geomagnetic conditions in the dataset: quiet and disturbed. As a threshold between these two conditions, the 25^{th} percentile of the index's cumulative distribution was chosen. As it is possible to see in Figure 5.19, it corresponds to AE = 50 nT.

The results are displayed in Figure 5.20. The quiet distributions are shown in the left column,

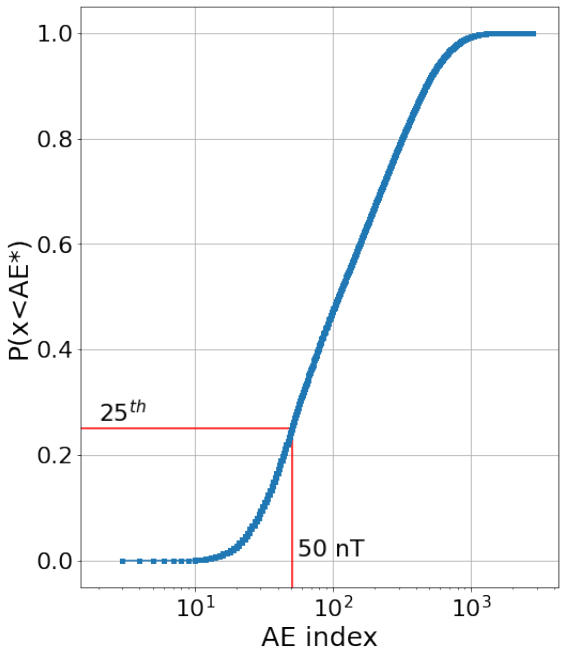

Figure 5.19: Cumulative distributions of AE index during the period from from July 15$^{\text{th}}$, 2014 to December 31$^{\text{st}}$, 2017, with red lines indicating the 25^{th} percentile and its relative value in nT.

while the disturbed distributions are shown on the right. In this case, the two hemispheres are not separated. This is because, as shown in Figure 5.15, the Northern hemisphere presents fewer GPS LoL events, and separating them according to the aforementioned geomagnetic conditions makes it difficult to visualize the distribution, especially during quiet periods. As a result, the two hemispheres are considered together in order to better visualize the global impact of geomagnetic activity.

During geomagnetic disturbed periods, the area covered by the two data sets tends to be larger than that covered during quiet periods, reaching lower magnetic latitudes. The number of events increases dramatically in correspondence with the cusp and on the night side. Particularly on the night side, the region affected by both LoL events and plasma fluctuations with values of $\gamma(2)$ and RODI satisfying the ellipse criterion reaches $\sim |60°|$ of magnetic latitude between 21:00 and 03:00 MLT. With regard to this region, the MIT might play a role in the development of ionospheric irregularities and GPS LoL events. This structure lies typically between the footprints of the plasmapause/plasmaspheric boundary layer (Carpenter and Lemaire, 2004, Pierrard and Voiculescu, 2011) and the equatorward boundary of the auroral oval. It can have a significant impact on the propagation of radio signals and, consequently, on the GPS signal because of the resulting large density gradient characterizing the area. In addition, Aa et al. (2020) showed that the trough depth exhibits a clear increasing trend with increasing geomagnetic activity, as tracked by the Kp index value, similarly to what is found here for GPS LoL events and for N_e fluctuations that satisfy the ellipse's criterion. Anyway, this link should be further examined because the other MIT climatological dependencies reported by Aa et al. (2020) agree only partially with the ones of LoLs and N_e fluctuations distributions. However, the comparison is not straightforward because their analysis is done considering only quiet geomagnetic conditions when examining the dependencies of the MIT on magnetic coordinates, local season and solar activity.

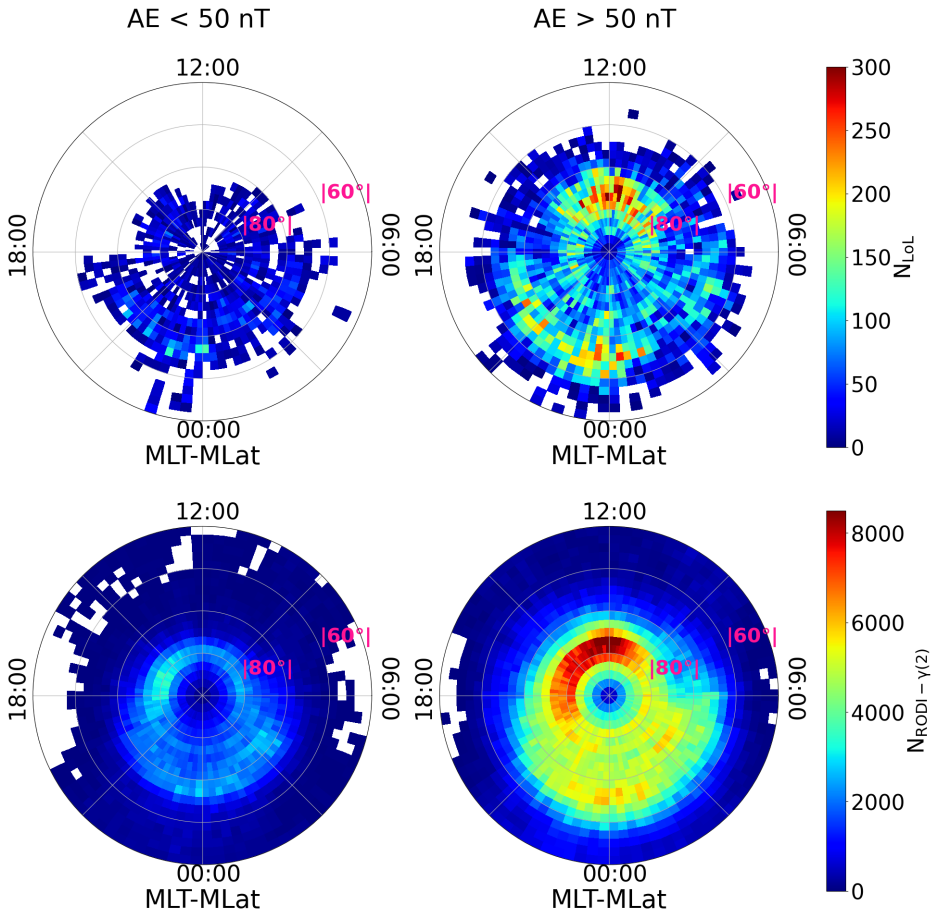

Figure 5.20: Comparison of the spatial distribution of GPS LoL events at mid and high latitudes ($|\text{MLat}| > 50°$) and the spatial distribution of N_e fluctuations with values for $\gamma(2)$ and RODI that are potentially capable of producing GPS LoL events during periods of quiet (left column) and disturbed (right column) geomagnetic activity conditions, respectively. In this case the datasets of both hemispheres have been joined. Credits: Lovati et al. (2023b)

Anyhow, the number of LoL events and the number of N_e fluctuations with a turbulent character are significantly higher during disturbed geomagnetic period, being respectively the 87% and 77% of the total number each type of event. This confirms their significance of in the framework of Space Weather, as also supported by the fact that solar activity appears to favor both LoL events as well as the formation of electron density irregularities that can trigger them. In fact, the ionospheric activity in polar, sub-auroral, and mid-latitude regions is primarily associated with geomagnetic storms and substorms, coronal mass ejections, and coronal holes (Cherniak et al., 2014) and the GPS LoL events, as well as the turbulent irregularities associated with them, seem to be no exception.

5.2.5 Dependence on IMF

A thorough discussion is required when analyzing the relationship of LoL events or electron density fluctuations that satisfy the ellipse's criterion with IMF and plasma conditions, especially when compared to other dependency scenarios. Connecting the conditions observed by Swarm satellites at a specific time and location to the solar wind and IMF conditions that might induce changes in the high-latitude ionospheric medium is not a straightforward task. The interest in the effect of the interplanetary conditions is attributable to the fact that, as explained in Section 1.4, the ionospheric irregularities at high-latitude are deeply influenced by the IMF's configuration. Consequently, the IMF's configuration may also influence the development and spatio-temporal distribution of LoL events. To investigate this relationship, the statistical dependence of GPS LoL events on IMF orientation is examined, taking into account the reconstructed ionospheric convection patterns obtained using SuperDARN model (see Section 2.3). IMF components for the period July 15, 2014 to December 31, 2021 were downloaded from OMNI dataset (see Section 2.2).

The left column of Figure 5.21 illustrates the distributions of the three IMF components during the considered time period. The resulting PDF for IMF B_y and B_z components is presented in the first row on the left. The distribution displays two symmetrical peaks with respect to both the $B_y = 0$ and $B_z = 0$ axes, corresponding to the almost exclusively eastward and westward directions (Haaland et al., 2007). Both are centered around $B_z = 0$, while $B_y \simeq \pm 2\ nT$. The joint PDF for IMF B_x and B_y components can be found in the second row on the left of Figure 5.21. The distribution displays two peaks roughly located on the bisector $B_y = -B_x$. This behavior can be explained by the spiral structure of the IMF, where a positive sign of its B_y component is often accompanied by a negative sign of the B_x component, and vice versa (Karpachev et al., 1995).

To assign appropriate values of the IMF components that could have triggered favorable ionospheric conditions for each GPS LoL event, it is necessary to consider the time delay required for the IMF to produce variations in the magnetospheric-ionospheric convection system. It is not straightforward to evaluate this delay, since it depends on various factors, such as the local time (Murr and Hughes, 2001), the solar wind velocity (Yu and Ridley, 2009), or the type of IMF turning (Dods et al., 2017, Ruohoniemi and Greenwald, 1996). The high-latitude ionospheric convection can be considered as a combination of two time-varying patterns: one resulting from the coupling of the solar wind and magnetosphere at the dayside magnetopause and the other from the release of energy from the geomagnetic tail. The flows caused by the dayside coupling are more prominent on the dayside and typically dominate there. These flows are associated with an expanding polar cap region and exhibit excitation and decay within approximately 10 minutes after the IMF changes direction to the South and North, respectively (Dods et al., 2017, Ruohoniemi and Greenwald, 1996). The flows resulting from the energy release in the tail, primarily during substorms, are most intense on the nightside, and are associated with a contracting polar cap boundary. These flows are triggered on a timescale of approximately one hour after the IMF turns South (Lockwood et al., 1990). Therefore, the time delay was chosen by selecting a value midway between the delay that characterizes MLT around noon (few minutes, Dods et al. (2017), Ruohoniemi et al. (1993)) and that of the nightside ($\sim$ 1 hour, Lockwood et al. (1990)). Consequently, to each LoL event is assigned an average IMF value based on the values obtained between 20 and 40 minutes before the event. This choice appears to be a reasonable timescale for the IMF to induce global effects in the high-latitude ionosphere, and it has previously been used for statistical studies (Coley and Heelis,

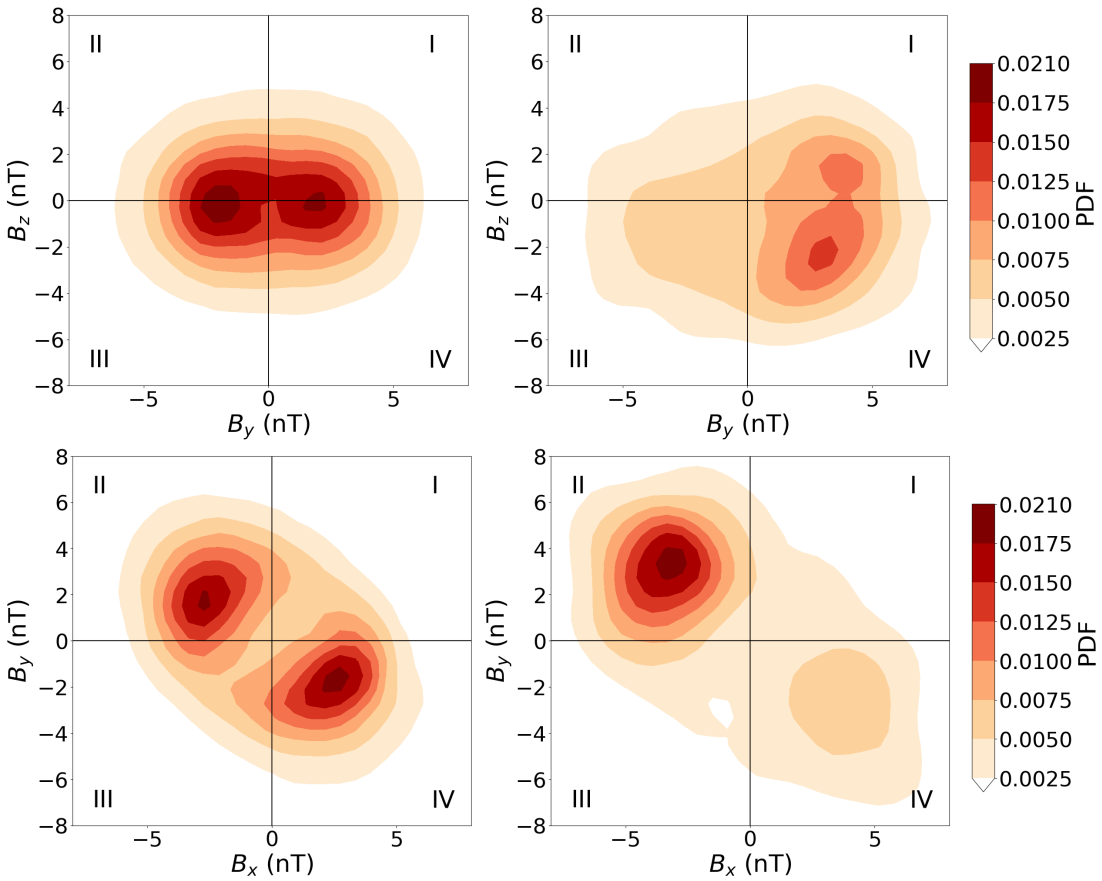

Figure 5.21: *First row:* on the left there is the joint PDF of B_y and B_z obtained from all OMNI data recorded from July 15, 2014 to December 31, 2021, and on the right is the joint PDF of B_y and B_z conditioned on the occurrence of LoL events. *Second row*: on the left there is the joint PDF of B_x and B_y obtained from all OMNI data recorded from July 15, 2014 to December 31, 2021, and on the right is the joint PDF of B_x and B_y conditioned on the occurrence of LoL events. Credits: Lovati et al. (2023c)

1998, Consolini et al., 2021, De Michelis et al., 2017, Jin et al., 2020, Moen et al., 2015).
Then, of each Swarm LoL in the dataset, only the first 5 seconds of the event are considered. This decision was forced by the need to be able to accurately identify the IMF orientations that might have led to the onset of LoL events in the ionosphere. The joint PDF of the B_y and B_z components, conditioned on the first 5 seconds of each GPS LoL event, is shown in the first row of the right column of Figure 5.21. The main peak is located at $B_y > 0$ and $B_z < 0$, suggesting that LoL events are more likely to occur during periods with a particular IMF orientation. Thus, a specific range of IMF clock-angle, which includes the IV sector in particular but also a portion of the I sector ($B_y > 0$, $B_z > 0$), results in favoring LoL events. The IV sector implies negative B_z values, which enhance magnetic reconnection at the low-latitude dayside magnetopause, strongly influencing plasma motions in the polar regions with the formation of the two large-scale convective cells. The B_y sign, on the other hand, influences the location and shape of the cells. The most advantageous condition appears to be $B_y > 0$. A similar trend is observed in the second row of the right column of Figure 5.21, where the joint PDF of B_x and B_y values, relative to the first five seconds of GPS LoL events, exhibits a single main peak for $B_y > 0$ and $B_x < 0$. These results demonstrate that the IMF patterns associated with GPS LoL events differ significantly from those of corresponding to the overall distribution.

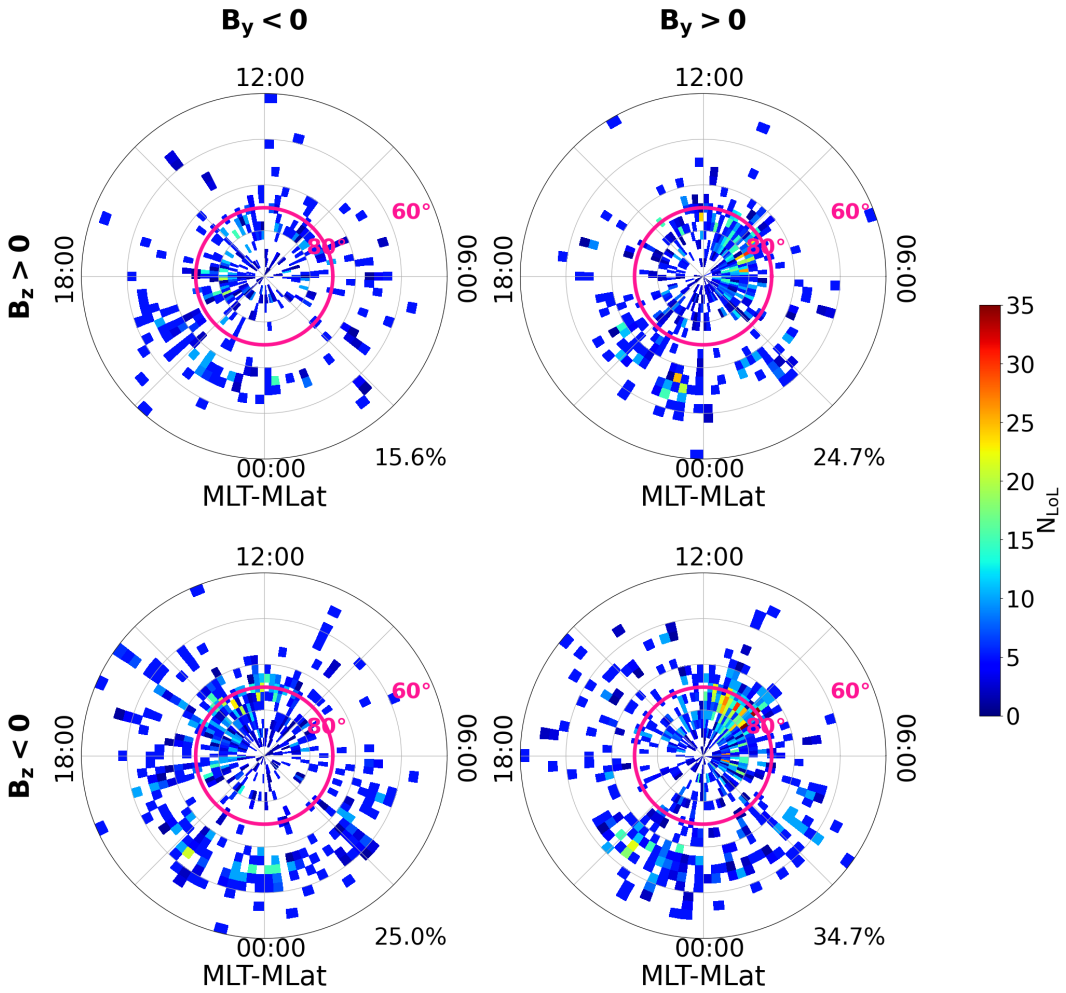

Figure 5.22: Polar view of LoL events spatial distribution for the Northern hemisphere (MLat $\geq 50°$), for four different IMF sectors in the GSM yz-plane. Maps have been drawn using data recorded onboard Swarm A and Swarm B from April 15, 2014 to December 31, 2021. MLat = 75° N can be distinguished by the magenta colored curve. Percentage at bottom right of each plot indicates the fraction of events characterized by that particular IMF configuration, with respect to the total number of events. Credits: Lovati et al. (2023c)

GPS LoL events location and IMF orientation in the B_y-B_z plane

The analysis, then, begin by mapping the LoL events as a function of four quadrant defining the IMF orientation in the GSM yz-plane. The goal is to investigate whether LoL event occurrences are influenced by IMF orientation, and to determine whether there exist any spatial pathways privileged for LoL occurrences, as a function of IMF orientation. Figure 5.22 depicts a polar view of these events in the Northern hemisphere. When the number of LoL events relative to each GSM yz-plane sector are compared, it is possible to see that the most populated sector has $B_y > 0$ and $B_z < 0$ (34.7%), while the sector with the most unfavorable conditions has $B_y < 0$ and $B_z > 0$ (15.6 %). The remaining two are nearly evenly populated ($\sim$ 25%). Upon examining the LoLs occurrence maximum relative to the cusp region, it shifts towards dawn or dusk depending on the sign of the IMF B_y component. This phenomenon is evident in both hemispheres, as will be shown below.
A magenta curve was added to each of the four polar maps in Figure 5.22, corresponding to the MLat value of 75°. This curve allows to distinguish two regions: one at higher latitude (MLat $\geq 75°$),

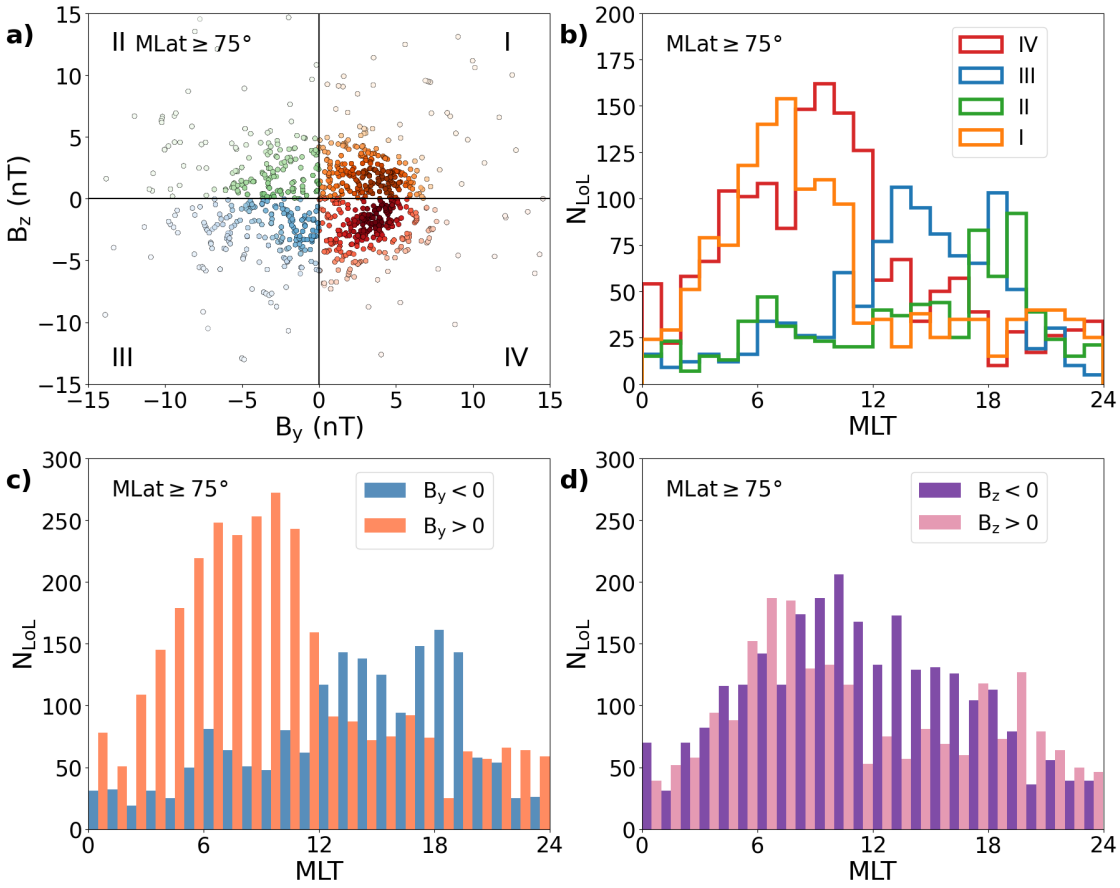

Figure 5.23: *a):* LoL events distribution at MLat $\geq 75°$ as a function of IMF B_y and B_z values. Different colors have been chosen for each sector and, within each sector, the intensity of the chosen color provides an indication of the number of events; *b):* LoL event distributions in each IMF sector as a function of MLT. The colors of the traces match those in the panel a). *c):* LoL event distributions as a function of MLT, according to the different sign of the IMF B_y component; *d):* LoL event distributions as a function of MLT, according to the different sign of the IMF B_z component. Credits: Lovati et al. (2023c)

which includes the polar cusp and polar region, and one at a lower latitude ($50° \leq$ MLat $< 75°$), which essentially includes the auroral oval. This distinction is helpful when comparing these findings to earlier research that looked at the auroral ovals and/or polar caps phenomena.

Figure 5.23 provides a detailed examination of GPS LoL events observed in the Northern hemisphere at high latitudes (MLat $\geq 75°$) as a function of IMF orientation on the GSM yz-plane. This Figure 5.23 is composed of four panels, each describing different characteristics of the LoLs.
Panel a) shows the distribution of LoL events as a function of B_y and B_z values. Different colors have been assigned to each sector and the intensity of each color corresponds to the number of events. As the color gets darker, the number of LoL events linked to a given pair of IMF values increases. The majority of LoL events tend to cluster in the sector with $B_z < 0$ and $B_y > 0$, although even the one with $B_z > 0$ and $B_y > 0$ has a significant number of events, as seen in Figures 5.21 and 5.22.
In panel b) of Figure 5.23, the number of LoLs recorded in each IMF sector varies with MLT. To more easily distinguish the trend of the number of LoLs with MLT for each IMF sector, the colors of the traces match those in panel a). According to the trends reported in panel b), the majority of LoL events takes place near the noon sector, confirming the cusp as the most affected region.

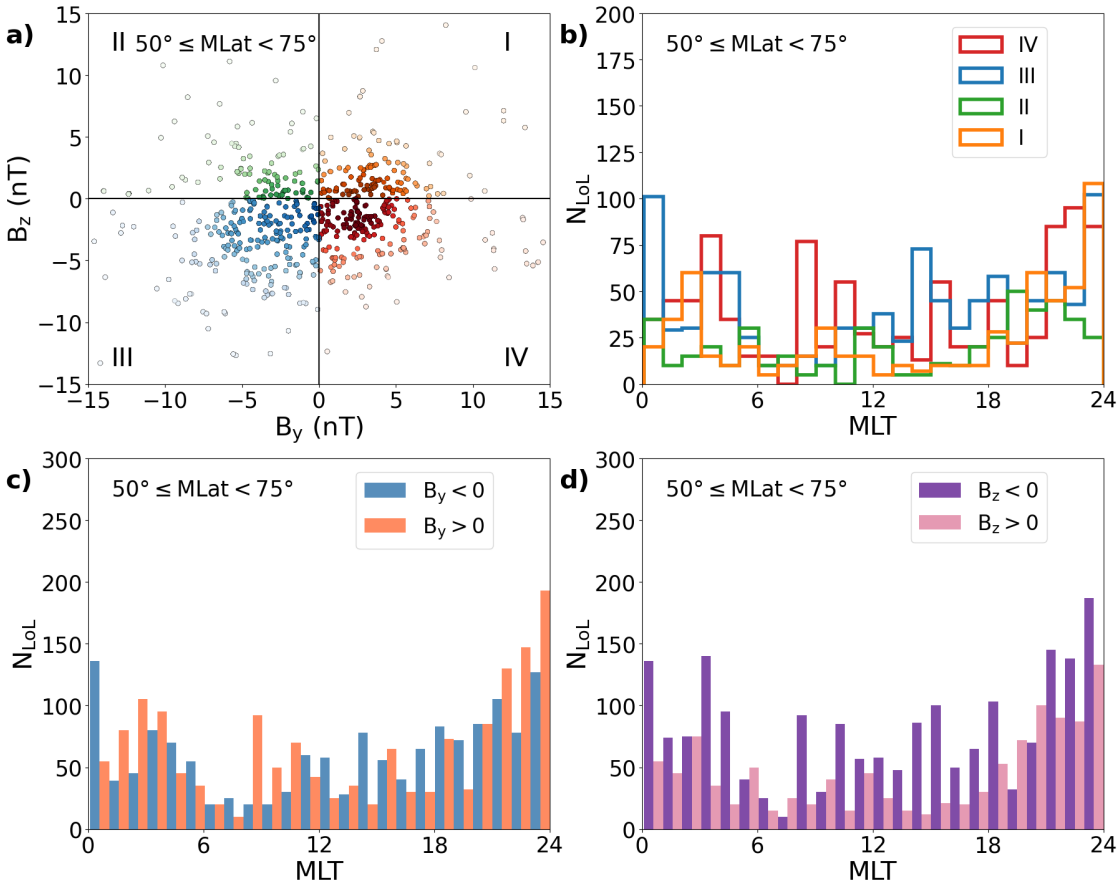

Figure 5.24: *a):* LoL events distribution at 50° ≤ MLat < 75° as a function of IMF B_y and B_z values. Different colors have been chosen for each sector and, within each sector, the intensity of the chosen color provides an indication of the number of events; *b):* LoL event distributions in each IMF sector as a function of MLT. The colors of the traces match those in the panel a). *c):* LoL event distributions as a function of MLT, according to the different sign of the IMF B_y component; *d):* LoL event distributions as a function of MLT, according to the different sign of the IMF B_z component. Credits: Lovati et al. (2023c)

The events distribution is not symmetrical with respect to midday, but there is an excess of events in sectors 06:00-12:00 MLT, dominated primarily by the conjunction with $B_y > 0$. This trend is more pronounced in panel c) of the same Figure, where the number of LoL events is reported as a function of the sign of IMF B_y component, once again as a function of MLT. When B_y component is positive, LoL events tend to be concentrated in the midnight-dawn-noon sector.
In panel d) of Figure 5.23, it is shown the trend of the number of LoL events as a function of MLT, considering only the sign of the B_z component. The plot clearly indicates a tendency for LoL events to cluster around midday and to be more numerous in the case of a negative B_z.

The same analysis was performed on the LoLs recorded in the auroral oval region (50° ≤ MLat < 75°). The results obtained from the analysis are presented in Figure 5.24. Panels a) and b) indicate that LoL events tend to occur more frequently for $B_z < 0$. In particular, they tend to occur more frequently at night, specifically between the hours after sunset and in the early morning (18:00-03:00). Additionally, several LoL events are also observed around noon. They are associated with events occurring on the cusp and extending to magnetic latitudes below the 75° threshold set for this analysis. Unlike the patterns observed at higher latitudes, the LoL events at these latitudes do not exhibit a preferred MLT path as a function of B_y or B_z signs.

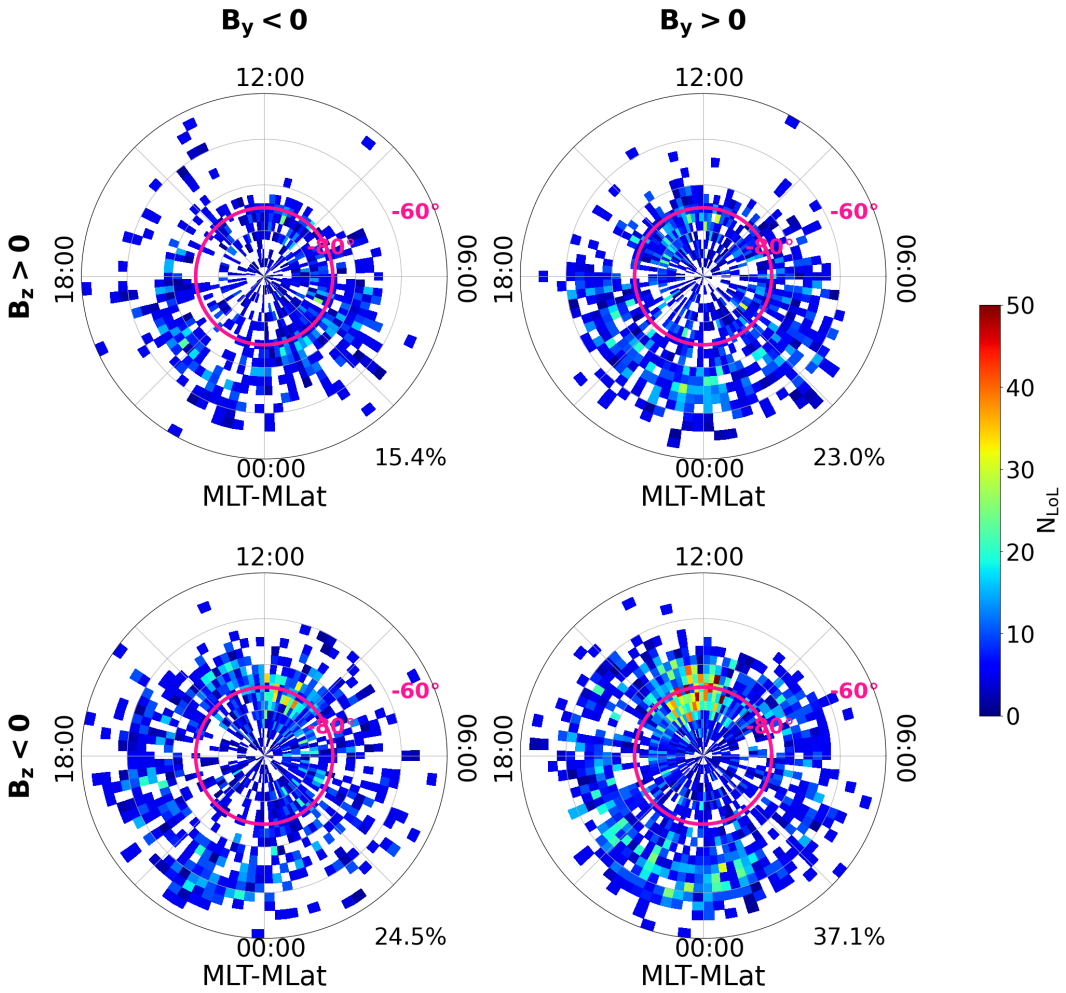

Figure 5.25: Polar view of LoL events spatial distribution for the Southern hemisphere in a QD magnetic latitude (MLat $\leq -50°$ N) and MLT reference frame, for four different IMF sectors in the GSM yz-plane. Maps have been drawn using data recorded onboard Swarm A and Swarm B from April 15, 2014 to December 31, 2021. MLat $= -75°$ N can be distinguished by the magenta colored curve. Percentage at bottom right of each plot indicates the fraction of events characterized by that particular IMF configuration, with respect to the total number of events. Credits: Lovati et al. (2023c)

The same study was performed in the Southern hemisphere, where there are more LoL events (see Figure 5.25). Here, the distributions are even clearer than those of the Northern Hemisphere. The shift of the concentration of events in the cusp region toward dawn or dusk depending on IMF B_y sign, previously mentioned, is also visible here. However, the shift is reversed compared to the one seen in Figure 5.22, because B_y's effect is mirrored in the two hemispheres. This feature is consistent with recent findings regarding the dependence of PCPs on the sign of the IMF B_y component (Spicher et al., 2017) and will be deepened in Section 5.2.6. Additionally, the maxima in the cusp are more distinct when $B_z < 0$. As in the case of the Northern hemisphere (see Figure 5.22), also here the majority of events take place when the B_z component is negative, which corresponds to period of enhanced magnetic reconnection at the dayside magnetopause. In this configuration of the IMF, the two cells pattern covers a larger area and descends to lower latitudes, resulting in a higher rate of open flux in the magnetosphere and more efficient convection of the high-latitude plasma. In fact, LoL events associated with $B_z < 0$ are distributed over a wider region, reaching lower magnetic latitudes than during positive B_z periods, both on the dayside and on the nightside.

Moreover, LoLs appear to be favored by a positive configuration of the B_y component, particularly between 21:00 and 01:00 MLT, at lower latitudes.

The just described features are evident in the results presented in Figures 5.26 and 5.27. The dependence of LoLs on IMF orientation in the Southern hemisphere are analyzed in the same way as in the Northern hemisphere, considering the events occurring at magnetic latitudes greater and less than $-75°$. Figure 5.26 presents a detailed analysis of the LoL events observed at high latitudes (MLat $\leq -75°$) in relation to the IMF orientation on the GSM yz-plane.
Panel a) shows the distribution of LoL events as a function of B_y and B_z values, indicating that the LoLs' majority cluster in the sector with $B_z < 0$ and $B_y > 0$.
In panel b), the number of LoLs recorded in each sector is plotted as a function of MLT, revealing that most of the events occur close to noon, confirming the cusp as the area with the highest number of LoLs. The distribution is not symmetric with respect to noon, with more events occurring in the time periods between 12:00 and 18:00 MLT, due to events characterized by $B_y > 0$.
This trend is more visible in panel c), where the number of LoL events is shown as a function of the IMF B_y sign, and then as a function of MLT. Here, LoL events tend to concentrate at high latitudes in the midnight-dusk-noon sector when the IMF B_y component is positive.
Finally, panel d) reports the trend of the number of LoL events as a function of the MLT is reported, taking only the sign of B_z into account. This plot clearly shows that LoL events tend to increase with negative values of B_z and to cluster around noon.

Figure 5.27 displays the LoL distributions in the area enclosed by the coordinates $-75° <$ MLat $\leq -50°$, yielding results similar to Figure 5.24. The early morning and late evening distribution peaks, which correspond to the events occurring in the night-side auroral oval, are even more distinct in this instance.
Panel c) of Figure 5.27 confirms that $B_y > 0$ is the most favorable condition for LoL occurrence in the nightside auroral oval region. Additionally, both B_z orientations contribute equally during the night; around noon, the peak corresponding to the cusp's lower latitudes, which is favored by negative B_z conditions, can be observed once again.
However, what can be notice from both Figure 5.24 and 5.27 is that the IMF B_y and B_z influence on LoLs' MLT coordinate in this MLat band is not straightforward. Excluding the events happening in the daily hours, which are dominated by the already described behavior followed by the cusp's lower part, the events occurring in the night sector do not show a clear MLT dependence on the IMF B_y and B_z components.

GPS LoL events location and IMF orientation in the B_x-B_y plane

The previous analysis was repeated, this time considering different IMF orientations in the GSM xy-plane. The goal is to investigate whether there is a specific effect associated with the IMF B_x component. Only the results for the Southern Hemisphere are shown here, where the greater number of events provides clearer insights into their characteristics. The results in the Northern Hemisphere, on the other hand, are comparable. Figure 5.28 represents the GPS LoL events spatial distribution at mid and high latitude, depending on the B_x and B_y signs. As one can see, the configurations with the highest number of GPS LoLs are those in which the signs of the B_x and B_y components are opposite. This reflects the anti-correlation between the two components, which was already observed when looking at their joint PDF (see Figure 5.21's second row) and that is due to

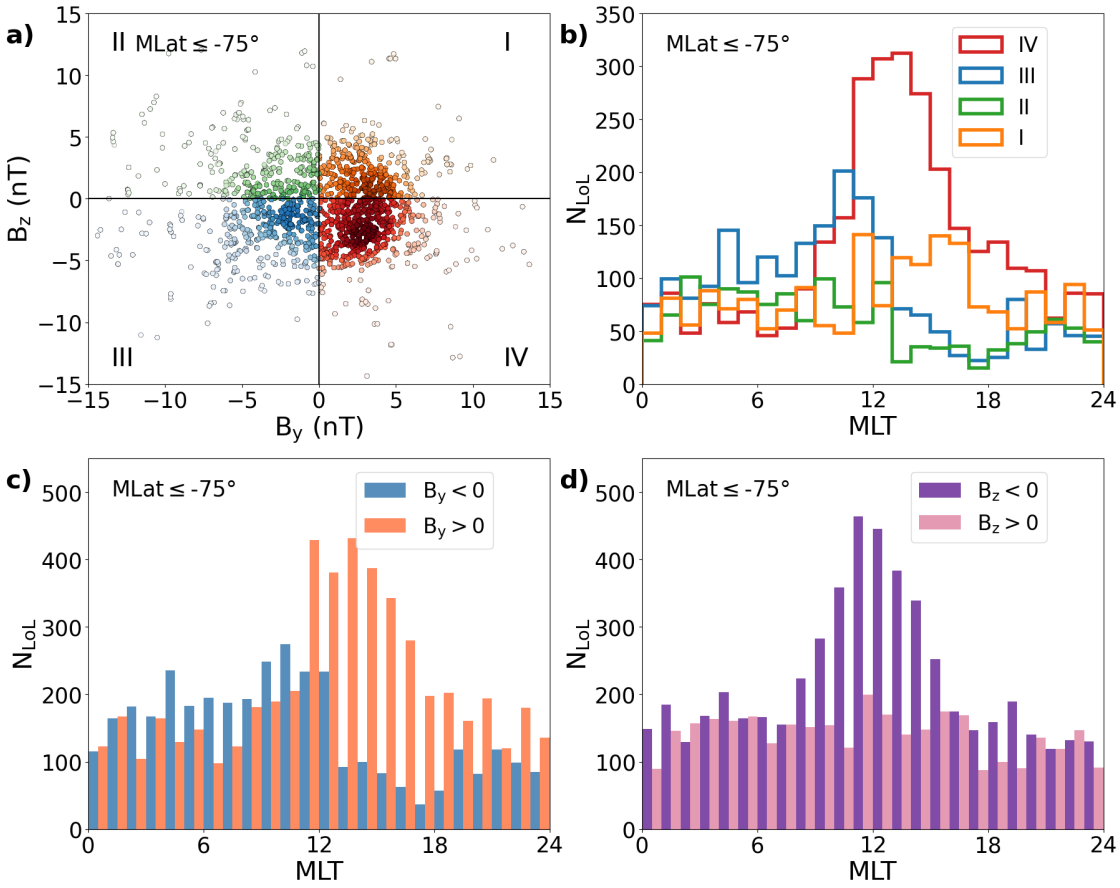

Figure 5.26: *a):* GPS LoL events distribution at MLat $\leq -75°$ as a function of IMF B_y and B_z values. Different colors have been chosen for each sector and, within each sector, the intensity of the chosen color provides an indication of the number of events; *b):* GPS LoL event distributions in each IMF sector as a function of MLT. The colors of the traces match those in the panel a). *c):* GPS LoL event distributions as a function of MLT, according to the different sign of the IMF B_y component; *d):* GPS LoL event distributions as a function of MLT, according to the different sign of the IMF B_z component. Credits: Lovati et al. (2023c)

the spiral structure of the IMF. The configuration with negative values of the B_x component and positive values of B_y is more favorable to the occurrence of GPS LoLs, hosting nearly half of the total number of events. The effect of the IMF B_x component on the spatial distribution of GPS LoLs appears to be similar to that of B_y in the GSM yz-plane. In fact, as shown for the Southern hemisphere in Figure 5.28 (results in the Northern hemisphere are comparable), the events in the cusp region shift from dawn to dusk when the B_x component changes from positive to negative values. However, there is a portion of LoL events for both the Northern (not displayed for brevity) and Southern hemispheres that is roughly 20% of the total and corresponds to the case where B_x and B_y have the same sign. Even though the number of events in this case is insufficient to result in distinct features on the MLat-MLT maps, they are significant enough to deserve further investigation.

The similarity between the effects of IMF B_x on the spatial distribution of GPS LoLs and those of IMF B_y, is visible also in Figure 5.29. This figure presents the LoL events observed at high latitudes (MLat $\leq -75°$), as a function of MLT and IMF orientation on the GSM xy-plane. Panel a) displays the distribution of LoL events as a function of B_x and B_y values, with most events

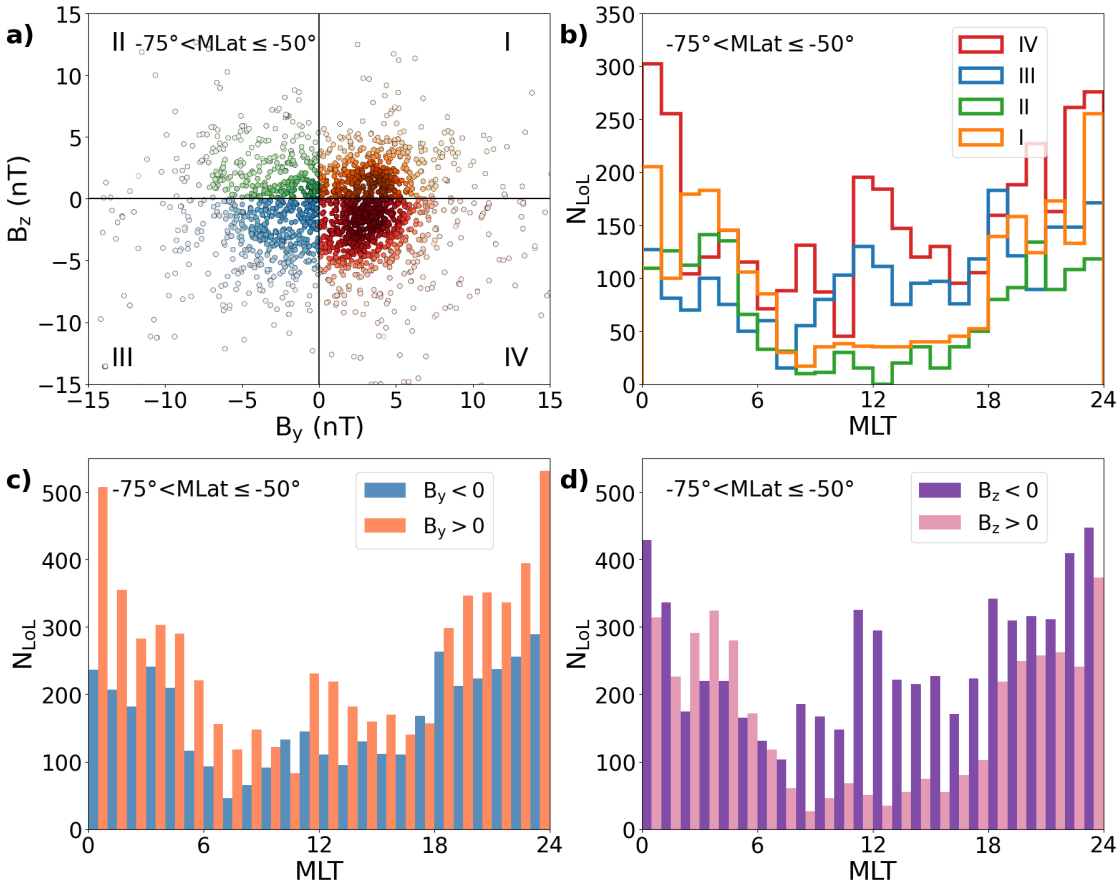

Figure 5.27: *a):* LoL events distribution at $-75° < \text{MLat} \leq -50°$ as a function of IMF B_y and B_z values. Different colors have been chosen for each sector and, within each sector, the intensity of the chosen color provides an indication of the number of events; *b):* LoL event distributions in each IMF sector as a function of MLT. The colors of the traces match those in the panel a). *c):* LoL event distributions as a function of MLT, according to the different sign of the IMF B_y component; *d):* LoL event distributions as a function of MLT, according to the different sign of the IMF B_z component. Credits: Lovati et al. (2023c)

concentrated in the II sector. The associated distribution of LoL events as a function of MLT is shown in green in panel b), and it reveals a peak shifted towards the afternoon hours rather than being centered around noon. The most intriguing findings are presented in panels c) and d) of the Figure, where the LoLs distribution is reported as a function of MLT taking into account the sign of the IMF B_x and B_y components, respectively. Comparing these two panels one can notice that the MLT distribution associated with $B_x < 0$ (in blue on the left) is very similar to the one relative to $B_y > 0$ (in pink on the right), and vice versa, confirming that these two IMF components seem to produce the same effect on the LoL events distribution, but associated with opposite signs. The results obtained for the latitude band $-75° < \text{MLat} \leq -50°$ are analogous and, therefore, not shown.

GPS LoLs' duration and IMF conditions

The possible correlation between the LoL event's duration and the related IMF conditions is investigated. To achieve this task, the cumulative distribution of LoLs' duration is examined, considering both the hemispheres together, and dividing the events into three different groups of increasing duration. The division into three groups was decided by taking into account the distinctive shape

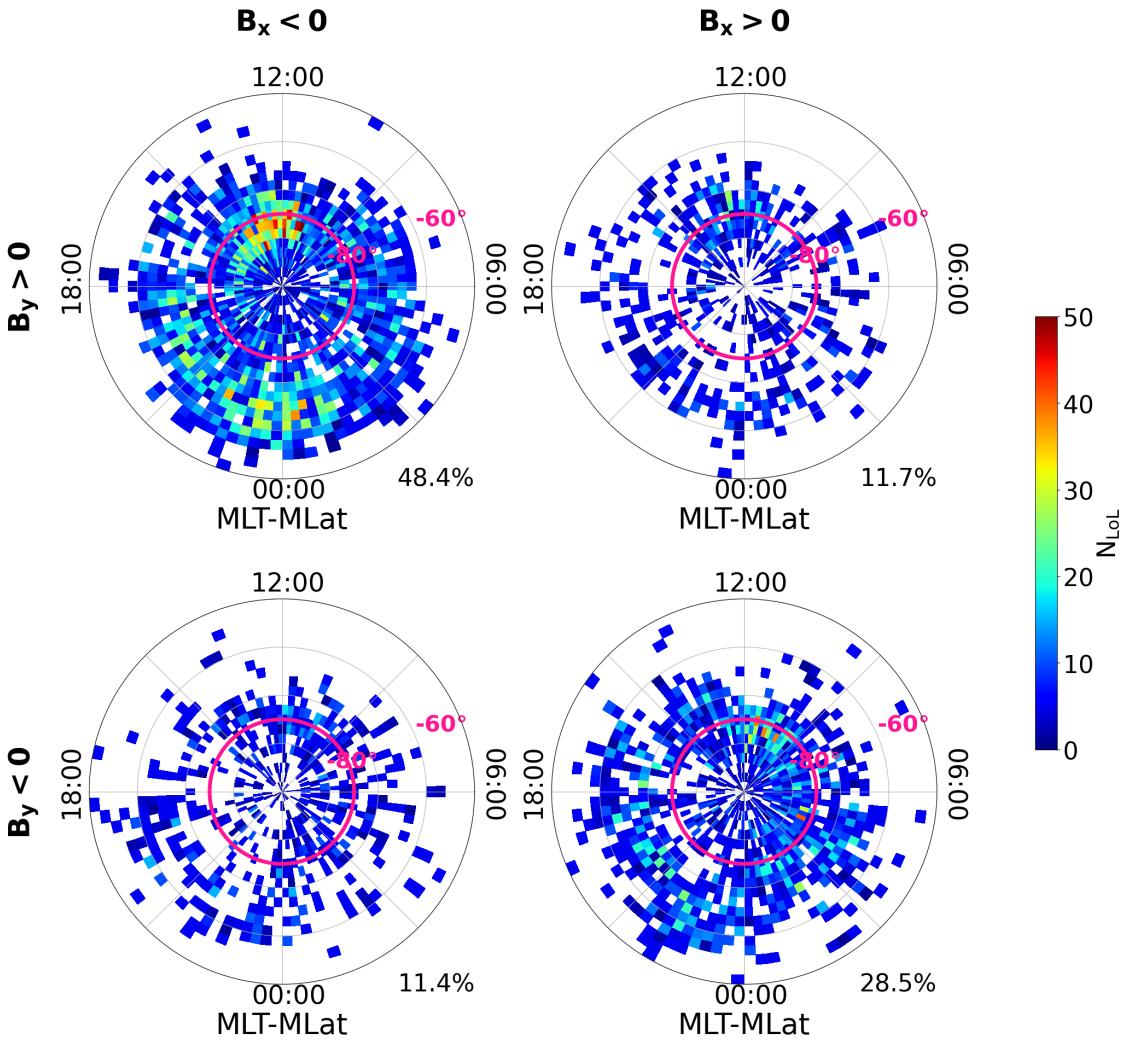

Figure 5.28: Polar view of LoL events spatial distribution for the Northern hemisphere (MLat $\geq 50°$ N), for four different IMF sectors in the GSM xy-plane. Maps have been drawn using data recorded onboard Swarm A and Swarm B from April 15, 2014 to December 31, 2021. MLat = 75° N can be distinguished by the magenta colored curve. Percentage at bottom right of each plot indicates the fraction of events characterized by that particular IMF configuration, with respect to the total number of events. Credits: Lovati et al. (2023c)

of the cumulative distribution (see Figure 5.30 on the left), which is characterized by an extremely high number of events with a time duration (ΔT) of about 18/19 seconds, as also found by Xiong et al. (2018). By setting two thresholds in the cumulative distribution at approximately 9% and 78%, the events are divided into those with $\Delta T < 18$ s, those with 18 s $\leq \Delta T \leq 19$ s, and those with $\Delta T > 19$ s.

Considering all the events that compose each group, their B_y and B_z average values were extracted, providing three representative vectors in the yz-plane. Figure 5.30 reports the cumulative distribution of LoL duration on the left, with the resulting IMF vectors in the yz-plane on the right. Vectors are colored according to the LoLs' group they refer to. In agreement with what is shown in the upper right plot of Figure 5.21, all three vectors in both hemispheres are located in the IV sector. It's worth noting that the green and the orange vectors, which represent the groups of events with the shortest and longest duration respectively, have similar module. The purple vector, representing approximately 70% of the events, which lasted 18 or 19 s, is associated with a lower IMF module

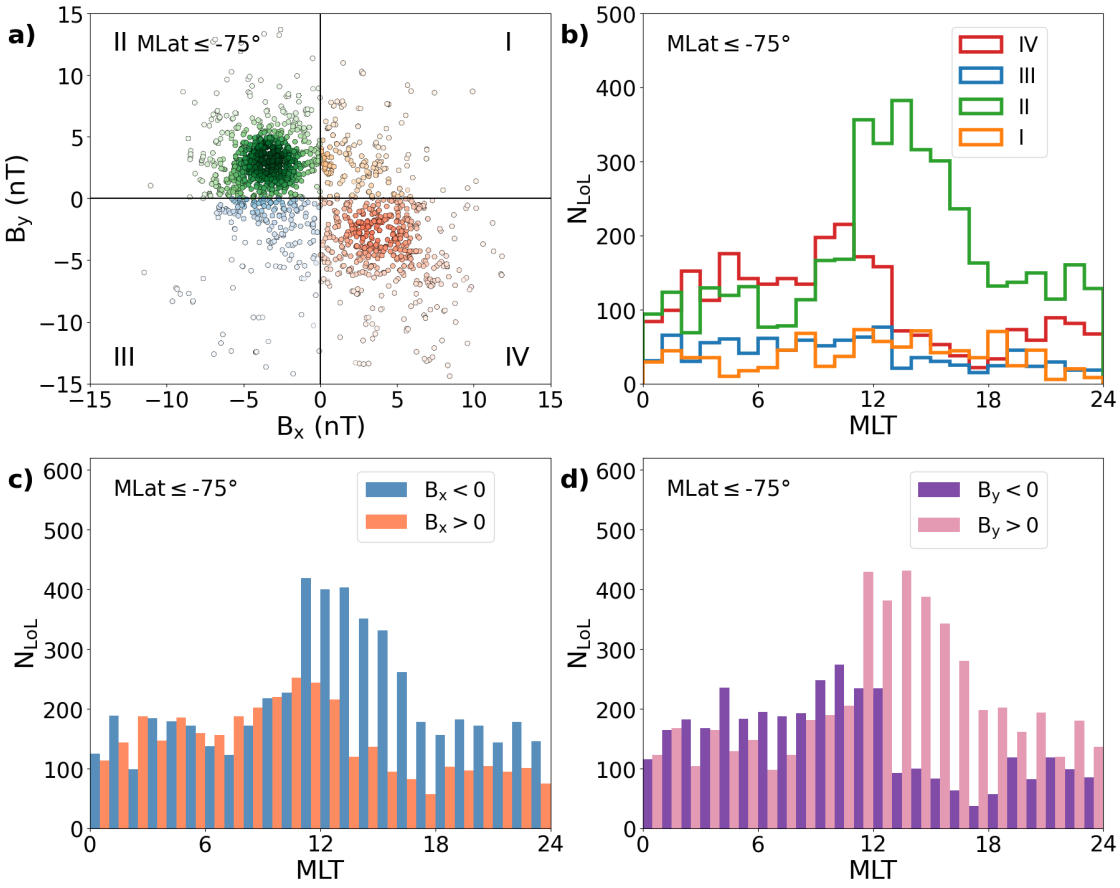

Figure 5.29: *a):* LoL events, occurred at MLat $\leq -75°$, are represented by circles colored according to the the IMF sector in GSM xy-plane they belong to. Darker color indicates higher grouping of points; *b):* LoL event distributions in each IMF sector as a function of MLT. The colors of the traces match those in the panel a) *c):* Distributions of LoL events as a function of MLT and with respect to the IMF B_x component sign; *d):* Distributions of LoL events as a function of MLT and with respect to the IMF B_y component sign

in the yz-plane.

It appears that there is not a clear correlation between the duration of LoL events and the IMF's strength, as the higher module is associated with LoLs of both extremely short and longer duration.

GPS LoL events location with respect to SuperDARN convection pattern

As demonstrated by the preceding analysis, IMF orientation, which controls plasma motions in the high latitude ionosphere, has an effect on LoL events. By using the electrostatic potential maps obtained from the empirical convection model, based on SuperDARN data (see Section 2.3 for more details), the spatial distribution of LoL events on magnetic latitude-MLT plane is compared to the high-latitude convective cells (Chisham et al., 2007). SuperDARN model, known as the CS10, can reproduce the mesoscale features of ionospheric convection patterns at high latitudes for a wide range of solar wind, IMF, and dipole tilt angle parameter values. Thus, for each of the four possible IMF orientations in the GSM yz-plane, an average pattern of the high-latitude ionospheric convection pattern was generated. Each pattern is obtained considering as input data the root mean squared values of B_z, B_y, and solar wind velocity obtained from OMNI data, in the periods associated with the occurrence of LoL events, in each selected IMF sector and setting the dipole tilt angle to $-10°$ for Northern hemisphere and $10°$ for Southern hemisphere. As seen in Section 5.2.2,

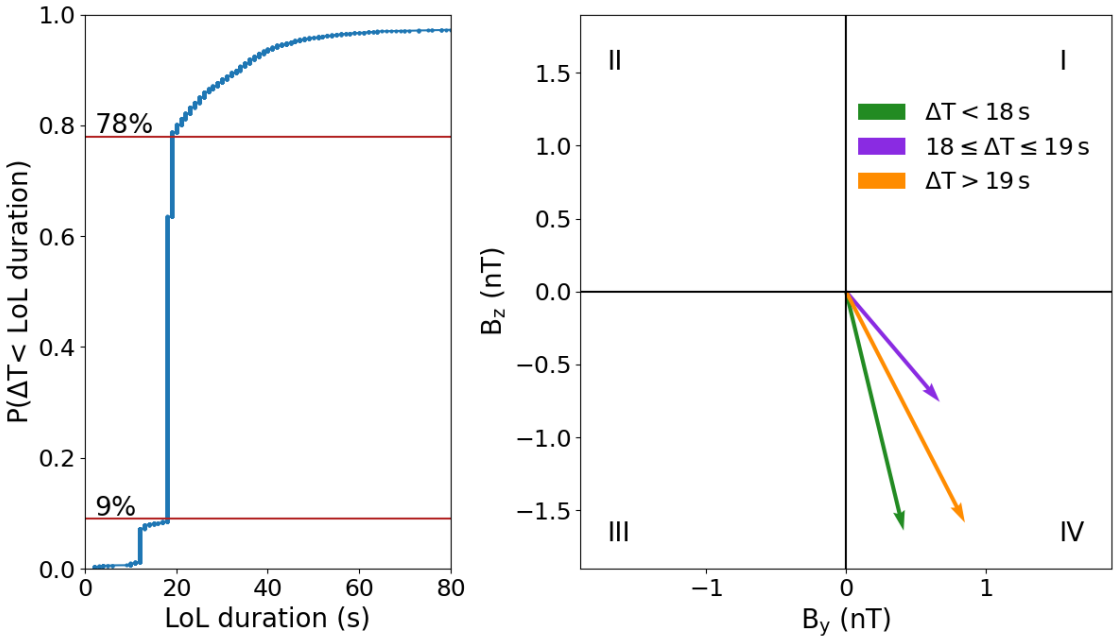

Figure 5.30: On the left is the cumulative distribution of LoL duration, with two horizontal red lines representing the two ΔT threshold values that classified LoLs into one of three groups. The mean IMF vector projections in the yz-plane are shown on the right. Each vector is constructed by taking into account the IMF values associated with a specific class of LoL events. The green vector represents all LoL events that last less than 18 seconds. The purple vector corresponds to events with 18 s $\leq \Delta T \leq$ 19 s. Finally, the orange vector is obtained by taking into account the longest events ($\Delta T >$ 19 s). This diagram combines events that occur in both hemispheres. Credits: Lovati et al. (2023c)

LoL events typically occur more frequently between September and May, thus they are centered on either local winter or local summer conditions, depending on the hemisphere, which is why these values for the dipole tilt angle were chosen.

Figure 5.31 displays the electrostatic potential maps generated in this way and the LoL events in the Northern hemisphere, on the magnetic latitude-MLT plane. It is interesting to note that the LoL events that occur at the cusp and over the polar cap preferentially appear in the space between the two cells, following the plasma motion trajectory toward the night-side, especially when the IMF B_y component is positive. The events that make up the night-side band, on the other hand, typically occur at the edge of convective cells, where the flow begins to turn back toward the Sun, moving from lower latitudes in the dawn and dusk sectors. A similar pattern can be seen in the Southern Hemisphere, as shown in Figure 5.32, where the just described behavior here is easier to be recognized when B_z is negative and thus the plasma convection is more effective.

This corroborate the link between LoL events occurrence and the regions with ionospheric irregularities primarily related to certain types of instabilities. These can be the gradient-drift instability, which arises from the interaction between plasma density gradients and electric fields, the Kelvin-Helmholtz instability, which arises from the shear between plasma flows with different velocities, and the current-convective instability, caused by a turbulent heating of the plasma due to the passage of a current. All of these instabilities typically take place in the cusp, in the auroral oval, and near the dawn and dusk terminators (Greenwald et al., 2002). These instabilities can also lead to the development of a turbulent regime in the plasma, supporting the possible relevant role of the irregularities identified thanks to RODI and $\gamma(2)$ in particular.

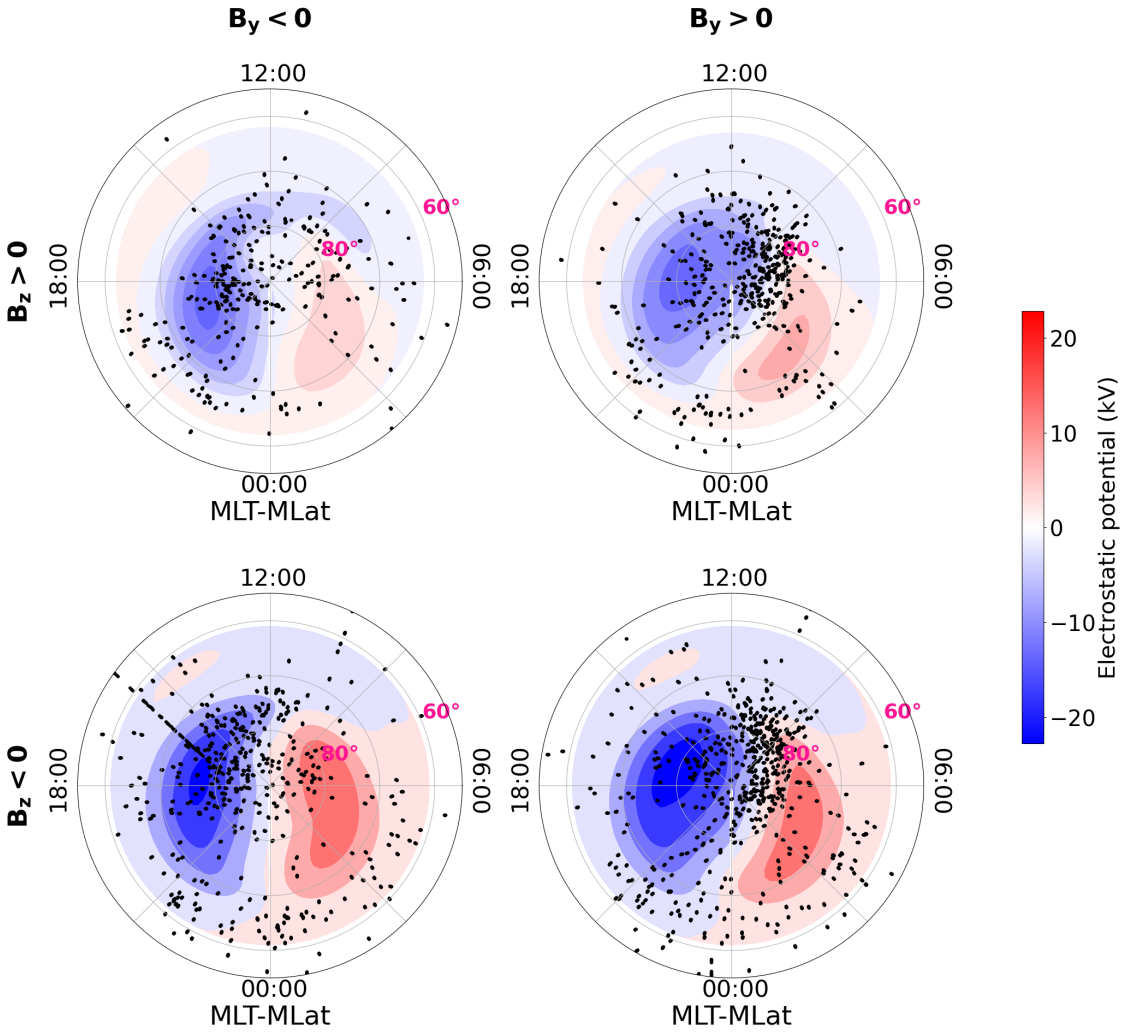

Figure 5.31: Comparison between GPS LoL events recorded by Swarm constellation and SuperDARN polar potential maps obtained using the statistical convection model CS10. Data are reported as a function of MLT and MLat in the Northern hemisphere according to different IMF orientations in the GSM yz-plane. Color is used to represent electrostatic potential using the scale on the right. A black dot is used to represent each LoL event that happened under that IMF conditions. Credits: Lovati et al. (2023c)

N_e fluctuations satisfying the ellipse's criterion location and IMF orientation in the B_y-B_z plane

As in the other cases where the dependencies on external factors are investigated, Figures 5.33 and 5.34 report the distributions of the N_e fluctuations satisfying the ellipse's criterion depending on the relative conditions of the IMF components in the GSM yz-plane, for the two hemispheres. Figure 5.33 illustrates the Northern hemisphere, and it should be compared with Figure 5.22. On the other hand, Figure 5.34 corresponds to the Southern hemisphere, with its counterpart for LoL events shown in Figure 5.25.

The first observation pertains to the distribution of event percentages across each yz-quadrant. In both hemispheres, fluctuations in electron density (N_e) with RODI and $\gamma(2)$ within the selection ellipse exhibit a more uniform distribution among the four regions of the yz-plane, in contrast to what is observed for LoL events. In the Northern hemisphere, the percentages are approximately evenly distributed, each close to 25%. In the Southern hemisphere, there is a slightly higher percentage in

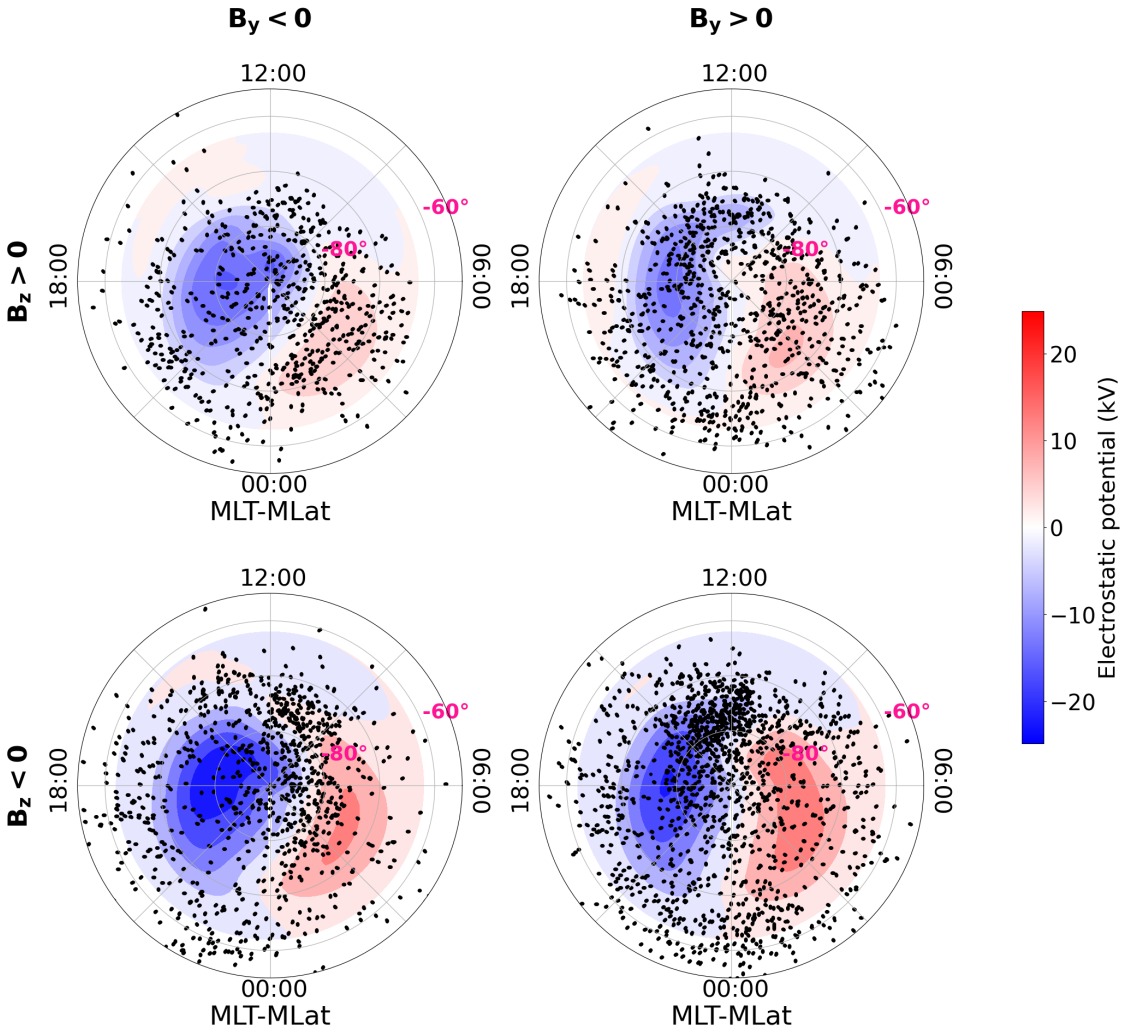

Figure 5.32: Comparison between GPS LoL events recorded by Swarm constellation and SuperDARN polar potential maps obtained using the statistical convection model CS10. Data are reported as a function of MLT and MLat in the Southern hemisphere according to different IMF orientations in the GSM yz-plane. Color is used to represent electrostatic potential using the scale on the right. A black dot is used to represent each LoL event that happened under that IMF conditions. Credits: Lovati et al. (2023c)

the fourth quadrant ($B_y > 0$ and $B_z < 0$), akin to the pattern seen in LoL events. However, this difference is not as pronounced as depicted in Figure 5.25.

Another notable distinction between the distribution of LoLs in the fourth quadrants and that of N_e fluctuations meeting the ellipse's criteria is the significant disparity in the positions of their maxima. For instance, upon comparing Figure 5.25 and Figure 5.34 it becomes evident that, especially in the two quadrants characterized by positive B_z (the first row of both figures), the maxima in the observed fluctuations of N_e do not align with similarly significant maxima in the LoL distribution. This contrast is particularly noticeable in the region on the nightside between 01:00 and 05:00 MLT, centered at magnetic latitude (MLat) approximately around $-75°$.
Similarly, this aspect is noticeable in the Northern hemisphere when examining the second quadrant ($B_y < 0$ and $B_z > 0$) in Figure 5.33. The peak at very high latitudes (MLat approximately around 80°), occurring between 15:00 and 19:00 MLT, is absent in the equivalent quadrant of Figure 5.22.

However, the differences found in the distributions of the two types of events by looking at the dependence on IMF orientation are very intriguing. The fact that the most significant deviations

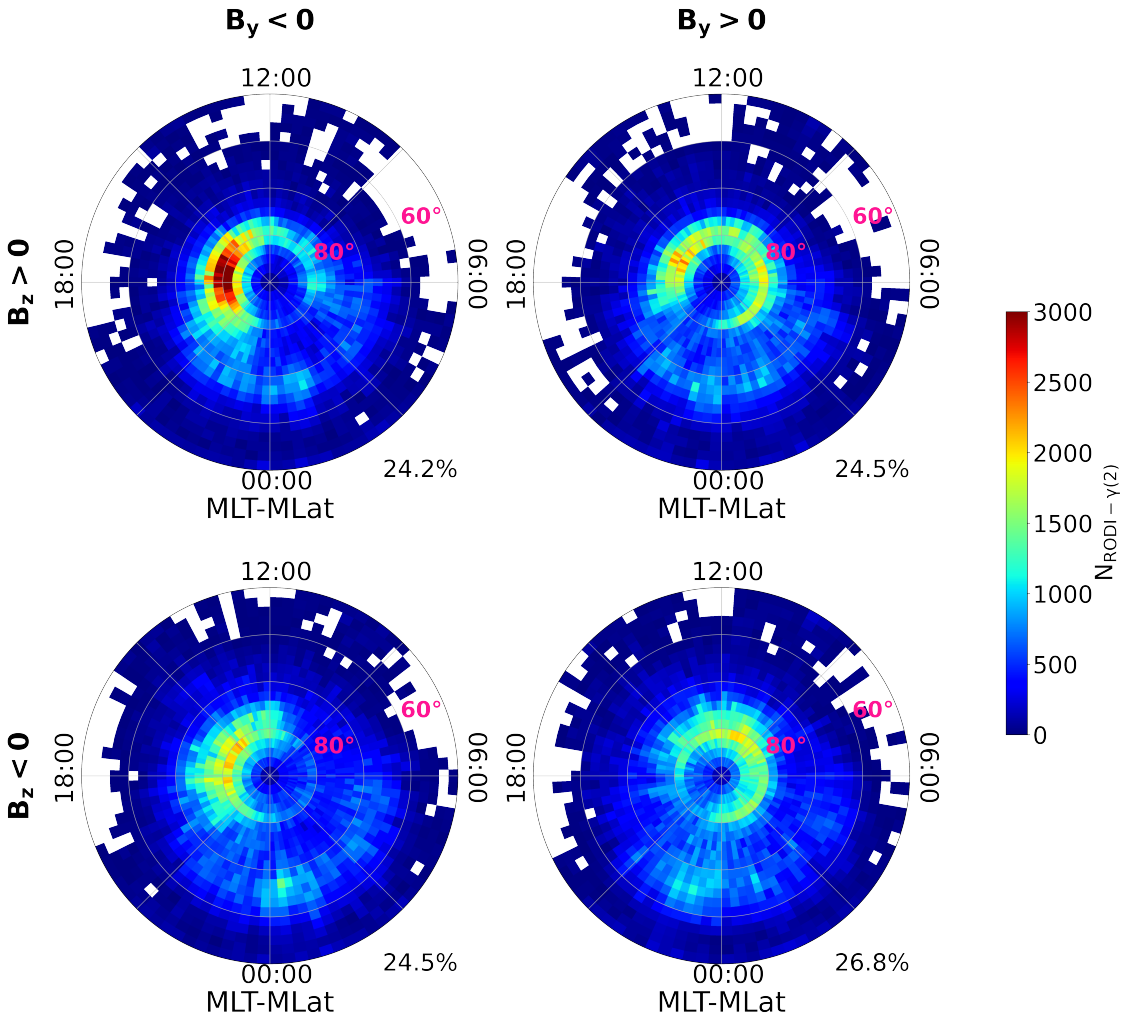

Figure 5.33: Polar view of the spatial distribution of N_e fluctuations as defined by $\gamma(2)$ and RODI values within the ellipse of Figure 5.14, for the Northern hemisphere (MLat $\geq 50°$ N) and for four different IMF sectors in the GSM xy-plane. Maps have been drawn using data recorded onboard Swarm A and Swarm B from April 15, 2014 to December 31, 2021. Percentage at bottom right of each plot indicates the fraction of events characterized by that particular IMF configuration, with respect to the total number of events.

are found in the quadrants relative to the more unfavorable conditions for LoLs, i.e. $B_z > 0$ and $B_Y < 0$, is encouraging because it may imply that the IMF can help providing the additional condition needed to better define the irregularities at the base of GPS LoL events. To better clarify this point, let's focus on the first comparison between LoLs and N_e fluctuations verifying the ellipse's criterion not conditioned to any external factors, provided in Figure 5.15. Here, the two anomalous maxima in the selected irregularities (see the second row) were already recognizable in both hemisphere, at approximately MLat$\simeq 80°$ and between 15:00 and 19:00 MLT in the North and centered at MLat$\simeq -75°$ and between 01:00 and 05:00 MLT in the South. These were unexpected and remained unexplained in the analysis. The studies on the dependence on the seasonal, solar and geomagnetic activity conditions didn't shed some lights on the origin of this discrepancy between LoLs and N_e fluctuations defined by $\gamma(2)$ and RODI values within the ellipse of Figure 5.14. Finally, when examining the categorization of events within the four quadrants of the IMF yz-components plane, it becomes apparent that the prominent maxima found in the distribution of N_e fluctuations are largely confined to sectors less associated with LoL events. Therefore, integrating information

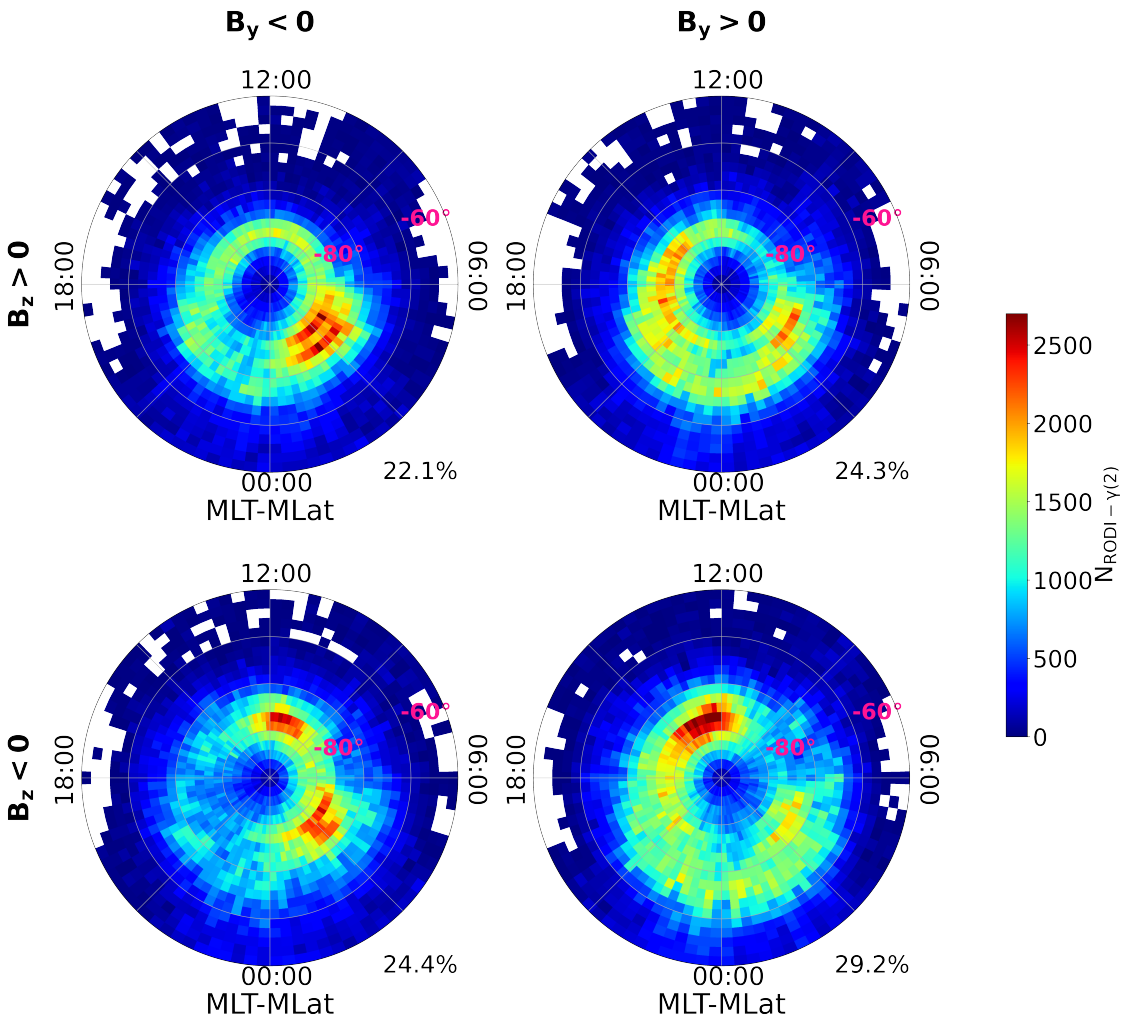

Figure 5.34: Polar view of the spatial distribution of N_e fluctuations as defined by $\gamma(2)$ and RODI values within the ellipse of Figure 5.14, for the Southern hemisphere (MLat $\leq -50°$ N) and for four different IMF sectors in the GSM xy-plane. Maps have been drawn using data recorded onboard Swarm A and Swarm B from April 15, 2014 to December 31, 2021. Percentage at bottom right of each plot indicates the fraction of events characterized by that particular IMF configuration, with respect to the total number of events.

about the IMF orientation into the selection process for identifying N_e fluctuations can prove to be beneficial in eliminating these maxima. This, in turn, contributes to a more precise delineation of irregularities that can serve as proxies for GPS LoL events.

5.2.6 GPS LoL events and Polar Cap Patches

PCPs are a significant type of plasma density irregularity seen at high latitudes. They are plasma density enhancements, probably caused by the segmentation of the TOI, whose triggering mechanism is anyhow still debated (Clausen and Moen, 2015). Once formed, plasma convection transports them over the polar cap. When PCPs are sorted by IMF B_y sign, their spatial distribution is characterized by a dawn-dusk asymmetry, with a higher number found in the Northern postnoon and prenoon sectors for negative and positive IMF B_y components, respectively. The phenomenon has an interhemispheric asymmetry (Spicher et al., 2017). This feature is consistent with the findings presented in Section 5.2.5, regarding the dependence of LoLs and the IMF orientation.
The strong correlation between the characteristics of PCPs and LoL events suggests that these plasma density irregularities may be at the origin of a part of the high-latitude LoL events.
This hypothesis is supported also by Cherniak and Zakharenkova (2016) and Xiong et al. (2019), who both investigated the effect of PCPs formed during the 2015 St. Patrick's Day storm on the GPS receivers onboard Swarm A and B. They discovered that both satellites lost contact with several GPSs while crossing different patches. In particular, Xiong et al. (2019) investigated why Swarm B lost GPS signal on all eight channels, while Swarm A only on four, despite passing through PCPs with comparable magnitudes of dense plasma and taking into account that satellites at lower altitudes are typically more affected by LoL events. The impact on GPS signal, according to the provided explanation, is also dependent on where the PCPs are located. Swarm B encountered patches near the cusp, where they become more structured and are accompanied by a number of instabilities. Patches become less organized and have less impact on the GPS signal after the polar cap's plasma convection. In fact, plasma density irregularities can travel for hours and over long distances with their names varying depending on where they are observed. Plasma density enhancement occurring within the polar cap are called PCPs, otherwise, they are referred to as auroral blobs (Jin et al., 2019). This because of the different mechanisms that may be in charge of their generation and development.
Furthermore, the comprehensive statistical analysis of PCPs based on approximately 3.5 years of Swarm data, as conducted in the study by Tozzi et al. (2023), unequivocally reveals distinctive features of these structures when contrasted with the surrounding environment. These features encompass electron density fluctuations exhibiting a steeper energy spectrum, which can be associated with the presence of gradient drift instability and Kelvin-Helmholtz instability. Additionally, PCPs exhibit higher values of RODI, signifying larger density fluctuations. Notably, these characteristics are prevalent in both hemispheres and tend to become more prominent with increasing levels of geomagnetic activity.

Given the many similarities between LoLs and PCPs behaviors, as well as the previously identified concomitant events, it was decided to investigate their relationship. This to see the impact of PCPs on GNSS and to investigate if they could be one of the high-latitude irregularities at the base of LoLs.

The analysis was conducted on LoL events recorded by Swarm A during the 3.5-year interval, from July 16, 2014 to February 28, 2018. The decision to restrict the period with respect to the previous Sections, was done because of the non availability of the AE index during the entire time interval under study (see Section 2.2). This index was be necessary to investigate LoLs' and PCPs' characteristics for two levels of geomagnetic activity, as will be presented in Figure 5.37.

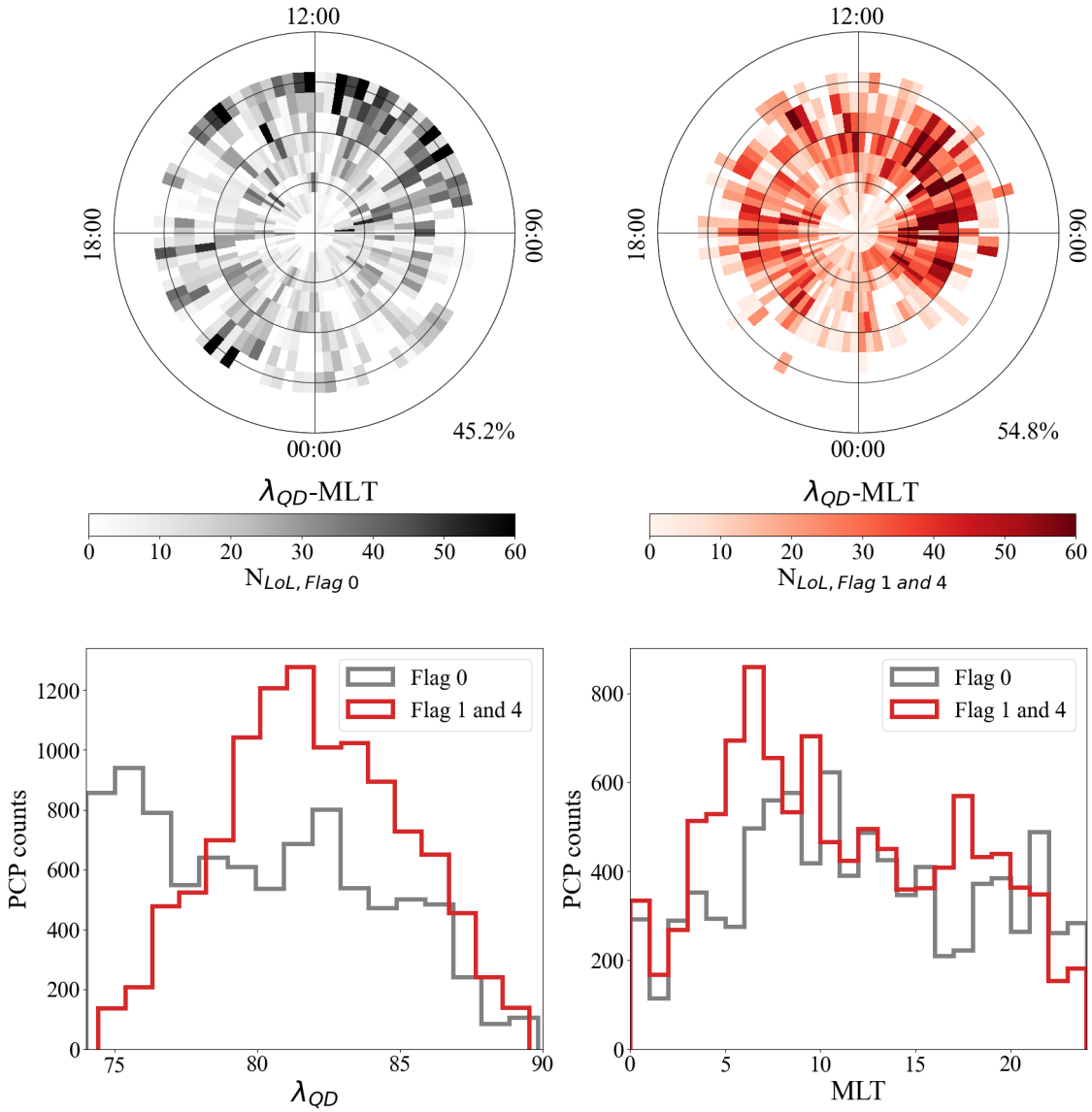

Figure 5.35: Northern Hemisphere. Top: spatial distribution of LoL events occurring in the presence (right) and absence (left) of PCPs as a function of magnetic latitude (λ_{QD}) and MLT. Circles are drawn at MLat of 70°, 75°, 80°, and 85°. The percentage at the bottom right of each plot indicates the percentage of LoLs coinciding and not coinciding with PCPs. Bottom: distribution of LoL events as a function of magnetic latitude (λ_{QD}) (left) and MLT (right). Gray indicates LoLs occurring in absence of PCPs, red indicates LoLs occurring in the presence of PCPs. Credits: analogue of Figure 10 of Tozzi et al. (2023)

As explained in Section 2.1, as part of Swarm's Level 2 products, there is the PCP flag, which indicates whether a Swarm satellite is passing through a PCP as it travels its orbit. Thanks to this flag it was possible to discriminate LoLs occurred simultaneously to PCPs from those occurred in absence of PCPs. GPS LoL events associated with Flag PCP equal to 1 or 4 are in the first group, while the ones associated with Flag PCP = 0 are in the second group (see Table 2.2).
Figure 5.35 displays the corresponding results for the Northern hemisphere. In detail, the upper plots represent LoL spatial distributions: on the left the number of LoLs occurred in absence of PCPs; on the right the number of LoLs occurred in presence of PCPs. The two bottom plots represent the histograms indicating how the number of LoLs occurring in presence (red) and in absence (gray) of PCPs varies with magnetic latitude (left) and MLT (right).

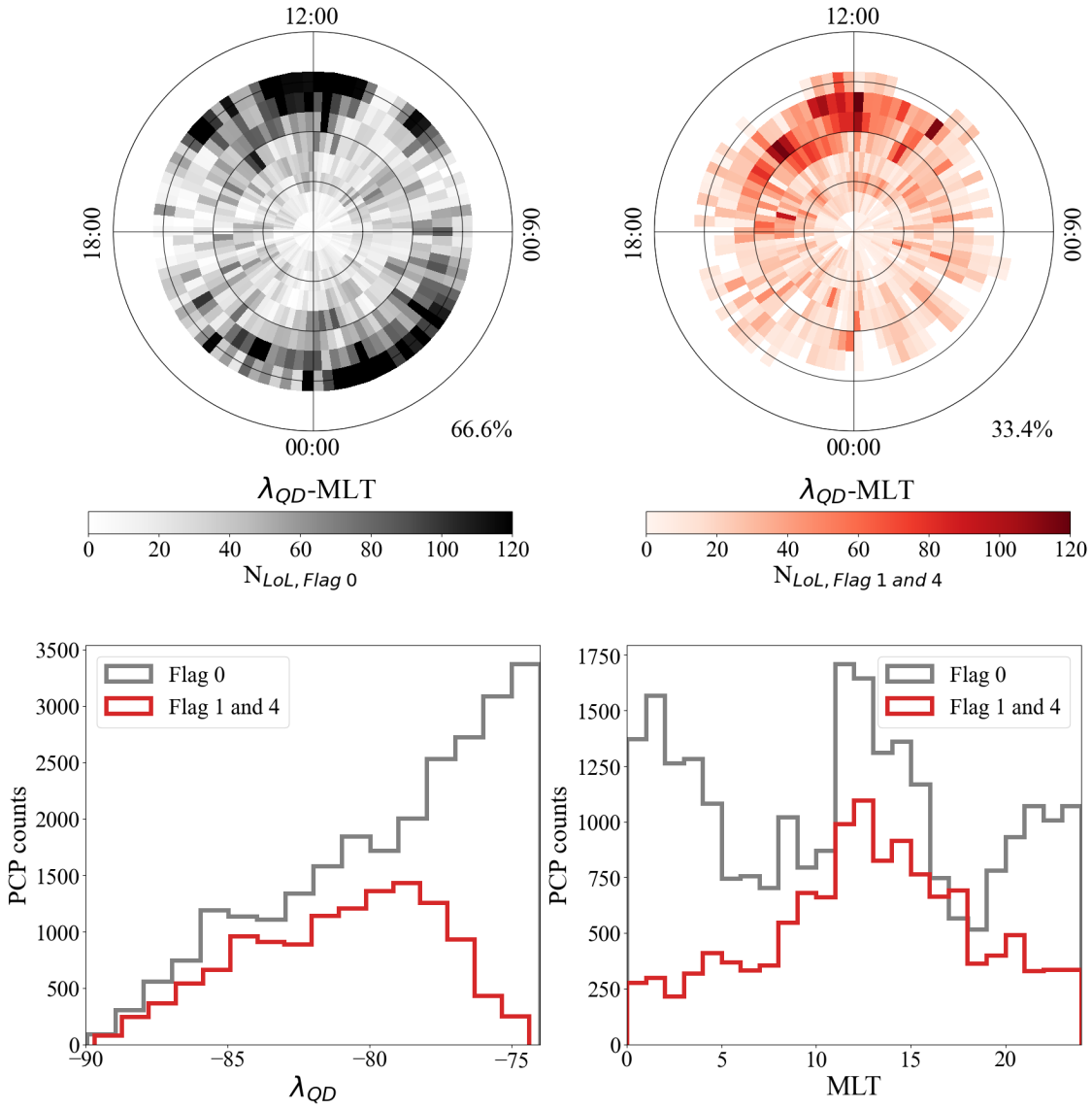

Figure 5.36: Southern Hemisphere. Top: spatial distribution of LoL events occurring in the presence (right) and absence (left) of PCPs as a function of magnetic latitude (λ_{QD}) and MLT. Circles are drawn at MLat of -70°, -75°, -80°, and -85°. The percentage at the bottom right of each plot indicates the percentage of LoLs coinciding and not coinciding with PCPs. Bottom: distribution of LoL events as a function of magnetic latitude (λ_{QD}) (left) and MLT (right). Gray indicates LoLs occurring in absence of PCPs, red indicates LoLs occurring in the presence of PCPs. Credits: analogue of Figure 11 of Tozzi et al. (2023)

As indicated by the percentage shown in the bottom right corner of each map in the first row of Figure 5.35, more than half of the events coincide with PCPs in this hemisphere. These events, indicated in red-scale on the right, exhibit a spatial distribution characterized by a peak in the range of MLat 80° ÷ 85°, mainly at MLTs between approximately 05:00 and 10:00 MLT. Another, less evident, region where LoLs occur more frequently in the presence of PCPs can be found around 18:00 MLT. LoLs that do not coincide with PCPs (grey-scale on the left) have a more uniform distribution.

The same analysis was conducted for the Southern hemisphere, as shown in Figure 5.36. In this case, the percentage of LoL events coinciding with PCPs is around one-third of the total number of events, therefore lower than in the Northern hemisphere. The plot on the top right of Figure 5.36,

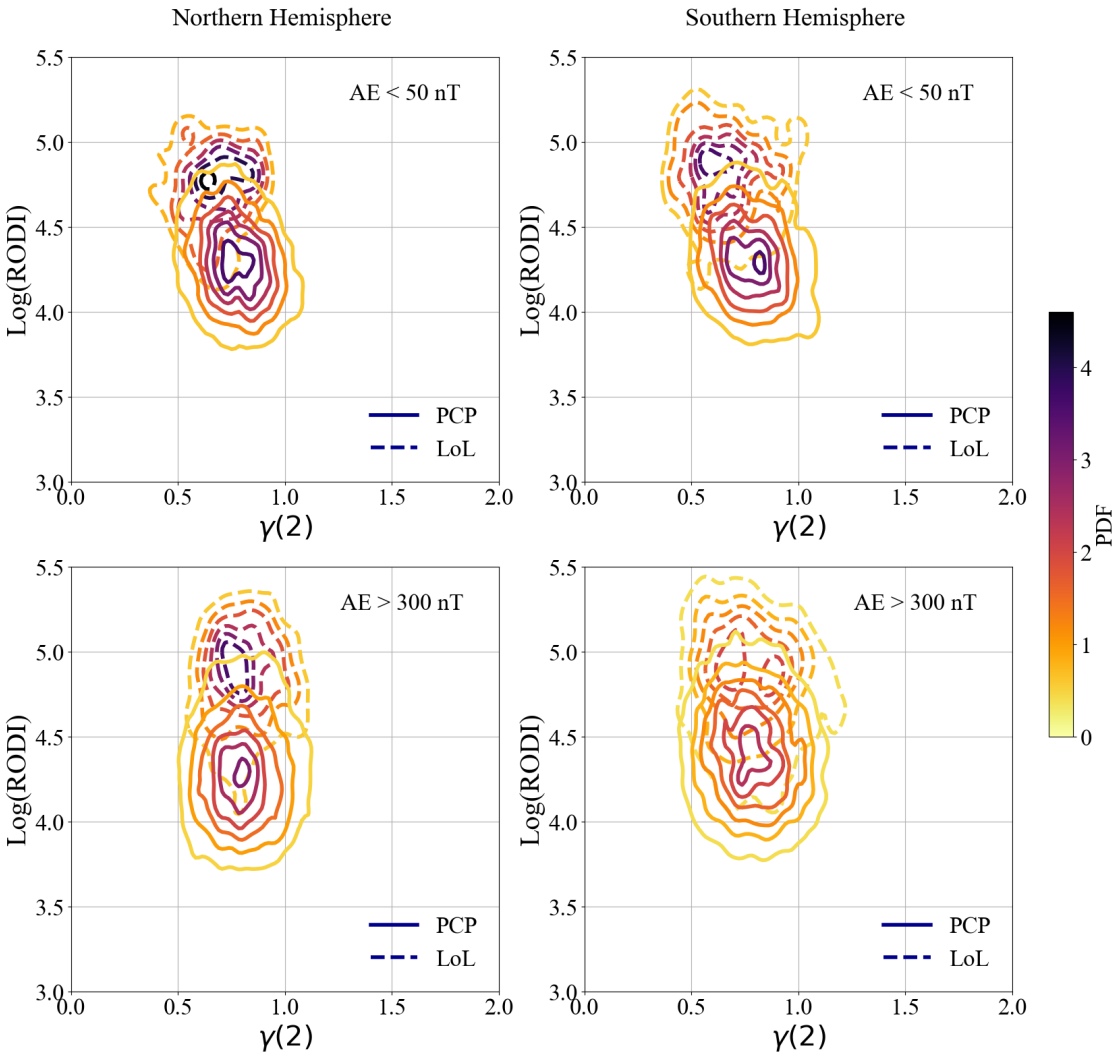

Figure 5.37: Joint probability distributions between RODI and $\gamma(2)$ associated with PCPs (solid contours) and LoL events (dashed contours), for two levels of geomagnetic activity (quiet on top and disturbed on bottom), in the Northern hemisphere (left) and Southern hemisphere (right). Credits: analogue of Figure 12 of Tozzi et al. (2023)

showing the spatial distribution of LoLs coinciding with PCPs (red-scale map), exhibits only one main peak in the dayside sector, between approximately 11:00 and 17:00 MLT. In the same MLT sector, there is also a peak in the distribution of LoL events that occurred in absence of PCPs (map on the top left in grey-scale), but it is shifted to lower magnetic latitudes compared to the peak in the distribution of LoL events coinciding with PCPs. Additionally, this distribution has another significant peak below approximately around 75° in the early morning hours (from 01:00 to 05:00 MLT). As a result, unlike in the Northern hemisphere, LoLs occurring in the absence of PCPs does not have the almost uniform character shown in Figure 5.35.

Finally, the joint distributions of RODI and $\gamma(2)$ values under the conditions of both LoL and PCP events are compared. Figure 5.37 shows the results for both hemispheres and two levels of geomagnetic activity. The upper plots display the distributions during quiet periods, i.e. when AE $<$ 50 nT, while the bottom plots report the distributions during disturbed conditions, when AE $>$ 300 nT. The level curves of the joint distribution conditioned to LoLs' occurrence (indicated by dashed contours) are shifted towards higher values of RODI when compared to those associated with

PCPs (indicated by solid contours). The displacement of the two distributions with respect to $\gamma(2)$ is not as pronounced as the displacement with respect to RODI, especially during disturbed periods. This is probably linked to the similar dynamical properties characterizing the two phenomena. The area where the two distributions overlap provides a rough indication of LoLs occurring in presence of PCPs. In fact, the Northern hemisphere has a larger superposed region, consistent with a higher coincidence rate of LoL events with PCPs than the Southern hemisphere. Precisely, during periods of low geomagnetic activity, 51.4% of LoL events coincide with PCPs; a percentage that increases to 57.4% for AE$>$ 300 nT. In contrast, for the Southern hemisphere, only 20.1% of all LoL events happening during AE$<$ 50 nT coincide with PCPs, a percentage which significantly increases to 45.7% during high geomagnetic activity periods.

The difference between the two hemispheres could be ascribed to the varying occurrence rate of PCPs. Interestingly, despite a lower occurrence of PCPs, the number of LoLs is higher in the Southern hemisphere (see Figure 5.15). Furthermore, the spatial distribution of LoL events that coincide with PCPs differs from that of events that do not coincide (see Figures 5.35 and 5.36). A possible explanation is that there are different types of irregularities at the base of LoLs occurring at high latitudes. The one associated with PCPs seems to play a very important role, being responsible of such an high portion of events, especially during disturbed geomagnetic periods and especially in the Northern hemisphere.

Overall, PCPs are confirmed as ionospheric irregularities that actively contribute to the loss of electromagnetic signals propagating through the ionosphere. However, a complete overlap between the presence of these irregularities and the occurrence of GPS LoLs is not observed. The comparison of joint distributions between RODI and $\gamma(2)$ for ionospheric irregularities associated with PCPs and LoL events (see Figure 5.37) highlights that only PCPs with significantly high RODI values have the potential to trigger a LoL event.

5.3 Building a GPS LoL hazard map

The primary purpose of the analysis presented in the present Chapter is to achieve a more precise description of the class of plasma density irregularities at the base of Swarm LoLs occurrences. An accurate definition of these N_e fluctuations, which characterize the ionospheric F-layer in which Swarm is flying, can serve as a proxy for GPS LoL events, assisting in the attempt of building a statistical model for assessing the hazard of this harmful effect for GNSS performance.

So far, what has been deduced is that the class of irregularities at the base of LoL events occupies a well-defined region within the $\gamma(2)$-RODI space, as depicted in Figure 5.14. This class is characterized by intense electron density fluctuations, as indicated by the remarkably high RODI value, and suggests the presence of a distinct turbulent regime, as inferred from the limited range of $\gamma(2)$ values.
After isolating this irregularities class using the ellipse shown in Figure 5.14 and defined by the coefficient in Table 5.1, its climatological dependencies were compared with those of LoLs events. It emerged that both types of events have the highest occurrence rate during the same seasons (see Section 5.2.2), they peak in the years of high solar activity (see Section 5.2.3), and the majority of them occur during geomagnetically disturbed times (see Section 5.2.4). Their distribution in magnetic latitude and MLT is very similar, with the major difference represented by the fact that LoL events are rare in comparison to the plasma fluctuations fulfilling the ellipse's criterion, being approximately 1 or 2 order of magnitude less in the same locations.
The dependence on the IMF orientation was also deepened. GPS LoL events appear to be favoured by a specific range of IMF clock-angle in the GSM yz-plane, involving $B_z < 0$ and $B_y > 0$ in particular. Dividing the LoLs distributions into quadrant of the yz-plane (see Figures 5.22, 5.23, 5.24, 5.25, 5.26 and 5.27) has an effect on the events' location in MLat-MLT. A clear example is the shift toward the morning or the evening hours of the maxima located in the cusp, depending on B_y sign. Moreover, LoLs seem to follow the structure of the two-cell convection pattern as depicted by SuperDARN model (see Figure 5.28 and 5.29). The electron density fluctuations characterized by RODI and $\gamma(2)$ values inside the ellipse are also affected by the signs of IMF B_y and B_z, as can be seen in Figure 5.33 and 5.34. However, there are some relevant differences with respect to the distributions into yz-quadrants of LoL events, which nevertheless could help in identifying a better definition of the ionospheric irregularities at the base of LoLs.

At this stage, the central question arises: do the identified parameters provide a sufficiently precise foundation for constructing a model to evaluate the hazard associated with LoLs? Or is it necessary to explore potential alternative mechanisms or external influences?
In order to attempt to answer these problems, it was decided to approach the subject as a *binary classification problem*. Section 3.3 has handled the subject.

More specifically, the aim is to determine whether a LoL event is presently occurring based on the available parameters. Dealing with rare events complicates this task due to the resulting imbalanced dataset. In fact, moments when there is not a LoL, hereafter referred to as 'label 0', are significantly more frequent than those moments characterized by the loss of GPS signal, which will now be denoted with label 1. The dataset utilized for this analysis was built first selecting all Swarm A and B data with $|\text{MLat}| \geq 50°$, for the period from July 15$^{\text{th}}$ 2014, when sTEC sampling rate was increased to 1 Hz (Van Den Ijssel et al., 2016), to December 31$^{\text{st}}$ 2015. The idea to reduce the usual

dataset to only 1,5 years was taken in order to focus on the period where GPS LoLs concentrate (see Figure 5.18) and thus decrease the disparity between data labeled as 0 with respect to the ones labeled as 1. Taking these measures, of all the selected instants in the dataset, the ones during which a LoL event is ongoing are only $0,44\%$ of the total. Therefore, even limiting the period under analysis this remains a very imbalanced problem.

However, as mentioned in Section 3.3, there are approaches to address this issue, for example making the model evaluate more the ability to correctly classify the less populated class, rather than the other during the training phase. In the following, this classification problem is treated using two different models, explained in Section 3.3, namely the Logistic Regression and the Decision Tree, which are available on *Scikit-learn*. Both algorithm have a *cost-sensitive* version, which is applicable specifying a *class weighting*. As a result, the weighting penalizes the model less for errors in labeling the majority class, while it penalizes the model more for errors regarding the correct labeling of the minority class (Brownlee, 2020b). Both the classical and cost-sensitive versions of Logistic Regression and Decision Tree models were attempted in the analysis. The results will be presented in the next Sections (5.3.1 and 5.3.2).

The two different classification models, with their two cost-sensitive and non cost-sensitive versions, were applied to five different sets of data, which followed the progression of the conceptual analysis carried out in the present Chapter. The period, the magnetic latitude selection and the two involved Swarm's satellite remain the same, what changes is the number of parameters, or features, selected in each case. The datasets are the following:

1. **Set A:** magnetic latitude, MLT, RODI, $\gamma(2)$;
2. **Set B:** magnetic latitude, MLT, RODI, $\gamma(2)$, day of the year (doy);
3. **Set C:** magnetic latitude, MLT, RODI, $\gamma(2)$, doy, F10.7;
4. **Set D:** magnetic latitude, MLT, RODI, $\gamma(2)$, doy, F10.7, AE;
5. **Set E:** magnetic latitude, MLT, RODI, $\gamma(2)$, doy, F10.7, AE, IMF B_y, IMF B_z, $v_{x,\,sw}$;

In fact, the first dataset, namely Set A, reflects the first raised matter, i.e. are RODI and $\gamma(2)$ enough to describe the electron density fluctuations underneath GPS LoL events? This issue was treated in Section 5.2.1. Then, with the goal of comparing the dependencies on external parameters of LoLs and of the irregularities identified with the ellipse's criterion, other parameters were added to the analysis: in Section 5.2.2 the doy was utilized, added here in Set B; in Section 5.2.3 the F10.7 tracked the level of solar activity and here was included in Set C; in Section 5.2.4 the AE index was employed to distinguish between quiet and disturbed geomagnetic periods and it was added to the previous parameters in Set D. Finally Set E contains also few interplanetary parameters, namely the IMF B_y and B_z components, widely employed in Section 5.2.5, as well as the x-component of the solar wind $v_{x,\,sm}$. This last parameters was added because of the potential relationship between LoLs and the high-latitude convection pattern. Since the electrostatic potential maps showed in Figures 5.28 and 5.29 are obtained from SuperDARN model, it was decided to take into consideration inside Set E all the input parameters necessary to obtain a SuperDARN convection map. These are precisely B_y, B_z, $v_{x,\,sw}$ and the tilt angle, but the contribute of the last one is already taken into account considering the seasonal period thanks to the doy.

	Predicted Positive	Predicted Negative	
Actual Positive	**TP** True Positive	**FN** False Negative	Sensitivity $\frac{TP}{(TP+FN)}$
Actual Negative	**FP** False Positive	**TN** True Negative	Specificity $\frac{TN}{(TN+FP)}$
	Precision $\frac{TP}{(TP+FP)}$	Negative Predictive Value $\frac{TN}{(TN+FN)}$	Accuracy $\frac{TP+TN}{(TP+TN+FP+FN)}$

Figure 5.38: Visual representation of a confusion matrix. It tabulates the actual values of a dataset against the values predicted by the considered model. The matrix consists of four key components: True Positives (correctly predicted positive instances), True Negatives (correctly predicted negative instances), False Positives (incorrectly predicted as positive), and False Negatives (incorrectly predicted as negative). In correspondence of each row and column there is the performance metrics that involves the terms of the same row or column. At the bottom right there is also the Accuracy, which is calculated using all the four key components. Credits: Medium.

The idea to proceed by adding one or few parameters at each step is connected to the necessity to understand how much they contribute and to see when the precision reached by the classification algorithm is satisfying. The purpose was to see if it was possible to label around 90% of the events properly. In fact, this could be a sufficiently high threshold, taking into account that a portion of the instants during which a LoL is ongoing (thus, labeled as 1) could be due to a technical time required for the GPS signal to reconnect, even if the satellite has already left the irregularity region and, thus, the in-situ measurements are no longer reflecting the characteristics of a plasma fluctuation that could have triggered the event.

Each one of the just described datasets was randomly divided into a training and a testing subsets, the first containing the 75% of data and the second the 25%. The first is necessary to train the model, while the second to test its performance on yet-unseen data. Therefore, after obtaining the model by feeding it with the training subset, its performance can be evaluated by seeing how it performs on the test set and using some tools like the confusion matrix, showed in Figure 5.38. It is a table, used in classification analysis, necessary to assess the performance of a ML model. It helps in understanding how well the model is classifying instances into different categories. The key components of a confusion matrix are:

- *True Positive (TP):* the instances where the model correctly predicted the positive class.
- *True Negative (TN):* the instances where the model correctly predicted the negative class.
- *False Positive (FP):* the instances where the model predicted the positive class, but it was actually the negative class. This is also known as a *Type I error*.
- *False Negative (FN):* the instances where the model predicted the negative class, but it was actually the positive class. This is also known as a *Type II error*.

These provide valuable insights into the model's accuracy and error types. In fact, from the confusion matrix, several important performance metrics can be derived. They are:

- *Accuracy:* The proportion of correctly classified instances out of the total instances.
- *Precision (Positive Predictive Value):* the proportion of TPs out of all positive predictions made by the model.
- *Recall or Sensitivity*: the proportion of TPs out of all actual positives in the dataset.
- *Specificity:* The proportion of TNs out of all actual negatives in the dataset.
- *Negative Predictive Value (NPV):* the proportion of TNs out of all instances predicted as negative by the model.
- *F1-Score:* The harmonic mean of precision and recall, providing a balance between the two metrics.

These metrics help in understanding the strengths and weaknesses of a classification model. For example, high Precision indicates low false positive rate, while high Recall indicates low false negative rate. The choice of metric to focus on depends on the specific problem and the relative costs of false positives and false negatives. In the case of the analysis carried out in this work, the actual negatives represent only a small fraction ($\sim 0.44\%$) of the actual positives. Therefore, using NPV and Specificity as performance metrics becomes crucial. This is because traditional metrics like Accuracy, Precision, Recall and F1 score can be misleading in this case. Indeed, the NPV focuses on the TNs, which are especially important in scenarios where identifying actual negatives is critical, like in this case where the actual negatives are precisely the LoLs.

Furthermore, given the imbalance of the dataset, reaching a high NPV indicates that the model is efficient at correctly identifying TNs, lowering the chance of false alarms. Even if the FNs are a significantly small fraction of the total actual positives, indicating a very high Recall or Sensitivity, this does not imply that they are also a small fraction of the total predicted negative values, due to the significant disproportion between the actual positives (here labeled as 0, i.e. no LoL) and negatives (here labeled as 1, i.e. a LoL is occurring). As a result, in this example, the goal is to achieve a high NPV rather than a high Recall.

Similarly, also Specificity becomes valuable in this context. It assists in understanding how well the model performs in correctly identifying the minority class (negatives), which is of higher interest compared to the performance on the majority class. In other words, in the presented case, it is more important for the models to learn to correctly identify LoLs, rather than to excel in learning conditions unrelated to them. Summarizing, in imbalanced datasets with many more actual positives than negatives, it is expected to easily reach very high Precision, Recall and Accuracy, but this doesn't mean that the model is successfully reaching the proposed goal. In this scenario, NPV and Specificity provide a more reliable assessment of a model's performance, since they offer insights into the model's ability to accurately classify negatives (ongoing LoLs), which are significantly underrepresented.
Below, you'll find a list of all the performance metrics for both models, with a higher emphasis placed on NPV and Specificity.

Sets:	A		B		C		D		E	
	NB	B	NB	B	NB	B	NB	B	NB	B
Accuracy	1.0	0.88	1.0	0.88	1.0	0.88	1.0	0.86	1.0	0.87
Precision	1.0	1.0	1.0	1.0	1.0	1.0	1.0	1.0	1.0	1.0
Recall	1.0	0.88	1.0	0.88	1.0	0.88	1.0	0.86	1.0	0.87
Specificity	0.06	0.79	0.06	0.79	0.06	0.80	0.06	0.80	0.06	0.80
NPV	0.40	0.03	0.40	0.03	0.35	0.03	0.35	0.02	0.36	0.03
F1 score	1.0	0.94	1.0	0.94	1.0	0.93	1.0	0.92	1.0	0.93

Table 5.2: Performance metrics for 10 Logistic regression models. Specifically for each set (indicated by the letters A, B, C, D, E) there are 2 models, one not balanced (NB) and one balanced (B).

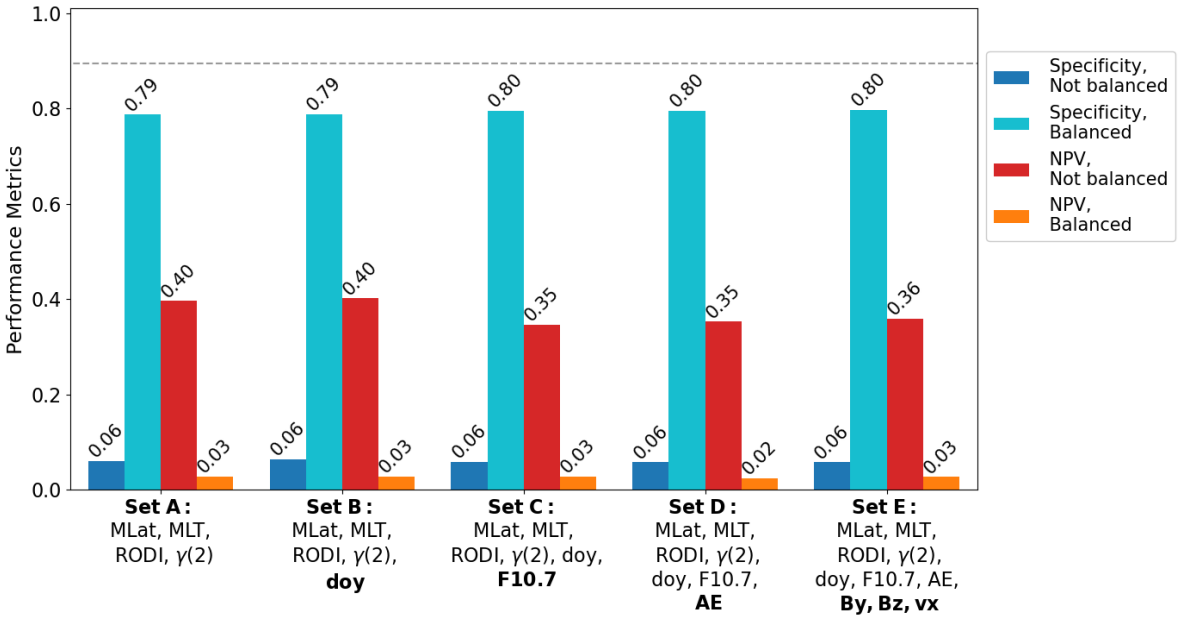

Figure 5.39: Specificity and NPV values for 10 different Logistic Regression models. Specifically, there are 2 models, one balanced and the other not balanced, for each one of the 5 sets of features, indicated along the x-axis. For each set the group of features is specified. The parameters in bold are the ones that have been added with respect to the previous set. The dashed line indicates the 0.9 threshold.

5.3.1 Logistic Regression

Firstly, the sets of data listed in the previous Section were utilized as input features for the Logistic Regression model, provided by Scikit-learn (see `https://scikit-learn.org/stable/modules/generated/sklearn.linear_model.LogisticRegression.html`) and described in Section 3.3.1. It was decided to employ Logistic Regression because it is one of the most simple and interpretable ML supervised classification models. However, it is not very suitable for imbalanced classification directly, but it can be modified to take the skewed distribution into account (Brownlee, 2020b). This can be done by specifying the *class_weight* hyperparameter of the class *sklearn.linear_model.LogisticRegression*. In particular, to obtain a cost-sensitive Logistic Regression model, the *class_weight* is set equal to *"balanced"* mode, which uses the values of the depended variable Y (in this case the LoL flag series) to automatically adjust weights inversely proportional to class frequencies in the input data. If *class_weight* is not specified, the two classes are supposed to have weight one.

Sets:	A		B		C		D		E	
	NB	B	NB	B	NB	B	NB	B	NB	B
Accuracy	1,0	1,0	1,0	1,0	1,0	1,0	1,0	1,0	1,0	1,0
Precision	1,0	1,0	1,0	1,0	1,0	1,0	1,0	1,0	1,0	1,0
Recall	1,0	1,0	1,0	1,0	1,0	1,0	1,0	1,0	1,0	1,0
Specificity	0,70	0,69	0,80	0,80	0,83	0,83	0,87	0,86	0,90	0,89
NPV	0,74	0,77	0,84	0,87	0,87	0,89	0,89	0,91	0,92	0,93
F1 score	1,0	1,0	1,0	1,0	1,0	1,0	1,0	1,0	1,0	1,0
Depth	44	53	42	54	38	51	39	59	45	63

Table 5.3: Performance metrics and tree's depth for 10 Decision Trees models. Specifically for each set (indicated by the letters A, B, C, D, E) there are 2 models, one not balanced (NB) and one balanced (B).

The performance metrics regarding all the attempts with the 5 sets and the not balanced (*class_ weight* = None) and balanced (*class_ weight* = "balanced") versions of the algorithm are listed in Table 5.2. As expected for imbalanced dataset, Accuracy, Precision, Recall and F1 score are very high for all sets and especially for the not balanced version. On the other hand, Specificity and NPV values are not satisfactory. To better visualize the models performance, these two metrics are represented graphically in Figure 5.39. As one can notice, for each set of data, the not balanced version of the Logistic Regression model produce a very low Specificity, always around 0.06, and a higher, but not yet satisfactory, level of the NPV, around 0.37. When considering the cost-sensitive version of the model (with balanced weights), the Specificity increases remarkably, reaching approximately 0.8, which is an encouraging value, but NPV drops dramatically to 0.03. It means that the FNs are far too many, and this is reflected also in the lowering of the Accuracy, the Recall and the F1 score, visible in Table 5.2, with respect to the not balanced case. Additionally, a significant aspects is that the values of the two relevant metrics do not change significantly adding more information, i.e. the performance does not improve for the sets with more features, actually, in some cases it gets slightly worse.

What can be deduced at the time is that: or the provided information is insufficient to predict GPS LoLs satisfactorily, or the Logistic Regression, balanced or not, is not a suitable model for the problem under consideration.

Part of the problem could be attributable to potential dependencies between the given variables. Logistic Regression works well with independent variables, as explained in Section 3.3.1. The features provided here as input may be interconnected to some extent. For instance, disturbed geomagnetic activity conditions, as tracked by the AE index and present in Set D and E, are associated with both high solar activity, and thus high F10.7 index, as well as a high rate of magnetic reconnection at the magnetopause, which is associated with large negative IMF B_z values. This may help to explain why performance metrics do not improve after the addiction of features that may be related in some way and to some degree. A subsequent trial was carried out using an alternative ML classification algorithm, namely the Decision Tree, in an effort to determine whether the poor performance is attributable to the inadequacy of the Logistic Regression model for this specific problem rather than the volume of available data.

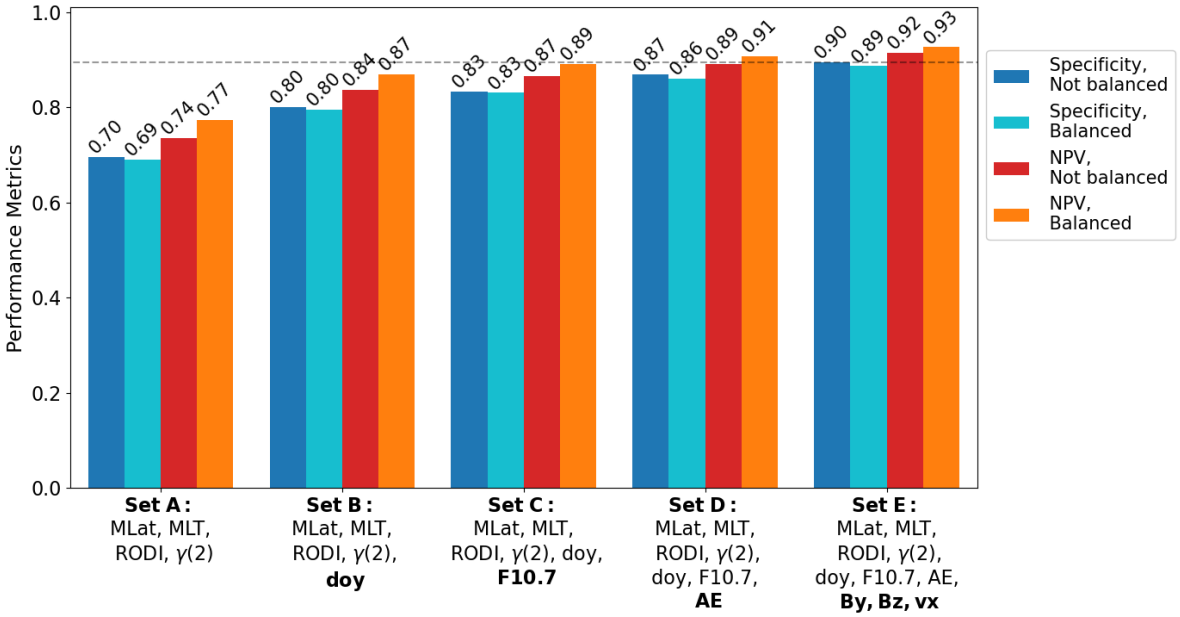

Figure 5.40: Specificity and NPV values for 10 different Decision Trees models. Specifically, there are 2 models, one balanced and the other not balanced, for each one of the 5 sets of features, indicated along the x-axis. For each set the group of features is specified. The parameters in bold are the ones that have been added with respect to the previous set. The dashed line indicates the 0.9 threshold.

5.3.2 Decision Trees

Even in this case, the 5 parameter sets, described in Section 5.3, were used to train 10 different Decision Tree models. Namely, each set has two relative models, one not balanced and the other balanced, thanks to the specification of the classes weights, as in the Logistic Regression case (see Section 5.3.1). The model is provided by Scikit-learn (`https://scikit-learn.org/stable/modules/tree.html`), where it is possible to specify the *class_weight* hyperparameter. As in the case of the previous Section, the not balanced version has *class_weight* = None, while the cost-sensitive Decision Tree is obtained setting *class_weight* = "balanced". Following this procedure, the obtained performance metrics are listed in Table 5.3, where the Depth of the obtained Trees, i.e. the maximum distance between the root and any leaf, is also reported, giving an indication of the complexity of the obtained models. Since the aim is reaching high Specificity and NPV values in particular, the trend of these two metrics, depending on the features' sets, is graphically presented in Figure 5.40.

A general improvement of all the performance metrics can be noticed from both Table 5.3 and Figure 5.40. Focusing on the Figure, one can see a high value of both Specificity and NPV in all cases and for both the not balanced and balanced versions of the models. In particular, the Decision Trees where the class weights are not specified have a slightly higher (~ 0.01) Specificity with respect to the balanced case, while the NPV is always slightly higher (~ 0.02) in the balanced version, with this difference growing smaller adding parameters to the train set (going from Set A to Set E). Unlike the Logistic Regression case, there is a clear improvement of both metrics after adding new features to the sets, with a mean value of 0.73 for Set A, 0.83 for Set B, 0.86 for Set C, 0.88 for Set D and 0.91 for Set E. Finally the two models obtained with Set E, i.e. with all the parameters treated in the previous Sections of this Chapter, reach the threshold of 0.9, meaning

Sets:	A		B		C		D		E	
	NB	B	NB	B	NB	B	NB	B	NB	B
MLT	22.9	19.5	19.5	15.0	18.7	12.0	15.7	10.1	11.4	7.1
MLat	18.3	17.1	15.6	12.7	15.5	11.6	13.7	10.5	10.9	8.5
RODI	40.4	50.7	34.5	47.5	33.2	46.5	31.8	45.4	30.4	44.8
$\gamma(2)$	18.5	12.7	13.9	8.2	13.5	7.0	10.7	5.7	7.2	4.0
doy	-	-	16.5	16.5	9.5	11.6	7.7	9.3	4.8	7.2
F10.7	-	-	-	-	9.5	11.3	8.1	9.8	5.5	7.4
AE	-	-	-	-	-	-	12.4	9.2	7.1	6.0
B_y, B_z, $v_{x,sw}$	-	-	-	-	-	-	-	-	22.6	15.1

Table 5.4: Percentage features' importance for 10 Decision Trees models. Specifically for each set (indicated by the letters A, B, C, D, E) there are 2 models, one not balanced (NB) and one balanced (B). When the feature is not part of the set it is indicated with - symbol. In the case of Set E, the features' importance of the three interplanetary parameters are summed together.

that approximately the 90% of LoL events are correctly labeled. This results is in favor of the hypothesis that the identified parameters can be enough to build a satisfactory model for the LoLs hazard evaluation. Moreover, it is encouraging to see that having only the information on RODI and $\gamma(2)$, as well as Swarm's satellite position in magnetic coordinates, namely working with Set A, is sufficient to correctly identify almost 73% of the GPS LoL events.

When dealing with Decision Tree models it is possible to obtain the relative importance of each involved feature. For the models considered in this Section, the percentage features' importance is presented in Table 5.4. In all the cases, RODI is the most important parameter, always giving more than 30% of the contribute, no matter the number of given features. This confirms the key role of this parameter in being a sort of proxy for LoL events, as it was proposed by De Michelis et al. (2021a) and it was visible in Figures 5.11 and 5.14.

The magnetic coordinates together start giving approximately 40% of the contribute for Set A, and slowly loosing importance, arriving to Set E where their joint contribution is of $\sim 20\%$ for the not balanced case and of $\sim 15\%$ for the balanced one. In fact, for all sets, the two magnetic coordinates weigh less in the cost-sensitive version of the Decision Tree model. However, they remain important contributors even in Set E.

Also $\gamma(2)$ sees a reduction of its relative importance going from Set A to Set E, arriving to reach the 4% in the last case. However, part of its information could be shared also with other parameters, reducing its importance in the dataset characterized by a higher number of features.

The other parameters like doy, F10.7, AE and the interplanetary ones show always a contribute form $\sim 5\%$ upward, helping to gradually improve the performance of the obtained Decision Tree models, as showed in Table 5.3 and Figure 5.40. To know the relative contribution of B_y, B_z and $v_{x,sw}$ individually one can get a good estimation by dividing by 3 their summed percentual importance, since their contributes are very similar to each other.

Other attempts have been pursued, adding additional parameters like the electron density or the Rate Of change of electron TEmperature Index (ROTEI), to take in consideration also the fluctuations in the plasma temperature, or dividing the high latitude region into sectors that are more or less characterized by LoLs occurrence and obtaining separate models for each area. However, the performance did not improve with respect to the results obtained with Set E.

The obtained models can be improved and further tested, for example conducting a *pruning* phase, in order to simplify the obtained Decision Trees and avoid over-fitting (more details in Section 3.3.2). It would be also interesting to test the obtained models on the LoLs recorded by Swarm in correspondence of the solar maximum of cycle 25^{th} and see if their performance remains optimal.
Moreover, the same problem can be treated with more complex models, particularly in the context of anomaly detection. Given the highly imbalanced nature of the considered dataset, where the emphasis lies on identifying anomalies (LoLs in this case), specialized techniques can be employed to refine the analysis. One promising avenue involves taking advantage of the temporal aspect of Swarm data. Time-series anomaly detection methods, such as Seasonal-Trend decomposition and Long Short-Term Memory (LSTM) networks, can be explored. In particular, LSTM networks, with their ability to capture long-term dependencies in sequential data, are particularly effective in modeling complex temporal relationships and detecting anomalies in time-series. Alternatively, unsupervised learning techniques like Isolation Forests or One-Class Support Vector Machines (SVM) hold great potential. These methods do not rely on labeled data and are proficient in isolating anomalies between normal instances.

However, the analysis carried out and presented here acts as proof of concept. While employing a simple method, it serves to verify whether the available information is sufficient for determining the occurrences of LoL events. Certainly, there is room for improvement, but this preliminary investigation provides a foundational understanding of the informational sufficiency for event detection. The obtained Decision Tree models will form the foundation of a future statistical model that will provide maps of the ionospheric high-latitude region, indicating the potential risk of LoL signal interruptions. This model would be dependent on some external parameters, which could be those identified in the best-performing set, i.e. Set E, and thus doy, F10.7, AE, and the interplanetary parameters. However, in some cases a model with fewer external parameters would be preferable, in order to avoid, for instance, the delays due to data distribution, which is a particularly valid consideration in the case of AE for example. Nevertheless, it's important to note that relying solely on the doy feature (see performance metrics for Set B) yields a $\sim 83\%$ precision in correctly identifying LoLs. This accuracy could be enhanced further through the implementation of more sophisticated models.
The construction of such a LoLs' risk evaluation model could play a key role in the reduction of Space Weather damaging effect on GNSS in the high-latitude ionospheric F-region.

Chapter 6

Conclusions

The high-latitude ionosphere is a region characterized by a complex plasma dynamics and a variety of different physical phenomena. Here, a fundamental role is played by the almost vertical geomagnetic field, who couples this region firstly with the magnetosphere and then with the IMF, embedded in the solar wind. This geospace coupling regards mass, momentum and energy transport across a very wide region and a broad range of scales, and therefore inherently exhibits a cross-regional and multiscale nature (Nishimura et al., 2021).
The goal of the present work was to deepen the ionospheric plasma dynamics in this challenging region, by considering different scales, starting with a global view of the two hemispheres, and then move onto structures and irregularities in the meso-scale (ten to hundreds of km) and small-scale ($\lesssim$ 10 km) domain. This in order to evaluate the relative importance of different mechanisms and external factors, with a special attention on the possible impact on specific human technologies, like GNSS. The analysis relies in particular on the constant monitoring of the ionospheric plasma carried on by the ESA constellation mission Swarm, which continued to acquire data since December 2013 to the present day. The specific of the mission, as well as all the other utilized parameters, have been outlined in Chapter 2.

The analysis started by exploring the plasma structure at large scale, meaning $\gtrsim$ 1000 km. The ionospheric high-latitude region ($|\text{MLat}| \geq 50°$) experiences the effects of factors like solar and geomagnetic activity, solar illumination as well as other aspects of the interaction with the magnetosphere and solar wind coupled system. In order to recognize and isolate the different contributors and spatial scales affecting these regions, the MEMD method, described in Section 3.1, was applied to the electron density distribution above 50° magnetic latitude in the Northern hemisphere. The studied period spanned from 1 January 2016 to 31 December 2021, characterized by a low level of the solar activity, enabling a focused exploration of other variables influencing electron density distribution. In particular, the decomposition was applied to six different configuration of the electron density distribution, i.e. three seasonal periods (equinoxes have been grouped together because of the similar illumination conditions) and two levels of geomagnetic activity, describing quiet and disturbed conditions respectively. This translated in applying MEMD to six different maps (showed in Figure 4.3). The resulting modes were analyzed in terms of their spatial distribution in magnetic coordinates, as well as in terms of their relative energy contribution to the original electron density distribution and their characteristics scale. The results were analogous for the six different con-

figuration, making possible to obtain 4 fundamental modes and a residue in each one of the cases (see Figures 4.6, 4.9, 4.10, 4.11, 4.12, 4.13). The first fundamental mode is associated with the noise, while the second is in agreement with the satellite orbit, being probably linked to the data acquisition procedure. Both modes are associated with low energy contribution and do not show peculiar differences depending on the season and the geomagnetic activity level. The most relevant are the third and fourth fundamental modes, which can be connected with the actual ionospheric dynamics and bring a higher contribution in energy. These two modes show an effective dependence on both seasons and geomagnetic activity. They have been both compared with the SuperDARN convection pattern (see Figures 4.15 and 4.16), in order to visualize their possible connection with the large-scale plasma motion. What emerged is that the two-cells convective pattern showed to be significantly in accordance with the the third mode in particular, playing a crucial role for the comprehension of its nature. During disturbed geomagnetic conditions, this mode seems to capture the signature of the magnetic cusp, the accumulation of enhanced electron density on the nightside and the delimitation of the two cells over the polar cup. The situation is less pronounced during geomagnetically quiet periods, probably because of the predominantly positive IMF B_z component. On the other hand, the fourth fundamental mode did not show a high degree of agreement with the convective pattern, however it depicts the day-night asymmetry due to the different photoionization of the ionospheric region, which is deeply linked to the seasonal period, both in terms of intensity of the effect, as well as the different portion of the high-latitude region interested by the solar illumination. Moreover, when comparing the two levels of geomagnetic activity, the fourth mode maintains the same seasonal patterns, with only the intensity level of the asymmetry varying. The four described fundamental modes need to be added to the residue to compose the initial electron density distribution. What emerged from the study of these residues is that they represent the baseline of the electron density distribution, aligning with the known seasonal and geomagnetic differences observed in the ionospheric F-layer.
These results contribute significantly to the deeper comprehension of the dynamical processes governing electron density distribution at mid and high latitudes, accounting for specific times of the year and varying geomagnetic activity levels. Additionally, the analysis aided in estimating the energy contributions of each process. By incorporating these distributions and energy contributions into ionospheric models, a more precise and detailed representation of the ionosphere can be achieved, enabling more accurate predictions of future ionospheric conditions. Moreover, it would be very interesting to repeat the analysis considering the years of high solar activity and see which is the contribution of the different moment of the solar cycle on the modes and if these modes are anyway analogue to the one found during solar minimum years.

Then the analysis was addressed to smaller scales, starting to focus on the possible effects of ionospheric irregularities. The first phenomena that has been taken into consideration is the potential development of diamagnetic or pressure-gradient currents in the high-latitude ionosphere. In fact the presence of irregularities gives rise to inhomogeneities also in the plasma pressure distribution. As depicted in Figure 4.17, around regions of local enhancement or drop of the pressure, a current originates, generating itself a magnetic field, whose orientation is opposite with respect to the ambient magnetic field, causing its reduction. This diamagnetic effect can affect the in-situ measurement of the geomagnetic field made by orbiting satellite. For this reason it is very beneficial

to get to know more about the distribution and entity of this type of current, especially in a region where this effect was poorly studied at the time of the analysis, i.e. the high-latitudes ionosphere. Using geomagnetic field, plasma density and electron temperature measurements recorded on board Swarm A satellite, for the period from April 2014 to March 2018, the flow patterns of the pressure-gradient current were reconstructed in the region with $|\text{MLat} \geq 50°|$. Moreover, their dependencies on geomagnetic activity, season and solar forcing drivers were obtained. Although having small intensity, these currents appear to be a ubiquitous phenomenon at ionospheric high latitudes characterized by well defined flow patterns. The most affected region resulted to be the magnetic cusp, the polar region and the auroral oval, coinciding with the regions that are known to be most characterized by irregularities. Passing from quiet to disturbed geomagnetic periods, the current doesn't vary significantly in its intensity, but it follows the shift towards lower magnetic latitudes of the feature to which it is associated. Local summer resulted to be a period of higher current's module with respect to local winter conditions. Moreover, the current undergoes a decrease of its intensity with the decaying phase of solar activity cycle. Finally, regardless of seasonal, geomagnetic, or solar conditions, the intensity of the pressure-gradient current value in the Southern hemisphere is consistently higher than in the Northern. These findings can be used to correct magnetic field measurements for diamagnetic current effect, to improve modern and precise magnetic field models, as well as to reach a deeper understanding of the impact of ionospheric irregularities on ionospheric dynamics at small-scale sizes of a few tens of kilometers. In the future, it would be intriguing to deepen the diamagnetic currents dependence from altitude, conducting the same procedure on Swarm B data. In this way it will be possible to better understand the three-dimensional structure of this current.

However, the most relevant part of the work is dedicated to another effect linked to the presence of irregularities in the ionosphere, which is the disruption of the GNSS signal in its path toward a receiver. Swarm mission suffer of this harmful effect when its connection with the GPS satellites is interrupted, with a consequent decrease in the positioning accuracy. The aim of the work was to identify which irregularities were at the base of these events, what were their characteristics and determine if it was possible to isolate them along Swarm's satellites tracks and to use them as a proxy for LoL events. Two parameters were used to start working on these tasks: the RODI and the second-order scaling exponent $\gamma(2)$, evaluated from the second-order structure function of the electron density fluctuations. Their values in correspondence of LoLs were examined, both for events occurring at high latitude ($|\text{MLat}| \geq 50°$), and for those occurring in the equatorial band ($|\text{MLat}| \leq 30°$), which occurred between mid-July 2014 to the end of 2021. The initial analysis revealed that GPS LoLs were associated with extremely high values of RODI ($> 10^4(\text{cm}^{-3}\text{s}^{-1})$), meaning that they are linked to very strong fluctuations in the electron density distribution. Moreover, they are characterized by a restricted interval of $\gamma(2)$ values, implying that turbulent processes may be associated with the irregularities at the base of LoLs.The fact that both the $\gamma(2)$ range and the RODI level associated with the occurrence of LoL events showed some variation between high and low latitudes suggested that these events were caused by different physical mechanisms. As a result, the successive analysis concentrated on high-latitudes events. In fact, at that stage, it was not possible to definitively link them to specific known types of irregularity, given the wide range of phenomena occurring in this region, leading to a correspondingly diverse set of instability types.

To determine if the found class of irregularities could act as a proxy of GPS LoLs events in the high-latitude region, firstly it was selected in the space of parameters given by RODI and $\gamma(2)$ values. In view of the shape of the joint PDF distribution associated with the occurrence of LoL events (see Figure 5.14), it was chosen to use an ellipse to fit the level curve corresponding to 1/10 of the probability density maximum. All those instants of time being characterized by RODI and $\gamma(2)$ values together inside this ellipse were selected to represent the class of density fluctuations that could be at the origin of LoLs. Successively the distribution in magnetic coordinates of the found class of irregularities and the one of LoLs themselves were compared (see Figures 5.15 and 5.16). The two distributions showed a high degree of agreement, though a significant divergence emerged in the occurrence rates. In fact, the number of LoL events resulted lower by one or two order of magnitude than the number of N_e fluctuations with values of $\gamma(2)$ and RODI potentially capable of triggering LoLs. This fact revealed the ellipse criterion to be a necessary but not sufficient condition for LoL events.
In order to keep checking if the identified class of N_e fluctuations follows the same climatological behaviours as LoLs, the dependencies of both types of events on solar activity, local season, geomagnetic and interplanetary conditions were explored. This in order to see if it was also possible to identify another parameter that could help in the improvement of the irregularity class description. Despite the imbalance in the occurrence rates, LoLs and N_e fluctuations selected with the ellipse's criterion showed the same seasonal dependence, peaking in the same times of the year and in the same locations (Figure 5.17), the same solar activity trend, being favored in years of solar maximum (Figure 5.18), and the same tendency to occur predominantly during geomagnetic disturbed periods (Figure 5.20).
A more in-depth comment is needed when discussing the relationship with interplanetary conditions, highlighted by the values of the IMF components associated with the events of interest. Even if some dependencies of LoLs events were already known at the time of the analysis, for example Pezzopane et al. (2021) showed the Swarm's LoLs behavior depending on magnetic coordinate, day of the year and solar cycle, the associated IMF conditions were not yet deepened by other works that the authors knew. To summarize, LoL events tend to occur more frequently when $B_z < 0$ and $B_y > 0$ and their spatial distribution in the magnetic latitude and MLT coordinate systems is affected by the signs of both B_y and B_z, with the cusp and polar cap regions showing the strongest effects. In particular, an asymmetric distribution of LoL events appeared over 75° magnetic latitude. In the Northern hemisphere, more events occur in the post-noon sector with negative IMF B_y, and in the pre-noon sector with positive IMF B_y. This behavior is mirrored in the Southern hemisphere. At lower latitudes (50°-75°), IMF B_y does not significantly affect the event distribution, which mainly concentrates in the night sector for both hemispheres. On the other hand, negative IMF B_z periods are characterized by a wider areas characterized by LoL events, which can occur at lower magnetic latitudes. Additionally, a connection was confirmed between IMF B_y and B_x, primarily due to the IMF spiral structure. This interplanetary influence highlighted the connection between LoL events and the high-latitude convection pattern, as showed also by a comparison with SuperDARN potential maps (see Figures 5.33 and 5.34). As in the other dependencies cases, also the distribution of N_e fluctuations with RODI and $\gamma(2)$ inside the ellipse of Figure 5.14 depending on IMF B_y and B_z components was checked. Some relevant differences with LoL events emerged, like the more uniform distribution into the 4 quadrants of the $B_y - B_z$ plane and a disparity in the

position of some maxima. These differences resulted to be very intriguing, reveling the potential of the IMF parameters to better defining the irregularities at the base of GPS LoLs.
Another interesting aspect of the relationship between LoLs and the interplanetary conditions was the similarities with the known characteristics of PCPs. Thus, it was decided to utilize the PCP flag provided by Swarm's Level 2 data, to check the coincidence between LoL and this specific type of irregularity. The analysis was done considering the period from mid-July 2014 to the end of February 2018 and considering only LoLs occurred at $|\text{MLat}| \geq 75°$, which is the region interested by the possible occurrence of PCPs. What emerged is that in the Northern hemisphere $\sim 55\%$ of LoL events coincided with PCPs. In the Southern hemisphere the percentage of coincidence goes down to $\sim 33\%$. However, both percentages increase (to $\sim 57\%$ and $\sim 46\%$ respectively) when considering disturbed geomagnetic times, in accordance with a wider overlapping of the joint PDF between RODI and $\gamma(2)$ associated with the two types of events (see Figure 5.37). This analysis confirmed PCPs as an important source of disturbance for GNSS signals at very high latitudes and shed some lights on the origin of a significant portion of Swarm LoL events in this region.
Lastly, in order to corroborate the obtained description of the N_e fluctuation class at the base of LoL events, a test has been done through the use of two simple ML algorithms, i.e. Logistic Regression and Decision Tree. This in order to see if the information gathered up to that point was enough to determine the possible occurrence of LoLs. The results were very intriguing in the case of Decision Trees models, whose relevant performances metrics are reported in Figure 5.40. When training the model with the complete set of parameters utilized in the previous Sections (magnetic coordinates, RODI, $\gamma(2)$, day of the year, F10.7 and AE indices and interplanetary parameters), $\sim 90\%$ of the LoL events are correctly classified, despite their being extremely rare with respect to the entire period under analysis. However, if one considers only the magnetic coordinate together with RODI and $\gamma(2)$ values, which represented the initial parameters utilized in the identification of the irregularities at the base of LoLs, the model correctly classifies the $\sim 73\%$ of the events already. These results can be certainly further improved, for example by using more sophisticated models. Nevertheless, they provided an encouraging confirmation on the validity of the carried out analysis, by demonstrating that the available information was sufficient for determining the occurrences of LoL events.

The just described work on Swarm LoL events provided a comprehensive view on these damaging events and on the specifics of the irregularities at their base. In particular, the detailed description of the class of turbulent N_e fluctuations associated with GPS signal interruption is to be considered the base for the future construction of a statistical model for the LoLs hazard evaluation in the high-latitude region. Such a model could be very beneficial for future missions orbiting at the same heights in the polar ionosphere, contributing to mitigate this harmful Space Weather effect.

All the treated topics collectively contribute to improve the comprehensive understanding of ionospheric dynamics in a very complex region, profoundly affected by Space Weather phenomena, offering useful hints for the mitigation of different deleterious effects. Moreover, the exploration of various aspect of the high-latitude ionospheric irregularities provides additional elements to the much-debated issue of North-South asymmetries in the Earth's magnetic field, which translates in a different magnetosphere–ionosphere coupling related phenomena.

Bibliography

Swarm product specification for L2 products and auxiliary products. Available online: *https* : *//earth.esa.int/eogateway/documents/*20142/37627/*swarm* − *level* − 2 − *product* − *specification.pdf/*2979*b*351 − *b*6*a*2 − 69*b*6 − 8539 − 9*ed*9*f*32984*f*0, a.

Swarm L2 IBI Product Description. Available online: *https* : *//earth.esa.int/eogateway/documents/*20142/37627/*Swarm* − *Level* − 2 − *IBI* − *product* − *description.pdf/*3*e*9*f*6*c*3*a* − 1*ffc* − *ea*53 − 0161 − *a*18*b*63*f*90*c*6*f*, b.

Swarm General Supporting Information. Available online: *https* : *//esastar* − *publication.sso.esa.int/api/filemanagement/download?url* = *emits.sso.esa.int/emits* − *doc/ASTRIUMLIM/SWARM*$_N$*adir*$_A$*ntenna/SW.LI.EAD.SY.*0004*.pdf*, 2007.

Swarm Mission - Constellation and Orbit Evolution. Available online: *https* : *//earth.esa.int/eogateway/missions/swarm/constellation* − *and* − *orbit* − *evolution.*, 2023a.

Swarm Overview - Satellite Design. Available online: *https* : *//earth.esa.int/eogateway/missions/swarm/description.*, 2023b.

E. Aa, S. Zou, P. J. Erickson, S.-R. Zhang, and S. Liu. Statistical analysis of the main ionospheric trough using swarm in situ measurements. *Journal of Geophysical Research: Space Physics*, 125 (3):e2019JA027583, 2020.

J. Aarons. Global morphology of ionospheric scintillations. *Proceedings of the IEEE*, 70(4):360–378, 1982.

J. Aarons, J. Mullen, H. Whitney, A. Johnson, and E. Weber. Uhf scintillation activity over polar latitudes. *Geophysical Research Letters*, 8(3):277–280, 1981.

S.-I. Akasofu and S. Chapman. Solar-terrestrial physics. 1972.

T. Alberti, F. Giannattasio, P. De Michelis, and G. Consolini. Linear versus nonlinear methods for detecting magnetospheric and ionospheric current systems patterns. *Earth and Space Science*, 7 (7):e2019EA000559, 2020.

P. Alken. Observations and modeling of the ionospheric gravity and diamagnetic current systems from champ and swarm measurements. *Journal of Geophysical Research: Space Physics*, 121(1): 589–601, 2016.

P. Alken, S. Maus, A. Richmond, and A. Maute. The ionospheric gravity and diamagnetic current systems. *Journal of Geophysical Research: Space Physics*, 116(A12), 2011.

P. Alken, A. Maute, and A. Richmond. The f-region gravity and pressure gradient current systems: a review. *Space Science Reviews*, 206(1-4):451–469, 2017.

P. Alken, E. Thébault, C. D. Beggan, H. Amit, J. Aubert, J. Baerenzung, T. Bondar, W. Brown, S. Califf, A. Chambodut, et al. International geomagnetic reference field: the thirteenth generation. *Earth, Planets and Space*, 73(1):1–25, 2021.

M. U. B. Altaf, T. Gautama, T. Tanaka, and D. P. Mandic. Rotation invariant complex empirical mode decomposition. In *2007 IEEE International Conference on Acoustics, Speech and Signal Processing-ICASSP'07*, volume 3, pages III–1009. IEEE, 2007.

S. K. Antiochos, J. A. Linker, R. Lionello, Z. Mikić, V. Titov, and T. H. Zurbuchen. The structure and dynamics of the corona—heliosphere connection. *Space science reviews*, 172:169–185, 2012.

K. Baker and S. Wing. A new magnetic coordinate system for conjugate studies at high latitudes. *Journal of Geophysical Research: Space Physics*, 94(A7):9139–9143, 1989.

S. Basu, S. Basu, E. MacKenzie, P. F. Fougere, W. R. Coley, N. C. Maynard, J. D. Winningham, M. Sugiura, W. B. Hanson, and W. R. Hoegy. Simultaneous density and electric field fluctuation spectra associated with velocity shears in the auroral oval. *Journal of Geophysical Research*, 93 (A1):115–136, 1988. doi: 10.1029/JA093iA01p00115.

S. Basu, E. MacKenzie, and S. Basu. Ionospheric constraints on vhf/uhf communications links during solar maximum and minimum periods. *Radio Science*, 23(03):363–378, 1988.

S. Basu, S. Basu, K. Groves, H.-C. Yeh, S.-Y. Su, F. Rich, P. Sultan, and M. Keskinen. Response of the equatorial ionosphere in the south atlantic region to the great magnetic storm of july 15, 2000. *Geophysical Research Letters*, 28(18):3577–3580, 2001.

S. Basu, K. Groves, S. Basu, and P. Sultan. Specification and forecasting of scintillations in communication/navigation links: Current status and future plans. *Journal of Atmospheric and Solar-Terrestrial Physics*, 64(16):1745–1754, 2002.

W. Baumjohann and R. Nakamura. Magnetospheric contributions to the terrestrial magnetic field. 2007.

W. Baumjohann and R. Treumann. *Basic space plasma physics*. World Scientific, 1996.

R. Benzi and F. Toschi. Lectures on turbulence. *Physics Reports*, 1021:1–106, 2023.

A. Bergin, S. C. Chapman, and J. W. Gjerloev. AE, D_{ST}, and Their SuperMAG Counterparts: The Effect of Improved Spatial Resolution in Geomagnetic Indices. *Journal of Geophysical Research (Space Physics)*, 125(5):e27828, 2020. doi: 10.1029/2020JA027828.

A. Bhardwaj, C. M. Lisse, and K. Dennerl. X-rays in the solar system. In *Encyclopedia of the Solar System*, pages 1019–1045. Elsevier, 2014.

A. Bigazzi, C. Cauli, and F. Berrilli. Lower-thermosphere response to solar activity: an empirical-mode-decomposition analysis of GOCE 2009-2012 data. *Annales Geophysicae*, 38(3):789–800, June 2020. doi: 10.5194/angeo-38-789-2020.

D. Blagoveshchenskii. Effect of geomagnetic storms (substorms) on the ionosphere: 1. a review. *Geomagnetism and aeronomy*, 53(3):275–290, 2013.

E. Y. Boateng and D. A. Abaye. A review of the logistic regression model with emphasis on medical research. *Journal of data analysis and information processing*, 7(4):190–207, 2019.

E. Britannica et al. *Britannica concise encyclopedia*. Encyclopaedia Britannica, Inc., 2008.

J. Brownlee. 4 types of classification tasks in machine learning: *https* : $//machinelearningmastery.com/types-of-classification-in-machine-learning/.$, 2020a.

J. Brownlee. Cost-sensitive logistic regression for imbalanced classification: *https* : $//machinelearningmastery.com/cost-sensitive-logistic-regression/.$, 2020b.

J. Brownlee. Cost-sensitive decision trees for imbalanced classification: *https* : $//machinelearningmastery.com/cost-sensitive-decision-trees-for-imbalanced-classification/.$, 2020c.

S. Buchert, F. Zangerl, M. Sust, M. André, A. Eriksson, J.-E. Wahlund, and H. Opgenoorth. Swarm observations of equatorial electron densities and topside GPS track losses. *Geophysical Research Letters*, 42(7):2088–2092, 2015.

N. Buzulukova. *Extreme events in geospace: Origins, predictability, and consequences*. Elsevier, 2017.

P. Cannon, M. Angling, J. Heaton, N. Rogers, and A. Shukla. The effects of space weather on radio systems: with a focus on hf systems. *Effects of space weather on technology infrastructure*, pages 185–201, 2005.

V. Carbone and A. Pouquet. An introduction to fluid and mhd turbulence for astrophysical flows: Theory, observational and numerical data, and modeling. In *Turbulence in Space Plasmas*, pages 71–128. Springer, 2009.

H. C. Carlson. Sharpening our thinking about polar cap ionospheric patch morphology, research, and mitigation techniques. *Radio Science*, 47(4), 2012. doi: https://doi.org/10.1029/2011RS004946. URL `https://agupubs.onlinelibrary.wiley.com/doi/abs/10.1029/2011RS004946`.

D. Carpenter and J. Lemaire. The Plasmasphere Boundary Layer. *Annales Geophysicae*, 22(12): 4291–4298, 2004. doi: 10.5194/angeo-22-4291-2004.

P. Charbonneau. Dynamo models of the solar cycle. *Solar and Stellar Dynamos: Saas-Fee Advanced Course 39 Swiss Society for Astrophysics and Astronomy*, pages 87–151, 2013.

A. T. Chartier, C. N. Mitchell, and E. S. Miller. Annual occurrence rates of ionospheric polar cap patches observed using swarm. *Journal of Geophysical Research: Space Physics*, 123(3): 2327–2335, 2018.

I. Cherniak and I. Zakharenkova. High-latitude ionospheric irregularities: differences between ground-and space-based GPS measurements during the 2015 St. Patrick's Day storm. *Earth, Planets and Space*, 68(1):1–13, 2016.

I. Cherniak, I. Zakharenkova, and A. Krankowski. Approaches for modeling ionosphere irregularities based on the tec rate index. *Earth, Planets and Space*, 66(1):1–5, 2014.

I. Cherniak, I. Zakharenkova, and S. Sokolovsky. Multi-instrumental observation of storm-induced ionospheric plasma bubbles at equatorial and middle latitudes. *Journal of Geophysical Research: Space Physics*, 124(3):1491–1508, 2019.

G. Chisham, M. Lester, S. Milan, M. Freeman, W. Bristow, A. Grocott, K. McWilliams, J. Ruohoniemi, T. Yeoman, P. L. Dyson, et al. A decade of the Super Dual Auroral Radar Network (SuperDARN): Scientific achievements, new techniques and future directions. *Surveys in geophysics*, 28:33–109, 2007.

C. Chiuderi and M. Velli. *Basics of plasma astrophysics*. Springer, 2015.

H. S. Choi, H. Kil, Y. S. Kwak, Y. D. Park, and K. S. Cho. Comparison of the bubble and blob distributions during the solar minimum. *Journal of Geophysical Research (Space Physics)*, 117 (A4):A04314, 2012. doi: 10.1029/2011JA017292.

L. B. N. Clausen and J. I. Moen. Electron density enhancements in the polar cap during periods of dayside reconnection. *Journal of Geophysical Research: Space Physics*, 120(6):4452–4464, 2015. doi: https://doi.org/10.1002/2015JA021188. URL `https://agupubs.onlinelibrary.wiley.com/doi/abs/10.1002/2015JA021188`.

W. Coley and R. Heelis. Structure and occurrence of polar ionization patches. *Journal of Geophysical Research: Space Physics*, 103(A2):2201–2208, 1998.

G. Consolini. Self-organized criticality: A new paradigm for the magnetotail dynamics. *Fractals*, 10(03):275–283, 2002.

G. Consolini, R. Tozzi, P. De Michelis, I. Coco, F. Giannattasio, M. Pezzopane, M. F. Marcucci, and G. Balasis. High-latitude polar pattern of ionospheric electron density: Scaling features and imf dependence. *Journal of Atmospheric and Solar-Terrestrial Physics*, 217:105531, 2021.

E. Cousins and S. Shepherd. A dynamical model of high-latitude convection derived from SuperDARN plasma drift measurements. *Journal of Geophysical Research: Space Physics*, 115(A12), 2010.

S. Cowley. The causes of convection in the Earth's magnetosphere: A review of developments during the IMS. *Reviews of Geophysics*, 20(3):531–565, 1982.

S. Cowley, J. Morelli, and M. Lockwood. Dependence of convective flows and particle precipitation in the high-latitude dayside ionosphere on the X and Y components of the interplanetary magnetic field. *Journal of Geophysical Research: Space Physics*, 96(A4):5557–5564, 1991.

G. Crowley. Critical review of ionospheric patches and blobs. *Review of Radio Science 1993–1996*, pages 619–648, 1996.

I. A. Daglis. Ring current dynamics. *Space Science Reviews*, 124(1):183–202, 2006.

T. N. Davis and M. Sugiura. Auroral electrojet activity index AE and its universal time variations. *Journal of Geophysical Research*, 71(3):785–801, 1966.

P. De Michelis, G. Consolini, and R. Tozzi. Magnetic field fluctuation features at swarm's altitude: A fractal approach. *Geophysical Research Letters*, 42(9):3100–3105, 2015.

P. De Michelis, G. Consolini, R. Tozzi, and M. F. Marcucci. Observations of high-latitude geomagnetic field fluctuations during St. Patrick's Day storm: Swarm and SuperDARN measurements. *Earth, Planets and Space*, 68(1):105, 2016. doi: 10.1186/s40623-016-0476-3.

P. De Michelis, G. Consolini, R. Tozzi, and M. F. Marcucci. Scaling Features of High-Latitude Geomagnetic Field Fluctuations at Swarm Altitude: Impact of IMF Orientation. *Journal of Geophysical Research (Space Physics)*, 122(10):10,548–10,562, 2017. doi: 10.1002/2017JA024156.

P. De Michelis, A. Pignalberi, G. Consolini, I. Coco, R. Tozzi, M. Pezzopane, F. Giannattasio, and G. Balasis. On the 2015 st. patrick's storm turbulent state of the ionosphere: Hints from the swarm mission. *Journal of Geophysical Research: Space Physics*, 125(8):e2020JA027934, 2020.

P. De Michelis, G. Consolini, A. Pignalberi, R. Tozzi, I. Coco, F. Giannattasio, M. Pezzopane, and G. Balasis. Looking for a proxy of the ionospheric turbulence with Swarm data. *Scientific Reports*, 11:6183, 2021a. doi: 10.1038/s41598-021-84985-1.

P. De Michelis, G. Consolini, R. Tozzi, A. Pignalberi, M. Pezzopane, I. Coco, F. Giannattasio, and M. F. Marcucci. Ionospheric Turbulence and the Equatorial Plasma Density Irregularities: Scaling Features and RODI. *Remote Sensing*, 13(4):759, 2021b. doi: 10.3390/rs13040759.

P. De Michelis, G. Consolini, A. Pignalberi, G. Lovati, M. Pezzopane, R. Tozzi, F. Giannattasio, I. Coco, and M. F. Marcucci. Ionospheric Turbulence: A Challenge for GPS Loss of Lock Understanding. *Space Weather*, 20(7):e03129, 2022. doi: 10.1029/2022SW003129.

B. De Ville. Decision trees. *Wiley Interdisciplinary Reviews: Computational Statistics*, 5(6):448–455, 2013.

F. Di Mare, A. Spicher, L. B. N. Clausen, W. J. Miloch, and J. I. Moen. Turbulence and Intermittency in the Winter Cusp Ionosphere Studied With the ICI Sounding Rockets. *Journal of Geophysical Research (Space Physics)*, 126(8):e29150, 2021. doi: 10.1029/2021JA029150.

J. Dods, S. Chapman, and J. Gjerloev. Characterizing the ionospheric current pattern response to southward and northward imf turnings with dynamical supermag correlation networks. *Journal of Geophysical Research: Space Physics*, 122(2):1883–1902, 2017.

J. W. Dungey. Interplanetary magnetic field and the auroral zones. *Phys. Rev. Lett.*, 6:47–48, Jan 1961. doi: 10.1103/PhysRevLett.6.47. URL `https://link.aps.org/doi/10.1103/PhysRevLett.6.47`.

G. Earle, M. Kelley, and G. Ganguli. Large velocity shears and associated electrostatic waves and turbulence in the auroral f region. *Journal of Geophysical Research: Space Physics*, 94(A11): 15321–15333, 1989.

R. Ebert, D. McComas, H. Elliott, R. Forsyth, and J. Gosling. Bulk properties of the slow and fast solar wind and interplanetary coronal mass ejections measured by ulysses: Three polar orbits of observations. *Journal of Geophysical Research: Space Physics*, 114(A1), 2009.

Y. Ebihara, Y. Miyoshi, K. Asamura, and M. Hirahara. Microburst cusp ion precipitation observed with reimei. *Journal of Geophysical Research: Space Physics*, 113(A3), 2008.

E. Echer, W. Gonzalez, F. Guarnieri, A. Dal Lago, and L. Vieira. Introduction to space weather. *Advances in Space Research*, 35(5):855–865, 2005.

J. A. Eddy. *The Sun, the Earth, and Near-Earth space: A guide to the Sun-Earth system*. Government Printing Office, 2009.

O. Engvold, J.-C. Vial, and A. Skumanich. *The Sun as a Guide to Stellar Physics*. Elsevier, 2018.

R. C. Fear. The northward imf magnetosphere. *Magnetospheres in the solar system*, pages 293–309, 2021.

C. C. Finlay, N. Olsen, and L. Tøffner-Clausen. DTU candidate field models for IGRF-12 and the CHAOS-5 geomagnetic field model. *Earth, Planets and Space*, 67(1):1–17, 2015.

L. Fisk and N. Schwadron. The behavior of the open magnetic field of the sun. *The Astrophysical Journal*, 560(1):425, 2001.

P. Flandrin, G. Rilling, and P. Goncalves. Empirical Mode Decomposition as a Filter Bank. *IEEE Signal Processing Letters*, 11(2):112–114, 2004. doi: 10.1109/LSP.2003.821662.

M. Fligge and S. Solanki. The solar spectral irradiance since 1700. *Geophysical Research Letters*, 27(14):2157–2160, 2000.

R. Foldes and F. Berrilli. Characterisation of flare Soft X-ray distribution with solar magnetic activity. In *Journal of Physics: Conference Series*, volume 1548, page 012011. IOP Publishing, 2020.

J. Foster, A. Coster, P. Erickson, J. Holt, F. Lind, W. Rideout, M. McCready, A. Van Eyken, R. Barnes, R. Greenwald, et al. Multiradar observations of the polar tongue of ionization. *Journal of Geophysical Research: Space Physics*, 110(A9), 2005.

J. C. Foster. Storm time plasma transport at middle and high latitudes. *Journal of Geophysical Research: Space Physics*, 98(A2):1675–1689, 1993.

J. C. Foster, P. J. Erickson, A. J. Coster, J. Goldstein, and F. J. Rich. Ionospheric signatures of plasmaspheric tails. *Geophys. Res. Lett.*, 29(13):1623, 2002. doi: 10.1029/2002GL015067.

P. Foukal. Extension of the F10. 7 index to 1905 using Mt. Wilson Ca K spectroheliograms. *Geophysical research letters*, 25(15):2909–2912, 1998.

E. Friis-Christensen, H. Lühr, and G. Hulot. Swarm: A constellation to study the Earth's magnetic field. *Earth, planets and space*, 58(4):351–358, 2006.

U. Frisch. *Turbulence: The Legacy of A. N. Kolmogorov*. Cambridge University Press, 1995. doi: 10.1017/CBO9781139170666.

N. Y. Ganushkina, M. Liemohn, and S. Dubyagin. Current systems in the earth's magnetosphere. *Reviews of Geophysics*, 56(2):309–332, 2018.

K. J. Genestreti, L. Kistler, and C. Mouikis. The role and dynamics of oxygen of ionospheric origin in magnetopause reconnection. 2012.

F. Giannattasio, P. De Michelis, G. Consolini, V. Quattrociocchi, I. Coco, and R. Tozzi. Characterising the electron density fluctuations in the high-latitude ionosphere at Swarm altitude in response to the geomagnetic activity. *Annals of Geophysics*, 2019.

J. Gjerloev. The SuperMAG data processing technique. *Journal of Geophysical Research: Space Physics*, 117(A9), 2012.

J. Goldstein and B. R. Sandel. The Global Pattern of Evolution of Plasmaspheric Drainage Plumes. *Geophysical Monograph Series*, 159:1, 2005. doi: 10.1029/159GM02.

I. Golovchanskaya and B. Kozelov. On the origin of electric turbulence in the polar cap ionosphere. *Journal of Geophysical Research: Space Physics*, 115(A9), 2010.

I. Golovchanskaya, A. Ostapenko, and B. Kozelov. Relationship between the high-latitude electric and magnetic turbulence and the birkeland field-aligned currents. *Journal of Geophysical Research: Space Physics*, 111(A12), 2006.

L. Golub and J. M. Pasachoff. *The solar corona*. Cambridge University Press, 2010.

N. Gondarenko and P. Guzdar. Plasma patch structuring by the nonlinear evolution of the gradient drift instability in the high-latitude ionosphere. *Journal of Geophysical Research: Space Physics*, 109(A9), 2004.

R. A. Greenwald, S. G. Shepherd, T. S. Sotirelis, J. M. Ruohoniemi, and R. J. Barnes. Dawn and dusk sector comparisons of small-scale irregularities, convection, and particle precipitation in the high-latitude ionosphere. *Journal of Geophysical Research: Space Physics*, 107(A9):SIA–1, 2002.

S. Haaland, G. Paschmann, M. Förster, J. Quinn, R. Torbert, C. McIlwain, H. Vaith, P. Puhl-Quinn, and C. Kletzing. High-latitude plasma convection from Cluster EDI measurements: method and IMF-dependence. In *Annales Geophysicae*, volume 25, pages 239–253. Copernicus GmbH, 2007.

R. A. Haaser, G. D. Earle, R. A. Heelis, J. Klenzing, R. Stoneback, W. R. Coley, and A. G. Burrell. Characteristics of low-latitude ionospheric depletions and enhancements during solar minimum. *Journal of Geophysical Research (Space Physics)*, 117(A10):A10305, 2012. doi: 10.1029/2012JA017814.

C. J. Hegarty and E. Chatre. Evolution of the global navigation satellitesystem (gnss). *Proceedings of the IEEE*, 96(12):1902–1917, 2008.

Y. Hobara, F. Lefeuvre, M. Parrot, and O. A. Molchanov. Low-latitude ionospheric turbulence observed by Aureol-3 satellite. *Annales Geophysicae*, 23(4):1259–1270, 2005. doi: 10.5194/angeo-23-1259-2005.

D. W. Hosmer Jr, S. Lemeshow, and R. X. Sturdivant. *Applied logistic regression*, volume 398. John Wiley & Sons, 2013.

N. E. Huang, Z. Shen, S. R. Long, M. C. Wu, H. H. Shih, Q. Zheng, N.-C. Yen, C. C. Tung, and H. H. Liu. The empirical mode decomposition and the Hilbert spectrum for nonlinear and non-stationary time series analysis. *Proceedings of the Royal Society of London. Series A: mathematical, physical and engineering sciences*, 454(1971):903–995, 1998.

R. D. Hunsucker and J. K. Hargreaves. *The high-latitude ionosphere and its effects on radio propagation*. Cambridge University Press, 2007.

H. E. Hurst. Methods of using long-term storage in reservoirs. *Proceedings of the institution of civil engineers*, 5(5):519–543, 1956.

D. L. Hysell and E. B. Shume. Electrostatic plasma turbulence in the topside equatorial F region ionosphere. *Journal of Geophysical Research (Space Physics)*, 107(A10):1269, 2002. doi: 10.1029/2001JA000227.

T. Iijima and T. A. Potemra. The amplitude distribution of field-aligned currents at northern high latitudes observed by Triad. *Journal of Geophysical Research*, 81(13):2165–2174, 1976.

J.-M. Jahn and J. Labelle. Rocket measurements of high-altitude spread F irregularities at the magnetic dip equator. *Journal of Geophysical Research*, 103(A10):23427–23442, 1998. doi: 10.1029/97JA02636.

G. James, D. Witten, T. Hastie, R. Tibshirani, et al. *An introduction to statistical learning*, volume 112. Springer, 2013.

Y. Jin and K. Oksavik. GPS scintillations and losses of signal lock at high latitudes during the 2015 St. Patrick's Day storm. *Journal of Geophysical Research: Space Physics*, 123(9):7943–7957, 2018.

Y. Jin, J. I. Moen, and W. J. Miloch. Gps scintillation effects associated with polar cap patches and substorm auroral activity: Direct comparison. *Journal of Space Weather and Space Climate*, 4:A23, 2014.

Y. Jin, J. I. Moen, W. J. Miloch, L. B. Clausen, and K. Oksavik. Statistical study of the gnss phase scintillation associated with two types of auroral blobs. *Journal of Geophysical Research: Space Physics*, 121(5):4679–4697, 2016.

Y. Jin, A. Spicher, C. Xiong, L. B. Clausen, G. Kervalishvili, C. Stolle, and W. J. Miloch. Ionospheric plasma irregularities characterized by the swarm satellites: Statistics at high latitudes. *Journal of Geophysical Research: Space Physics*, 124(2):1262–1282, 2019. doi: 10.1029/2018JA026063.

Y. Jin, C. Xiong, L. Clausen, A. Spicher, D. Kotova, S. Brask, G. Kervalishvili, C. Stolle, and W. Miloch. Ionospheric plasma irregularities based on in situ measurements from the swarm satellites. *Journal of Geophysical Research: Space Physics*, 125(7):e2020JA028103, 2020.

Y. Jin, D. Kotova, C. Xiong, S. M. Brask, L. B. N. Clausen, G. Kervalishvili, C. Stolle, and W. J. Miloch. Ionospheric Plasma IRregularities - IPIR - Data product based on data from the Swarm satellites. *Journal of Geophysical Research: Space Physics*, 2022. doi: 10.1029/2021JA030183. URL `https://doi.org/10.1029/2021JA030183`.

Y. Kamide and A. C.-L. Chian. *Handbook of the solar-terrestrial environment*. Springer Science & Business Media, 2007.

A. Karpachev, G. Deminova, and S. Pulinets. Ionospheric changes in response to IMF variations. *Journal of atmospheric and terrestrial physics*, 57(12):1415–1432, 1995.

M. C. Kelley. *The Earth's ionosphere: Plasma physics and electrodynamics*. Academic press, 2009.

M. C. Kelley, T. L. Franz, and G. Prasad. On the turbulent spectrum of equatorial spread F: A comparison between laboratory and space results. *Journal of Geophysical Research (Space Physics)*, 107(A12):1432, 2002. doi: 10.1029/2002JA009398.

H. Kil and R. Heelis. Global distribution of density irregularities in the equatorial ionosphere. *Journal of Geophysical Research: Space Physics*, 103(A1):407–417, 1998.

G. King and L. Zeng. Logistic regression in rare events data. *Political analysis*, 9(2):137–163, 2001.

C. Kingsford and S. L. Salzberg. What are decision trees? *Nature biotechnology*, 26(9):1011–1013, 2008.

P. M. Kintner and C. E. Seyler. The status of observations and theory of high latitude ionospheric and magnetospheric plasma turbulence. *Space Science Review*, 41(1-2):91–129, 1985. doi: 10.1007/BF00241347.

P. M. Kintner, H. Kil, T. L. Beach, and E. R. de Paula. Fading timescales associated with gps signals and potential consequences. *Radio Science*, 36(4):731–743, 2001.

M. G. Kivelson and C. T. Russell. *Introduction to space physics*. Cambridge university press, 1995.

D. Knudsen, E. Donovan, L. Cogger, B. Jackel, and W. Shaw. Width and structure of mesoscale optical auroral arcs. *Geophysical Research Letters*, 28(4):705–708, 2001.

W. Knudsen. Magnetospheric convection and the high-latitude f 2 ionosphere. *Journal of Geophysical Research*, 79(7):1046–1055, 1974.

A. N. Kolmogorov. The local structure of turbulence in incompressible viscous fluid for very large reynolds. *Numbers. In Dokl. Akad. Nauk SSSR*, 30:301, 1941.

M. Kono. *Treatise on Geophysics, Volume 5: Geomagnetism*. Elsevier, 2010.

E. Kontar, J. Perez, L. Harra, A. Kuznetsov, A. Emslie, N. Jeffrey, N. Bian, and B. Dennis. Turbulent kinetic energy in the energy balance of a solar flare. *Physical Review Letters*, 118(15): 155101, 2017.

B. Kozelov and I. Golovchanskaya. Scaling of electric field fluctuations associated with the aurora during northward imf. *Geophysical research letters*, 33(20), 2006.

F. R. Kschischang. The hilbert transform. *University of Toronto*, 83:277, 2006.

J. Labelle, M. C. Kelley, and C. E. Seyler. An analysis of the role of drift waves in equatorial spread F. *Journal of Geophysical Research*, 91(A5):5513–5525, 1986. doi: 10.1029/JA091iA05p05513.

K. M. Laundal and A. D. Richmond. Magnetic coordinate systems. *Space Science Reviews*, 206 (1-4):27–59, 2017.

K. M. Laundal, S. M. Hatch, and T. Moretto. Magnetic effects of plasma pressure gradients in the upper f region. *Geophysical Research Letters*, 46(5):2355–2363, 2019.

M. Lester. Ionospheric convection and its relevance for space weather. *Advances in Space Research*, 31(4):941–950, 2003.

Y. Liu, L. Fu, J. Wang, and C. Zhang. Study of GNSS loss of lock characteristics under ionosphere scintillation with GNSS data at Weipa (Australia) during solar maximum phase. *Sensors*, 17(10): 2205, 2017.

M. Lockwood and H. C. Carlson Jr. Production of polar cap electron density patches by transient magnetopause reconnection. *Geophysical Research Letters*, 19(17):1731–1734, 1992. doi: https://doi.org/10.1029/92GL01993. URL `https://agupubs.onlinelibrary.wiley.com/doi/abs/10.1029/92GL01993`.

M. Lockwood, S. Cowley, and M. Freeman. The excitation of plasma convection in the high-latitude ionosphere. *Journal of Geophysical Research: Space Physics*, 95(A6):7961–7972, 1990.

M. Lockwood, I. McCrea, S. E. Milan, J. Moen, J. Cerisier, and A. Thorolfsson. Plasma structure within poleward-moving cusp/cleft auroral transients: EISCAT Svalbard radar observations and an explanation in terms of large local time extent of events. In *Annales Geophysicae*, volume 18, pages 1027–1042. Springer Verlag Göttingen, Germany, 2000.

M. Lockwood, H. Opgenoorth, A. Van Eyken, A. Fazakerley, J.-M. Bosqued, W. Denig, J. Wild, C. Cully, R. Greenwald, G. Lu, et al. Coordinated cluster, ground-based instrumentation and low-altitude satellite observations of transient poleward-moving events in the ionosphere and in the tail lobe. In *Annales Geophysicae*, volume 19, pages 1589–1612. Copernicus GmbH, 2001.

L. Lomidze, D. J. Knudsen, J. Burchill, A. Kouznetsov, and S. C. Buchert. Calibration and validation of swarm plasma densities and electron temperatures using ground-based radars and satellite radio occultation measurements. *Radio Science*, 53(1):15–36, 2018.

W. Lotko and B. Zhang. Alfvénic heating in the cusp ionosphere-thermosphere. *Journal of Geophysical Research: Space Physics*, 123(12):10–368, 2018.

G. Lovati, P. De Michelis, G. Consolini, and F. Berrilli. Pressure-gradient current at high latitude from swarm measurements. *Remote Sensing*, 14(6):1428, 2022.

G. Lovati, P. De Michelis, T. Alberti, and G. Consolini. Unveiling the core patterns of high-latitude electron density distribution at swarm altitude. *Remote Sensing*, 15(18):4550, 2023a.

G. Lovati, P. De Michelis, G. Consolini, M. Pezzopane, A. Pignalberi, and F. Berrilli. Decomposing solar and geomagnetic activity and seasonal dependencies to examine the relationship between gps loss of lock and ionospheric turbulence. *Scientific Reports*, 13(1):9287, 2023b.

G. Lovati, P. De Michelis, G. Consolini, M. Pezzopane, A. Pignalberi, and F. Berrilli. Gps loss of lock events and their dependence on the interplanetary magnetic field orientation. *Journal of Geophysical Research: Space Physics*, 128(7):e2023JA031411, 2023c.

H. Lühr and S. Maus. Solar cycle dependence of quiet-time magnetospheric currents and a model of their near-earth magnetic fields. *Earth, planets and space*, 62(10):843–848, 2010.

H. Lühr, M. Rother, S. Maus, W. Mai, and D. Cooke. The diamagnetic effect of the equatorial Appleton anomaly: Its characteristics and impact on geomagnetic field modeling. *Geophysical Research Letters*, 30(17), 2003.

H. Lühr, M. Korte, and M. Mandea. The recent geomagnetic field and its variations. In *Geomagnetic field variations*, pages 25–63. Springer, 2009.

L. Lyons, T. Nagai, G. Blanchard, J. Samson, T. Yamamoto, T. Mukai, A. Nishida, and S. Kokubun. Association between geotail plasma flows and auroral poleward boundary intensifications observed by canopus photometers. *Journal of Geophysical Research: Space Physics*, 104(A3):4485–4500, 1999.

S. Maheshwari and A. Kumar. Empirical mode decomposition: theory & applications. *International Journal of Electronic Engineering*, pages 873–878, 2014.

D. P. Mandic and V. S. L. Goh. *Complex valued nonlinear adaptive filters: noncircularity, widely linear and neural models*. John Wiley & Sons, 2009.

C. Martinis, J. Baumgardner, M. Mendillo, S.-Y. Su, and N. Aponte. Brightening of 630.0 nm equatorial spread-F airglow depletions. *Journal of Geophysical Research (Space Physics)*, 114 (A6):A06318, 2009. doi: 10.1029/2008JA013931.

D. McComas, S. Bame, B. Barraclough, W. Feldman, H. Funsten, J. Gosling, P. Riley, R. Skoug, A. Balogh, R. Forsyth, et al. Ulysses' return to the slow solar wind. *Geophysical Research Letters*, 25(1):1–4, 1998.

D. McComas, B. Barraclough, H. Funsten, J. Gosling, E. Santiago-Muñoz, R. Skoug, B. Goldstein, M. Neugebauer, P. Riley, and A. Balogh. Solar wind observations over ulysses' first full polar orbit. *Journal of Geophysical Research: Space Physics*, 105(A5):10419–10433, 2000.

D. McComas, H. Elliott, N. Schwadron, J. Gosling, R. Skoug, and B. Goldstein. The three-dimensional solar wind around solar maximum. *Geophysical research letters*, 30(10), 2003.

S. Milan, G. Provan, and B. Hubert. Magnetic flux transport in the dungey cycle: A survey of dayside and nightside reconnection rates. *Journal of Geophysical Research: Space Physics*, 112 (A1), 2007.

T. Miller. Explanation in artificial intelligence: Insights from the social sciences. *Artificial intelligence*, 267:1–38, 2019.

J. Moen, X. Qiu, H. Carlson, R. Fujii, and I. McCrea. On the diurnal variability in F2-region plasma density above the EISCAT Svalbard radar. In *Annales geophysicae*, volume 26, pages 2427–2433. Copernicus Publications Göttingen, Germany, 2008.

J. Moen, K. Oksavik, L. Alfonsi, Y. Daabakk, V. Romano, and L. Spogli. Space weather challenges of the polar cap ionosphere. *Journal of Space Weather and Space Climate*, 3:A02, 2013.

J. Moen, K. Hosokawa, N. Gulbrandsen, and L. B. N. Clausen. On the symmetry of ionospheric polar cap patch exits around magnetic midnight. *Journal of Geophysical Research: Space Physics*, 120(9):7785–7797, 2015.

M. Moldwin. *An Introduction to Space Weather*. Cambridge University Press, 2008.

C. Molnar. *Interpretable machine learning*. Lulu. com, 2020.

W. J. Murdoch, C. Singh, K. Kumbier, R. Abbasi-Asl, and B. Yu. Definitions, methods, and applications in interpretable machine learning. *Proceedings of the National Academy of Sciences*, 116(44):22071–22080, 2019.

D. Murr and W. Hughes. Reconfiguration timescales of ionospheric convection. *Geophysical Research Letters*, 28(11):2145–2148, 2001.

M. N. Murty, V. S. Devi, M. N. Murty, and V. S. Devi. Decision trees. *Pattern Recognition: An Algorithmic Approach*, pages 123–146, 2011.

T. Neubert and F. Christiansen. Small-scale, field-aligned currents at the top-side ionosphere. *Geophysical Research Letters*, 30(19), 2003.

P. Newell and J. Gjerloev. Evaluation of SuperMAG auroral electrojet indices as indicators of substorms and auroral power. *Journal of Geophysical Research: Space Physics*, 116(A12), 2011.

H. Niederreiter. *Random number generation and quasi-Monte Carlo methods*. SIAM, 1992.

Y. Nishimura, Y. Deng, L. R. Lyons, R. M. McGranaghan, and M. D. Zettergren. Multiscale dynamics in the high-latitude ionosphere. *Ionosphere dynamics and applications*, pages 49–65, 2021.

NOAA. Definition of the ionospheric regions (structures): *https://www.ngdc.noaa.gov/stp/iono/ionostru.html*.

M. Noja, C. Stolle, J. Park, and H. Lühr. Long-term analysis of ionospheric polar patches based on CHAMP TEC data. *Radio Science*, 48(3):289–301, 2013. doi: 10.1002/rds.20033.

N. Olsen. A new tool for determining ionospheric currents from magnetic satellite data. *Geophysical Research Letters*, 23(24):3635–3638, 1996.

N. Olsen, H. Lühr, T. J. Sabaka, M. Mandea, M. Rother, L. Tøffner-Clausen, and S. Choi. CHAOS—a model of the Earth's magnetic field derived from CHAMP, Ørsted, and SAC-C magnetic satellite data. *Geophysical Journal International*, 166(1):67–75, 2006.

J. Park, K. W. Min, J.-J. Lee, H. Kil, V. P. Kim, H.-J. Kim, E. Lee, and D. Y. Lee. Plasma blob events observed by KOMPSAT-1 and DMSP F15 in the low latitude nighttime upper ionosphere. *Geophysical Research Letter*, 30(21):2114, 2003. doi: 10.1029/2003GL018249.

J. Park, R. Ehrlich, H. Lühr, and P. Ritter. Plasma irregularities in the high-latitude ionospheric f-region and their diamagnetic signatures as observed by champ. *Journal of Geophysical Research: Space Physics*, 117(A10), 2012.

J. Park, M. Noja, C. Stolle, and H. Lühr. The Ionospheric Bubble Index deduced from magnetic field and plasma observations onboard Swarm. *Earth, Planets and Space*, 65:1333–1344, 2013.

H. L. Pécseli. Spectral properties of electrostatic drift wave turbulence in the laboratory and the ionosphere. *Annales Geophysicae*, 33(7):875–900, 2015. doi: 10.5194/angeo-33-875-2015.

H. L. Pécseli, T. Mikkelsen, and S. E. Larsen. Drift wave turbulence in low-β plasmas. *Plasma Physics*, 25(11):1173–1197, 1983. doi: 10.1088/0032-1028/25/11/001.

F. Pedregosa, G. Varoquaux, A. Gramfort, V. Michel, B. Thirion, O. Grisel, M. Blondel, P. Prettenhofer, R. Weiss, V. Dubourg, J. Vanderplas, A. Passos, D. Cournapeau, M. Brucher, M. Perrot, and E. Duchesnay. Scikit-learn: Machine learning in Python. *Journal of Machine Learning Research*, 12:2825–2830, 2011.

P. Peeters, P. C. Simon, O. R. White, G. De Toma, G. J. Rottman, T. N. Woods, and B. G. Knapp. Mg II core-to-wing solar index from high resolution GOME data. 1997.

Z. Peng, C. Wang, and Y. Hu. Role of IMF Bx in the solar wind-magnetosphere-ionosphere coupling. *Journal of Geophysical Research: Space Physics*, 115(A8), 2010.

L. Perna and M. Pezzopane. foF2 vs solar indices for the Rome station: Looking for the best general relation which is able to describe the anomalous minimum between cycles 23 and 24. *Journal of atmospheric and solar-terrestrial physics*, 148:13–21, 2016.

M. Pezzopane and A. Pignalberi. The ESA Swarm mission to help ionospheric modeling: a new NeQuick topside formulation for mid-latitude regions. *Scientific Reports*, 9:12253, 2019. doi: 10.1038/s41598-019-48440-6.

M. Pezzopane, A. Pignalberi, I. Coco, G. Consolini, P. De Michelis, F. Giannattasio, M. F. Marcucci, and R. Tozzi. Occurrence of GPS Loss of Lock Based on a Swarm Half-Solar Cycle Dataset and Its Relation to the Background Ionosphere. *Remote Sensing*, 13(11):2209, 2021. doi: 10.3390/rs 13112209.

J. Phillips, S. Bame, A. Barnes, B. Barraclough, W. Feldman, B. Goldstein, J. Gosling, G. Hoogeveen, D. McComas, M. Neugebauer, et al. Ulysses solar wind plasma observations from pole to pole. *Geophysical research letters*, 22(23):3301–3304, 1995.

V. Pierrard and M. Voiculescu. The 3d model of the plasmasphere coupled to the ionosphere. *Geophysical Research Letters*, 38(12), 2011.

A. Pignalberi. Titipy: A python tool for the calculation and mapping of topside ionosphere turbulence indices. *Computers & Geosciences*, 148:104675, 2021.

A. Pignalberi, M. Pezzopane, and B. Nava. Optimizing the NeQuick Topside Scale Height Parameters Through COSMIC/FORMOSAT-3 Radio Occultation Data . *IEEE Geoscience and Remote Sensing Letters*, 19, 2022. doi: 10.1109/LGRS.2021.3096657.

G. Prölss. Subauroral electron temperature enhancement in the nighttime ionosphere. In *Annales Geophysicae*, volume 24, pages 1871–1885. Copernicus GmbH, 2006.

G. W. Prolss and M. K. Bird. *Physics of the Earth's space environment: an introduction*. Springer, 2004.

A. Quarteroni, R. Sacco, and F. Saleri. *Numerical mathematics*, volume 37. Springer Science & Business Media, 2010.

J. R. Quinlan. *C4. 5: programs for machine learning*. Elsevier, 2014.

A. J. Quinn, V. Lopes-dos Santos, D. Dupret, A. C. Nobre, and M. W. Woolrich. EMD: Empirical Mode Decomposition and Hilbert-Huang Spectral Analyses in Python. *Journal of Open Source Software*, 6(59):2977, 2021. doi: 10.21105/joss.02977. URL `https://doi.org/10.21105/joss.02977`.

D. V. Reames. Quiet-time spectra and abundances of energetic particles during the 1996 solar minimum. *The Astrophysical Journal*, 518(1):473, 1999.

N. Rehman and D. P. Mandic. Empirical mode decomposition for trivariate signals. *IEEE Transactions on signal processing*, 58(3):1059–1068, 2009.

N. Rehman and D. P. Mandic. Multivariate empirical mode decomposition. *Proceedings of the Royal Society A: Mathematical, Physical and Engineering Sciences*, 466(2117):1291–1302, 2010.

C. Reigber, P. Schwintzer, K.-H. Neumayer, F. Barthelmes, R. König, C. Förste, G. Balmino, R. Biancale, J.-M. Lemoine, S. Loyer, et al. The champ-only earth gravity field model eigen-2. *Advances in Space Research*, 31(8):1883–1888, 2003.

I. G. Richardson. Energetic particles and corotating interaction regions in the solar wind. *Space Science Reviews*, 111(3):267–376, 2004.

L. F. Richardson. *Weather prediction by numerical process*. University Press, 1922.

Richmond. Ionospheric electrodynamics using magnetic apex coordinates. *Journal of geomagnetism and geoelectricity*, 47(2):191–212, 1995.

A. Richmond and A. Maute. Ionospheric electrodynamics modeling. *Modeling the ionosphere–thermosphere system*, pages 57–71, 2014.

A. Richmond, E. Ridley, and R. Roble. A thermosphere/ionosphere general circulation model with coupled electrodynamics. *Geophysical Research Letters*, 19(6):601–604, 1992.

H. Rishbeth and I. Müller-Wodarg. Why is there more ionosphere in january than in july? the annual asymmetry in the f2-layer. In *Annales Geophysicae*, volume 24, pages 3293–3311. Copernicus Publications Göttingen, Germany, 2006.

R. Robinson and S. Mende. Ionization and electric field properties of auroral arcs during magnetic quiescence. *Journal of Geophysical Research: Space Physics*, 95(A12):21111–21121, 1990.

A. Rodger, M. Pinnock, J. Dudeney, K. Baker, and R. Greenwald. A new mechanism for polar patch formation. *Journal of Geophysical Research: Space Physics*, 99(A4):6425–6436, 1994.

A. S. Rodger and A. C. Graham. Diurnal and seasonal occurrence of polar patches. *Annales Geophysicae*, 14(5):533–537, 1996. doi: 10.1007/s00585-996-0533-5.

A. S. Rodger, R. J. Moffett, and S. Quegan. The role of ion drift in the formation of ionisation troughs in the mid- and high-latitude ionosphere - a review. *Journal of Atmospheric and Terrestrial Physics*, 54:1–30, 1992. doi: 10.1016/0021-9169(92)90082-V.

J. Ruohoniemi and K. Baker. Large-scale imaging of high-latitude convection with Super Dual Auroral Radar Network HF radar observations. *Journal of Geophysical Research: Space Physics*, 103(A9):20797–20811, 1998.

J. Ruohoniemi and R. Greenwald. Statistical patterns of high-latitude convection obtained from Goose Bay HF radar observations. *Journal of Geophysical Research: Space Physics*, 101(A10): 21743–21763, 1996.

J. Ruohoniemi, R. Greenwald, O. De la Beaujardiere, and M. Lester. The response of the high-latitude dayside ionosphere to an abrupt northward transition in the IMF. In *Annales Geophysicae*, volume 11, pages 544–555, 1993.

C. Russell. The solar wind interaction with the Earth's magnetosphere: A tutorial. *IEEE transactions on plasma science*, 28(6):1818–1830, 2000.

C. Russell. Solar wind and interplanetary magnetic field: A tutorial. *GEOPHYSICAL MONOGRAPH-AMERICAN GEOPHYSICAL UNION*, 125:73–90, 2001.

C. Russell. The structure of the magnetopause. *Planetary and Space Science*, 51(12):731–744, 2003.

P. Sandholt and C. J. Farrugia. Poleward moving auroral forms (pmafs) revisited: responses of aurorae, plasma convection and birkeland currents in the pre-and postnoon sectors under positive and negative imf b y conditions. In *Annales Geophysicae*, volume 25, pages 1629–1652. Copernicus Publications Göttingen, Germany, 2007.

K. H. Schatten, J. M. Wilcox, and N. F. Ness. A model of interplanetary and coronal magnetic fields. *Solar Physics*, 6:442–455, 1969.

F. G. Schmitt and Y. Huang. Stochastic analysis of scaling time series: From turbulence theory to applications. 2016.

R. Schunk and A. Nagy. *Ionospheres: physics, plasma physics, and chemistry*. Cambridge university press, 2009.

H. Schwabe. Sonnenbeobachtungen im jahre 1843. von herrn hofrath schwabe in dessau. *Astronomische Nachrichten, volume 21, issue 15, p. 233*, 21:233, 1844.

P. C. Sen, M. Hajra, and M. Ghosh. Supervised classification algorithms in machine learning: A survey and review. In *Emerging Technology in Modelling and Graphics: Proceedings of IEM Graph 2018*, pages 99–111. Springer, 2020.

M. Snow, J. Machol, R. Viereck, T. Woods, M. Weber, D. Woodraska, and J. Elliott. A revised magnesium II core-to-wing ratio from SORCE SOLSTICE. *Earth and Space Science*, 6(11): 2106–2114, 2019.

S. K. Solanki, B. Inhester, and M. Schüssler. The solar magnetic field. *Reports on Progress in Physics*, 69(3):563, 2006.

A. Spicher, W. J. Miloch, and J. I. Moen. Direct evidence of double-slope power spectra in the high-latitude ionospheric plasma. *Geophysical Research Letters*, 41(5):1406–1412, Mar. 2014. doi: 10.1002/2014GL059214.

A. Spicher, L. B. N. Clausen, W. J. Miloch, V. Lofstad, Y. Jin, and J. I. Moen. Interhemispheric study of polar cap patch occurrence based on Swarm in situ data. *Journal of Geophysical Research: Space Physics*, 122(3):3837–3851, 2017. doi: 10.1002/2016JA023750.

T. Spohn, D. Breuer, and T. Johnson. *Encyclopedia of the solar system.* Elsevier, 2014.

J. C. Stoltzfus. Logistic regression: a brief primer. *Academic emergency medicine*, 18(10):1099–1104, 2011.

B. G. Tabachnick, L. S. Fidell, and J. B. Ullman. *Using multivariate statistics*, volume 6. pearson Boston, MA, 2013.

S. W. Tam, T. Chang, P. M. Kintner, and E. Klatt. Intermittency analyses on the sierra measurements of the electric field fluctuations in the auroral zone. *Geophysical Research Letters*, 32(5), 2005.

T. Tanaka and D. P. Mandic. Complex empirical mode decomposition. *IEEE Signal Processing Letters*, 14(2):101–104, 2007.

K. Tapping. The 10.7 cm solar radio flux (F10. 7). *Space weather*, 11(7):394–406, 2013.

A. Tashchilin and E. Romanova. Numerical modeling the high-latitude ionosphere. In *Solar-Terrestrial Magnetic Activity and Space Environment: Proc. COSPAR Colloquium. Amsterdam*, volume 14, 2002.

G. I. Taylor. The spectrum of turbulence. *Proceedings of the Royal Society of London. Series A-Mathematical and Physical Sciences*, 164(919):476–490, 1938.

P. J. Teunissen and O. Montenbruck. *Springer handbook of global navigation satellite systems*, volume 10. Springer, 2017.

E. Thébault, C. C. Finlay, C. D. Beggan, P. Alken, J. Aubert, O. Barrois, F. Bertrand, T. Bondar, A. Boness, L. Brocco, et al. International geomagnetic reference field: the 12th generation. *Earth, Planets and Space*, 67(1):1–19, 2015.

E. G. Thomas and S. G. Shepherd. Statistical patterns of ionospheric convection derived from mid-latitude, high-latitude, and polar superdarn hf radar observations. *Journal of Geophysical Research: Space Physics*, 123(4):3196–3216, 2018.

W. B. Thompson. *An introduction to plasma physics*. Elsevier, 2013.

D. Torr, M. Torr, and P. Richards. Causes of the f region winter anomaly. *Geophysical Research Letters*, 7(5):301–304, 1980.

J. T. Towards Data Science. Towards Data Science "Logistic Regression Explained". Available online: $https://towardsdatascience.com/logistic-regression-explained-9ee73cede081$., 2020.

R. Tozzi, P. De Michelis, G. Lovati, G. Consolini, A. Pignalberi, M. Pezzopane, I. Coco, F. Giannattasio, and M. F. Marcucci. Polar cap patches scaling properties: Insights from swarm data. *Remote Sensing*, 15(17):4320, 2023.

R. T. Tsunoda. High-latitude F-region irregularities: A review and synthesis. *Reviews of Geophysics*, 26(4):719–760, 1988. doi: 10.1029/RG026i004p00719.

R. T. Tsunoda, R. C. Livingston, J. McClure, and W. Hanson. Equatorial plasma bubbles: Vertically elongated wedges from the bottomside f layer. *Journal of Geophysical Research: Space Physics*, 87(A11):9171–9180, 1982.

R. T. Tsunoda, I. Haggstrom, A. Pellinen-Wannberg, A. Steen, and G. Wannberg. Direct evidence of plasma density structuring in the auroral F region ionosphere. *Radio Science*, 20(4):762–784, 1985. doi: 10.1029/RS020i004p00762.

N. A. Tsyganenko. A magnetospheric magnetic field model with a warped tail current sheet. *Planetary and Space Science*, 37(1):5–20, 1989.

R. K. Ulrich and J. E. Boyden. Carrington coordinates and solar maps. *Solar Physics*, 235:17–29, 2006.

Y. C. Unruh and S. K. Solanki. The wavelength dependence of solar irradiance variations. In *Cool Stars, Stellar Systems, and the Sun*, volume 154, page 700, 1998.

I. G. Usoskin. A history of solar activity over millennia. *Living Reviews in Solar Physics*, 20(1):2, 2023.

R. Vaishnav, C. Jacobi, and J. Berdermann. Long-term trends in the ionospheric response to solar extreme-ultraviolet variations. In *Annales Geophysicae*, volume 37, pages 1141–1159. Copernicus GmbH, 2019.

J. Van Den Ijssel, B. Forte, and O. Montenbruck. Impact of Swarm GPS receiver updates on POD performance. *Earth, Planets and Space*, 68:1–17, 2016.

S. Vennerstrom and T. Moretto. Monitoring auroral electrojets with satellite data. *Space Weather*, 11(9):509–519, 2013.

D. Verscharen, K. G. Klein, and B. A. Maruca. The multi-scale nature of the solar wind. *Living Reviews in Solar Physics*, 16(1):1–136, 2019.

W. Wang, A. Burns, and T. Killeen. A numerical study of the response of ionospheric electron temperature to geomagnetic activity. *Journal of Geophysical Research: Space Physics*, 111(A11), 2006.

S. Watanabe and H. Oya. Occurrence characteristics of low latitude ionosphere irregularities observed by impedance probe on board the Hinotori satellite. *Journal of Geomagnetism and Geoelectricity*, 38(2):125–149, Jan. 1986. doi: 10.5636/jgg.38.125.

D. F. Webb and T. A. Howard. Coronal mass ejections: Observations. *Living Reviews in Solar Physics*, 9(1):1–83, 2012.

A. Wernik, J. Secan, and E. Fremouw. Ionospheric irregularities and scintillation. *Advances in Space Research*, 31(4):971–981, 2003.

N. Wiener, editor. *Time Series*. M.I.T. Press, 1964.

R. F. Woodman and C. La Hoz. Radar observations of f region equatorial irregularities. *Journal of Geophysical Research*, 81(31):5447–5466, 1976.

Z. Wu and N. E. Huang. A study of the characteristics of white noise using the empirical mode decomposition method. *Proceedings of the Royal Society of London Series A*, 460(2046):1597–1611, 2004. doi: 10.1098/rspa.2003.1221.

C. Xiong, C. Stolle, and H. Lühr. The swarm satellite loss of gps signal and its relation to ionospheric plasma irregularities. *Space weather*, 14(8):563–577, 2016.

C. Xiong, C. Stolle, and J. Park. Climatology of gps signal loss observed by swarm satellites. In *Annales Geophysicae*, volume 36, pages 679–693. Copernicus Publications Göttingen, Germany, 2018.

C. Xiong, F. Yin, X. Luo, Y. Jin, and X. Wan. Plasma patches inside the polar cap and auroral oval: the impact on the spaceborne GPS receiver. *Journal of Space Weather and Space Climate*, 9:A25, 2019.

M. Yamada, R. Kulsrud, and H. Ji. Magnetic reconnection. *Reviews of Modern Physics*, 82(1):603, 2010.

T. Yokoyama, S.-Y. Su, and S. Fukao. Plasma blobs and irregularities concurrently observed by ROCSAT-1 and Equatorial Atmosphere Radar. *Journal of Geophysical Research (Space Physics)*, 112(A5):A05311, 2007. doi: 10.1029/2006JA012044.

M. Yoshida, T. Shimizu, and S. Toriumi. Which component of solar magnetic field drives the evolution of interplanetary magnetic field over the solar cycle? *The Astrophysical Journal*, 950 (2):156, 2023.

Y. Yu and A. J. Ridley. Response of the magnetosphere-ionosphere system to a sudden southward turning of interplanetary magnetic field. *Journal of Geophysical Research: Space Physics*, 114 (A3), 2009.

S. Zhang, L. He, and L. Wu. Statistical study of loss of GPS signals caused by severe and great geomagnetic storms. *Journal of Geophysical Research: Space Physics*, 125(9):e2019JA027749, 2020.

J. B. Zirker. Coronal holes and high-speed wind streams. *Reviews of Geophysics*, 15(3):257–269, 1977.

S. Zou, M. B. Moldwin, A. J. Ridley, M. J. Nicolls, A. J. Coster, E. G. Thomas, and J. M. Ruohoniemi. On the generation/decay of the storm-enhanced density plumes: Role of the convection flow and field-aligned ion flow. *Journal of Geophysical Research (Space Physics)*, 119(10):8543–8559, 2014. doi: 10.1002/2014JA020408.

Acknowledgements

Grazie alla mia supervisor Paola De Michelis, per la costanza e la disponibilità a seguirmi in ogni aspetto di questa esperienza.
Grazie al mio supervisor Francesco Berrilli, per le bellissime lezioni iniziali e per gli utili consigli.
Grazie ai colleghi dell'INGV, che mi hanno fatto sentire accolta in tutte le occasioni e con cui è stato un piacere collaborare.
Grazie a tutte le altre persone preziose che questo dottorato mi ha fatto incontrare: Giusy, Mirko, Marco, Giulia, Feliciana, Alessandro e Matteo. Ci siamo visti poco, ma è stato sempre bellissimo.
Grazie a Mamma, Papà e Stivolo. Per credere in me anche quando io non ci credo per niente, per il sostegno, l'affetto e la pazzia costanti, per le feste più belle di sempre.
Grazie a Nonno Gustavo per la forza, per aver superato tutto con la solita dolcezza infinita.
Grazie a Nonna Nadia per essere la nostra roccia e per farmi ridere sempre un po' troppo.
Grazie ad entrambi per le estati nel posto più bello che ci sia e per gli americani di montagna.
Grazie alla Vitto, proprio perché è la Vitto.
Grazie a Lezie, perché ogni volta è come se non fosse passato un istante dall'ultima.
Grazie a Sara, per tutti gli anni assieme, per essere il mio supporto costante, per aiutarmi anche quando non lo chiedo, per le risate e per le guance marshmallow.
Grazie a Marty, per essere la moglie che non mi merito ma che sono infinitamente felice di aver trovato. Per aver scelto proprio quel posto nel lontano Ottobre 2014.
Grazie ad Abbio, perché ogni Orsetto di Cioccolato ha bisogno del suo Coso e viceversa.
Grazie alla Tribù Trevisan, per avermi accolto nel loro mondo colorato e affettuoso.
Grazie a Chiara, per la dolcezza e per le ossessioni condivise.
Grazie a tutto il gruppo di Specola Beach, per ogni cosa fatta assieme, dagli spritzini, alle cene, alle anatre, al cappuccino e complimenti, al "ma siete amici", al black humor, al BlackMetaller, alle opinioni forti, alle degustazioni lacrimose.
Un grazie particolare ad Erica, Marty e Ro, per essere delle amiche fondamentali, ognuna nel suo modo speciale.
Grazie ad Ame per gli incoraggiamenti continui di questi ultimi 3 anni, per gli scleri, per le passeggiatine (ma sei pazzo?) e per riuscire sempre a farmi ridere. A buon rendere.
Grazie a Cande, Gamling, Nor, Raboso, Robolo, Sgargarock e Sinistria per le avventure più assurde (sia dentro che fuori Thytzë), per aver reso CTC un pennuto estremamente fortunato (sia dentro che fuori Thytzë).
Grazie a Muschio, Giulo e Ghiandy, per essere comparsi nella nostra famiglia e aver reso ogni giornata estremamente più buffa.
Grazie a dodie, per aver reso magici i momenti che più mi terrorizzavano.
Grazie all'Aiarnola e alle sue amiche, per essere sempre lì e per essere sempre con me.
Grazie a Piero, anche se grazie non sarà mai abbastanza. Per esserci stato ogni giorno, per aver reso leggero anche il momento più impegnativo, per le canzoni del mese, per le gitegitegite, per i tramontini, per parlare maleais, per i piantini, per i cervellini siamesi (che bella Danta), per le infinite Tassoni e gli infiniti cetriolini Zuccato (passati, presenti e futuri), per capire sempre. Per essere la cosa più naturale e la più eccezionale.